HIGH-FIDELITY GRAVITY MODELING APPLIED TO SPACECRAFT TRAJECTORIES AND LUNAR INTERIOR ANALYSIS

A Dissertation

Submitted to the Faculty

of

Purdue University

by

Loïc P.R. Chappaz

In Partial Fulfillment of the

Requirements for the Degree

of

Doctor of Philosophy

December 2015

Purdue University

West Lafayette, Indiana

‘ The important thing is not to stop questioning. One cannot help but be in awe when he contemplates the mysteries of eternity, of life, of the marvelous structure of reality. It is enough if one tries merely to comprehend a little of this mystery every day. ’

Albert Einstein

Pour Papily et Mimine

ACKNOWLEDGMENTS

The people in my life have always inspired me to question and seek understanding of random aspects of the world. My family, friends, teachers, and colleagues have supported and motivated me throughout my education. First of all, I want to express my inexhaustible gratitude toward my entire family, my parents and sister particularly, who always supported me, and whom I left to broaden my knowledge at Purdue. Here, I found a new family to inspire me, and I want to thank them for their support and their love. Without their continued support, this work would not have been possible. Over the last several years at Purdue, first as my teacher, and later as my advisor, Professor Howell continuedly challenged me academically. She is an extremely talented and passionate teacher who naturally communicates her passion to students. I am deeply grateful for the opportunity to work with Professor Howell, and I hope this collaboration will continue to be as rewarding and fruitful in the future. I am also thankful for the help and guidance from the members in the research group. Through my graduate studies, I also had the privilege to work with Prof. Melosh, most recently within the context of and supported by NASA's GRAIL mission, an invaluable and enriching experience. Last summer, I had the great opportunity to work at the Jet Propulsion Laboratory under the guidance of Dr. Broschart whom I thank for his mentoring and serving on my committee; I hope to have the chance to collaborate with him again in the future. Additionally, I would like to thank Professor Longuski for serving on my committee, I also enjoyed learning from this highly-skilled teacher through the classes I attended in the field of astrodynamics. I also appreciate the opportunity to work in the Rune and Barbara Eliasen Aerospace Visualization Laboratory that offers state of the art visualization tools. I also thank the Department of Aeronautics and Astronautics and the College of Engineering for

providing partial financial support. I enjoyed being a Teaching Assistant for Professor Howell, it certainly was an enriching experience.

TABLE OF CONTENTS

LIST OF TABLES

LIST OF FIGURES

Figure Page

Figure Page

ABSTRACT

Chappaz, Loïc P.R. Ph.D., Purdue University, December 2015. High-Fidelity Gravity Modeling Applied to Spacecraft Trajectories and Lunar Interior Analysis. Major Professor: Kathleen C. Howell.

As the complexity and boldness of emerging mission proposals increase, and with the rapid evolution of the available computational capabilities, high-accuracy and high-resolution gravity models and the tools to exploit such models are increasingly attractive within the context of spaceflight mechanics, mission design and analysis, and planetary science in general. First, in trajectory design applications, a gravity representation for the bodies of interest is, in general, assumed and exploited to determine the motion of a spacecraft in any given system. The focus is the exploration of trajectories in the vicinity of a system comprised of two small irregular bodies. Within this context, the primary bodies are initially modeled as massive ellipsoids and tools to construct third-body trajectories are developed. However, these dynamical models are idealized representations of the actual dynamical regime and do not account for any perturbing effects. Thus, a robust strategy to maintain a spacecraft near reference third-body trajectories is constructed. Further, it is important to assess the perturbing effect that dominates the dynamics of the spacecraft in such a region as a function of the baseline orbit. Alternatively, the motion of the spacecraft around a given body may be known to extreme precision enabling the derivation of a very high-accuracy gravity field for that body. Such knowledge can subsequently be exploited to gain insight into specific properties of the body. The success of the NASA's GRAIL mission ensures that the highest resolution and most accurate gravity data for the Moon is now available. In the GRAIL investigation, the focus is on the specific task of detecting the presence and extent of subsurface features, such as empty lava tubes beneath the mare surface. In addition to their importance for understanding

the emplacement of the mare flood basalts, open lava tubes are of interest as possible habitation sites safe from cosmic radiation and micrometeorite impacts. Tools are developed to best exploit the rich gravity data toward the numerical detection of such small features.

1. INTRODUCTION

In trajectory design applications, a gravity representation for the bodies of interest is, in general, assumed and exploited to determine the motion of a spacecraft in any given system. Alternatively, the motion of the spacecraft around a given body may be known to extreme precision enabling the derivation of a very high-accuracy gravity field for that body. Such knowledge can subsequently be exploited to gain insight into specific properties of the body. Both analyses require the development of tools to model non-trivial gravity fields with high accuracy and construct strategies to exploit such information to achieve a specific goal.

1.1 Problem Definition

In recent years, several spacecraft have been delivered to the vicinity of small irregular bodies and more complex missions are under development. In 2001, after a series of orbital revolutions to bring the NEAR spacecraft closer to the asteroid 433 Eros and to gather more scientific observations, the vehicle landed on the asteroid surface. [1] Launched in 2007, the current Dawn project is another mission to multiple irregular bodies, with a spacecraft that orbited Vesta for over a year and has now arrived at the dwarf planet Ceres. [2] Currently, ESA's Rosetta spacecraft is orbiting comet 67P/ChuryumovGerasimenko and has successfully delivered a lander to the comet's surface for further exploration of this very irregular body. [3, 4] In 2016, the NASA mission OSIRIS-REX is scheduled to deliver a spacecraft to the asteroid 1999 RQ36 to collect regolith samples and to investigate this potentially hazardous object. [5] Based on such initial steps, the number of proposals involving such spacecraft destinations is generally increasing. In addition, current estimates indicate that approximately sixteen percent of the known near-Earth asteroid population may be

binaries [6] and a few new mission concepts are emerging to visit binary systems comprised of irregular bodies. The ESA-led MarcoPolo-R mission was initially proposed to visit a near-Earth binary asteroid [7] and a NASA AMES investigation proposed a future mission scenario to explore the binary system Didymos. [8] The Asteroid Impact and Deflection Assessment (AIDA) is another mission scenario currently under development conjointly at NASA and ESA whose target is the binary asteroid Didymos. This scenario aims to demonstrate the kinetic impactor concept to deflect an asteroid by impacting the secondary component of the binary system. [9] With other complex plans emerging, further exploration of the dynamical behavior in such an environment is warranted. Yet, to successfully design trajectories to reach such small, arbitrarily-shaped bodies and to explore the nearby regions, a more thorough understanding of the dynamical environment in the vicinity of such systems is required. Typically, in multiple-body regimes, high-fidelity dynamical models are not well-suited to preliminary design. Thus, simplified dynamical models are often exploited to construct baseline trajectories assuming that such models are reasonable representations of the dynamical environment. In this regime, periodic orbits are solutions of particular interest and a key factor to assess the suitability of any orbit for a given scenario is often its stability. Ultimately, trajectories that are initially constructed in an idealized dynamical model require validation in a higher-fidelity model. To maintain a spacecraft near a path that exhibits some desirable characteristics, an automated and autonomous strategy that accounts for unmodeled accelerations would also allow to further leverage baseline trajectories constructed with simplified models.

Recently, the success of NASA's GRAIL mission - a twin spacecraft formation revolving around the Moon in a quasi-circular polar orbit - now provides the highest resolution and most accurate gravity data for the Moon. In contrast to spacecraft trajectory design applications, that is, scenarios where the gravity environment is uncertain and thus is approximated to construct spacecraft motion options, the relative motion of the GRAIL spacecraft is known to unprecedented precision, and consequently allows the determination of the gravity field of the Moon to very high

accuracy. Such detailed information about the gravity of a body allows to investigate surface features but also the interior structure of the body. The low altitude at which some of this data was collected in the GRAIL extended mission potentially allows the detection of small-scale surface or subsurface features. However, the interpretation of high-resolution gravity field models is not trivial and tools to best exploit such information must be developed.

1.2 Engineering and Science Synergy

Through the lifetime of a spacecraft mission, from inception to end-of-life, numerous people are involved in such an endeavor. Often, two teams of people are distinguished, engineering and science. Both teams are, of course, essential to the success of the mission. While the fundamental principles that both engineers and scientists rely upon are the same, often, technical language, notations, and labels differ. Also, each team operates under a different set of objectives, constraints, and perspectives, all of which must, or as much as possible, fit together. Thus, close collaboration and exchange between teams are essential, and yet, typical education tracks for engineering and science only overlap to some very limited extent. Consequently, knowledge and skills to interact with each other during a mission is initially lacking and must be gained through experience, hence, resulting in a lesser efficient process.

During my graduate curriculum at Purdue, I had the chance to collaborate with Prof. Melosh, in the Earth, Atmospheric, and Planetary Science department, through two research projects. Thanks to this collaboration, I learned quantities of fascinating information by simply attending his research group meeting. In addition, through my involvement with the GRAIL mission, I had the great opportunity to attend science team meetings and be closely involved with mission realities. I strongly believe that this enriching scientific experience is a great complement to my core engineering education, and that such a formation would be beneficial to any student that aims

to be involved in spacecraft missions, or any collaborative project, in the future. While one may remain mainly interested in engineering disciplines, or science, it is very beneficial to be exposed to the other side of that same coin. Synergy between the two disciplines, as it translates to synergy between teams during mission design, operation, and analysis, is invaluable to the success of any mission. Hence, such exposure should be encouraged and facilitated for students that are pursuing a degree in such fields. One may even envision a program that would include in its curriculum both engineering and science classes and projects, tailored to the sciences essential to mission design and operation, including planetary science, spacecraft design and spaceflight mechanics.

1.3 Previous Contributors

1.3.1 Historical Overview

In 1609, Kepler first postulated that celestial bodies travel on conic paths rather than on circular orbits or combinations of epicycles. However, not until 1687 did a mathematical model for the relative two-body problem (2BP) confirmed Kepler's observations with Newton's publication of *Principia*. This decisive breakthrough inspired a search for an analytical solution to the general problem of n-bodies moving under the universal law of gravitation. Later, in 1710, Bernoulli proved that conic sections entirely describe the relative motion of two bodies under Newton's law of gravitation. Then, growing interest in the motion under the influence of more than two bodies led to the search for solutions to increasingly complex and new problems, in particular, the three-body problem (3BP). In 1722, Euler, a student of Bernoulli, introduced the idea of a synodic, or rotating, coordinate frame to approach the 3BP in an application to his lunar theories. In the same year, Lagrange establishes the existence of five equilibrium solutions in the restricted Sun-Jupiter 3BP. From Lagrange's findings emerged the prediction that the equilateral libration points in the Sun-Jupiter system host the Trojan asteroids. Exploiting the synodic frame to derive

the equations of the motion for the 3BP, in 1836, Jacobi demonstrated the existence of an integral of the motion, labelled the Jacobi integral or Jacobi constant. The existence of this constant led to another concept known as 'zero velocity surfaces', as originally introduced by Hill in 1878, that define regions in space accessible to the third body. In the last two decades of the nineteenth century, Poincaré also explored the three-body problem and, in 1881, introduced the first-return map, or Poincaré map, as a tool for the study of the stability of periodic orbits [10]. Such a technique requires computer power not available until recently, thus, Poincaré was not able to verify or apply this concept in the 1890's. Later, in 1899, Poincaré demonstrated in his second volume of *Les Méthodes Nouvelles de la Mécanique Céleste* that in the restricted 3BP there exist no transcendental, or non-algebraic, integrals of the motion in addition to the Jacobi constant. But a century later, the Poincaré map is rapidly becoming a key tool in complex trajectory analysis.

The n-body problem does not allow analytical solutions that describe the motion under the influence of multiple bodies but, numerical exploration of the problem has received much more interest as the computational capabilities continue to increase. A new problem that is currently emerging is the behavior of an object in the vicinity of irregular bodies rather than bodies modeled as centrobaric. Regardless of the formulation that is adopted for the gravitational potential function, the study of the behavior of a particle moving under the influence of one or more irregularly-shaped bodies possesses similarities with the n-body problem, because the irregular body can be visualized as a collection of individual point masses. Thus, concepts developed in the study of the n-body problem, in particular the three-body problem, such as the existence of equilibrium solutions and Poincaré sections, are useful in the analysis of asteroid problems.

1.3.2 Models and Motion in the Vicinity of Irregularly-Shaped Bodies

The investigation of the dynamical behavior of a particle in the vicinity of irregularly-shaped bodies and the characterization of features through gravity analyses require models for the gravitational potential function that is associated with such a body. Three fundamental approaches emerged in the 1900's with the significant improvement of the observational technology to supply more detailed observations of the body and as the increasingly demanding computational resources that are required to implement such techniques become available. A first method appeared [11, 12] in the 1930's, based on expansions of the gravitational potential into a harmonic series. The coefficients for the harmonic series are determined from ground-based observations or from direct measurements that only became available much later during fly-bys. Assuming such coefficients are available for the body of interest, methods to evaluate the potential with this approach [11–14], as well as the incorporation of this representation into a dynamical model for trajectory computation, are well-known and widely employed [15–18]. Models including higher-order spherical harmonics are also used for navigation applications [19] in support of mission to such bodies. Another approach to model the gravitational attraction of an irregularly-shaped body consists in filling the body with point masses on an evenly spaced grid. Each point on the grid is assigned an individual mass such that the sum equals the total mass of the body [20,21]. Finally, as computational capabilities have improved, geometric models of the body to compute the gravity potential of a body have also emerged. Methods to generate a shape model in terms of simpler geometric constructs, such as tetrahedra, are available [22]. However, closed-form expressions for the gravitational potential employing this approach only appeared in 1994 derived by Werner [20]. Also, employing such a method for trajectory design or analysis is more recent, in part due to the fact that evaluating the potential of a polyhedron is computationally expensive. [23] Also, the dynamical environment in the vicinity of small irregularly-shaped bodies is very sensitive, in particular, perturbing effects that are often neglected during preliminary

design activities, such as solar tide, solar radiation pressure, body oblateness, can significantly impact the path of a third body. Thus, a necessity for autonomous guidance arises. In recent years, a control scheme that incorporates Multiple Sliding Surfaces Guidance (MSSG) has been investigated for soft landing on asteroids [24] and close proximity operations [25, 26] near an asteroid modeled as a tri-axial ellipsoid.

Current estimates indicate that approximately sixteen percent of the known near-Earth asteroid population may be binaries [6]. As a result, new mission concepts are emerging to visit binary systems comprised of irregular bodies. However, most investigations that involve binary systems have been interested in the motion of the primary system alone, or the motion of natural particles, such as ejecta. Previous analyses have investigated the dynamical environment in the vicinity of a pair of irregularly-shaped bodies where the primary system is represented as an ellipsoid-sphere model [27, 28]. The primary system can also be modeled as an ellipsoid-ellipsoid system [29] and effort has been dedicated in understanding the stability properties of such primary configurations. Some investigations have been completed with alternative approaches that are based on modeling of the primary bodies as geometric polyhedra [30, 31]. Such an approach is very computationally expensive, and while it is useful in analyzing the motion of the primary system alone, or to simulate the natural motion of particle such as ejecta, such an approach is not well-suited for trajectory design. In addition to the construction to primary system motion analysis, Bellerose et al. [27] also explore trajectories options for the robotic exploration of such systems. Also, the MSSG autonomous guidance law is further applied in binary and tertiary system environments [32, 33]. However, there is overall fewer investigations that aim to develop techniques to systematically compute trajectories that satisfy some set of desired characteristics, or solutions of interest such as periodic orbits.

1.3.3 GRAIL

In the GRAIL analysis, because the features of interest are beneath the lunar surface, traditional methods, such as surface imagery and altimetry, do not allow the detection of such features. In contrast, since gravity is sensitive to both surface and subsurface features, gravity-like quantities can, in theory, be leveraged to probe the interior of the Moon. Thus, exploiting the gravity data collected by the GRAIL spacecraft, small buried features may be detectable. Techniques that exploit gravity gradients are also employed on Earth to detect subsurface cavities [34], changes in the crustal structure [35], and even faulting events. [36] However, one key advantage to Earth-based analyses is the possibility for in-situ gravity surveys. For the lunar problem, both proposed strategies rely critically upon the unprecedented resolution and accuracy of the GRAIL gravity data.

1.3.4 Present Work

For trajectory design applications, the goal is to explore the motion of a third body in the vicinity of pair of small irregular bodies, specifically, binary asteroids. Initially, the familiar Circular Restricted Three Body Problem (CRTBP) is employed, that is, a model where the primary bodies are modeled as point masses. Within the context of exploring third-body trajectories in the vicinity of two small irregular bodies, two spherical primaries may not, in general, be a reasonable assumption. This more specific problem motivates the introduction of a dynamical model that incorporates more complexity in the primary system model. Instead, the primary bodies are modeled as massive ellipsoids rather than point masses. To explore the dynamical behavior of a third body near such systems, periodic orbits are of special interest. For ellipsoid-ellipsoid systems, a synchronous primary configuration represents a system that is analogous to the CRTBP. Thus, concepts and tools similar to those applied in the CRTBP are available. In non-synchronous systems, however, the motion of the primary system is not trivial and a Full Two-Body Problem (F2BP) is formu-

lated to describe the motion of the primary system. Then, the dynamical model that describes the behavior of a test particle is time-variant and the same tools are not directly applicable. However, these dynamical models are idealized representations of the actual dynamical regime and do not account for uncertainties in the physical properties of the bodies and other non-gravitational perturbing effects. Then, a design strategy to maintain a spacecraft near reference third-body trajectories that exhibit some desired characteristics is constructed incorporating multiple sliding surfaces guidance, one that is robust agains unmodeled perturbations. Further, within the context of exploring the dynamical behavior of a spacecraft near a pair of small irregular bodies, an important step in the analysis is an assessment of the perturbing effect that dominates the dynamics of the spacecraft in such a region as a function of the baseline orbit. Most common perturbations include the solar tide, solar radiation pressure, and asteroid oblateness. Then, similar to established developments, the goal is to assess the perturbation that arises from existence of a binary system, rather than a single body system.

In the GRAIL investigation, the focus is on the specific task of detecting the presence and extent of subsurface features, such as empty lava tubes beneath the mare surface. In addition to their importance for understanding the emplacement of the mare flood basalts, open lava tubes are of interest as possible habitation sites safe from cosmic radiation and micrometeorite impacts. [37] The existence of such natural caverns is now supported by Kaguyas discoveries of deep pits in the lunar mare. [38] In this investigation, tools are developed to best exploit the rich gravity data toward the numerical detection of such small features. Two independent strategies are considered: one based on gradiometry techniques and a second that relies on cross-correlation of individual tracks. The organization of this investigation is as follows:

- Chapter 2: In this chapter, different gravity models are developed, one based on gravity expansions, that is, spherical harmonics, a second one where the body is modeled as a massive tri-axial ellipsoid, and an alternative geometrical

model of the body, a polyhedron model. For the spherical harmonics approach, the general formulation for the gravitational potential is summarized. For the polyhedron model, the generation of a shape model for the body is discussed and the derivation of a closed-form expression for the gravitational potential is described.

- Chapter 3: Dynamical models that describe the primary system and third-body behavior for different levels of complexity in the primary system model are constructed. For time invariant dynamical models, the single integral of the motion, that is, the Jacobi constant, and zero velocity curves and surfaces are developed to qualitatively explore the problem. Also, the differential equations describing the motion of such a particle possess equilibrium solutions. In general, five equilibrium points emerge for a given system. However, for the dynamical models that incorporate even more complexity, the system is now time-variant and similar tools are not applicable anymore.

- Chapter 4: The study of the motion in the vicinity of the equilibrium points through a set of variational linear scalar equations offers further insight into the problem. Additionally, in a problem that does not allow an analytical solution, the state transition matrix (STM) is defined to aid in predicting the path of a particle based upon linear approximations. Then, differential corrections algorithms that effectively exploit the STM are developed to compute trajectories that satisfy some desired set of characteristics. Also, continuation methods to generate families of similar orbits are discussed. Periodic orbits are particular solutions of great interest in investigating the dynamical behavior of a particle in the vicinity of an irregularly-shaped body but their computation is not trivial. Thus, numerical tools that utilize differential corrections techniques are incorporated into a general algorithm to compute such solutions. General qualitative characteristics of sample periodic solutions, such as stability and bifurcations, are also discussed in this chapter. Finally, mapping techniques

are also introduced to aid further describe the dynamical behavior of the third body.

- Chapter 5: To explore the dynamical behavior of a third body within the vicinity of two primaries, periodic orbits are of special interest. For primary system models with gradually increasing complexity, a large set of periodic orbits is generated. Such periodic orbits are then used to construct a trajectory that satisfies some desired characteristics via an automated strategy to construct a nearby sequence of arcs in such systems. Also, in an effort to further characterize the effect of nonspherical primaries on the behavior of the third body, Poincaré maps are leveraged. Finally, in an initial assessment of the robustness, stability, or feasibility of a given solution under more realistic simulation conditions, selected orbits that are pre-computed with an idealized model are employed as initial guesses in a differential corrections algorithm to produce bounded trajectories that retain similar characteristics in a higher-fidelity dynamical models where the primaries are constructed as polyhedra.

- Chapter 6: The focus of the analysis in Chapter 5 is the behavior of a third body in the vicinity of a system comprised of two irregular bodies that might represent a binary leveraging simplified system models. In this chapter, to include uncertainties in the physical properties of the bodies and other non-gravitational perturbing effects, a strategy to maintain a spacecraft near reference third-body trajectories that exhibit some desired characteristics is constructed incorporating multiple sliding surfaces guidance. To maintain the spacecraft in orbit near a desired reference path, a 'coast and thrust' scheme is proposed.

- Chapter 7: While synchronous systems, or close-to-synchronous systems, are available in the known asteroid population, systems also exist where the primaries move in a configuration that is not fixed relative to any frame, labeled 'non-synchronous' systems. First, non-synchronous primary systems are constructed such that the the motion is periodic. Then, similar to the synchronous

analysis, periodic orbits and tours are constructed exploiting similar numerical tools. Finally, mapping techniques, now leveraging finite-time Lyapunov exponent, are also exploited to specifically investigate the transition between synchronous and non-synchronous systems and the effect onto the third-body behavior.

- Chapter 8: The objective in this chapter is to assess the perturbation that arises from the existence of the secondary body in a binary system, labeled 'binary effect'. To compare the relative strength of several perturbing effects across the parameter space, 'zonal maps' are introduced. The prediction of the binary effect is initially validated using arbitrary initial conditions that are numerically propagated in the circular restricted three-body problem. Then, the validity of the zonal map is further assessed through the numerical integration of initial conditions, that correspond to pre-computed periodic orbits, with a high-fidelity dynamical model.

- Chapter 9: The focus of this investigation is the detection and extent of empty lava tubes beneath the mare surface exploiting the gravity data collected by the GRAIL spacecraft. Two independent strategies, one based on gradiometry techniques and a second that relies on cross-correlation of individual data tracks, are combined into an automated algorithm that aims to construct local maps of the lunar surface and highlight the possible detection of features of interest. The proposed algorithm is first validated using Schroeter Vallis, the largest known lunar sinuous rille, as a test feature. Then, another region near a South channel of Rima Sharp is also discussed. Finally, forward modelling techniques are exploited to further characterize the potential lava tube candidates that are identified in this analysis.

- Chapter 10: The results of this investigation are summarized and future areas of research are proposed.

2. HIGH-FIDELITY GRAVITY MODELS

The most commonly used gravitational model to develop the mathematical structure for a force due to a massive body is Newton's law, that is, an inverse square gravity law governing the attractive force between each pair of particles. This model is easiest to apply if the bodies are reduced to point masses. In astrodynamics, the bodies in the model include spacecraft as well as planets and moons. Spacecraft size and mass are usually sufficiently small with respect to the other bodies in the model to justify a point mass assumption. The more massive bodies, that is, planets and moons, are also assumed point masses in most applications: relatively large planets and moons are usually modeled as pseudo-spherical with uniform radial density. In this sense, these bodies are centrobaric. Given such properties, motion in a typical spacecraft-planet-moon system is reasonably modeled using the classical force model consistent with Newton's law involving the force between two particles. For such problems, the Newtonian model supplies an analytical expression for the gravity potential.

In the current investigation, rather than strictly centrobaric models, irregularly-shaped bodies, such as asteroids, and a very detailed representation of the Moon, are the focus. In this case, it is not reasonable to assume that the body is a point mass and, thus, the Newtonian gravitational model to appropriately describe the gravitational force must be extended. Rather than modeling a body as a single particle, consider three different models, one based on gravity expansions, that is, spherical harmonics, and two alternative geometric models of the body, an ellipsoid and a polyhedron model. These models are frequently employed for nonspherical bodies. In each case, analytical expressions to supply exact gravity information for any one body are not available. Each model incorporates some assumptions and only produces an approximation of the actual gravity field. Each approach includes

both advantages and drawbacks and the most appropriate model depends on the application.

2.1 Model Based on Spherical Harmonics

The classical approach to model the gravity field associated with an arbitrary body originates with a model for the body as a collection of particles or differential elements. Then, it is straightforward to derive the gravitational force on a point mass external to the body due to a specific differential mass element within the body as an inverse square law between a pair of particles. The net force due to all the mass elements is then generated by integrating over the mass distribution representing the body. However, the appropriate mass distribution is often not well-known, poorly modeled, or too complex for application. Thus, a more practical approach is an expansion of the gravitational potential into a harmonic series.

To develop a gravity model for an arbitrary body, initially formulate the problem in terms of a classical two-body point mass system. Consider a particle P of mass m_p positioned in three-dimensional space at the location (x, y, z) under the attraction of another particle P_m of mass m at the corresponding location (x_m, y_m, z_m). Define the location of particle P mathematically in terms of an inertial Cartesian coordinate frame with basis vectors $\hat{i}$, $\hat{j}$ and $\hat{k}$ such that the position vector from the base point O to the location of P is defined as $\bar{r}_{m_p}$ for the unit mass and is written $\bar{r}_{m_p} = x\hat{i}+y\hat{j}+z\hat{k}$. The relative locations of the two particles are illustrated in Figure 2.1 and the relative vector $\bar{r}$ locates P relative to P_m. The gravitational force on particle P due to the existence of P_m is written as the gradient of a potential function U,

$$\bar{f} = \bar{\nabla} U = \bar{\nabla} \left\{ G\frac{m}{r} \right\} \tag{2.1}$$

where G is the gravitational constant, r is the distance between the unit mass m_p and the point mass m and $\bar{\nabla}$ is the gradient operator defined in terms of Cartesian

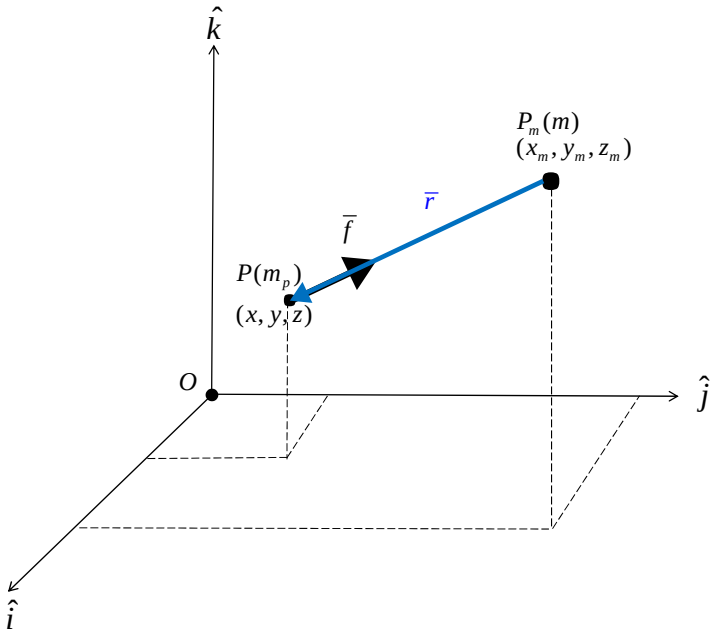

Figure 2.1. Relative positions in the classical two-body problem

coordinates as $\hat{i}\frac{\partial u}{\partial x}+\hat{j}\frac{\partial u}{\partial y}+\hat{k}\frac{\partial u}{\partial z}$, where u is a scalar function. Note that overbars denote vectors.

Now consider an extended rigid body in contrast to a point mass; let the attracting mass P_m be only one particle, or differential element, of the body B. The field point P corresponds again to a point mass located at (x, y, z) under the attraction of a differential mass dm, as depicted in Figure 2.2. Then, if $\bar{r}$ is a vector locating P relative to the differential element, the scalar r is the distance between the differential mass and the field point. The net gravitational potential due to all the mass elements is then generated by integrating over the mass distribution that is representative of the body. Effectively, the integral represents the sum over a collection of differential mass elements dm. The net potential is evaluated as an integral over the volume to produce the gravity potential for the rigid body,

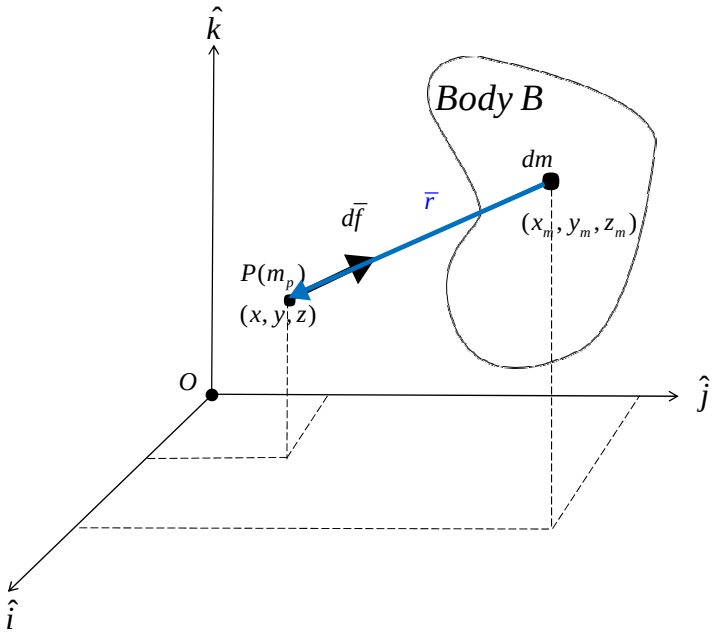

Figure 2.2. Relative positions to locate a point mass and an element of of the extended body

$$U = G \iiint_{body} r^{-1} \rho dV = G \iiint_{body} \frac{\rho(x,y,z)}{r(x,y,z)} dxdydz \tag{2.2}$$

where $dm = \rho dV$ is the differential mass and ρ the density at $r(x, y, z)$. Note that the density may be a function of the location of any differential element.

Given a nonspherical body such that a point mass model is no longer a valid approximation for the gravity field, the evaluation of the volume integral in Eqn. (2.2) requires a model to reflect the shape and density function. The spherical harmonics approach essentially delivers an approximation for the gravity field that is associated with a body of uniform density that is perturbed from a spherical reference shape. Thus, the potential for a point mass is expanded about the spherical reference to generate an infinite series that represents the potential of the nonspherical body. A

rich literature is available, in particular Kaula [13], that details the derivation of the gravitational potential function for an arbitrary body in terms of an infinite series of harmonics originating from the gravity potential for a point mass. [12–14]

To summarize the details of the derivation of the gravitational potential function, consider first the potential function for a point mass. The simple expression is written as,

$$U = \frac{GM}{r} \tag{2.3}$$

Given this potential function, the gravity force is obtained from the vector gradient of the scalar potential, $\bar{\nabla}U$. The component of the gravity force on the field particle in a particular direction is then evaluated as,

$$f_x = \frac{\partial U}{\partial x} = -GM\frac{x}{r^3} \tag{2.4}$$

where f_x is the component of the gravity force in the inertial x direction; components in the other inertial directions are similar. Correspondingly, the second partial derivative is,

$$\frac{\partial^2 U}{\partial x^2} = GM\left(-\frac{1}{r^3} + \frac{3x^2}{r^5}\right) \tag{2.5}$$

Second partials corresponding to y and z are straightforward. Since gravity is a conservative force, that is, the gravity force is the gradient of some scalar potential function U, the potential in free space satisfies Laplace's equation, $\bar{\nabla}^2 U = 0$. [39] Summing the second derivatives for the three Cartesian coordinates, x, y, and z, Laplace's equation is,

$$\bar{\nabla}^2 U = \frac{\partial^2 U}{\partial x^2} + \frac{\partial^2 U}{\partial y^2} + \frac{\partial^2 U}{\partial z^2} = GM\left(-\frac{3}{r^3} + \frac{3(x^2+y^2+z^2)}{r^5}\right) = 0 \tag{2.6}$$

A solution for the gravitational potential is then available by solving the differential equation, that is, Laplace's equation in Eqn. (2.6). Since the spherical harmonics model relies on a spherical reference shape, it is perhaps more appropriate to solve the differential equation as expressed in terms of spherical coordinates rather than Cartesian coordinates. To rewrite the Laplacian of U in terms of spherical coordinates, define the following transformation,

$$\begin{aligned} x &= r\cos\lambda\cos\phi \\ y &= r\sin\lambda\cos\phi \\ z &= r\sin\phi \end{aligned} \tag{2.7}$$

where λ, ϕ, and r are the longitude, latitude, and radial distance that locate the field point with respect to the differential mass element, respectively, and are defined such that $\lambda \in [0, 2\pi]$ and $\phi \in [0, \frac{\pi}{2}]$. To convert Laplace's equation in Eqn. (2.6) to spherical coordinates, the partial derivatives of each spherical coordinate with respect to the rectangular coordinates must be available. Such derivatives are generated by differentiating Eqn. (2.7) with respect to λ, ϕ, and r, in turn, and then solving the simultaneous differential equations for $d\lambda$, $d\phi$, and dr. Using these differential quantities to transform the second partial derivatives of the potential expression from Cartesian to spherical coordinates, Laplace's equation in spherical coordinates is obtained by substituting the spherical partial derivatives into Eqn. (2.6), that is,

$$r^2\nabla^2 U = \frac{\partial}{\partial r}\left(r^2\frac{\partial U}{\partial r}\right) + \frac{1}{\cos\phi}\frac{\partial}{\partial\phi}\left(\cos\phi\frac{\partial U}{\partial\phi}\right) + \frac{1}{\cos^2\phi}\frac{\partial^2 U}{\partial\lambda^2} = 0 \tag{2.8}$$

A solution to $\bar{\nabla}^2 U = 0$ is then achievable with the method of separation of variables [13], producing an expression for the gravitational potential U of the form,

$$U = R(r)\Phi(\phi)\Lambda(\lambda) \tag{2.9}$$

Substituting Eqn. (2.9) into Laplace's equation in Eqn. (2.8), the multivariate differential equation separates into three univariate ordinary differential equations with well-known solutions [40,41], in particular, functions that are labeled as solid spherical harmonics [42]. First, define,

$$F_{l,m,1}(\lambda) = \cos m\lambda \tag{2.10}$$

$$F_{l,m,2}(\lambda) = \sin m\lambda \tag{2.11}$$

for non-negative integers m and l. Also, define the associated Legendre functions [43] $P_l^m(x)$ for integers l and m such that $0 \leq m \leq l$, and for x in $-1 \leq x \leq 1$ such that,

$$P_l^m(x) = \frac{(1-x^2)^{m/2}}{2^l l!} \frac{d^{l+m}}{dx^{l+m}}(x^2-1)^l \tag{2.12}$$

Then, the 'geodetically normalized surface spherical harmonics', denoted hereafter, 'spherical harmonics', of degree l and order m are defined as,

$$H_{l,m,n}(\phi,\lambda) = (A_{l,m})^{-1/2} P_l^m(\sin\phi) F_{l,m,n}(\lambda) \tag{2.13}$$

with values $n = 1, 2$. The normalization constants $A_{l,m}$ are written,

$$A_{l,0} = \frac{1}{2l+1} \tag{2.14}$$

$$A_{l,m} = \frac{1}{2(2l+1)} \frac{(l+m)!}{(l-m)!} \tag{2.15}$$

For a given degree l, there exist $2l+1$ spherical harmonics, as defined in Eqn. (2.13), that form an orthonormal set over the surface of a sphere. More conveniently, the solid spherical harmonics are defined as,

$$V_{l,m,n}(r,\phi,\lambda) = r^{-(l+1)} H_{l,m,n}(\phi,\lambda) \tag{2.16}$$

and satisfy Laplace's equation. As a consequence, a linear combination of solutions also satisfies Eqn. (2.8) and is represented by the sum,

$$U(r,\phi,\lambda) = \sum_{l=2}^{\infty} \sum_{m=0}^{l} a_{l,m} V_{l,m,1}(r,\phi,\lambda) + b_{l,m} V_{l,m,2}(r,\phi,\lambda) \tag{2.17}$$

where $a_{l,m}$ and $b_{l,m}$ are constant coefficients, assuming that the infinite sum in Eqn. (2.17) converges uniformly and sufficiently rapidly to allow term-by-term differentiation in Laplace's equation in Eqn. (2.8). Convergence of such a series for twice differentiable functions, such as the solid spherical harmonics function V, is previously established [44]. Note that when a gravitational potential is expanded in the form of Eqn. (2.17), the coefficients $a_{l,m}$ and $b_{l,m}$ are defined with an inconvenient dimension of *potential per unit length*$^{l-1}$. Thus, a scaled version of Eqn. (2.17) is typically employed such that the constants are dimensionless. After scaling, the complete real solution to Laplace's equation for the gravity potential, in spherical coordinates, is written, [13, 19, 42]

$$U(r,\phi,\lambda) = \frac{GM}{r} \left\{ 1 + \sum_{l=2}^{\infty} \sum_{m=0}^{l} \left(\frac{a_0}{r} \right)^l P_l^m(\sin\phi) [C_{lm} \cos m\lambda + S_{lm} \sin m\lambda] \right\} \tag{2.18}$$

where M is the total mass of the body and a_0, sometimes denoted α, is the largest equatorial radius. The coefficients C_{lm}, S_{lm} are the gravity harmonic coefficients that represent dimensionless fractions of the spherically symmetric potential on the surface $r = a_0$. These coefficients are computed either by evaluating the integrals over the volume of the body or, in practice, by radio tracking data from a spacecraft during a close encounter with the body of interest. In the expression in Eqn. (2.18), the sum

over l originates at $l = 2$ because the degree-zero term is explicitly factored out, that is, GM/r, and represents the potential of a spherically symmetric mass distribution. Also, the degree-one terms vanish from the definition of the working frame where the origin is defined at the center of mass of the body. Regarding the associated Legendre polynomials, these functions are computed from the recurrent expression,

$$(l-m)P_l^m = x(2l-1)P_{l-1}^m - (l+m-1)P_{l-1}^m \tag{2.19}$$

where a closed form expression for the starting value is,

$$P_m^m = (-1)^m(2m-1)!!(1-x^2)^{m/2} \tag{2.20}$$

Evaluating the relationship in Eqn. (2.19) with $l = m+1$ and noting that $P_{m-1}^m = 0$ yields,

$$P_{m+1}^m = x(2m+1)P_m^m \tag{2.21}$$

The associated Legendre polynomials for any degree and order are then computed from the expressions in Eqns. (2.20) and (2.21).

A gravity model represented as a harmonic series possesses advantages. Such series are guaranteed to converge beyond a circumscribing sphere, or minimum sphere; the series can be truncated to equate the accuracy of the field model to the resolution required. Also, given a specific body, evaluating the series to a reasonable order is fairly inexpensive in terms of computational resources. However, there are also disadvantages when incorporating harmonic expansions. First, the gravity force that is computed using this model is always an approximation to the actual field force due to the mass of the body as a result of the truncation of the series; the accuracy depends on the degree of the truncated series. Additionally, the series is not guaranteed to

converge inside the circumscribing sphere, and, in fact, the series often diverges. Techniques to compute the gravity force at the surface of the body do exist, but such approaches are not valid in a global sense and require recomputation of the series at each radius. Therefore, the exterior form of the harmonic expansion is never applicable to particles near or within the surface when considering an irregularly-shaped body. For planetary applications, the divergence may not exist or may be ignored because the body is reasonably modeled as spherical. However, the study of irregularly-shaped bodies, such as asteroids, requires analysis of the particle dynamics inside the circumscribing sphere and, potentially, down to the surface. Certainly, in the case of trajectories to support missions that involve close encounters or landings on asteroids, accurate gravity modeling down to the surface is required. Using the harmonic series model, the surface dynamics as well as the entire region inside the sphere are excluded by necessity. Finally, for particles within the gravity field, the harmonic expansions yield no information concerning the location of the particle relative to the body, that is, the field point might exist either inside or outside the body's volume. For spacecraft navigation applications, another technique must be implemented to detect this critical parameter. As stated by Werner and Scheeres in 1996 [20]:

> "'A spacecraft becomes kinetically challenged if it flies into an asteroid."'

Nevertheless, a gravitational expansion in terms of spherical harmonics is very useful if incorporated appropriately.

2.2 Model Based on an Ellipsoid Shape of the Body

The spherical harmonics representation for the gravitational potential of a massive body supplies a very fine description of the mass distribution of the body of interest, assuming sufficient information is available. Within the context of preliminary design for small-body mission scenarios, detailed information about the primitive bodies in a given system may not be available. Then, consider a simplified approach where a body

is modeled as a massive tri-axial ellipsoid with constant density. Recall the definition for the location of particle P in terms of an inertial Cartesian coordinate frame with basis vectors $\hat{i}$, $\hat{j}$ and $\hat{k}$ such that the position vector from the base point O to the location of P is defined as $\bar{r}_{m_p}$ for the unit mass and is written $\bar{r}_{m_p} = x\hat{i} + y\hat{j} + z\hat{k}$. The gravitational potential due to a massive tri-axial ellipsoid with semi-major axes α, β, and γ onto the unit mass is expressed as, [27, 45]

$$U = \frac{3}{4}\int_{\lambda}^{\infty} \phi(\bar{r}_{m_P}, w)\frac{dw}{\Delta(w)} \tag{2.22}$$

where the functional ϕ is defined as,

$$\phi(\bar{r}_{m_P}, w) = 1 - \frac{x}{\alpha^2 + w} - \frac{y}{\beta^2 + w} - \frac{z}{\gamma^2 + w} \tag{2.23}$$

and,

$$\Delta(w) = \sqrt{(\alpha^2 + w)(\beta^2 + w)(\gamma^2 + w)} \tag{2.24}$$

Then, the gravitational force on particle P due to the existence of P_m is written as the gradient of the potential function U:

$$\bar{\nabla}U = -xR_{j\alpha}\hat{i} - yR_{j\beta}\hat{j} - zR_{j\gamma}\hat{k} \tag{2.25}$$

where,

$$R_{j\alpha} = \frac{3}{2}\int_{0}^{\infty} \frac{du}{(u + \lambda + \alpha^2)\Delta(u + \lambda)} \tag{2.26}$$

$$R_{j\beta} = \frac{3}{2}\int_{0}^{\infty} \frac{du}{(u + \lambda + \beta^2)\Delta(u + \lambda)} \tag{2.27}$$

$$R_{j\gamma} = \frac{3}{2}\int_{0}^{\infty} \frac{du}{(u + \lambda + \gamma^2)\Delta(u + \lambda)} \tag{2.28}$$

In contrast to the spherical harmonics expansion approach, this simplified representation supplies a lower-fidelity description of the gravity of the irregular body. However, such an approach is useful to initially explore the dynamical behavior of a third body, e.g., a spacecraft, in the vicinity of nonspherical bodies.

2.3 Model Based on a Polyhedron Shape of the Body

Another alternate approach to the spherical harmonic expansions for the representation of the gravitational potential is a model that 'constructs' the body as a constant density polyhedron. There is no restriction on the geometric complexity in the polyhedron model: concavities in its surface (e.g., craters) can be included as well as interior voids (e.g., caves), overhangs, and holes that extend through the entire body (torus). Also, no penalty occurs for including fine details; it is not necessary to discretize the entire body at a constant resolution to focus analysis on only one region. This formulation offsets several drawbacks that are apparent in a spherical harmonics representation. First, the gravitational potential is exact for a given shape and density. The resolution of the calculated field depends directly on the level of discretization selected for a particular shape. However, the polyhedron is still an approximation for the actual shape of the body and the accuracy of the gravity field is consistent with its shape determination. Second, the gravity force that is computed from this approach is exact and valid at a distance from infinity to the surface of the body, that is, there is no region of divergence. This property associated with the polyhedron approach is particularly appropriate for the study of surface dynamics or for the analysis of orbits and trajectories that pass close to the body (at least closer than the radius of the minimum sphere corresponding to the equivalent spherical harmonics model). Such a capability is required for missions involving landings or operations in the close vicinity of an asteroid or moon. Finally, as a particular advantage for trajectory analysis, a polyhedron algorithm can detect the relative position of a point, that is, the relative location is apparent even if the position is within the physical

boundaries of the body. Detection of a point inside the volume is accomplished by evaluating the Laplacian of the gravitational potential. The field point falls inside the body if the Laplacian exists, but if it vanishes, the point is beyond the volume of the body. However, as required in trajectory design applications, repeatedly computing the gravitational potential for a particle is very expensive in terms of the computational cost and the cost increases with the resolution of the shape discretization. With the current computational resources, however, such an approach is increasingly affordable and may offer additional insight into the problem. Also, because of its formulation, the polyhedron model assumes a constant density at this time. This fact is generally true for most irregularly-shaped bodies of interest.

2.3.1 Polyhedron Shape Model

To develop the gravitational potential in terms of a polyhedron model, the body is constructed as a constant density polyhedron. The shape approximation for the body is accomplished by discretizing the body into tetrahedrons that are combined to produce a single coherent polyhedron. Precise topographical knowledge of the body is required. In this investigation, the shape information is supplied by radio tracking data from previous missions involving close encounters with an individual body. From the interpretation of images recorded by instruments on-board the spacecraft, the surface of the body is discretized into a set of discrete points that describes the shape of the body. The data is then available in terms of spherical coordinates locating various observed points on the surface of the body relative to its center, that is, longitude, latitude, and distance. A detailed methodology to generate the tetrahedron shape model from the topographical data is described by Khushalani. [46] Essentially, the method relies on constructing numbered vertices from the topographical data to generate a set of faces that approximate the shape of the body. First, the complete latitude range from $90°N$ to $90°S$ is subdivided into smaller finite divisions with constant spacing. The longitude range $0 - 360°$ is similarly segmented. In general, the

step size for the discretization in terms of longitude, $dlon$, as well as latitude, $dlat$, is dictated by the available data for a particular body. Vertices are then numbered beginning with the $90°S$ vertex, i.e., number 1. Then, the $(80°S, 0°)$ vertex is numbered 2, the $(80°S, dlon°)$ vertex is numbered 3, continuing uniformly along the $80°S$ latitude circle. Then, the numbering process is repeated along every other latitude circle as defined by the discretized latitude range. As a consequence, every observed point, represented by three spherical coordinates, is correlated with a vertex number. Next, faces are defined by three vertices, with vertices ordered in a counter-clockwise manner, so that the normal to the faces is directed away from the body. For instance, the first face f_1 is defined by the vertices v_2, v_3, and v_1, in this order. Similar to the vertex numbering process, faces are defined and numbered along every latitude circle originating from the $80°S$ latitude ring to $80°N$. The face numbering procedure generates a table of faces, referenced by a 'face number'; the three vertices corresponding to the face are then represented by the previously defined vertex numbers. Thus, a set of numbered faces, defined by three vertices with known positions in terms of spherical coordinates, is generated. The set of faces describes the shape of the body as represented by the topographical data. Finally, the vertices are more conveniently expressed in terms of Cartesian coordinates employing the transformation,

$$\begin{aligned} x &= r\cos\lambda\cos\phi \\ y &= r\sin\lambda\cos\phi \\ z &= r\sin\phi \end{aligned} \tag{2.29}$$

where (λ, ϕ, r) are the spherical coordinates, that is, longitude, latitude, and distance of the numbered vertices.

The development of a tetrahedron shape is applied to produce geometric models for two irregularly-shaped bodies: Phobos and asteroid 433 Eros. The shapes that are generated for both bodies appear in Figures 2.3 and 2.4. Although Phobos is a moon, the polyhedron model that results from the available data demonstrates significant

topographical features, motivating a non-spherical model. Two representations of Phobos, generated with two different levels of discretization are illustrated in Figure 2.3. In Figure 2.3(a), the model is constructed from topographical data with a 10 degree resolution in longitude and latitude that captures the general shape of the body as well as the main surface irregularities. Then, in Figure 2.3(b), the model features a higher resolution for the shape discretization and finer surface features emerge. Since the accuracy of the gravity potential that is ultimately computed depends on the resolution of the mesh, the accuracy of the potential may be directly assessed from the fidelity of the approximation for the shape. In contrast, Eros is a very elongated and oblate asteroid, not well-suited to classical gravity models. Here, the shapes that are generated via the polyhedron numerical approach better reflect the actual shape of the body, therefore, the polyhedron model produces an improved higher-fidelity approximation for the actual gravity potential compared to the simpler approximation supplied by the ellipsoid model.

2.3.2 Gravity Potential, Acceleration and Gradient Matrix

To compute the gravity potential for an irregular body using the polyhedron approach, the complex shape of the body is discretized into a collection of simpler rigid bodies for which closed-form expressions for the gravity potential, acceleration and gravity gradient are available. The gravitational potential for the entire body is then determined by adding the contribution from each discrete tetrahedron. This concept is illustrated in Figure 2.5: for a given field point X_t at time t, the gravity force contribution from each tetrahedron $\{\bar{F}_1, ..., \bar{F}_j, \bar{F}_{j+1}, ...\}$ is added to produce a sum for the total gravity force $\bar{F}_T$ exerted by the body on the particle. Werner [20,47] derived closed-form expressions for the gravity potential, acceleration, gradient matrix and Laplacian using this strategy to generate the total gravity force. The following summary details this method.

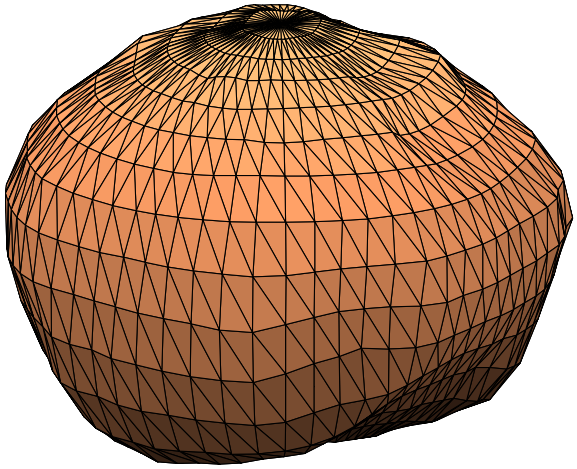

(a) Polyhedron discretization with 2040 faces

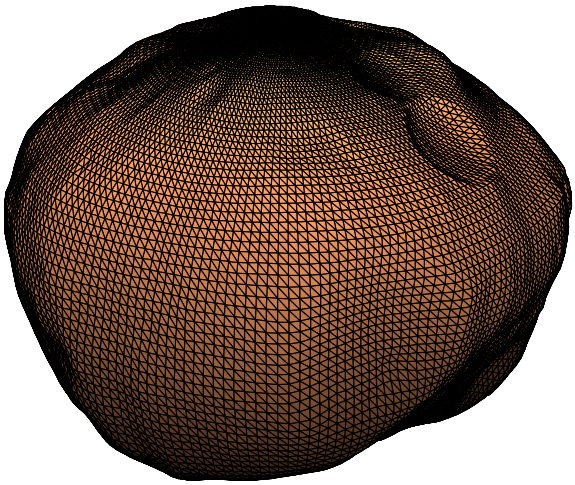

(b) Polyhedron discretization with 32040 faces

Figure 2.3. Shape model for Phobos: polyhedron discretization generated from topographical data with two levels of resolution in longitude and latitude

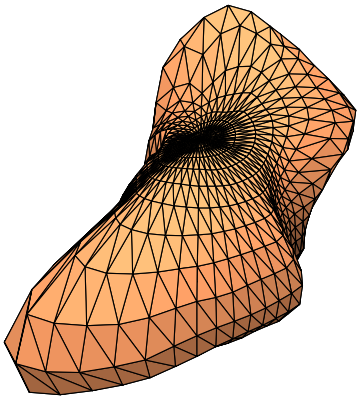

(a) Polyhedron discretization with 2040 faces, projection on the equatorial plane of the body

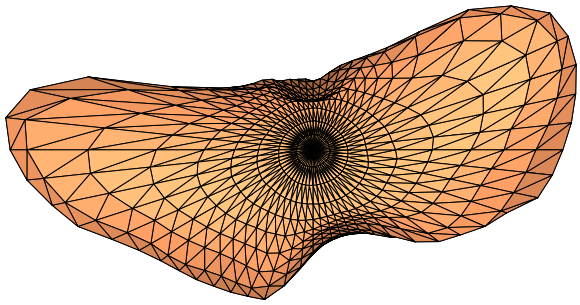

(b) Polyhedron discretization with 2040 faces, three-dimensional view

Figure 2.4. Shape model for 433 Eros: polyhedron discretization with 2040 faces generated from topographical data with a 10 degree resolution in longitude and latitude

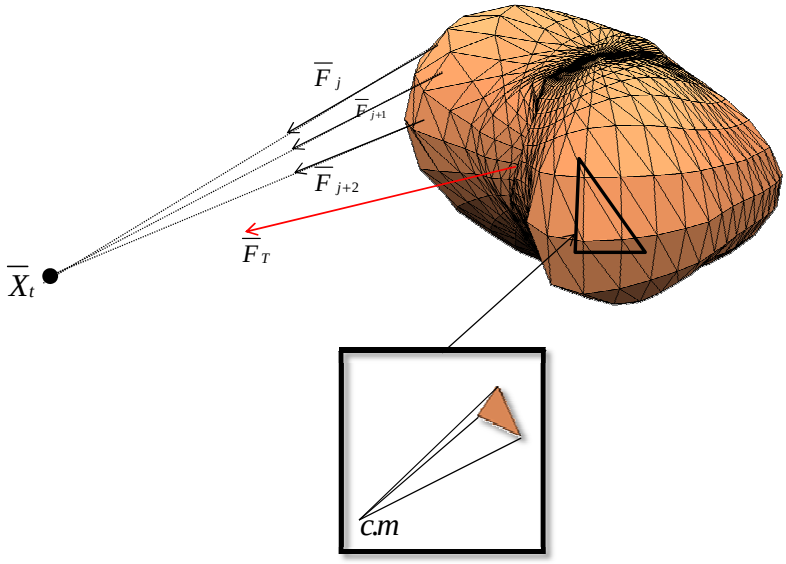

Figure 2.5. Gravity force computation from polyhedron discretization of the body. In the zoom box is represented an individual tetrahedron, whose fourth vertex is the center of mass of the body

To construct a gravity model for an irregularly-shaped body employing the polyhedron approach, first recall the problem formulation in terms of a classical two-body system where the bodies are modeled as point masses. Consider a particle P, of mass m_p, in three-dimensional space at the location (x, y, z), that is, coordinates in terms of an inertial frame; the particle location is expressed relative to an inertially fixed point O. Assume that particle P moves under the attraction of another particle P_m, of mass m, one that is located at the point (ξ, η, ζ), also located with respect to an inertially fixed point O, and, expressed relative to an inertial coordinate frame. De-

fine the location mathematically in terms of an inertial Cartesian coordinate frame with basis unit vectors $\hat{i}$, $\hat{j}$ and $\hat{k}$ such that the position vector $\bar{r}_{m_p}$ for the unit mass is written $\bar{r}_{m_p} = x\hat{i} + y\hat{j} + z\hat{k}$. The problem formulation appears in Figure 2.6. Note

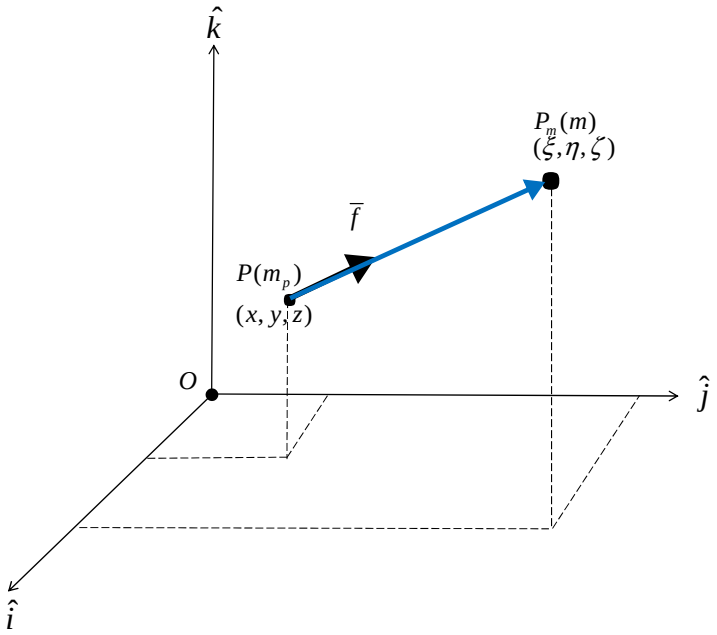

Figure 2.6. Classical formulation of the two-body problem in classical mechanics

that the figure is same as Figure 2.1 but, for this analysis, the vector $\bar{r}$ now locates the point mass P_m with respect to the particle P. Assuming a point mass, the gravitational force due to the existence of P_m acting on P is written as the gradient of the potential function U, that is,

$$\bar{f} = \bar{\nabla} U = \bar{\nabla} \left\{ G \frac{m}{r} \right\} \tag{2.30}$$

where G is the universal gravitational constant, r is the distance between the unit mass m_p and the point mass m and $\bar{\nabla}$ is the gradient operator defined in terms of Cartesian coordinates as $\hat{i}\frac{\partial u}{\partial x} + \hat{j}\frac{\partial u}{\partial y} + \hat{k}\frac{\partial u}{\partial z}$, where u is any scalar function.

Consider an extended rigid body in contrast to a point mass. Let the attracting particle P_m be only one particle or differential element of the body B. The field point P again corresponds to a unit point mass located at (x, y, z) under a gravitational attraction due to the existence of P_m, that is, a differential mass dm, as depicted in Figure 2.7. Again, note that the figure is similar to Figure 2.2 but, the vector $\bar{r}$

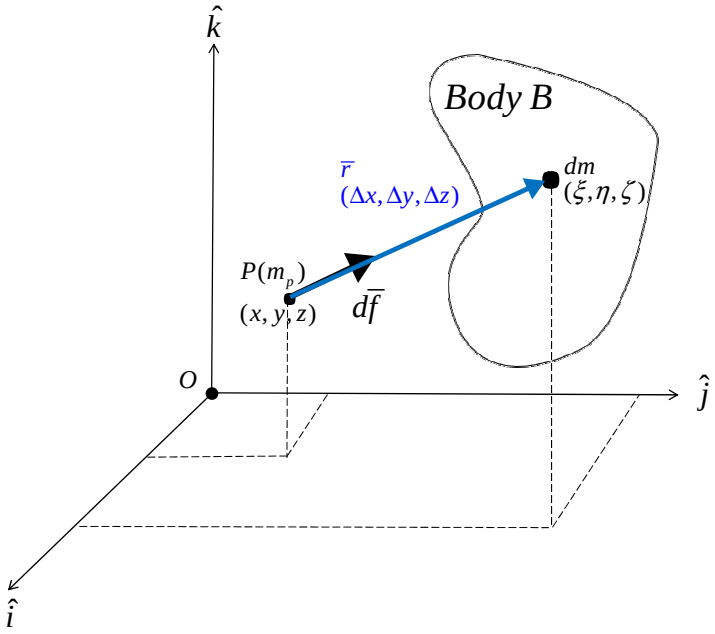

Figure 2.7. Point mass - Extended body formulation

now locates the differential mass dm with respect to the field point P. Then, r is the distance from the field point to the differential mass element. Let the vector $\bar{r}$ originate at the unit mass corresponding to the field point (x, y, z) and terminate at the differential mass dm in the body at (ξ, η, ζ), such that $\bar{r} = \Delta x\hat{i} + \Delta y\hat{j} + \Delta z\hat{k}$. The net gravity force on P due to the existence of the body B is the sum of the differential gravity forces due to each differential mass element. Consistent with this formulation, the net gravitational potential due to all the differential mass elements is also generated by integrating over the mass distribution of the body. Assuming a

constant density, σ, throughout the body, such that $dm = \sigma dV$, the potential is then expressed as,

$$U = G \iiint_{body} r^{-1} dm = G\sigma \iiint_{body} \frac{1}{r} dV \tag{2.31}$$

One approach to evaluate U is to seek a vector-valued function $\bar{w} = \bar{w}(\xi, \eta, \zeta)$ such that $\bar{\nabla} \bullet \bar{w} = r^{-1}$. If such a function exists, the Gauss Divergence theorem [48] allows the potential to be expressed as an integral over the surface of the body instead of its volume. The theorem states that the divergence of a vector field $\bar{w}$, one integrated throughout a volume V, is equal to the inner product of the surface normal $\hat{n}$ and the vector field, integrated over the surface S of the volume,

$$\iiint_V \nabla \bullet \bar{w} dV = \iint_S \hat{n} \bullet \bar{w} dS \tag{2.32}$$

For application of the theorem, the volume V must be bounded and connected, the surface of the volume, i.e., S must be piecewise smooth and orientable, and the vector $\bar{w}$ as well as its first derivative must exist and be continuous throughout V and on S [48]. A polyhedron, that is, a 3D rigid body comprised of a collection of tetrahedrons with planar triangular faces, satisfies these requirements. Thus, the desired vector field function that satisfies $\bar{\nabla} \bullet \bar{w} = \frac{1}{r}$ is $\bar{w} = \frac{1}{2}\hat{r} = \frac{\bar{r}}{2r}$. As a consequence, the potential function is then written in the form,

$$U = G\sigma \iiint_V \frac{1}{r} dV = \frac{1}{2} G\sigma \iint_S \hat{n} \bullet \hat{r} dS \tag{2.33}$$

where $\hat{r} = \frac{\bar{r}}{r} = \frac{\Delta x}{\zeta}\hat{i} + \frac{\Delta y}{\eta}\hat{j} + \frac{\Delta z}{\xi}\hat{k}$, consistent with the Gauss Divergence theorem.

The three-dimensional rigid body is now approximated as a polyhedron. To each triangular planar face f is assigned a Cartesian coordinate system with the origin at the field point; the vector basis is oriented such that $\hat{k}$ is aligned with the outward-

pointing normal of the face $\hat{n}_f$. Unit vectors $\hat{i}$ and $\hat{j}$ lie parallel to the face plane. The components of the previously defined $\bar{r}$ vector, namely Δx, Δy, Δz, are expressed in terms of this coordinate system with Δz constant for a given face. The face and edges definitions appear in Figure 2.8. The total surface integral is then split into a

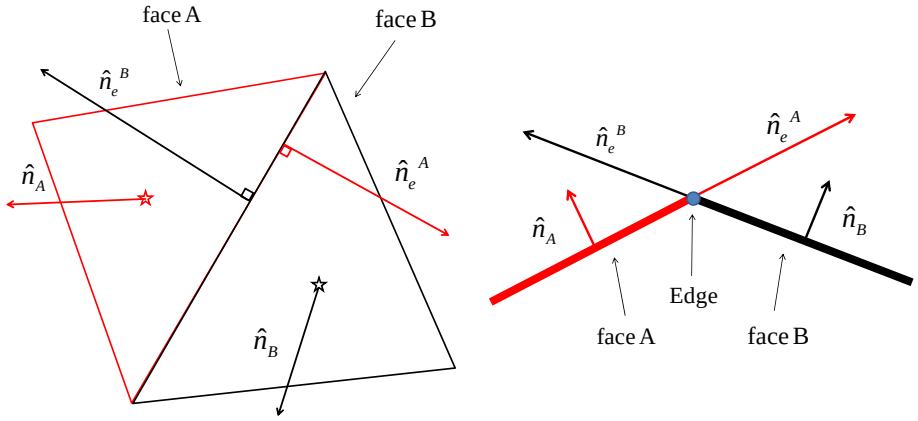

(a) (b)

Figure 2.8. To each face is associated an outward pointing normal $\hat{n}_f$. Each edge shares two faces, thus, two outward pointing normals, one with respect to each face, is defined for each edge, $\hat{n}_e^f$

sum of integrals over the faces of the polyhedron,

$$\begin{aligned} 2U &= G\sigma \iint_S \hat{n} \bullet \hat{r} dS = G\sigma \sum_{faces} \left[\iint_{face} \hat{n}_f \bullet \frac{\bar{r}}{r} dS \right] \\ &= G\sigma \sum_{faces} \hat{n}_f \bullet \bar{r_f} \iint_{face} \frac{1}{r} dS \end{aligned} \tag{2.34}$$

Since the potential is integrated over one face at a time, $\Delta z = \hat{n}_f \bullet \bar{r}$ is constant over the integration on a single face. Thus, $\bar{r}$ is constant as well and is equal to $\bar{r}_f$, the vector from the field point to any point on the face plane. The integral $\int\int_{face} \frac{1}{r} dS$ is clearly the potential over a planar region, and is calculated as a line integral around the boundary of each face of the polyhedron and another term involving the planar

region itself. Similar to $\bar{r}_f$, define another vector $\bar{r}_e$ from the field point to any point along a line defined by the edge e. Using algebraic manipulations, and parameterizing each edge to relate the 'edge' coordinate system to the 'face' frame, to add 'edge' and 'planar face' contribution, this integral is written as the difference between a line integral and a surface integral,

$$\iint_{polygon} \frac{1}{r} dS = \sum_{e \in edges} \hat{n}_e^f \bullet \bar{r}_e^f \cdot \int_e \frac{dS}{r} - \hat{n}_f \bullet \bar{r}_f \cdot \omega_f \tag{2.35}$$

where $\hat{n}_e^f$ is the outward-pointing normal to the edge e such that $\hat{n}_e^f$ is perpendicular to e and lies in the face plane of f as apparent in Figure 2.8. The factor ω_f in Eqn. (2.35) represents the solid angle described by the planar region S as seen from the field point. This factor is also the projection of the surface S onto a unit sphere centered on the field point, as illustrated in Figure 2.9. The integral form of ω_f is,

$$w_f = \iint_S \frac{\Delta z}{r^3} dS \tag{2.36}$$

A more explicit form appears in the final results. Then, the integral $\int_e \frac{dS}{r}$ from Eqn. (2.35) is the potential of a 1D wire. Previous authors [11, 47] demonstrate that this integral is expressed only in terms of the distances l_1 and l_2, that is, the distances between the field point and the two extremities of the wire as well as the edge length e. Let L_e^f be the line integral for each face f such that,

$$L_e^f = \int_e \frac{1}{r} ds = \ln \frac{l_1 + l_2 + e}{l_1 + l_2 - e} \tag{2.37}$$

The dimensionless factors L_e^f and w_f represent the contribution to the total gravitational potential of each edge and face in the polyhedron shape. Substituting the expressions related to $\iint_f \frac{1}{r} dS$ into Eqn. (2.35)-(2.37) into Eqn. (2.34), the potential function is,

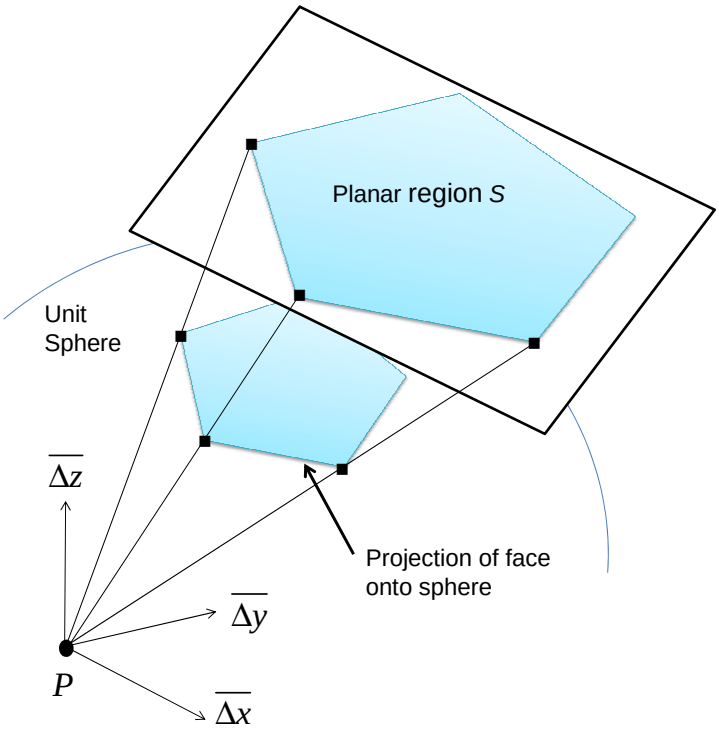

Figure 2.9. The factor ω_f represented as the projection of the surface S onto a unit sphere centered on the field point [47]

$$
\begin{aligned}
U &= \frac{1}{2} G\sigma \sum_{faces} \hat{n}_f \bullet \bar{r}_f \iint_f \frac{1}{r} dS \\
&= \frac{1}{2} G\sigma \sum_{faces} \bar{r}_f \bullet \hat{n}_f \left[\left(\sum_{e \in edges} \hat{n}_e^f \bullet \bar{r}_e^f \cdot L_e^f \right) - \hat{n}_f \bullet \bar{r}_f \cdot \omega_f \right] \\
&= \frac{1}{2} G\sigma \sum_{faces} \left(\sum_{e \in edges} \bar{r}_f \bullet \hat{n}_f \hat{n}_e^f \bullet \bar{r}_e^f \cdot L_e^f \right) - \frac{1}{2} G\sigma \sum_{faces} \bar{r}_f \bullet \hat{n}_f \hat{n}_f \bullet \bar{r}_f \cdot \omega_f
\end{aligned}
\tag{2.38}
$$

Recall that two adjacent faces share a common edge e. The summation in Eqn. (2.38) does not consider repeated edges. Incorporating information concerning common edges results in the elimination of redundant terms and allows the nested sums in

Eqn. (2.38) to be simplified. Then, rather than vectors or matrices, employing dyads allows further simplification, i.e., $\hat{r}_f \bullet \hat{n}_f \hat{n}_e^f \bullet \bar{r}_e^f$ and $\hat{r}_f \bullet \hat{n}_f \hat{n}_f \bullet \hat{r}_f$, and thus, the potential function expression. Dyads are convenient intrinsically for the expression of results. For two adjacent faces A and B that share a common edge P_1P_2, define a dyad $\bar{\bar{E}}_{12} = \hat{n}_A \hat{n}_{12}^A + \hat{n}_B \hat{n}_{21}^B$ expressed in terms of the two edge normals that are associated with the common edge P_1P_2, that is, the edge that joins the vertices P_1 and P_2, as well as the normals corresponding to the faces A and B. To each edge P_iP_j is associated a dyad $\bar{\bar{E}}_e = \bar{\bar{E}}_{ij}$. It is also convenient to define a face dyad $\bar{\bar{F}}_f = \hat{n}_f \hat{n}_f$ for each triangular face f in the polyhedron shape. Then, the gravitational potential is written,

$$U = \frac{1}{2} G\sigma \sum_{edges} \bar{r}_e \bullet \bar{\bar{E}}_e \bullet \bar{r}_e \cdot L_e - \frac{1}{2} G\sigma \sum_{faces} \bar{r}_f \bullet \bar{\bar{F}}_f \bullet \bar{r}_f \cdot \omega_f \tag{2.39}$$

where $\bar{\bar{E}}_e$ and $\bar{\bar{F}}_f$ are 3×3 dyads that implicitly represent the transformation from the 'edge' frame and 'face' frame to a common 'body' frame that allow the summation of all the individual tetrahedron gravitational potential contributions. Then, the gravity acceleration and the gravity gradient matrix are derived by differentiating the potential function once, and twice successively, respectively. The Laplacian of the potential function is also directly available from differentiating the gravitational potential.

In summary, closed-form expressions for the gravity potential, acceleration, gravity gradient matrix and the Laplacian for a polyhedron approximation for the body are available. A triangular face f is defined by an outward-pointing normal $\hat{n}_f$ and a face dyad $\bar{\bar{F}}_f$. Similarly, for each face f, an edge e possesses an outward-pointing normal perpendicular to both e and the face normal $\hat{n}_f$, as well as an edge dyad $\bar{\bar{E}}_e$. Let $\bar{r}_i$ represent the vector from the point field to the polyhedron vertex P_i with length $\| \bar{r}_i \| = r_i$. For each edge e that connects the vertices P_i and P_j of length e_{ij}, the dimensionless factor L_e is,

$$L_e = \ln \frac{r_i + r_j + e_{ij}}{r_i + r_j - e_{ij}} \tag{2.40}$$

Similarly, for a triangular face f defined by the vertices P_i, P_j and P_k, the dimensionless factor ω_f is written as,

$$\omega_f = 2 \arctan \frac{\bar{r}_i \bullet \bar{r}_j \times \bar{r}_k}{r_i r_j r_k + r_i(\bar{r}_j \bullet \bar{r}_k) + r_i(\bar{r}_j \bullet \bar{r}_k) + r_i(\bar{r}_j \bullet \bar{r}_k)} \tag{2.41}$$

Finally, closed form expressions for the gravity potential, acceleration, gravity gradient matrix, and the Laplacian are,

$$U = \frac{1}{2} G\sigma \sum_{edges} \bar{r}_e \bullet \bar{\bar{E}}_e \bullet \bar{r}_e \cdot L_e - \frac{1}{2} G\sigma \sum_{faces} \bar{r}_f \bullet \bar{\bar{F}}_f \bullet \bar{r}_f \cdot \omega_f \tag{2.42}$$

$$\bar{\nabla} U = -\frac{1}{2} G\sigma \sum_{edges} \bar{\bar{E}}_e \bullet \bar{r}_e \cdot L_e + \frac{1}{2} G\sigma \sum_{faces} \bar{\bar{F}}_f \bullet \bar{r}_f \cdot \omega_f \tag{2.43}$$

$$\bar{\nabla}\bar{\nabla} U = -\frac{1}{2} G\sigma \sum_{edges} \bar{\bar{E}}_e \cdot L_e + \frac{1}{2} G\sigma \sum_{faces} \bar{\bar{F}}_f \cdot \omega_f \tag{2.44}$$

$$\nabla^2 U = -G\sigma \sum_{faces} \omega_f \tag{2.45}$$

where G is the gravitational constant, σ is the constant density of the body, $\bar{r}_e$ and $\bar{r}_f$ are the vectors from the point field to the edge e and face f, respectively. Then, $\bar{\bar{E}}_e$ and $\bar{\bar{F}}_f$ are the edge and face dyads, respectively.

With the polyhedron approach, the spherical harmonics formulation and the ellipsoid model previously defined, approximations for the gravitational potential of an irregularly-shaped body, with different levels of fidelity, are available. Each model possesses advantages and drawbacks. The most appropriate gravity model depends on the application. Next, these gravity models are implemented into a mathematical model that describes the motion of a particle in the vicinity of an irregularly-shaped body to investigate the dynamical behavior of a particle in such an environment.

3. DYNAMICAL MODELS FOR MOTION IN THE VICINITY OF IRREGULARLY-SHAPED BODIES

Within the context of trajectory exploration in systems comprised of small irregular bodies, a first step in the analysis is the development of a dynamical model that describes the motion of the primary system. Then, to incorporate the motion of a third body, additional dynamical models that describe the third-body behavior for different levels of complexity in the primary system model are constructed. The complexity and formulation of the dynamical models yield equations of motion that do not allow analytical solutions that describe the behavior of a particle under the influence of such a gravity field. However, numerical exploration offers significant insight into the problem. For time invariant dynamical models, these equations admit one integral of the motion, labelled the Jacobi constant. From this singular constant, zero velocity curves and surfaces bounding the motion of the particle in the vicinity of the primary system are defined. Also, the differential equations describing the motion of such a particle possess equilibrium solutions. In general, five equilibrium points emerge for a given system relative to a rotating frame of reference. However, for the dynamical models that incorporate even more complexity, the system is now time-variant and similar tools are not applicable anymore.

3.1 Circular Restricted Three-Body Problem (CRTBP)

3.1.1 Motion of the primary system

In the CRTBP, the two primaries are point masses, labeled P_1 and P_2 with masses m_1 and m_2, respectively. The mass parameter of the system is defined as $\mu = \frac{m_2}{m_1+m_2}$ and the orbits of the two bodies are assumed to be coplanar and circular relative to

the system barycenter. A barycentric rotating frame is defined such that the z-axis is aligned with the angular velocity of the primary system, the x-axis is directed from P_1 to P_2, and the y-axis completes the right-handed basis.

3.1.2 Three-body dynamical model

The equations of motion for a third body in the CRTBP are derived from Newton's second law of motion, that is, the acceleration of a particle in the gravity field is derived from the gradient of the gravitational potential function. As expressed in the rotating frame, the EOMs are written as,

$$\ddot{\bar{\rho}} + 2\bar{\omega} \times \dot{\bar{\rho}} + \bar{\omega} \times (\bar{\omega} \times \bar{\rho}) + \dot{\bar{\omega}} \times \bar{\rho} = \frac{\partial U}{\partial \bar{\rho}} \tag{3.1}$$

where $\omega = n\hat{z}$ and n is constant and equal to 1 in the nondimensional unit system, $\bar{\rho} = x\hat{x} + y\hat{y} + z\hat{z}$ denotes the location of the third body in the rotating frame with respect to the primary system barycenter. Thus, under the assumptions in the CRTBP, the nondimensional EOMs are reduced to,

$$\ddot{\bar{\rho}} = \left[2n\dot{y} + U_x^*, -2n\dot{x} + U_y^*, U_z^*\right] \tag{3.2}$$

where $U^*(x, y, z, n) = \frac{1}{2}n^2\left(x^2 + y^2\right) + \frac{1-\mu}{d} + \frac{\mu}{r}$ is the pseudo-potential function, d and r represent the distances between the third body and the primaries P_1 and P_2, respectively. Then, the quantities U_x^*, U_y^*, and U_z^* represent the partial derivatives of U^* with respect to the nondimensional coordinates of the third body position. The EOMs are time-invariant and there is a unique known integral of the motion, labeled the Jacobi constant, defined as $C = 2U^* - v^2$ where v denotes the magnitude of the velocity vector of the third body relative to a rotating observer.

3.2 Sphere-Ellipsoid Systems

A first step in increasing the complexity of the model for the primary system and, consequently, the model that describes the motion of a third body that evolves near such a system, is to consider each primary as a massive body rather than a point mass. Consider a configuration such that the primary P_1 is a constant density tri-axial ellipsoid and P_2 is a sphere.

3.2.1 Motion of the primary system

To describe the mutual motion of a pair of massive bodies, consider the Full Two-Body Problem (F2BP). Define one primary, P_1, as an ellipsoid with semi-major axes α, β, and γ, and let P_2, the second primary, be spherical. [27, 45] The distance separating the two primaries, between their respective centers of mass, is denoted r. Both bodies are uniform with constant density. In general, the motion of P_2, with respect to P_1, is numerically simulated in a rotating frame (R_{P_1}) that is fixed in the primary body and moves as the ellipsoidal primary P_1, with unit vectors that are aligned along the ellipsoid semi-major axes. A second rotating frame (R_{P_2}), one that is rotating with the second primary, i.e., P_2, is also introduced, as illustrated in Figure 3.1. The EOMs for the mutual motion of a sphere and an ellipsoid are derived from Newton's second law of motion, as viewed by an inertial observer. To facilitate numerical exploration, a set of characteristic quantities to nondimensionalize the equations are introduced. The characteristic distance is selected as the largest ellipsoid semi-major axes α and the characteristic time is defined as the inverse of the mean orbital motion of the system at this radius, that is, $t^* = \sqrt{\alpha/G(m_1 + m_2)}$. In the rotating frame that is fixed in the ellipsoid, the nondimensional translational and rotational equations of motion are written,

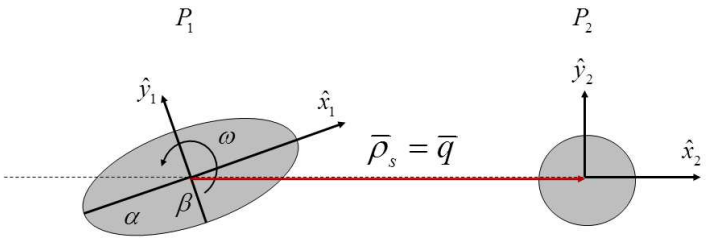

Figure 3.1. Sphere-ellipsoid full two-body problem geometry

$$\ddot{\bar{\rho}}_s + 2\bar{\omega} \times \dot{\bar{\rho}}_s + \bar{\omega} \times (\bar{\omega} \times \bar{\rho}_s) + \dot{\bar{\omega}} \times \bar{\rho}_s = \frac{\partial U_{e_1}}{\partial \bar{\rho}_s} \tag{3.3}$$

$$\bar{\bar{I}} \cdot \dot{\bar{\omega}} + \bar{\omega} \times \bar{\bar{I}} \cdot \bar{\omega} = -\mu \bar{\rho}_s \times \frac{\partial U_{e_1}}{\partial \bar{\rho}_s} \tag{3.4}$$

where $\bar{\rho}_s = x_s\hat{x}_1 + y_s\hat{y}_1 + z_s\hat{z}_1$ is the nondimensional position vector that denotes the location of the center of mass of the spherical primary with respect to the ellipsoid center of mass in the ellipsoid-fixed rotating frame, $\bar{\omega}$ is the angular spin rate of the ellipsoidal primary such that $\bar{\omega}$ is aligned with the inertial $\hat{Z}$ direction, $\bar{\bar{I}}$ is the inertia dyadic for the ellipsoid and associated with its center of mass, and U_{e_1} represents the gravitational potential. Dots denote derivatives with respect to time as viewed by an observer in the working rotating frame, that is, R_{P_1}. It is further assumed that the two primaries move along coplanar orbits, as viewed by an inertial observer, reducing the problem to a two Degree-Of-Freedom (DOF) Hamiltonian system, labeled $\bar{\rho}_s$ and $\bar{p}$. In Hamiltonian form, these EOMs are written in the form,

$$\dot{\bar{\rho}}_s = H_{\bar{p}} \;\; ; \;\; \dot{\bar{p}} = -H_{\bar{\rho}_s} \tag{3.5}$$

where $\bar{\rho}_s$ is the position vector that denotes the location of the sphere with respect to the ellipsoid in the R_{P_1} frame. Then, $\bar{p}$ denotes the corresponding inertial velocity vector, and H is the scalar Hamiltonian. Formulating the problem in terms of

Hamiltonian variables offers the advantage of explicit expressions for the angular rate ω and its rate of change $\dot{\omega}$. The Hamiltonian for the ellipsoid-sphere system is,

$$H = \frac{1}{2}\bar{p}.\bar{p} + \frac{\mu}{2I_{zz}}\left[K - \hat{z}\cdot(\bar{\rho}_s \times \bar{p})\right]^2 - U_{e_1} \tag{3.6}$$

where I_{zz} is the central ellipsoid moment of inertia along the inertial $\hat{Z}$ direction, K is the magnitude of the angular momentum of the system, and U_{e_1} denotes the mutual potential of the ellipsoid-sphere system, that is, computed as an elliptical integral. The simplified Hamiltonian equations of motion in Eqn. (3.5) are numerically integrated to simulate the behavior of any given ellipsoid-sphere system.

3.2.2 Three-body dynamical model (SETBP)

The motion of a massless third body is modeled assuming that the primary system is comprised of the two massive bodies, P_1 and P_2, as illustrated in Figure 3.2. Note in the figure that the third particle is located relative to the ellipsoid center of mass, as viewed in the ellipsoid-fixed frame, by the position vector $\bar{\rho}_e = x_e\hat{x}_1 + y_e\hat{y}_1 + z_e\hat{z}_1$. Similar to the full two-body problem, the equations of the motion that describe the behavior of a massless particle near a primary system are derived from Newton's second law, that is, the acceleration of a particle in the gravity field is derived from the gradient of the gravitational potential function. The EOMs are,

$$\ddot{\bar{\rho}}_e + 2\bar{\omega}\times\dot{\bar{\rho}}_e + \bar{\omega}\times(\bar{\omega}\times\bar{\rho}_e) + \dot{\bar{\omega}}\times\bar{\rho}_e = \frac{\partial U_{SE}}{\partial\bar{\rho}_e} + \frac{\partial U_{e_1}}{\partial\bar{\rho}_s} \tag{3.7}$$

where $\bar{\rho}_s$ represents the location of the sphere center of mass and $\bar{\omega}$ is the orbital angular rate of the ellipsoidal primary P_1. The symbol U_{SE} then denotes the gravitational potential defined as $U_{SE} = \mu U_s + (1-\mu)U_{e_1}$ where U_s and U_{e_1} represent the potentials that are associated with the sphere and the ellipsoid, respectively. Since no analytical solution to the EOMs exists, the set of differential equations is numerically

integrated along with the F2BP EOMs to simulate the motion of a massless third particle.

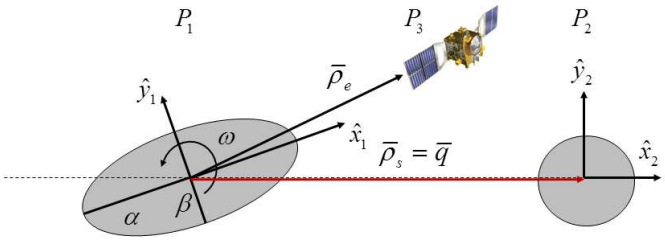

Figure 3.2. Three-body problem geometry under periodic F2BP

3.3 Ellipsoid-Ellipsoid Systems

The complexity in the dynamical model is further increased by considering a primary system that is comprised of two rotating ellipsoids, i.e., both P_1 and P_2 are modeled as tri-axial constant density ellipsoids. Similar to the Sphere-Ellipsoid problem, the motion of the primary system is first addressed before deriving the equations that govern the motion of a third massless body near such a system.

3.3.1 Motion of the primary system

One strategy to derive the equations of the motion that describe the time evolution of such a system is to assume that the mutual orbit of the two ellipsoids is coplanar and equatorial. Then, the problem can be fully described with four degrees of freedom, q_i, one distance and three angles. [29] First, an inertially fixed frame $(\hat{e_1}, \hat{e_2}, \hat{e_3})$ is defined such that the plane spanned by $(\hat{e_1}, \hat{e_2})$ is parallel to the orbital plane of the primary system. Then, a second frame is defined consistent with the rotating frame in the CRTBP, that is, the first base vector $\hat{s_1}$ is directed from P_1 to P_2 between the centers of mass, $\hat{s_3}$ is parallel to the angular orbital velocity of the primary system, and $\hat{s_2}$ completes the right-handed unit vector basis. Thus, the inertial and orbital frames are

related through a rotation about the inertial direction $\hat{e_3} = \hat{s_3}$ by the angle θ. Also, both ellipsoids are assumed to be rotating about the third inertial direction, $\hat{e_3}$, such that the orientation between the body fixed-frame $(\hat{x_i}, \hat{y_i}, \hat{z_i})$ that is associated with the primary i and the orbital frame is fully described by the angle ϕ_i. Consequently, $\hat{e_3} = \hat{z_1} = \hat{z_2}$. Finally, the distance r denotes the separation between the two primary bodies, as illustrated in Figure 3.3. Consider the Lagrangian defined as $L = T - V$,

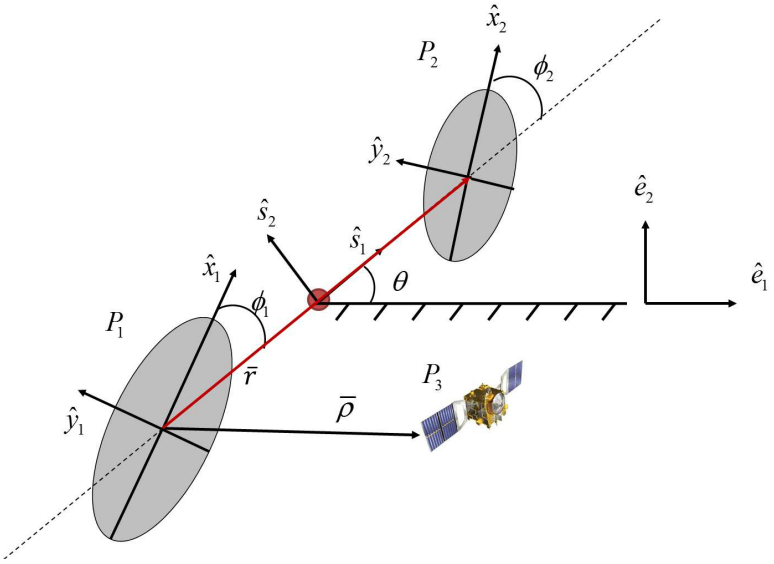

Figure 3.3. Ellipsoid-ellipsoid full two-body problem and three-body problem geometry

where T and V denote the kinetic and potential energy of the system, such that,

$$V(r, \phi_1, \phi 2) = -\frac{Gm_1m_2}{r}\left\{1 + \frac{1}{2r^2}\left[Tr(\bar{\bar{I}}_1) + Tr(\bar{\bar{I}}_2) - \frac{3}{2}\left(I_{1_x} + I_{1_y} - \cos 2\phi_1\left(I_{1_y} - I_{1_x}\right) + I_{2_x} + I_{2_y} - \cos 2\phi_2\left(I_{2_y} - I_{2_x}\right)\right)\right]\right\} \tag{3.8}$$

where G is the universal gravitational constant and $\bar{\bar{I}}_1$ and $\bar{\bar{I}}_2$ represent the central inertia dyadics associated with P_1 and P_2, respectively, such that $\bar{\bar{I}}_i = diag\left[I_{i_x}, I_{i_y}, I_{i_z}\right]$, $i = 1, 2$. Them, the kinetic energy can be written as,

$$T = \frac{1}{2}I_{1_z}(\dot{\phi}_1 + \theta)^2 + \frac{1}{2}I_{2_z}(\dot{\phi}_2 + \theta)^2 + \frac{1}{2}m\dot{r}^2 + \frac{1}{2}m(r\dot{\theta})^2 \tag{3.9}$$

where m denotes the reduced mass of the primary system defined as $m = m_1 m_2/(m_1 + m_2)$. Then, the Lagrangian equations of the motion for the primary system, of the form $d\left(\partial L/\partial \dot{q}_i\right)/dt = \partial L/\partial q_i$, are derived as follows,

$$\ddot{r} = \dot{\theta}r - \frac{1}{m}V_r \tag{3.10}$$

$$\ddot{\phi}_1 = -\left(1 + \frac{mr^2}{I_{1_z}}\right)\frac{1}{mr^2}V_{\phi 1} - \frac{1}{mr^2}V_{\phi 2} + 2\frac{\dot{r}\dot{\theta}}{r} \tag{3.11}$$

$$\ddot{\phi}_2 = -\left(1 + \frac{mr^2}{I_{2_z}}\right)\frac{1}{mr^2}V_{\phi 2} - \frac{1}{mr^2}V_{\phi 1} + 2\frac{\dot{r}\dot{\theta}}{r} \tag{3.12}$$

$$\ddot{\theta} = \frac{1}{mr^2}\left(V_{\phi 1} + V_{\phi 2}\right) - 2\frac{\dot{r}\dot{\theta}}{r} \tag{3.13}$$

where $V_r = \partial V/\partial r$, $V_{\phi 1} = \partial V/\partial \phi_1$, and $V_{\phi 2} = \partial V/\partial \phi_2$.

3.3.2 Three-body dynamical model (EETBP)

The motion of a massless third body is modeled assuming that the primary system is comprised of the two massive ellipsoids, P_1 and P_2, as illustrated in Figure 3.3. Note in the figure that the third particle is located relative to the first primary, P_1, center of mass, as viewed in the inertially-fixed frame, by the position vector $\bar{\rho} = x\hat{e}_1 + y\hat{e}_2 + z\hat{e}_3$. Similar to the full two-body problem, the equations of the motion that describe the behavior of a massless particle near a primary system are derived from Newton's second law. Expressed with respect to the inertial frame, the EOMs are,

$$\ddot{\bar{\rho}} = \frac{\partial U_{EE}}{\partial \bar{\rho}} \tag{3.14}$$

where the symbol U_{EE} then denotes the gravitational potential defined as $U_{EE} = (1-\mu)U_{e_1} + \mu U_{e_2}$ where U_{e_1} and U_{e_2} represent the potential that is associated with P_1

and P_2, respectively. Similar to the CRTBP and SETBP, where no analytical solution to the EOMs exists, the set of differential equations is also numerically integrated along with the F2BP EOMs to simulate the motion of a massless third particle.

3.4 Synchronous Systems

3.4.1 Definition

From the general formulation, equilibrium primary configurations, labeled synchronous systems, are identified, that is, a configuration such that the primaries P_1 and P_2 appear to be fixed in a common rotating frame. As the ellipsoid-ellipsoid problem is more general, the focus is on the definition and existence of synchronous ellipsoid-ellipsoid systems. Also, note that in the particular scenario where both primaries are spherical, i.e., ellipsoids with equal semi-major axes, the problem reduces to the CRTBP. Rather than solving explicitly for the equilibrium solution(s) of the EOMs, consider the total energy of the system, $E = T + V$. One approach to construct an equilibrium system is to solve for the conditions that yield stationary energy variations at a constant value of the angular momentum, that is, [49]

$$E_r = 0 \tag{3.15}$$

$$E_{\dot{r}} = 0 \tag{3.16}$$

$$E_{\phi_i} = 0 \tag{3.17}$$

$$E_{\dot{\phi}_i} = 0 \tag{3.18}$$

Because of the symmetry properties of the problem, equilibrium orientations occur such that the principal axes, i.e., the ellipsoid semi-major axes, are aligned with each other. The objective is, then, to determine the constant rate $\dot{\theta}$ for a given constant distance r and the orientation of the two primaries is such that $\Phi_i = 0, \pm\pi/2, \pi$, that is,

$$\dot{\theta^{*2}} = \frac{G(m_1+m_2)}{r^3}\left[1+\frac{3}{2r^2}\left\{Tr(\bar{\bar{I}}_1)+Tr(\bar{\bar{I}}_2)\right.\right.$$
$$\left.\left.-\frac{3}{2}(I_{1_x}+I_{1_y}\pm(I_{1_y}-I_{1_x})+I_{2_x}+I_{2_y}\pm(I_{2_y}-I_{2_x}))\right\}\right] \tag{3.19}$$

In summary, four equilibrium configurations exist. The focus in this investigation is on the long-axis equilibrium, that is, a primary orientation such that the largest semi-major axis directions corresponding to two ellipsoids, α_1 and α_2, are each aligned with the ellipsoid-ellipsoid direction $\hat{s}_1$. This configuration is notable as it is the smallest energy configuration and, thus, the most stable equilibrium orientation. [29] While synchronous systems, or close-to-synchronous systems, are available in the known asteroid population, systems also exist where the primaries move in a configuration that is not fixed relative to the rotating frame. For 'non-synchronous' systems, the spin rate of ellipsoidal body P_1 and the orbital rate of P_2 are different as viewed from the inertial frame.

3.4.2 Integrals of Motion

The equations of motion for synchronous systems are further simplified by defining a pseudo-potential function. The scalar pseudo-potential is derived from the potential function U, and is defined as,

$$U^* = U_{EE} + \frac{1}{2}(x^2+y^2) \tag{3.20}$$

The scalar equations of motion are then rewritten in their simplest form as a function of the pseudo-potential function,

$$\begin{aligned} \ddot{x} - 2\omega\dot{y} &= \frac{\partial U^*}{\partial x} \\ \ddot{y} + 2\omega\dot{x} &= \frac{\partial U^*}{\partial y} \\ \ddot{z} &= \frac{\partial U^*}{\partial z} \end{aligned} \tag{3.21}$$

where $\omega = \dot{\theta}$ is the angular rate of the primary system. In this form, the differential equations allow the existence of an integral of the motion, the Jacobi integral. An expression for the Jacobi integral is derived by introducing a dot product between the differential equations in Eqn. (3.21) and the rotating nondimensional velocity vector $\dot{\rho} = \dot{x}\hat{x} + \dot{y}\hat{y} + \dot{z}\hat{z}$,

$$\begin{aligned} \dot{x}\ddot{x} + \dot{y}\ddot{y} + \dot{z}\ddot{z} &= U_x^*\dot{x} + U_y^*\dot{y} + U_z^*\dot{z} \\ &= \frac{\partial U^*}{\partial \tau} \end{aligned} \tag{3.22}$$

The scalar expression in Eqn. (3.22) is then directly integrated over the nondimensional time τ to produce the integral of the motion, Jacobi integral, also labelled Jacobi constant,

$$\frac{1}{2}(\dot{x}\hat{x} + \dot{y}\hat{y} + \dot{z}\hat{z}) = \frac{1}{2}v^2 = U^* - \frac{C}{2} \tag{3.23}$$

where the constant of integration is defined as $-\frac{C}{2}$ for convenience. The Jacobi constant is then easily expressed as a function of the velocity and pseudo-potential, i.e.,

$$C = 2(U(x, y, z))^* - v^2 \tag{3.24}$$

where $v = \sqrt{\dot{x}^2 + \dot{y}^2 + \dot{z}^2}$ represents the magnitude of the particle velocity relative to the rotating frame. Note that since the Jacobi constant is a function of v^2 and the

pseudo-potential, U^*, it appears as an energy-like quantity. But, although one integral of the motion exists, it is not sufficient to yield an analytical solution. Nevertheless, the Jacobi integral is very useful for numerical investigation.

3.4.3 Equilibrium Solutions

The basic framework for the investigation of the dynamical model is now available. Equations of motion describing the behavior of a massless particle under the gravity influence of a pair of irregularly-shaped bodies serve as the mathematical model. Because no analytical solution to this set of scalar equations is available, one approach to initially explore the behavior is a search for particular solutions, such as equilibrium points. Such an equilibrium solution occurs only if the velocity and acceleration of the particle with respect to the rotating frame are equal to zero and, thus, are dependent on the formulation of the governing differential equations. Note that, the pseudo-potential is a function only of position. Thus, from Eqn. (3.21), the equilibrium solutions are determined by solving for constant locations $(x_{eq},\ z_{eq},\ z_{eq})$ such that the gradient of the pseudo-potential is equal to zero, that is,

$$\frac{\partial U^*}{\partial x} = \frac{\partial U^*}{\partial y} = \frac{\partial U^*}{\partial z} = 0 \tag{3.25}$$

In general, five points satisfying the stationary criteria emerge in this problem. These solutions are denoted by the symbol $L_i,\ i = 1, ..., 5$ and are ordered by the value of Jacobi constant. Equilibrium points are ordered from $i = 1$ for the largest Jacobi value, or lowest energy level, to $i = 5$ for the smallest value, or largest energy. The derivation of any analytical expressions for these equilibrium locations is challenging due to the nontrivial formulation of the gravitational potential function. Thus, numerical methods are employed to solve the equation in Eqn. (3.25). The equilibrium locations for a sample ellipsoid-sphere primary system with mass ratio $\mu = 0.2$ in the SETBP are illustrated in Figure 3.4. Note that there are three collinear points, labeled L_1, L_2, L_3 and two equilateral points L_4 and L_5. In summary, equilibrium

solutions relative to the rotating frame exist and, in general, five stationary points are located near a pair of irregularly-shaped body.

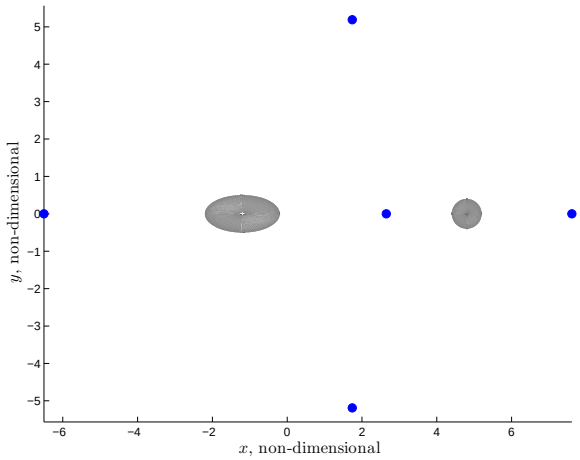

Figure 3.4. Lagrange points in the SE3BP - $\nu = 0.2$

Early evidence of the effect of nonspherical primaries on the behavior of a third body is supplied by computing the equilibrium solutions for an array of sphere-ellipsoid systems. From a system that is equivalent to the CRTBP regime, that is, an ellipsoid primary with semi-major axes $\alpha = \beta = \gamma = 1$, continuing semi-major axes parameters β and γ from 1 to 0.5, that is, from the initial sphere-sphere system toward an ellipsoid-sphere system with a very elongated primary, the corresponding equilibrium locations for each system are straightforwardly constructed. In Figure 3.5, the locations of the equilibrium positions are illustrated for systems with mass ratio $\mu = 0.3$ for the points L_1, L_2, L_3, and L_4 (L_5 is the mirror of L_4 across the x axis); the color scale, from blue to red, represents a decreasing value of the ellipsoid semi-major axes β and γ from 1 to 0.5 such that $\alpha = 1$ and $\beta = \gamma$. Note that as the ellipsoid primary becomes more elongated, from the initial sphere-sphere system, the locations of the equilibrium solutions migrate accordingly. The points L_1 and L_3 tend to shift toward P_1 while L_2 is migrating away from both primaries. Also, L_4 and L_5 move laterally toward the primaries, that is, along the y-axis direction, and migrate axially, that is, along the x-axis direction, toward P_2.

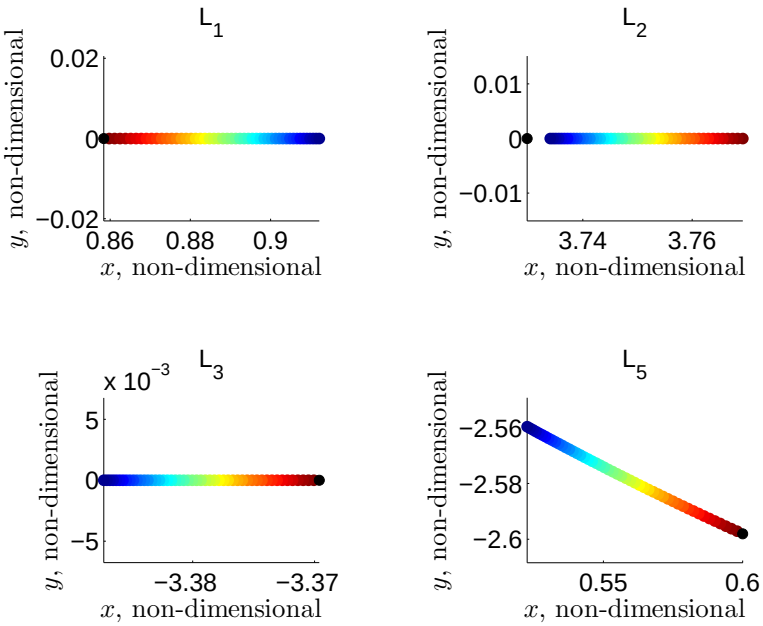

Figure 3.5. Continuation of equivalent Lagrange points from $\beta = \gamma = 1$ to $\beta = \gamma = 0.5$ - $\nu = 0.3$ - $r = 3$

3.4.4 Zero Velocity Curves and Surfaces

The equilibrium solutions and the Jacobi constant are the basis of another important concept. While no analytical solution exists to describe the motion of a particle in this dynamical environment, the motion is bounded under certain conditions. Reconsider the equation for the Jacobi integral,

$$C = 2(U(x, y, z))^* - v^2 \tag{3.26}$$

where the pseudo-potential is only a function of the position of the particle $(x,\ y,\ z)$. Rearranging this expression such that $v^2 = 2(U(x, y, z))^* - C$ suggests possible restrictions on the excursions of the particle P. Clearly, when $C > 2(U(x, y, z))^*$, v^2 becomes negative and yields an imaginary velocity. While perfectly valid mathematically, an imaginary velocity reflects a nonphysical motion for P. Thus, the position coordinates $(x,\ y,\ z)$ are constrained such that $C < 2(U(x, y, z))^*$. Zero relative

velocity in Eqn. (3.26) produces a limiting condition on the possible motion of P, that is,

$$2(U(x,y,z))^* - C = 0 \tag{3.27}$$

Therefore, for a given value of Jacobi constant, combinations of x, y, and z satisfy Eqn. (3.27). Together, the infinite number of solutions describe a surface in three-dimensional space that bounds the possible motion of P. The surface evolves as the value of the constant is modified. These surfaces delineate two regions: 1)where the motion is physically possible; and, 2)the inaccessible regions, i.e., when $C > 2(U(x,y,z))^*$, denoted *forbidden regions*. The regions where the velocity of P is real are split into interior regions, closer to the bodies, and an exterior region, as depicted in Figure 3.6 for a sample Jacobi value such that $C > C(L_1)$.

Without any external force applied to the particle inducing a change in the Jacobi constant value, the Zero Velocity Surfaces (ZVS) bound the motion of P throughout the time evolution. Note that, at a given value of Jacobi constant, the equilibrium points are a particular solution on these surfaces. Thus, the equilibrium point locations satisfy the zero relative velocity condition and, in addition, are subject to zero relative acceleration. In Figures 3.6 - 3.11, these surfaces are represented a sample ellipsoid-ellipsoid primary system as the Jacobi constant varies. On the left, three-dimensional views are plotted and offer direct visualization of the different types of regions as the energy increases. Also, on the right, projections of these surfaces onto the (x,y) plane trace closed curves denoted Zero Velocity Curves (ZVC). Because of their dynamical structure, these surfaces pass arbitrarily close to either body. In fact, since the differential equations incorporate the force model and not any physical dimensions, the ZVS can also emerge within the physical volume of the bodies.

For large values of Jacobi constant, e.g., when $C > C(L_1)$, the zero velocity condition in Eqn. (3.27) yields three solutions that separate four distinct regions, as illustrated in Figure 3.6. One surface surrounds each body, such that the interior

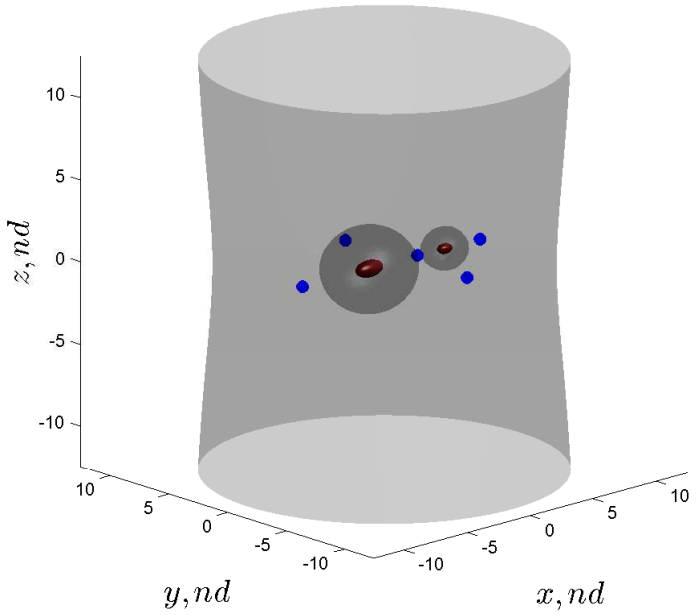

(a) ZVS for $C > C(L_1)$

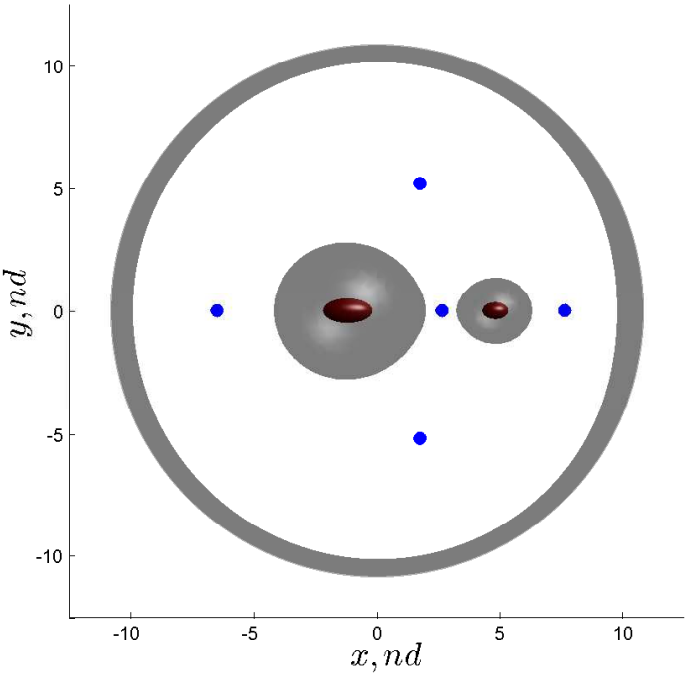

(b) ZVS for $C > C(L_1)$

Figure 3.6. Zero velocity surfaces for sample ellipsoid system for $C > C(L_1)$

region is defined as the volume between the ZVS and either body. In fact, the entire space inside these two surfaces is defined as the interior region but, from the perspective of a trajectory analyst, only the regions beyond the surface boundaries of the bodies are actually of interest. For values of the Jacobi constant that are sufficiently large, however, the interior region is completely contained inside the bodies and no motion is possible within the close vicinity of the body. The second, cylindrically-shaped zero velocity surface, separates the exterior region, far from the primaries, and the forbidden region. The forbidden region is isolated in the white area on the planar projection of the ZVS in Figures 3.7 - 3.11. Thus, for this level of energy, a particle P cannot approach either asteroid from afar or leave its surface or, even, move in close proximity, since crossing the zero velocity surfaces is not allowed.

As the value of Jacobi constant decreases, the inner surfaces begin to expand while the outer cylinder contracts, until the two inner surfaces initially centered around the primary bodies intersect at the first equilibrium point L_1 precisely when $C = C(L_1)$ (Figures 3.7(a) - 3.7(b)). Similarly, for increasing energies, the gateway at L_1 opens and the surfaces then collapse at L_2. In Figure 3.8(a), the gateway at L_1 is open and, in Figure 3.8(b), motion between the two primaries is now possible. As energy further increases, the L_2 gateway opens allowing pathways into and departing the vicinity of the body; a particle can leave the body's vicinity through the gateway at L_2, as illustrated in Figures 3.9(a) - 3.9(b).

With energy further increasing, similar to the L_2 region, the ZVS intersect at L_3 and the forbidden region splits into two distinct lobes, when $C = C(L_3)$, as plotted in Figure 3.9(a) - 3.9(b). Then, for $C < C(L_3)$, the L_3 gateway gradually opens and, as is apparent in the rotating frame in Figure 3.10(a) - 3.10(b), only specific fixed directions are available for approach or escape at a given level of energy.

As the energy level further increases, the two lobes corresponding to the forbidden zones shrink and reduce to a point at L_4 and L_5. Finally, for values smaller than $C(L_5)$, the in-plane ZVC vanish as well as any constraint on the motion of a particle within the (x, y) plane. However, out-of-plane surfaces that bound the motion of P

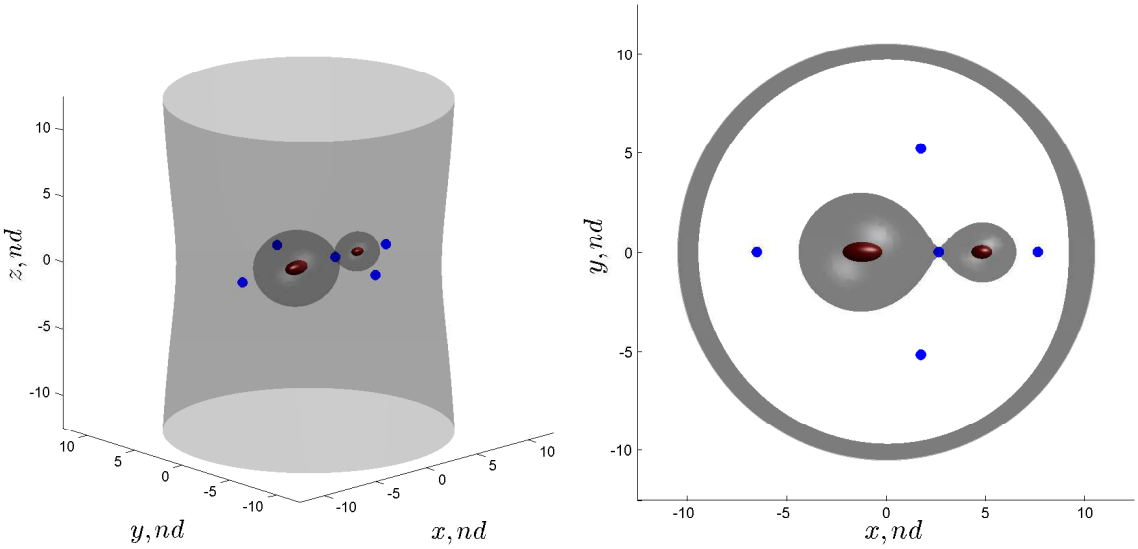

(a) $C = C(L_1)$, 3D view (b) $C = C(L_1)$, (x, y) view

Figure 3.7. Zero velocity surfaces for sample ellipsoid system for $C = C(L_1)$

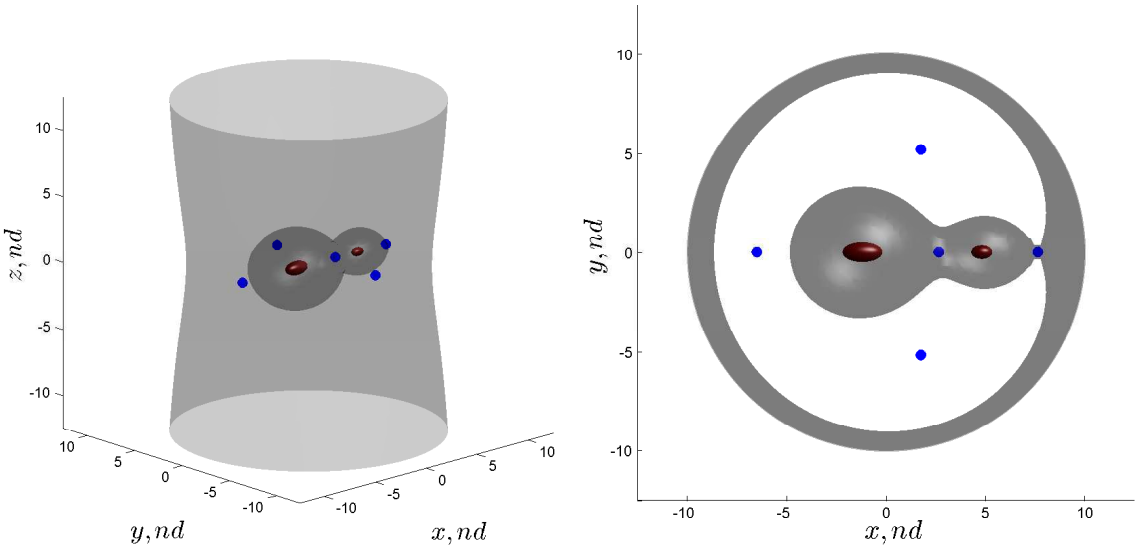

(a) $C = C(L_2)$, 3D view (b) $C = C(L_2)$, (x, y) view

Figure 3.8. Zero velocity surfaces for sample ellipsoid system for $C = C(L_2)$

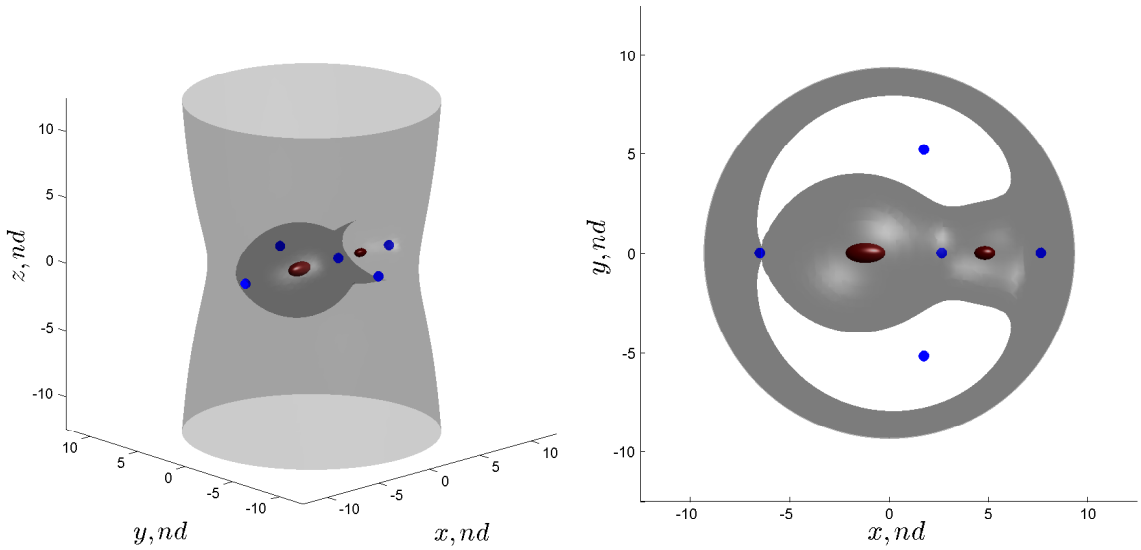

(a) $C = C(L_3)$, 3D view (b) $C = C(L_3)$, (x, y) view

Figure 3.9. Zero velocity surfaces for sample ellipsoid system for $C = C(L_3)$

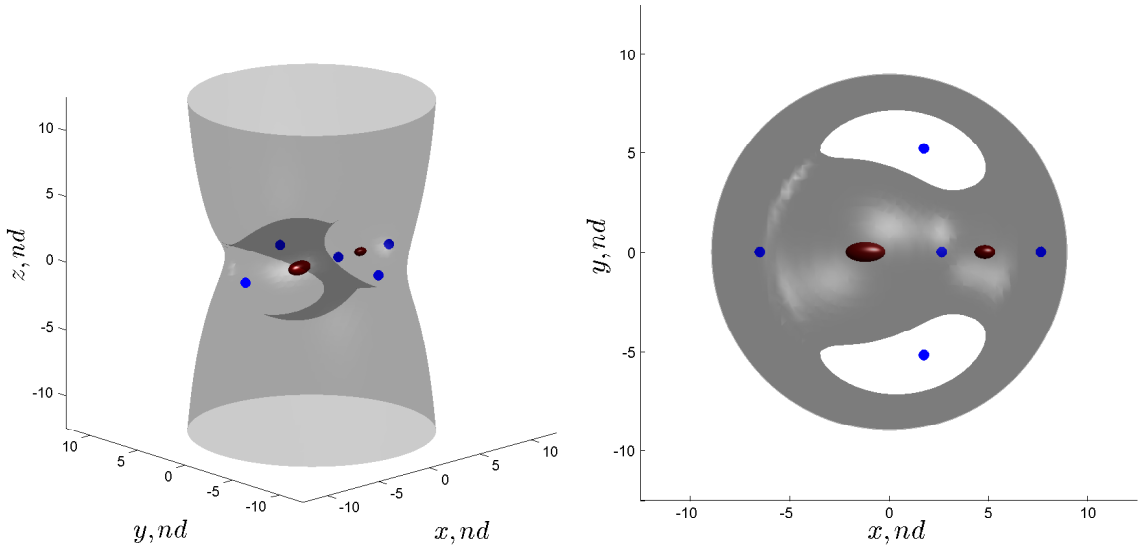

(a) $C(L_3) < C < C(L_4)$, 3D view (b) $C(L_3) < C < C(L_4)$, (x, y) view

Figure 3.10. Zero velocity surfaces for sample ellipsoid system for $C(L_3) < C < C(L_4) = C(L_5)$

in three-dimensional space still exist, as illustrated in Figures 3.11(a) - 3.11(b). As energy continues to increase, these out-of-plane structures also shrink and eventually disappear within the vicinity of the three-body system, clearing any constraints for the motion of a particle in the vicinity of the system. These considerations are based solely on numerical simulations near the sample ellipsoid-ellipsoid system. The mass ratio and shape of any other system involving nonspherical bodies produces further changes in the zero velocity surfaces and curves.

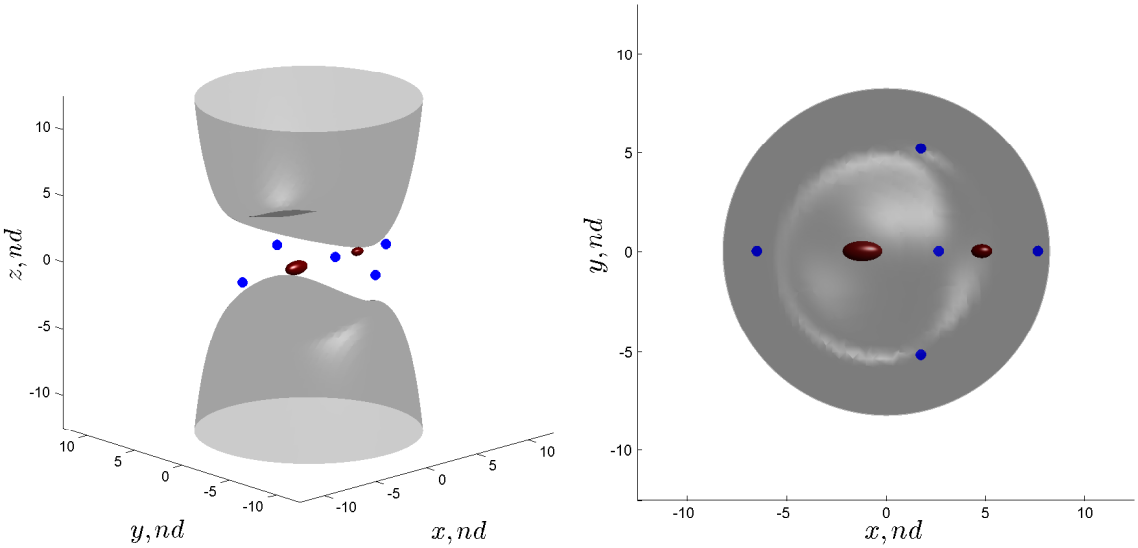

(a) ZVS for $C < C(L_4)$, 3D view

(b) ZVS for $C < C(L_4)$, (x, y) view

Figure 3.11. Zero velocity surfaces for sample ellipsoid system for $C < C(L_4) = C(L_5)$

3.5 Polyhedron-Polyhedron Systems

An alternate approach to the spherical or ellipsoidal shape model for the representation of the primaries in a given system is a model that constructs each body as a constant density polyhedron. There is no restriction on the geometric complexity in the polyhedron model; as a consequence, the relative orbital motion and the attitude

orientation of the two bodies are coupled. Note that polyhedron shape models for each primary can be constructed with symmetry properties that would yield equilibria primary configurations, or synchronous configurations. However, since such scenarios are captured by the simplified dynamical models, SETBP and EETBP, the focus is on systems with very irregular, hence, asymmetric, shape models.

3.5.1 Motion of the primary system

The coupled relative motion of a primary system, one such that each massive body is an arbitrarily-shaped but constant density polyhedron, can be numerically integrated. One approach exploits a semi-implicit Lie Group Variational Integrator (LGVI) and the discretized equations of the motion for the full two-body problem as expressed in a frame that is fixed with and centered at the primary P_1. [30, 50]. The EOMs are coupled and include both the relative orbital motion as well as the attitude of the two bodies as time evolves. As part of the integration process, the mutual forces and moments, that is, the resultant force and moment that each body exerts on one another, must be evaluated. There is no known exact method to compute these quantities for a pair of arbitrary polyhedra, rather the algorithm relies on an infinite series expansions of the gravitational potential function. Then, the force and moment terms are computed as the derivatives of the approximated potential function with respect to the relative position vector and the relative attitude matrix, respectively. [51,52] Also, the numerical integration is very computationally expensive and a trade-off between the resolution of the discretization for each shape model and the number of terms to include in the series expansion for the gravitational potential approximation is necessary to achieve reasonable computation times. For this analysis, a C++ program that leverages Message Passing Interface (MPI) is employed to perform the integration of the relative motion for a given binary system. Simulations are performed on Purdue University's cluster Coates using up to 2800 cores (350 nodes).

Equations of motion

A set of state variables that describe the orbital and attitude motion of the bodies is selected to complete numerical simulations of the coupled motion of the primary system. First, define the relative position vector, $\bar{R}$, the linear momentum, $\bar{P}$, and the angular momentum for the primary and secondary, $\bar{\Gamma}_A$ and $\bar{\Gamma}_B$, respectively. Then, the orientation of the bodies is described by the rotation matrix that relates the inertial frame to the primary-fixed frame, P, and the rotation matrix that relates the secondary-fixed frame to the primary-fixed frame T. Note that in this investigation, the rotations are defined in terms of the angles ψ_i, θ_i, and ϕ_i that correspond to the Euler angles for a $3-1-3$ sequence. For the semi-implicit Lie Group Variational Integrator (LGVI) formulation, the discretized equations of the motion for the full two-body problem, as expressed in a frame that is fixed with and centered at the primary P_1, are written as,

$$\bar{R}_{n+1} = \Phi_{A_n}^T \left(\bar{R}_n + \frac{h}{m}\bar{P}_n - \frac{h^2}{2m}\frac{\partial U_n}{\partial \bar{R}_n} \right) \tag{3.28}$$

$$\bar{P}_{n+1} = \Phi_{A_n}^T \left(\bar{P}_n - \frac{h}{2}\frac{\partial U_n}{\partial \bar{R}_n} \right) - \frac{h}{2}\frac{\partial U_{n+1}}{\partial \bar{R}_{n+1}} \tag{3.29}$$

$$\bar{\Gamma}_{B_{n+1}} = \Phi_{A_n}^T \left(\bar{\Gamma}_{B_n} - \frac{h}{2}\bar{M}_n \right) - \frac{h}{2}\bar{M}_{n+1} \tag{3.30}$$

$$\bar{\Gamma}_{A_{n+1}} = \Phi_{A_n}^T \left(\bar{\Gamma}_{A_n} + \frac{h}{2}\bar{R}_n \times \frac{\partial U_n}{\partial \bar{R}_n} + \frac{h}{2}\bar{M}_n \right) + \frac{h}{2}\bar{R}_{n+1} \times \frac{\partial U_{n+1}}{\partial \bar{R}_{n+1}} + \frac{h}{2}\bar{M}_{n+1} \tag{3.31}$$

$$T_{n+1} = \Phi_{A_n}^T \Phi_n T_n \tag{3.32}$$

$$P_{n+1} = P_n \Phi_{A_n} \tag{3.33}$$

$$hS\left(\Gamma_{B_n} - \frac{h}{2}M_n \right) = \Phi_n \left(T_n \bar{\bar{I}}_{d_B} T_n^T \right) - \left(T_n \bar{\bar{I}}_{d_B} T_n^T \right) \Phi_n^T \tag{3.34}$$

$$hS\left(\Gamma_{B_n} - \frac{h}{2}M_n \right) = \Phi_{A_n} \bar{\bar{I}}_{d_A} - \bar{\bar{I}}_{d_A} \Phi_{A_n}^T \tag{3.35}$$

where h is the fixed time step of the numerical integration process and quantities with subscript n and $n+1$ correspond to current and next step quantities, respectively. Then, m denotes the reduced mass of the primary system defined as $m = m_1 m_2/(m_1+$

m_2), U is the mutual gravitational potential function, and M denotes the mutual gravitational moment. Note that the last two equations are not explicit and must be solved numerically at each step of the numerical integration process for the matrices Φ_n and Φ_{A_n} that are required in the explicit EOMs.

Computational approach for implicit equations

The set of EOMs in Eqn. (3.35) is semi-implicit. The last two EOMs are solved numerically at each step of the numerical integration process for the matrices Φ_n and Φ_{A_n}. Note the Lyapunov-like form of the implicit equations,

$$S(\bar{g}) = FJ_d - J_dF^T \tag{3.36}$$

Two iterative approaches have been proposed to solve this class of equations, [50] one based on an exponential mapping and a second method that relies on Caley transformations. In this investigation, both methods are tested and the Caley implementation is arbitrarily retained. Given $f \in \Re^3$, the Caley transformation is a local diffeomorphism that maps $S(f) \in so(3)$ to $F \in SO(3)$, where,

$$F = cay\, S(f) = (I_{3\times3} + S(f))\,(I_{3\times3} - S(f))^{-1} \tag{3.37}$$

Applying the Caley transformation in Eqn. (3.37) to the general form in Eqn. (3.36) yields a vector equation that is similar to Eqn. (3.36),

$$G(f) = g + g \times f + (g^T f)f - 2Jf = 0 \tag{3.38}$$

and its Jacobian is expressed as,

$$\nabla G(f) = S(g) + (g^T f)I_{3\times3} + fg^T - 2J \tag{3.39}$$

Then, Eqn. (3.38) is iteratively solved using a Newton-Raphson scheme, that is,

$$f_{i+1} = f_i + \nabla G(f_i)^{-1}(g - G(f_i)) \tag{3.40}$$

This process is applied to the last two equations in the set of EOMs in Eqn. (3.35) to solved numerically for the matrices Φ_n and Φ_{A_n} at each step of the numerical integration process.

Mutual potential, force, and moment

The set of EOMs for the coupled relative motion of the primary system relies on the computation of the mutual force and moment that correspond to the polyhedron-shaped bodies. In this process, the evaluation of the mutual potential is also useful. A detailed derivation for these quantities is described by previous researchers [51–53] and the methodology is outlined here. In general, the mutual gravitational potential between two arbitrary rigid bodies, A and B, is expressed as,

$$U = G \iiint_A \iiint_B \frac{1}{d} \rho_A \rho_B dA dB \tag{3.41}$$

where ρ_A and ρ_B is the density of body A and B, respectively, and d denotes the relative distance between two infinitesimal volume elements dA and dB. Also define $\mathbf{r}$ as the relative position vector between the bodies' centroids, as viewed in the inertial frame. Note that symbols in bold font denote tensor quantities, including vectors (rank-1 tensor), matrices (rank-2), and higher-order tensors. For a primary system comprised of two polyhedra, the potential can be evaluated as the sum of each interaction between two possible pairs of tetrahedra in body A and B, denoted a and b, respectively,

$$U = G \sum_{a \in A} \sum_{b \in B} \iiint_a \iiint_b \frac{1}{d} \rho_a \rho_b da db \tag{3.42}$$

where da and db now represent the infinitesimal volume elements for each tetrahedron. Then, one approach to derive the mutual potential due to a pair of polyhedron-shaped bodies is to expand the term $1/d$ in terms of a Legendre polynomial series, such that,

$$U = G \sum_{a \in A} \sum_{b \in B} \rho_a \rho_b T_a T_b \left(\left[\frac{\mathbf{Q}}{r} \right] + \left[-\frac{\mathbf{Q_i w_i}}{r^3} \right] + \left[-\frac{\mathbf{Q_{ij} c_{ij}}}{2r^3} + \frac{\mathbf{3 Q_{ij} w_i w_j}}{2r^5} \right] + ... \right) \quad (3.43)$$

$$= G \sum_{a \in A} \sum_{b \in B} \rho_a \rho_b T_a T_b \left(\hat{U}_0 + \hat{U}_1 + \hat{U}_2 + ... \right) \quad (3.44)$$

where the subscripts i, j, and k varies from 1 to 6 and summations over repeated indexes is implied in all equations, consistent with Einstein's convention. Note that the expression in Eqn. (3.43) is comprised of a shape-dependent and a shape-independent part. In this form, the shape-dependent part is represented by the six-dimensional vector $\mathbf{w}_j$ and the rank-2 tensor $\mathbf{c}_{ij}$,

$$\mathbf{w}_j = \mathbf{r}_s \mathbf{v}_{sj}, \qquad \mathbf{c}_{ij} = \mathbf{v}_{si} \mathbf{v}_{sj} \quad (3.45)$$

where the subscript s varies from 1 to 3 and $\mathbf{v}_{sj}$ is defined as,

$$\mathbf{v}_{sj} \equiv \begin{bmatrix} \Delta x_1^a & \Delta x_2^a & \Delta x_3^a & -\Delta x_1^b & -\Delta x_2^b & -\Delta x_3^b \\ \Delta y_1^a & \Delta y_2^a & \Delta y_3^a & -\Delta y_1^b & -\Delta y_2^b & -\Delta y_3^b \\ \Delta z_1^a & \Delta z_2^a & \Delta z_3^a & -\Delta z_1^b & -\Delta z_2^b & -\Delta z_3^b \end{bmatrix} \quad (3.46)$$

where $[\Delta x_i^j, \Delta y_i^j, \Delta z_i^j]$ denotes the coordinate of the ith vertex of a given triangular face from the polyhedron model of body j with respect to the body centroid. Next, the shape-independent part is contained in the rank-k tensor $\mathbf{Q_{i_1 \ldots i_k}}$ that represents the integral over a 'standard' tetrahedron, that is, the tetrahedron defined by the vertices $(0,0,0)$, $(1,0,0)$, $(0,1,0)$, and $(0,0,1)$. Then, T_a and T_b in Eqn. (3.43) denote the Jacobians required to transform the integral from the standard tetrahedron to the actual shapes of a and of b, respectively. The details of the computation of the

tensors $\mathbf{Q_{i_1 \cdots i_k}}$ are described in Werner and Scheeres [53], the first three tensors are written as,

$$\mathbf{Q} = \frac{1}{36}, \qquad \mathbf{Q}_i = \frac{1}{144}[1\ 1\ 1\ 1\ 1\ 1], \qquad \mathbf{Q}_{ij} = \frac{1}{2880}\begin{bmatrix} 8 & 4 & 4 & 5 & 5 & 5 \\ 4 & 8 & 4 & 5 & 5 & 5 \\ 4 & 4 & 8 & 5 & 5 & 5 \\ 5 & 5 & 5 & 8 & 4 & 4 \\ 5 & 5 & 5 & 4 & 8 & 4 \\ 5 & 5 & 5 & 4 & 4 & 8 \end{bmatrix} \tag{3.47}$$

Based on such initial steps, the gravitational force that is exerted on Body A due to body B is derived as the partial derivative of the mutual potential function with respect to the relative position between the two bodies' centroid. As viewed in the inertial frame, the force is expressed as,

$$\mathbf{f_A} = G \sum_{a \in A} \sum_{b \in B} \rho_a \rho_b T_a T_b \left(\frac{\partial \hat{U}_0}{\partial \mathbf{r}} + \frac{\partial \hat{U}_1}{\partial \mathbf{r}} + \frac{\partial \hat{U}_2}{\partial \mathbf{r}} + ... \right) \tag{3.48}$$

Then, the gravitational moment on A can be derived as [54],

$$\mathbf{M_A} = -\zeta_P \times E^{\zeta} - \eta_P \times E^{\eta} - \xi_P \times E^{\xi} \tag{3.49}$$

where,

$$E^{\zeta} = \frac{\partial U}{\partial \zeta_P},\ E^{\eta} = \frac{\partial U}{\partial \eta_P},\ E^{\xi} = \frac{\partial U}{\partial \xi_P} \tag{3.50}$$

and ζ_P^T, η_P^T, and ξ_P^T are the rows of the rotation matrix that relates the orientation of the body A-fixed frame to the inertial frame, that is,

$$\mathbf{P} = \begin{bmatrix} -\zeta_P^T \\ -\eta_P^T \\ -\xi_P^T \end{bmatrix} \tag{3.51}$$

Finally, defining the tensor $\mathbf{E}_{\phi\theta} = \left[E^{\zeta}, E^{\eta}, E^{\xi}\right]$ with indices ϕ and θ, the vectors E^{ζ}, E^{η}, and E^{ξ} are compute as,

$$\mathbf{E}_{\phi\theta} = G \sum_{a \in A} \sum_{b \in B} \rho_a \rho_b T_a T_b \left(\frac{\partial \hat{U}_0}{\partial T_{\phi\theta}} + \frac{\partial \hat{U}_1}{\partial T_{\phi\theta}} + \frac{\partial \hat{U}_2}{\partial T_{\phi\theta}} + ... \right) \tag{3.52}$$

where $T_{\phi\theta}$ is previously defined as the rotation matrix that relates body B- and body A-fixed frames.

The computation of the potential, force, and moment terms for an arbitrary order, that is, including an arbitrary number of terms in the series expansion, is both extremely computationally expensive and tedious. While some patterns emerge in the form of the various terms in the series, automation of the evaluation of these series remain challenging. An alternative formulation [52] relies on recursive relations based on recursive properties of the Legendre function. Recall that the initial expression for the potential function is comprised of a shape-dependent and a shape-independent part. The alternative formulation is only concerned with the shape-dependent part of the expression and it can be demonstrated that three recursive tensor series, ϑ, ι, ϖ, are sufficient to compute the potential, force, and moment for an arbitrary order. Only the results from this strategy are outlined here, first, the tensor ϑ corresponds to the shape-dependent part of the potential,

$$\vartheta_{i_1 \ldots i_{n+1}} = -\frac{2n+1}{n+1} \frac{1}{r^2} \mathbf{w}_{i_{n+1}} \vartheta_{i_1 \ldots i_n} - \frac{n}{n+1} \frac{1}{r^2} \mathbf{c}_{i_n i_{n+1}} \vartheta_{i_1 \ldots i_{i-n}} \tag{3.53}$$

where the required initial conditions to initialize the series are,

$$\vartheta_{i_0} = \frac{1}{r}, \qquad \vartheta_{i_0 i_1} = -\frac{\mathbf{w}_{i_1}}{r^3} \tag{3.54}$$

as derived by the classical development for the mutual potential between two polyhedra. [51] Then, the shape-dependent part of the force is described by the tensor ι such that,

$$\begin{aligned}\iota_{\theta i_1 \ldots i_{n+1}} = \frac{2n+1}{n+1}\left(\frac{\mathbf{v}_{\theta i_{n+1}}}{r^2} - 2\frac{\mathbf{w}_{i_{n+1}}}{r^4}\mathbf{r}_\theta\right)\vartheta_{i_1\ldots i_n} - \frac{2n+1}{n+1}\frac{\mathbf{w}_{i_{n+1}}}{r^2}\iota_{\theta i_1\ldots i_n} \\ -\frac{n}{n+1}\frac{\mathbf{c}_{i_n i_{n+1}}}{r^2}\iota_{\theta i_1\ldots i_{n-1}} - \frac{2n}{n+1}\frac{\mathbf{c}_{i_n i_{n+1}}}{r^4}\mathbf{r}_\theta\vartheta_{i_1\ldots i_{n-1}}\end{aligned} \tag{3.55}$$

where the required initial conditions to initialize the series are,

$$\iota_{\theta i_0} = -\frac{\mathbf{r}_\theta}{r^3} \tag{3.56}$$

$$\iota_{\theta i_1} = -3\frac{\mathbf{r}_\theta \mathbf{w}_{i_1}}{r^5} + \frac{\mathbf{v}_{\theta i_1}}{r^3} \tag{3.57}$$

Finally, the shape-dependent part of the moment is represented by the tensor ϖ,

$$\begin{aligned}\varpi_{\phi\theta i_1\ldots i_{n+1}} = \frac{2n+1}{n+1}\frac{1}{r^2}\left[\mathbf{D}_{si_1\phi\theta}\mathbf{r}_s\vartheta_{i_1\ldots i_n} + \mathbf{w}_{1_{n+1}}\varpi_{\phi\theta i_1\ldots i_n}\right] \\ \frac{2n+1}{n+1}\frac{1}{r^2}\mathbf{v}_{si_n}\mathbf{D}_{si_1\phi\theta}\vartheta_{i_1\ldots i_{n-1}} - \frac{n}{n+1}\frac{1}{r^2}\mathbf{c}_{i_n i_{n+1}}\varpi_{\phi\theta i_1\ldots i_{n-1}}\end{aligned} \tag{3.58}$$

where the required initial conditions to initialize the series are,

$$\varpi_{\phi\theta i_1} = -\frac{\mathbf{r}_s\mathbf{D}_{si_1\phi\theta}}{r^3} \tag{3.59}$$

$$\varpi_{\phi\theta i_1 i_2} = -\frac{\mathbf{v}_{si_1}\mathbf{D}_{si_2\phi\theta}}{r^3} + 3\frac{\mathbf{w}_{i_1}\mathbf{D}_{si_2\phi\theta}\mathbf{r}_s}{r^5} \tag{3.60}$$

and the tensor $\mathbf{D}_{si_1\phi\theta}$ is defined as,

$$\mathbf{D}_{si_1\phi\theta} = \frac{\partial \mathbf{v_{sj}}}{\partial T_{\phi\theta}} \tag{3.61}$$

The final expressions for the mutual potential, force, and moment are directly obtained by multiplying the shape-dependent part of each quantity, ϑ, ι, and ϖ, respectively, with the shape-independent part, that is, the tensor $\mathbf{Q}$,

$$U_{mutual} = \vartheta_{i_1 \ldots i_n} \mathbf{Q}_{i_1 \ldots i_n} \tag{3.62}$$

$$F_{mutual} = \mathbf{Q}_{i_1 \ldots i_n} \iota_{i_1 \ldots i_n} \tag{3.63}$$

$$M_{mutual} = \mathbf{Q}_{i_1 \ldots i_n} \iota_{i_1 \ldots i_n} \tag{3.64}$$

The derived mutual force and moment are then evaluated for a prescribed order and substituted into the EOMs to allow the numerical simulation of the relative motion of a pair of polyhedron-shaped bodies.

3.5.2 Three-body dynamical model (PPTBP)

The motion of a massless third body is modeled assuming that the primary system is comprised of the two constant density polyhedra, P_1 and P_2, where the relative motion of the primary system is pre-computed. Note that the third particle is located relative to the primary P_1 center of mass, as viewed in the inertially-fixed P_1-centered frame. However, the problem can be similarly formulated for either primary as the central body. The equations of motion that describe the behavior of a massless particle near such a primary system are similar to the ellipsoid-ellipsoid problem, as expressed with respect to the inertial frame in Eqn. (3.14) where the symbol U_{EE} is replaced with U_{PP}. The symbol U_{PP} now denotes the gravitational potential defined as $U_{PP} = (1-\mu)U_{p_1} + \mu U_{p_2}$ where U_{p_1} and U_{p_2} represent the potential that is associated with the polyhedra P_1 and P_2, respectively. In contrast to the motion of the primary system, where the mutual gravitational potential is expressed in terms of an infinite series, the gravitational potential that is exerted on the massless third body by each polyhedron can be computed independently. For the gravitational potential, and consequently the gravitational force, exerted by a single constant density polyhedron onto a massless particle, there exists an exact closed-form solution. [20, 47] Thus, the gravitational potential is exact for a given shape and density. The resolution of the calculated field depends directly on the level of discretization selected for a particular shape. However, the polyhedron is still an approximation for the actual

shape of the body and the accuracy of the gravity field is consistent with its shape determination. In addition, the Solar Radiation Pressure (SRP) that is exerted on a spacecraft is a significant perturbing acceleration, especially in a scenario that involves small bodies, such as asteroids. In this analysis, a simple model that assumes the spacecraft is spherical and possesses a constant reflectivity is employed to include this perturbative effect into the model.

3.6 Conic Restricted Four-Body Problem (CR4BP) and Augmented CR4BP (ACR4BP)

The dynamical models introduced thus far are coherent, that is, the motion of the bodies in the system is consistent with the physical and dynamical attributes of the bodies. Within the context of wider scope analyses, a model that includes additional perturbations and parameterized models for the motion of the bodies is of interest. Consider a model that incorporates the gravitational attraction of the Sun and both components of the binary system. It is assumed that the secondary component in the binary system, P_2, evolves in a conic orbit with respect to the primary, P_1. Similarly, it is also assumed that the binary system is traveling along a conic orbit around the Sun centered at the binary barycenter. These two conic orbits can be fully described by the set of classical orbital elements $\bar{oe}_{P_2}$ and $\bar{oe}_{Sun}$ for P_2 and the Sun, respectively. Additionally, each component of the binary is modeled as a constant density polyhedron and the gravitational attraction that is associated with each body is computed consistent with its shape model. Such a model is labeled the Conic Restricted Four-Body Problem (CR4BP) in this analysis. Finally, in the Augmented CR4BP (ACR4BP), the solar radiation pressure that is exerted onto the spacecraft is also incorporated into the dynamical model. In this analysis, a simple model that assumes the spacecraft is spherical and possesses a constant reflectivity is employed to include this perturbing effect. Then, as expressed in an inertially fixed

frame centered at the primary P_1, the equations of motion for a spacecraft in the ACR4BP are written as,

$$\ddot{\bar{\rho}} = \frac{\partial U_{P_1}}{\partial \bar{\rho}} + \frac{\partial U_{P_2}(\bar{\rho}_{s/c\to P_2})}{\partial \bar{\rho}_{s/c\to P_2}} + \frac{\partial U_{Sun}(\bar{\rho}_{s/c\to Sun})}{\partial \bar{\rho}_{s/c\to Sun}} + \bar{a}_{SRP} \tag{3.65}$$

where $\bar{\rho}$, $\bar{r}_{P_2}$, $\bar{r}_{Sun}$ denote the nondimensional position vector with respect to P_1 of the spacecraft, P_2, and the Sun, respectively. Then, $\bar{\rho}_{s/c\to P_2} = \bar{\rho} - \bar{r}_{P_2}$, $\bar{\rho}_{s/c\to Sun} = \bar{\rho} - \bar{r}_{Sun}$. Also, the symbols U_{body} represent the gravitational potential function that is associated with the body in the subscript expression and $\bar{a}_{SRP}$ is the solar radiation pressure acceleration.

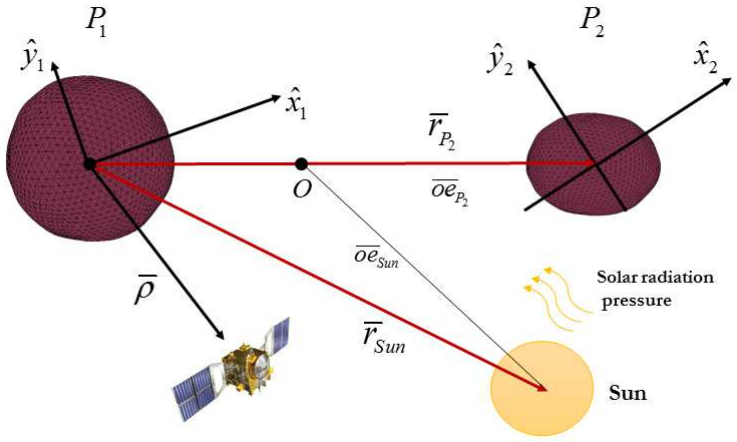

Figure 3.12. ACR4BP geometry

4. NUMERICAL METHODS AND ANALYSIS TOOLS

With a significant departure from an inverse square gravitational model, no analytical solutions are available to describe the motion of a particle in the vicinity of a pair of arbitrarily-shaped bodies. Given initial conditions that describe the position and velocity states for a particle, the subsequent path is numerically integrated; however, beyond straightforward integration, a path most likely must be generated to satisfy some given objective. Such a path may lie nearby a known trajectory arc. Thus, numerical tools that employ differential corrections techniques are implemented into a general algorithm to compute such solutions. Other numerical techniques, such as maps, are powerful tools to yield insight into the dynamical behavior in complex dynamical models and, even, serve to aid the construction of desired trajectory arcs.

4.1 Multivariate Newton Method

A variety of approaches can be used to formulate differential corrections algorithms, and numerous strategies are available. For this analysis, a general method is employed that introduces a set of free variables and constraints. First, consider a vector of free design variables, $\bar{X}$, with n elements,

$$\bar{X} = \begin{bmatrix} X_1 \\ \vdots \\ X_n \end{bmatrix} \tag{4.1}$$

Within the trajectory design context, $\bar{X}$ usually includes state vectors $\bar{x}_i$ as well as various integration times T_i. Slack variables and other quantities can also be added depending on the goal and the requirements of the targeting scheme. To ensure that

the trajectory satisfies the desired conditions, the free variables are subject to m scalar constraints that are represented in the constraint vector such that $\bar{F}(\bar{X}) = \bar{0}$,

$$\bar{F}(\bar{X}) = \begin{bmatrix} F_1(\bar{X}) \\ \vdots \\ F_m(\bar{X}) \end{bmatrix} = \bar{0} \tag{4.2}$$

In trajectory design applications, constraints typically include positions, velocities, timing conditions, and, possibly, various rates. Other constraints can also be included, such as periodicity. The objective is a solution vector $\bar{X}^*$ that satisfies the constraint equations, that is, $\bar{F}(\bar{X}^*) = \bar{0}$, within some acceptable level of accuracy. To compute such a solution requires an initial guess. Consider an initial free variable vector $\bar{X}^0$ such that $\bar{F}(\bar{X})$ is expanded about $\bar{X}^0$ using a Taylor series. Retaining only the linear terms, $\bar{F}(\bar{X})$ is approximated by,

$$\bar{F}(\bar{X}) \approx \bar{F}(\bar{X}^0) + D\bar{F}(\bar{X}^0)(\bar{X} - \bar{X}^0) \tag{4.3}$$

where $D\bar{F}(\bar{X}^0)$ is the m by n Jacobian matrix evaluated along the reference, i.e.,

$$D\bar{F}(\bar{X}^0) = \frac{\partial \bar{F}(\bar{X}^0)}{\partial \bar{X}^0} = \begin{bmatrix} \frac{\partial F_1}{\partial X_1} & \cdots & \frac{\partial F_1}{\partial X_n} \\ \vdots & \ddots & \vdots \\ \frac{\partial F_m}{\partial X_1} & \cdots & \frac{\partial F_m}{\partial X_n} \end{bmatrix} \tag{4.4}$$

As noted, the elements of $D\bar{F}(\bar{X}^0)$ represent the partial derivatives of the constraints with respect to the free variables, evaluated along $\bar{X}^0$. Then, from Eqn. (4.2), the updated solution $\bar{X}^*$ yields a constraint vector, $\bar{F}$, equal to zero. However, given an initial guess $\bar{X}^0$, the process to determine $\bar{X}^*$ is iterative. Thus, the expansion of $\bar{F}$ in Eqn. (4.3) is reduced and generalized to,

$$\bar{F}(\bar{X}^j) + D\bar{F}(\bar{X}^j)(\bar{X}^{j+1} - \bar{X}^j) = \bar{0} \tag{4.5}$$

where $\bar{X}^j$ and $\bar{X}^{j+1}$ represent the vector of free variables at the current and next iteration, respectively. Then, assuming a reasonable initial guess, Eqn. (4.5) is employed to iteratively solve for an $\bar{X}^{j+1}$ such that the error, $||\bar{F}(\bar{X})||$, approaches zero,

$$||\bar{F}(\bar{X}^{j+1})|| = ||\bar{F}(\bar{X}^*)|| = 0 \tag{4.6}$$

Because of the numerical nature of the procedure, the iterations proceed until the error is lower than a predefined convergence tolerance, ϵ,

$$||\bar{F}(\bar{X}^{j+1})|| < \epsilon \tag{4.7}$$

The actual implementation of the iterative procedure depends on the formulation of the problem, and two different cases are addressed. If the number of free variables equals the number of constraints, that is, $n = m$, then, the Jacobian matrix $D\bar{F}(\bar{X}^j)$ is square, and consequently invertible. Therefore, Eqn. (4.5) admits a unique solution $\bar{X}^{j+1}$,

$$\bar{X}^{j+1} = \bar{X}^j - D\bar{F}(\bar{X}^j)^{-1}\bar{F}(\bar{X}^j) \tag{4.8}$$

Alternately, when the number of free variables exceeds the number of constraints, $n > m$, the Jacobian matrix is no longer invertible, and, in general, the system of equations admits an infinite number of solutions. To select one from among all the possible solutions, some criteria must be defined. The minimum norm is one solution of particular interest in the trajectory design context, that is,

$$\bar{X}^{j+1} = \bar{X}^j - D\bar{F}(\bar{X}^j)\left[D\bar{F}(\bar{X}^j)D\bar{F}(\bar{X}^j)^T\right]^{-1}\bar{F}(\bar{X}^j) \tag{4.9}$$

The minimum norm solution minimizes the difference between the solution vectors from the current step, $\bar{X}^j$, to the next, $\bar{X}^{j+1}$. Essentially, an orthogonal projection is

used to compute the solution with the minimum deviation from the previous iteration. Note that the minimum norm solution is convenient but is only one possible criteria. Nevertheless, this minimum norm solution to the underconstrained system in Eqn. (4.5) is implemented throughout this investigation because it typically results in the solution closest to the initial guess $\bar{X}^0$, also retaining most of the desired characteristics of the baseline trajectory. When certain characteristics associated with the initial guess are more desired for inclusion in the final trajectory arc, some weighting ω_i can be included through the diagonal weighting matrix Q,

$$Q = \begin{bmatrix} \omega_1 & & \\ & \ddots & \\ & & \omega_n \end{bmatrix} \tag{4.10}$$

For evenly weighted free variables, the matrix Q is the $n \times n$ identity matrix. The weighted minimum norm solution is evaluated as follows,

$$\bar{X}^{j+1} = \bar{X}^j - Q^{-1} D\bar{F}(\bar{X}^j) \left[D\bar{F}(\bar{X}^j) Q^{-1} D\bar{F}(\bar{X}^j)^T \right]^{-1} \bar{F}(\bar{X}^j) \tag{4.11}$$

This general scheme that employs free variables and the associated constraints is applied in many different ways to analyze a wide range of trajectory targeting problems.

4.2 The Shooting Method

Targeting and other trajectory design strategies are enabled by the use of the state transition matrix within the context of various types of differential corrections algorithms. Corrections algorithms effectively exploit the STM to compute updates to the state that yield some desired path possibly meeting some constraint requirements.

4.2.1 State Transition Matrix

The shooting method relies on the explicit numerical integration of the path of the third-body given some initial state and also requires gradient information to relate changes in the final integrated state, $\bar{x}^t$, to changes in the initial state, $\bar{x}_0$, i.e., $\frac{\partial \bar{x}}{\partial \bar{x}_0}$ is constructed based on the State Transition Matrix (STM). Periodic orbits are also of great interest, and the computation of these and other solution arcs is aided by the availability of the STM as well. Within this context, the STM is a valuable tool to explore the dynamical behavior in the vicinity of any reference arc or solution. Specifically, the STM represents the sensitivity of a final state $\bar{x}(\bar{x}_0, t)$ to variations in an initial state $\bar{x}_0$. The STM allows prediction of a future response to an initial disturbance, and is used to linearly approximate the end state along the perturbed path. To derive the STM, consider a general n-dimensional system described by a set of first-order nonlinear equations, one that is represented by the general equation,

$$\dot{\bar{x}} = \bar{f}(\bar{x}) \tag{4.12}$$

where $\bar{f}$ is a nonlinear smooth function. Consider the set of first-order linear variational equations, derived from the linearization of the nonlinear equation in Eqn. (4.12) relative to a state, $\bar{x}_{ref}$, along some reference solution, such that the linear differential vector equation is written,

$$\delta\dot{\bar{x}} = A(t)\delta\bar{x} \tag{4.13}$$

where $A(t)$ is a $n \times n$ time-varying matrix, in general. The n-dimensional variational vector, $\delta\bar{x} = \bar{x} - \bar{x}_{ref}$, is the perturbation from the reference solution. The general solution to the linear system in Eqn. (4.13) is,

$$\delta\bar{x}(t) = \Phi(t, t_0)\delta\bar{x}(t_0) \tag{4.14}$$

where $\Phi(t, t_0)$ is the $n \times n$ state transition matrix. The STM essentially supplies a prediction for the variation of the final state at time t relative to the reference end state $\bar{x}_{ref}(t)$, that is, $\delta\bar{x}(t)$, given some initial perturbation $\delta\bar{x}(t_0)$ relative to the reference state $\bar{x}_{ref}(t_0)$ at t_0. The elements of the STM correspond to the partial derivatives of the end states with respect to the initial states, that is,

$$\Phi = \begin{bmatrix} \frac{\partial x(t)}{\partial x(t_0)} & \frac{\partial x(t)}{\partial y(t_0)} & \frac{\partial x(t)}{\partial z(t_0)} & \frac{\partial x(t)}{\partial \dot{x}(t_0)} & \frac{\partial x(t)}{\partial \dot{y}(t_0)} & \frac{\partial x(t)}{\partial \dot{z}(t_0)} \\ \frac{\partial y(t)}{\partial x(t_0)} & \frac{\partial y(t)}{\partial y(t_0)} & \frac{\partial y(t)}{\partial z(t_0)} & \frac{\partial y(t)}{\partial \dot{x}(t_0)} & \frac{\partial y(t)}{\partial \dot{y}(t_0)} & \frac{\partial y(t)}{\partial \dot{z}(t_0)} \\ \frac{\partial z(t)}{\partial x(t_0)} & \frac{\partial z(t)}{\partial y(t_0)} & \frac{\partial z(t)}{\partial z(t_0)} & \frac{\partial z(t)}{\partial \dot{x}(t_0)} & \frac{\partial z(t)}{\partial \dot{y}(t_0)} & \frac{\partial z(t)}{\partial \dot{z}(t_0)} \\ \frac{\partial \dot{x}(t)}{\partial x(t_0)} & \frac{\partial \dot{x}(t)}{\partial y(t_0)} & \frac{\partial \dot{x}(t)}{\partial z(t_0)} & \frac{\partial \dot{x}(t)}{\partial \dot{x}(t_0)} & \frac{\partial \dot{x}(t)}{\partial \dot{y}(t_0)} & \frac{\partial \dot{x}(t)}{\partial \dot{z}(t_0)} \\ \frac{\partial \dot{y}(t)}{\partial x(t_0)} & \frac{\partial \dot{y}(t)}{\partial y(t_0)} & \frac{\partial \dot{y}(t)}{\partial z(t_0)} & \frac{\partial \dot{y}(t)}{\partial \dot{x}(t_0)} & \frac{\partial \dot{y}(t)}{\partial \dot{y}(t_0)} & \frac{\partial \dot{y}(t)}{\partial \dot{z}(t_0)} \\ \frac{\partial \dot{z}(t)}{\partial x(t_0)} & \frac{\partial \dot{z}(t)}{\partial y(t_0)} & \frac{\partial \dot{z}(t)}{\partial z(t_0)} & \frac{\partial \dot{z}(t)}{\partial \dot{x}(t_0)} & \frac{\partial \dot{z}(t)}{\partial \dot{y}(t_0)} & \frac{\partial \dot{z}(t)}{\partial \dot{z}(t_0)} \end{bmatrix} \tag{4.15}$$

For convenience, the elements of the matrix are also defined as Φ_{ij} so that $\Phi(t, t_0) = \{\Phi_{ij}\}_{i=1,j=1}^{n,n}$. The matrix differential equation for the STM is obtained by substituting the general solution in the linear variational system, yielding,

$$\dot{\Phi}(t, t_0) = A(t)\Phi(t, t_0) \tag{4.16}$$

where the initial condition for the STM, $\Phi(t_0, t_0)$, is clearly,

$$\Phi(t_0, t_0) = I_{n\times n} \tag{4.17}$$

and $I_{n\times n}$ is the identity matrix. The STM also possesses useful properties, that is,

$$\Phi(t_2, t_0) = \Phi(t_2, t_1)\Phi(t_1, t_0) \tag{4.18}$$

$$\Phi(t_1, t_0) = \Phi^{-1}(t_0, t_1) \tag{4.19}$$

Simultaneous numerical integration of the equations of motion and the STM matrix differential equation in Eqn. (4.16), using the appropriate initial conditions, yields

the time history of the states for the motion of the particle as well as the associated state transition matrix elements. The concepts associated with the state transition matrix can be implemented in various numerical schemes to gain more insight into a wide variety of problems.

4.2.2 Additional Final State Derivative Relationships

The state transition matrix supplies gradient information that relates changes in the final integrated state to changes in the initial state. Such information is critical to the implementation of any shooting technique, both single- and multiple-shooting formulations. However, depending on the application, additional derivatives of the final state with respect to arbitrary parameters may be required. Specifically, in time-varying dynamical systems, e.g., non-synchronous primary system models, the assessment of the sensitivity with respect to the epoch, τ_i, is required. A general method to construct the final state derivatives with respect to an arbitrary parameter is first introduced and then applied to the specific task of evaluating the sensitivity of the final state with respect to the epoch time in time-varying dynamic systems.

Obtaining General Derivative Information

A range of complex dynamical models, with incrementally increasing levels of fidelity, that describe the motion of the primary system and, subsequently, the motion of a third body are characterized by various parameters, including the mass ratio, shape parameters for the primaries, and other additional parameters. While the evolution of a given trajectory arc is critically dependent upon the initial state, it is also heavily impacted by the underlying dynamical system parameters. Within the context of differential corrections algorithms, the sensitivity of the final integrated state with respect to such parameters is also important. The second-order differential equations that describe the motion of a third body, within the context of any of the

five dynamical models from Chapter 3, can be rewritten as a series of first-order differential equations such that,

$$\dot{\bar{x}} = \bar{f}(t, \bar{x}, \bar{\kappa}) \tag{4.20}$$

where $\bar{x}$ is the state vector and $\bar{\kappa}$ denotes a vector of parameters associated with the dynamical model. First, consider the general problem of obtaining the derivatives of the final state, $\bar{x}$, with respect to the parameter vector, $\bar{\kappa}$, i.e., $\frac{d\bar{x}}{d\bar{\kappa}}$. Noting that the parameters are assumed to be constant through any time evolution, a first-order equation for $\frac{d\bar{x}}{d\bar{\kappa}}$ is,

$$\frac{d}{dt}\left(\frac{d\bar{x}}{d\bar{\kappa}}\right) = \frac{d}{d\bar{\kappa}}\left(\frac{d\bar{x}}{dt}\right) \tag{4.21}$$

since $\bar{\kappa}$ and t are independent. Substituting Eqn. (4.20) into the time derivative of $\bar{x}$ and applying the chain rule yields,

$$\frac{d}{dt}\left(\frac{d\bar{x}}{d\bar{\kappa}}\right) = \frac{d}{d\bar{\kappa}}\dot{\bar{x}} \tag{4.22}$$

$$= \frac{d}{d\bar{\kappa}}\bar{f}(t, \bar{x}, \bar{\kappa}) \tag{4.23}$$

$$= \frac{\partial \bar{f}}{\partial \bar{x}}\frac{d\bar{x}}{\partial \bar{\kappa}} + \frac{\partial \bar{f}}{d\bar{\kappa}} \tag{4.24}$$

Recall the definition of the matrix $A(t) = \frac{\partial \bar{f}}{\partial \bar{x}}$, that relates changes in the vector field $\bar{f}(t, \bar{x}, \bar{\kappa})$ due to changes in the state, $\bar{x}$. Then, assuming the state vector is six-dimensional and the parameter vector is of length η, the $6 \times \eta$ equations that govern the sensitivity matrix, $\frac{d\bar{x}}{d\bar{\kappa}}$, are,

$$\frac{d}{dt}\left(\frac{d\bar{x}}{d\bar{\kappa}}\right) = A(t)\frac{d\bar{x}}{d\bar{\kappa}} + \frac{\partial \bar{f}}{\partial \bar{\kappa}} \tag{4.25}$$

and are subject to the initial conditions,

$$\frac{d\bar{x}}{d\bar{\kappa}}(0) = \bar{0}_{6\times\eta} \tag{4.26}$$

since varying the parameters cannot change the state at the initial time, i.e., after zero integration time. The additional differential equations in Eqn. (4.25) are simultaneously numerically integrated with the EOMs to allow the evaluation of the additional sensitivity matrix at any point along the integrated path.

Final State Derivatives with Respect to Epoch Time

The procedure to construct derivatives with respect to an arbitrary set of parameters is applied to the evaluation of final state derivatives with respect to the epoch time, τ_i, along any given trajectory arc, i.e., $\frac{d\bar{x}}{d\tau_i}$ in time-varying dynamical systems. The second-order differential equations that describe the motion of a third body, within the context of time-varying dynamical models presented in Chapter 3, can be rewritten as a series of first-order differential equations such that,

$$\dot{\bar{x}} = \bar{f}\left(t, \bar{x}, \sum_{i=2}^{N-1} \bar{R}_{1i}(\tau_i)\right) \tag{4.27}$$

where $\bar{R}_{1i}$ is the position vector of the massive bodies in the system relative to the primary P_1. The vector information, $\bar{R}_{1i}$, as a function of time, is available either analytically or numerically depending upon the dynamical model and is clearly a function of the epoch time τ_i, that governs the relative position of the massive bodies in the system. A first-order differential relationship for $\frac{d\bar{x}}{d\tau_i}$ is written as,

$$\frac{d}{dt}\left(\frac{d\bar{x}}{d\tau_i}\right) = \frac{d}{d\tau_i}\left(\frac{d\bar{x}}{dt}\right) \tag{4.28}$$

since t and τ_i are independent. Substituting Eqn. (4.27) in the time derivative of $\bar{x}$ and applying the chain rule yields the differential equation,

$$\frac{d}{dt}\left(\frac{d\bar{x}}{d\bar{\kappa}}\right) = \frac{d}{d\tau_i}\dot{\bar{x}} \tag{4.29}$$

$$= \frac{d}{d\tau_i}\bar{f}\left(t, \bar{x}, \sum_{i=2}^{N-1}\bar{R}_{1i}(\tau_i)\right) \tag{4.30}$$

$$= \frac{\partial \bar{f}}{\partial \bar{x}}\frac{d\bar{x}}{d\tau_i} + \sum_{i=2}^{N-1}\frac{\partial \bar{f}}{\partial \bar{R}_{1i}}\frac{\partial \bar{R}_{1i}}{\partial \tau_i} \tag{4.31}$$

The term $\frac{\partial \bar{f}}{\partial \bar{R}_{1i}}$ in Eqn. (4.31) is computed directly from the equations of motion through analytical or finite differencing methods and the term $\frac{\partial \bar{R}_{1i}}{\partial \tau_i}$ is rewritten as,

$$\frac{\partial \bar{R}_{1i}}{\partial \tau_i} = \frac{\partial \bar{R}_{1i}}{\partial t} = \bar{V}_{1i} \tag{4.32}$$

where $\bar{V}_{1i}$ is the relative velocity of body i with respect to the primary P_1 as viewed by an inertial observer. Substituting the definition of the matrix $A(t)$ and the velocity vector $\bar{V}_{1i}$ into Eqn. (4.31) gives the final result,

$$\frac{d}{dt}\left(\frac{d\bar{x}}{d\tau_i}\right) = A(t)\frac{d\bar{x}}{d\tau_i} + \sum_{i=2}^{N-1}\frac{\partial \bar{f}}{\partial \bar{R}_{1i}}\bar{V}_{1i} \tag{4.33}$$

where $\frac{d}{dt}\left(\frac{d\bar{x}}{d\tau_i}\right)$ is the differential equation that governs the sensitivity vector of the final integrated state with respect to the epoch time and is subject to the initial conditions,

$$\frac{d\bar{x}}{d\bar{\kappa}}(0) = \bar{0}_{6\times\eta} \tag{4.34}$$

The conjoint numerical integration of Eqn. (4.33) and the EOMs enables the evaluation of the epoch sensitivities at any point along the integrated trajectory path.

4.2.3 Single Shooting Algorithm

The most basic application of a targeting algorithm is the single shooting scheme. The terminology 'single shooting' implies a procedure that involves only one trajectory arc. Although an infinite number of problems can be formulated, the technique is demonstrated here for a simple but widely used scenario as an example. Consider a baseline trajectory arc defined by an initial state $\bar{x}_0$ at time t_0. Integrating this state forward in time for a time interval T yields a final state $\bar{x}(\bar{x_0}, t)$ at time $t = t_0 + T$. For simplicity, the flow $\bar{x}(\bar{x_0}, t)$ is abbreviated $\bar{x}^t$. Next, assume that the desired path terminates at a specified target state $\bar{r_d} = [x_d \ y_d \ z_d]^T$ rather than the baseline final state $\bar{x}^t$. The time-of-flight (TOF) is allowed to vary and labelled T for both trajectory arcs. Assume for this application that the initial position of the particle remains fixed throughout the corrections process; only the initial velocity states are allowed to change to reach the target location $\bar{r}_d$. Thus, the goal is a velocity vector at the initial position that yields the trajectory arc that delivers a particle to the specified target over the varying time interval T, as illustrated in Figure 4.1. In practical applications, allowing updates only to the initial velocity vector is sometimes equivalent to implementing an impulsive maneuver at the initial location.

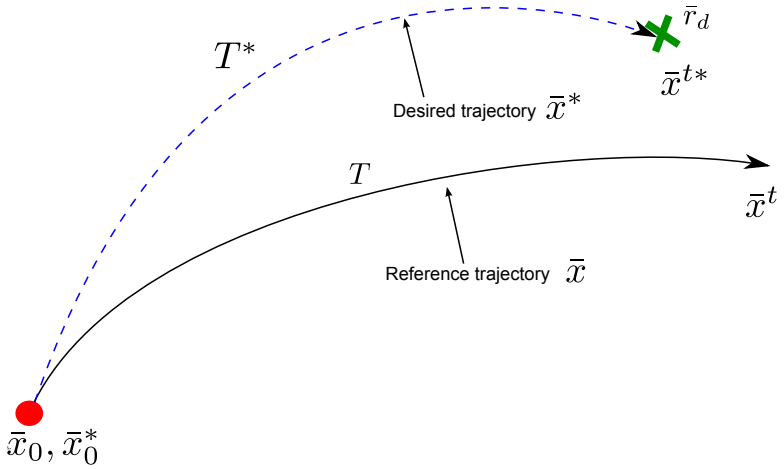

Figure 4.1. Single shooting algorithm

Using the general free variables and constraints approach, a targeting scheme to solve this problem is constructed. First, define the elements within the free variable vector, $\bar{X}$, such that the initial location is fixed. Therefore, the free variables are the velocity states at the initial time and the time of flight T, that is,

$$\bar{X} = \begin{bmatrix} \dot{x}_0 \\ \dot{y}_0 \\ \dot{z}_0 \\ T \end{bmatrix} \tag{4.35}$$

Next, the constraints in the vector $\bar{F}(\bar{X})$ are identified. In this application, the sole requirement is that the trajectory arc terminates at the target position $\bar{r_d} = [x_d \; y_d \; z_d]^T$. Thus, the constraint vector is,

$$\bar{F}(\bar{X}) = \begin{bmatrix} x^t - x_d \\ y^t - y_d \\ z^t - z_d \end{bmatrix} \tag{4.36}$$

to yield the constraint equation $\bar{F}(\bar{X}) = \bar{0}$ when the trajectory is delivered to the target location. With the free variables and constraints defined, the Jacobian matrix $D\bar{F}(\bar{X})$ is written and evaluated from Eqn. (4.4) and applied to this example,

$$D\bar{F}(\bar{X}) = \frac{\partial \bar{F}(\bar{X})}{\partial \bar{X}} = \begin{bmatrix} \frac{\partial x^t}{\partial \dot{x}_0} & \frac{\partial x^t}{\partial \dot{y}_0} & \frac{\partial x^t}{\partial \dot{z}_0} & \frac{\partial x^t}{\partial T} \\ \frac{\partial y^t}{\partial \dot{x}_0} & \frac{\partial y^t}{\partial \dot{y}_0} & \frac{\partial y^t}{\partial \dot{z}_0} & \frac{\partial y^t}{\partial T} \\ \frac{\partial z^t}{\partial \dot{x}_0} & \frac{\partial z^t}{\partial \dot{y}_0} & \frac{\partial z^t}{\partial \dot{z}_0} & \frac{\partial z^t}{\partial T} \end{bmatrix} \tag{4.37}$$

The partial derivatives of the constraints with respect to the free variables, i.e., the elements of the matrix $D\bar{F}(\bar{X})$, all relate a component of the final state on the integrated arc, $\bar{x}^t$, to elements of the initial state vector $\bar{x}_0$. Thus, the derivatives are the elements of the STM, and substituting for the appropriate terms, the Jacobian matrix is rewritten in the form

$$D\bar{F}(\bar{X}) = \begin{bmatrix} \Phi_{14} & \Phi_{15} & \Phi_{16} & \dot{x}^t \\ \Phi_{24} & \Phi_{25} & \Phi_{26} & \dot{y}^t \\ \Phi_{34} & \Phi_{35} & \Phi_{36} & \dot{z}^t \end{bmatrix} \tag{4.38}$$

where Φ_{ij} represents the element (i, j) of the STM. The Jacobian matrix is rectangular, since $n > m$, therefore the system admits an infinite number of solutions. From among all the possible paths, the minimum norm solution that supplies the arc closest to the baseline trajectory and is computed by iteratively solving Eqn. (4.9) for the solution vector $\bar{X}^*$ that satisfies the problem objectives.

4.2.4 Time-Invariant Multiple Shooting Algorithm

A single shooting scheme does not always produce an acceptable solution that satisfies the problem objectives. As an alternative, an approach that employs multiple integrated arcs, rather than a single trajectory segment, may be beneficial. A multiple shooting algorithm is based on the same fundamental concept as a single shooting scheme; it is implemented using the same general approach involving free variables and constraints. Essentially, a multiple shooting technique is a generalization of a single shooting approach and is envisioned as a series of simple targeters linked together. This multiple-arc targeting approach relies on discretizing the baseline arc from origin to terminal point into a set of segments joined at patch points that are identified at specified times along the baseline path. The state vector at each patch point is integrated forward; then, the patch points are all modified simultaneously to satisfy the trajectory constraints, as illustrated in Figure 4.2. In contrast, single shooting schemes only involve one integrated arc.

Decomposing the trajectory into multiple arcs increases the complexity of the targeting scheme but offers significant advantages. First, both techniques rely on linear variational equations, that is, single and multiple shooting techniques exploit linear approximations relative to a baseline trajectory. The accuracy of the linear approxi-

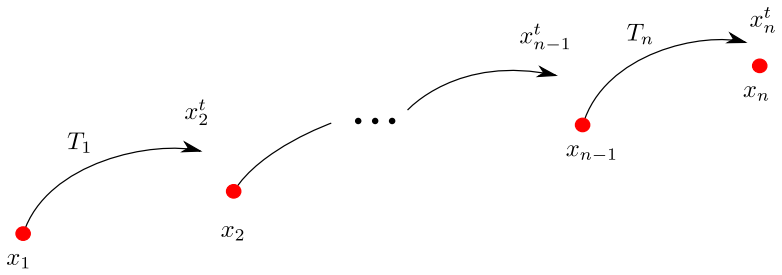

Figure 4.2. General multiple shooting algorithm

mation decreases as the variations are propagated in time, thus, using multiple arcs with shorter integration times significantly reduces the loss of accuracy typically associated with longer integrated arcs. Also, multiple shooting schemes allow much more control over the shape of the end-to-end trajectory by facilitating the implementation of path constraints at the intermediate patch points. In addition, constraints on the end-points are also easily accommodated. In Figure 4.2, the general concept for a multiple shooting approach is illustrated: the intermediate state vectors $\bar{x}_i$ identify the origin of each arc. Each state $\bar{x}_i$ is integrated over a time interval T_i yielding a final state vector for the corresponding arc i, $\bar{x}_{i+1}^t(\bar{x}_i, T_i)$ or, in a shortened notation, $\bar{x}_{i+1}^t$ for $i = \{1, ..., n\}$, where n is the number of patch points. As depicted in the diagram, the trajectory represented as a set of integrated arcs is likely to be discontinuous at the intermediate points in all seven states, that is, position, velocity and time.

A first multiple-shooting algorithm is constructed for time-invariant dynamical models, such as synchronous systems. In this application, the times of integration along each arc are all equal such that $T_i = \frac{T}{n}$ for $i = \{1, ..., n\}$ where n is the number of patch points that is selected to discretize the trajectory. The vector of free variables is then augmented with the total time of integration T,

$$\bar{X} = \begin{bmatrix} \bar{x}_1 \\ \vdots \\ \bar{x}_n \\ T \end{bmatrix} \tag{4.39}$$

The number of free variables is now $6n + 1$. Since the objective remains the same, the constraints vector is directly written as,

$$\bar{F}(\bar{X}) = \begin{bmatrix} \bar{x}_2^t - \bar{x}_2 \\ \vdots \\ \bar{x}_n^t - \bar{x}_n \end{bmatrix} = \bar{0} \tag{4.40}$$

to yield the constraint equation $\bar{F}(\bar{X}) = \bar{0}$. The Jacobian matrix $D\bar{F}(\bar{X})$ is again defined as the partial derivatives of the constraint equations with respect to the free variables,

$$D\bar{F}(\bar{X}) = \frac{\partial \bar{F}(\bar{X})}{\partial \bar{X}} = \begin{bmatrix} \frac{\partial \bar{x}_2^t}{\partial \bar{x}_1} & -\frac{\partial \bar{x}_2}{\partial \bar{x}_2} & & & \frac{\partial \bar{x}_2^t}{\partial T} \\ & \ddots & \ddots & & \vdots \\ & & \frac{\partial \bar{x}_n^t}{\partial \bar{x}_{n-1}} & -\frac{\partial \bar{x}_n}{\partial \bar{x}_n} & \frac{\partial \bar{x}_n^t}{\partial T} \end{bmatrix} \tag{4.41}$$

Elements of the STM and the appropriate identity matrices are substituted into the previous matrix. Also, recall that the time of integration along one segment is $T_i = \frac{T}{n}$, so the partial derivatives with respect to T are rewritten and $D\bar{F}(\bar{X})$ becomes,

$$D\bar{F}(\bar{X}) = \begin{bmatrix} \Phi(t_2, t_1) & -I_{6\times 6} & & & \frac{\dot{\bar{x}}_2^t}{n} \\ & \ddots & \ddots & & \vdots \\ & & \Phi(t_n, t_{n-1}) & -I_{6\times 6} & \frac{\dot{\bar{x}}_n^t}{n} \end{bmatrix} \tag{4.42}$$

The time derivatives in $D\bar{F}(\bar{X})$ are obtained by evaluating the vector field $\dot{\bar{x}} = \bar{f}(\bar{x})$ at the final state along each integrated arc i, $\bar{x}_i^t$. The Jacobian matrix is rectangular

again and of size $6(n-1) \times 6n+1$. Therefore, no unique solution to this problem exists. An iterative method to compute the minimum norm solution of the problem is implemented.

4.2.5 Time-Variant Multiple Shooting Algorithm

The time-invariant multiple shooting approach is extended to enable the computation of continuous trajectory arcs in time-varying dynamical systems, i.e., for non-synchronous primary system models. Rather than the total time of integration T alone, the vector of free variables now incorporates integration times for each arc, T_i, and the epoch time, or initial time, that is associated with each patch point, τ_i,

$$\bar{X} = \begin{bmatrix} \bar{x}_1 \\ \vdots \\ \bar{x}_n \\ T_1 \\ \vdots \\ T_{n-1} \\ \tau_1 \\ \vdots \\ \tau_n \end{bmatrix} \tag{4.43}$$

The number of free variables is now $8n-1$. The constraints for the time-varying formulation are augmented with time-continuity constraints such that,

$$\bar{F}(\bar{X}) = \begin{bmatrix} \bar{x}_2^t - \bar{x}_2 \\ \vdots \\ \bar{x}_n^t - \bar{x}_n \\ \tau_2 - (\tau_1 + T_1) \\ \vdots \\ \tau_n - (\tau_{n-1} + T_{n-1}) \end{bmatrix} = \bar{0} \tag{4.44}$$

to yield the constraint equation $\bar{F}(\bar{X}) = \bar{0}$. The Jacobian matrix $D\bar{F}(\bar{X})$ is again defined as the partial derivatives of the constraint equations with respect to the free variables,

$$D\bar{F}(\bar{X}) = \frac{\partial \bar{F}(\bar{X})}{\partial \bar{X}} = \begin{bmatrix} \frac{\partial \bar{x}_2^t}{\partial \bar{x}_1} & -\frac{\partial \bar{x}_2}{\partial \bar{x}_2} & & & \frac{\partial \bar{x}_2^t}{\partial T_1} & & & -\frac{\partial \bar{x}_2^t}{\partial \tau_1} & & & \\ & \ddots & \ddots & & & \ddots & & & \ddots & & \\ & & \frac{\partial \bar{x}_n^t}{\partial \bar{x}_{n-1}} & -\frac{\partial \bar{x}_n}{\partial \bar{x}_n} & & & \frac{\partial \bar{x}_n^t}{\partial T_{n-1}} & & & -\frac{\partial \bar{x}_n^t}{\partial \tau_{n-1}} & \\ & & & & \frac{\partial T_1}{\partial T_1} & & & -\frac{\partial \tau_1}{\partial \tau_1} & \frac{\partial \tau_2}{\partial \tau_2} & & \\ & & & & & \ddots & & & \ddots & \ddots & \\ & & & & & & -\frac{\partial T_{n-1}}{\partial T_{n-1}} & & & -\frac{\partial \tau_{n-1}}{\partial \tau_{n-1}} & -\frac{\partial \tau_n}{\partial \tau_n} \end{bmatrix} \tag{4.45}$$

Elements of the STM and the appropriate identity matrices are substituted into the previous matrix,

$$D\bar{F}(\bar{X}) =$$

$$\begin{bmatrix}
\Phi_1 & -I_{6\times6} & & & \dot{\bar{x}}_2^t & & & -\frac{\partial \bar{x}_2^t}{\partial \tau_1} & & & \\
& \ddots & \ddots & & & \ddots & & & \ddots & & \\
& & \Phi_{n-1} & -I_{6\times6} & & & \dot{\bar{x}}_n^t & & & & -\frac{\partial \bar{x}_n^t}{\partial \tau_{n-1}} \\
& & & & -1 & & & -1 & 1 & & \\
& & & & & \ddots & & & \ddots & \ddots & \\
& & & & & & -1 & & & -1 & 1
\end{bmatrix} \tag{4.46}$$

where $\Phi_i = \Phi(t_{i+1}, t_i)$. The time derivatives in $D\bar{F}(\bar{X})$ are obtained by evaluating the vector field $\dot{\bar{x}} = \bar{f}(\bar{x})$ at the final state along each integrated arc i, $\bar{x}_i^t$. The Jacobian matrix is rectangular again and of size $7(n-1) \times (8n-1)$. Therefore, consistent with the time-invariant scheme, no unique solution to this problem exists. An iterative method to compute the minimum norm solution of the problem is implemented.

4.3 Continuation Schemes

4.3.1 Single Parameter Continuation

Single and multiple shooting algorithms are useful to compute individual orbits or trajectory arcs that satisfy a set of constraints. However, the converged trajectories are only point solutions and do not yield complete information in the problem. It is often desirable to compute a set of related solutions, sometimes labelled a 'family', featuring some common characteristics. From a trajectory design point of view, a set of solutions potentially supplies more feasible scenarios to explore the mission objectives. From a dynamical perspective, to compute an entire family of solutions rather than a single solution also offers much more insight into the dynamical environment.

A variety of approaches are available to compute such families. Single parameter continuation implemented with a multiple or single shooting scheme may be the simplest technique. First, a converged orbit or trajectory arc is computed employing

a differential corrections technique, assuming a reasonable initial guess is available. Then, a specific parameter associated with the converged solution is selected and varied, frequently a quantity with physical significance. The perturbed solution is then used as an initial guess for the targeting algorithm to compute a new solution. Applying this process repeatedly, that is, stepping through the continuation parameter for increasing or decreasing values, a family of topologically similar trajectories is generated. Commonly used quantities for the continuation parameter include energy, time of flight, or other physical parameters such as initial position or velocity states along the arc. This approach is very straightforward and can be directly applied to trajectory computations. An example of a family generated by varying time of flight or energy as the natural parameter is illustrated in Figure 4.3. All members of the family are related through a common initial and end point.

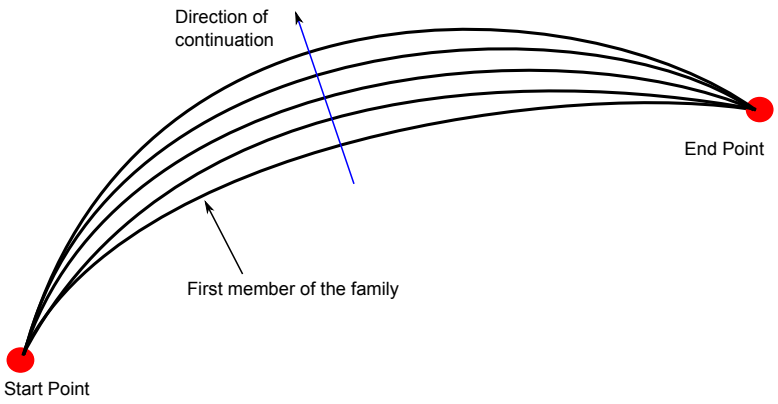

Figure 4.3. Single parameter continuation; TOF as the continuation parameter

4.3.2 Pseudo-Arclength Continuation

As an alternative to a physical quantity, a single parameter continuation scheme can also be formulated in terms of the well-known pseudo-arclength continuation method [55, 56]. Typically, single parameter continuation involves a quantity with some physical meaning. Thus, stepping through increasing or decreasing values of the parameter generally translates into some spatial step or a continual update in

the values of Jacobi constant or time of flight. However, in a pseudo-arclength continuation scheme, a step is computed in the specific direction tangent to the family. Consider a family generated using a general single parameter continuation technique. Each new member of the family $\bar{X}_i$ is computed from the previous converged solution $\bar{X}^*_{i-1}$, where $\bar{X}$ represents the free variable vectors as previously defined. Also, since $\bar{X}^*_{i-1}$ is the solution at the step $i-1$, this vector satisfies the constraint equation,

$$\bar{F}(\bar{X}^*_{i-1}) = \bar{0} \tag{4.47}$$

To compute the next member of the family, a step along a direction tangent to the family is developed. In general, the user-defined step size Δs possesses no physical meaning. For this application, consider a problem formulated consistent with the general free variables and constraints approach. Assume that the vector of design variables contains one more free variable than the number of constraints, i.e., $n = m + 1$. Given a converged member of the family, $\bar{X}^*_{i-1}$, a unit vector tangent to the family at $\bar{X}^*_{i-1}$ is obtained from the null vector, $\Delta\bar{X}^*_i$, of the Jacobian matrix, $D\bar{F}(\bar{X}_i)$, and possesses the same dimension as the associated free variable vector, that is, $\bar{X}^*_{i-1}$. To ensure that the next member of the family, $\bar{X}_i$, is located such that it is a 'distance' Δs from the previous member, $\bar{X}^*_{i-1}$, but along the family tangent direction, the constraint vector $\bar{F}(\bar{X}_i)$ is augmented with a pseudo-arclength constraint defined as,

$$\left(\bar{X}_i - \bar{X}^*_{i-1}\right) \Delta\bar{X}^*_{i-1} - \Delta s = 0 \tag{4.48}$$

Thus, the constraint vector for the pseudo-arclength continuation scheme is written as,

$$\bar{G}(\bar{X}_i) = \begin{bmatrix} \bar{F}(\bar{X}_i) \\ \left(\bar{X}_i - \bar{X}^*_{i-1}\right) \Delta\bar{X}^*_i - \Delta s \end{bmatrix} = \bar{0} \tag{4.49}$$

The augmented Jacobian matrix is derived from the partial derivatives of the augmented constraint vector with respect to the free variables, yielding,

$$D\bar{G}(\bar{X}_i) = \frac{\partial \bar{G}(\bar{X}_i)}{\partial \bar{X}_i} = \begin{bmatrix} D\bar{F}(\bar{X}_i) \\ \Delta \bar{X}_i^{*T} \end{bmatrix} \tag{4.50}$$

The augmented system is then constructed with as many free variables as constraints, thus, the Jacobian matrix is square. The corresponding unique solution is computed employing an iterative Newton method. Such a technique is generally more robust than other single-parameter continuation methods guaranteeing a set of unique solutions for the generated family. In the natural parameter approach, one specific physical quantity is selected for the algorithm to advance, either increasing or decreasing the value. In contrast, the pseudo-arclength method does not require any *a priori* knowledge of the evolution of the family from one member to next as the algorithm steps in the natural direction of expansion for the family.

4.4 Periodic Orbits Computation and Analysis in Synchronous Systems

4.4.1 Strategy to Compute Periodic Orbits

Periodic orbits are particular solutions that offer insight into the dynamical behavior of a particle in the vicinity of a system of irregularly-shaped bodies. Recall that no analytical solutions are available to describe the motion of a particle in the vicinity of a pair of arbitrarily-shaped bodies. Within this context, a general algorithm is developed to compute periodic solutions numerically in synchronous systems, that is, a time-invariant dynamical model. This approach still relies on a reasonable initial guess, or a baseline trajectory, to converge on the desired result, as illustrated in Figure 4.4.

A multiple shooting algorithm employs multiple segments, that originate from a set of patch points, to target a trajectory arc or orbit that satisfies a set of constraints or possesses some set of desired characteristics. A periodic orbit is a trajectory that

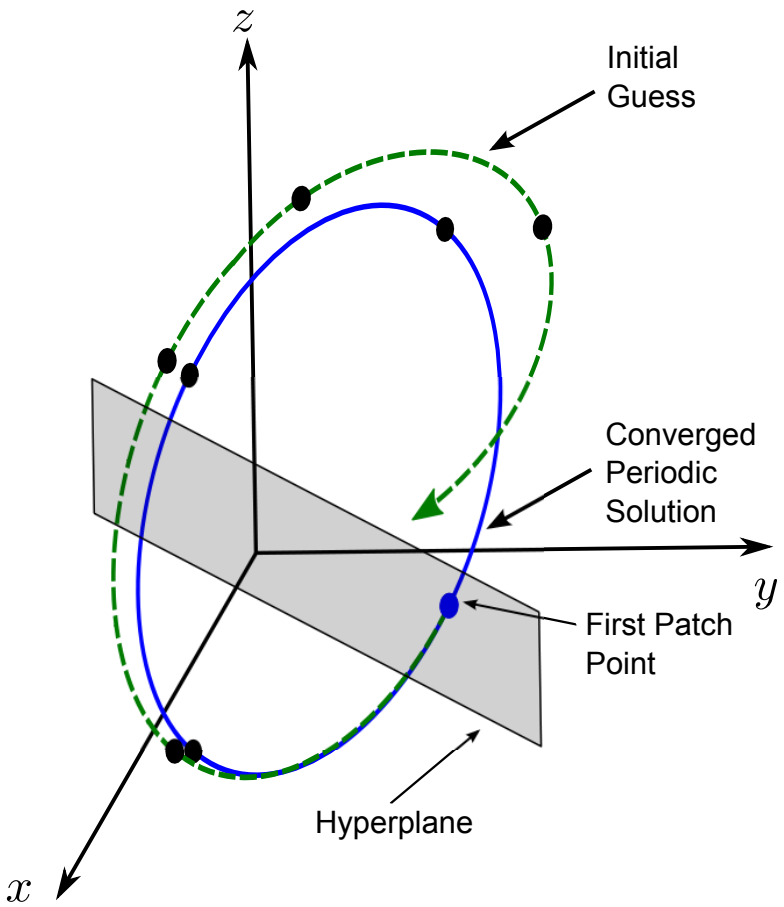

Figure 4.4. General strategy to compute periodic orbits

repeats itself in configuration space over a fixed period of time, P, denoting the period of the orbit. A periodic orbit is, in fact, a particular trajectory arc where the initial and final points along the path are continuous in position, velocity and time. Thus, the multiple shooting scheme, modified such that the final arc terminates at the initial point, that is, $\bar{x}_1^t = \bar{x}_1$ where $\bar{x}_1^t = \bar{x}(\bar{x_n}, t)$, is employed to compute these particular solutions. However, as in any numerical algorithm, there are practical considerations. Enforcing continuity between the first and last points in terms of the entire state vector, i.e., three position states and three velocity states, is generally not desirable because it may lead to convergence problems as the algorithm iteratively seeks the solution. Rather than constraining all six states, only five are explicitly targeted and

continuity is guaranteed via the Jacobi constant. Recall the definition of the integral of the motion for synchronous systems,

$$C = 2(U(x, y, z))^* - v^2 \tag{4.51}$$

The Jacobi constant relates the states through the pseudo-potential function U^*, a function of position only, and the square of the relative velocity v^2. Also, by definition, the Jacobi integral is constant along a continuous trajectory, therefore $C(\bar{x}_1) = C(\bar{x}_n^1)$. With this implicit additional equation, only five of the six states are explicitly enforced. In general, no additional constraints are necessary to ensure continuity.

In some particular scenarios where the desired periodic orbit possesses spatial symmetry with respect to a specific axis or plane, an additional constraint is useful to force the velocity vector at the last patch point to be directed parallel to the velocity at the first patch point. This complication is a consequence of the fact that the Jacobi constant expression involves only the magnitude of the relative velocity eliminating direction information. To offset this drawback, it may be convenient to operate on an surface of section, or hyperplane, a generally higher-dimensional plane that is transverse to the flow. Define a sample hyperplane,

$$\Sigma : y - y_{hyper} = 0 \tag{4.52}$$

where y is the second component of the nondimensional position vector that describes the location of a field point along the rotating direction parallel to the $\hat{y}$ axis. Then, the value y_{hyper} determines the location of Σ such that the hyperplane does, in fact, cross through the orbit and is, if possible, equal to zero for simplicity, that is, $\Sigma : y = 0$. Locating the first patch point on this surface can eliminate any ambiguity in the direction of the velocity at the last point after one revolution. The direction of the velocity vectors at these particular points is constrained to be the same, that is,

$$\text{sign}(\dot{y}_1^t) = \text{sign}(\dot{y}_1) \text{ where } \text{sign}(x) = \begin{cases} -1 & \text{if } x < 0, \\ 0 & \text{if } x = 0, \\ 1 & \text{if } x > 0. \end{cases} \tag{4.53}$$

where $\dot{y}_1^t = \dot{y}_1(\bar{x}_n, t)$ is the second component of the velocity vector that corresponds to the endpoint along the last integrated trajectory arc. For computational purposes, the constraint is expressed as a scalar expression. Introducing an additional slack variable, β, the constraint is formulated such that,

$$\dot{y}_1^t - \text{sign}(\dot{y}_1)\beta^2 = 0 \tag{4.54}$$

Then, the new endpoint constraint vector is written as,

$$\bar{x}_1^{*t} = \begin{bmatrix} x_1^t - x_1 \\ y_1^t - y_1 \\ z_1^t - z_1 \\ \dot{x}_1^t - \dot{x}_1 \\ \dot{y} - \text{sign}(\dot{y}_1)\beta^2 \\ \dot{z}_1^t - \dot{z}_1 \end{bmatrix} = \bar{0} \tag{4.55}$$

For this constraint to effectively enforce velocity continuity between the first and last patch point along the targeted arc throughout the correction process, the first patch point must remain on the hyperplane, that is,

$$y_1 - y_{hyper} = 0 \tag{4.56}$$

This last equation completes the additional set of constraints to define periodicity. Assuming a reasonable initial guess is available, an augmented time-invariant variable-time multiple shooting algorithm is constructed to generate periodic solutions. First,

recall the definition of the free variable vector comprised of the state vectors at the different intermediates points as well as the total time of integration T, augmented with the new slack variable β, that is,

$$\bar{X} = \begin{bmatrix} \bar{x}_1 \\ \vdots \\ \bar{x}_n \\ T \\ \beta \end{bmatrix} \tag{4.57}$$

The length of the new free variable vector is now $6n+2$. Next, the constraints in the vector $\bar{F}(\bar{X})$ are identified. In this application, the desired trajectory arc terminates at the initial point, or first patch point, that is, $\bar{r_d} = \bar{x}_1$. The constraint vector is therefore written in the form,

$$\bar{F}(\bar{X}) = \begin{bmatrix} \bar{x}_2^t - \bar{x}_2 \\ \vdots \\ \bar{x}_n^t - \bar{x}_n \\ \bar{x}_1^{*t} - \bar{x}_1 \\ y_1 - y_{hyper} \end{bmatrix} = \bar{0} \tag{4.58}$$

and includes the two additional constraints, that is, the vector constraint $\bar{x}_1^{*t} - \bar{x}_1 = \bar{0}$ and the scalar equation $y_1 - y_{hyper} = 0$ forming a vector of length $6n+1$. The new rectangular Jacobian matrix, of size $6n+1 \times 6n+2$, is obtained by evaluating the derivatives of the scalar constraint equations with respect to the free variables, i.e.,

$$D\bar{F}(\bar{X}) = \begin{bmatrix} \Phi(t_2,t_1) & -I_{6\times6} & & & \frac{\dot{x}_2^t}{n} & 0_{6\times1} \\ & \ddots & \ddots & & \vdots & \vdots \\ & & \Phi(t_n,t_{n-1}) & -I_{6\times6} & \frac{\dot{x}_n^t}{n} & \\ A & & & \Phi(t_1,t_n) & \frac{\dot{x}_1^t}{n} & B_{6\times1} \\ D_{1\times6} & 0_{1\times6} & \dots & \dots & 0 & 0 \end{bmatrix} \tag{4.59}$$

where the submatrices A, B, and D are defined as,

$$A = \begin{bmatrix} -1 & & & & & \\ & -1 & & & & \\ & & -1 & & & \\ & & & -1 & & \\ & & & & 0 & \\ & & & & & -1 \end{bmatrix} \tag{4.60}$$

$$B = \begin{bmatrix} 0 & 0 & 0 & 0 & 2\beta & 0 \end{bmatrix}^T \tag{4.61}$$

$$D = \begin{bmatrix} 0 & 1 & 0 & 0 & 0 & 0 \end{bmatrix} \tag{4.62}$$

Note that the expressions for the submatrices A, B, and D depend on the specified hyperplane. In this example, the hyperplane is defined as $y - y_{hyper} = 0$ but, depending on the target orbit, a hyperplane defined in terms of the components x or z may be more suitable. As mentioned above, the new Jacobian matrix is rectangular with an excess of one free variable, i.e., $n > m$. Thus, an infinite number of solutions is available and a minimum norm solution algorithm is implemented to iteratively converge on the periodic orbit closest to the initial guess. This multiple shooting method can also be reduced to a single shooting algorithm by considering one arc

defined by only one patch point, that is, the initial point or first patch point, without reformulating the problem. This scheme, regardless of the number of patch points, can also be directly implemented within a pseudo-arclength continuation scheme to compute a family of similar orbits rather than a single periodic orbit. Because a point solution, that is, one periodic orbit, does not offer much information or insight into the dynamical behavior of a particle in the vicinity of the primary system, the generation of larger sets of solutions, that is, families of periodic orbits, is the main focus of this investigation.

4.4.2 Stability of Periodic Orbits

A key factor to assess the suitability of a trajectory for a given application is often its stability. Stability is particularly relevant for a periodic orbit. Significant information concerning the stability of a particular solution is available from the first-order variational equations relative to the reference. For a periodic orbit, the monodromy matrix, M, is defined as the state transition matrix evaluated after exactly one orbital revolution, that is, $M = \Phi(t + P, t)$. The eigenvalues of the monodromy matrix are then computed for each orbit of interest, either a single trajectory or members of a same family of periodic orbits. The dynamical model for the motion of a particle in this problem represents a three degree of freedom Hamiltonian system. Consequently, the monodromy matrix admits six eigenvalues that occur in reciprocal and complex conjugate pairs [57]. Let the symbol λ_i denote some non-zero eigenvalue of M. If λ_i is real, then a second eigenvalue, λ_j, corresponds to λ_i to complete the reciprocal pair, such that $\lambda_j = 1/\lambda_i$. If λ_i is complex, another complex eigenvalue $\lambda_j = \lambda_i^*$ exists, where λ_i^* is the complex conjugate of λ_i. Additionally, Jordan and Smith demonstrate that periodic solutions only exist when one of the multipliers is unity [58]. Therefore, because of the reciprocal nature of the eigenvalues, for a periodic orbit, two of the six characteristic multipliers are equal to unity.

Given two unity eigenvalues that reflect periodicity, two pairs of characteristic multipliers remain to characterize the linear stability of the orbit. Based upon the magnitude of the eigenvalues, three different subspaces [59], that is, stable, unstable, and center, are defined such that,

$$|\lambda_j| > 1 \Leftrightarrow \text{unstable subspace},$$
$$|\lambda_j| = 1 \Leftrightarrow \text{center subspace},$$
$$|\lambda_j| < 1 \Leftrightarrow \text{stable subspace}.$$

From these definitions, the stability of the periodic orbit in a linear sense is clear: an orbit is defined as unstable if at least one the multipliers is of magnitude greater than one, that is, $|\lambda_j| > 1$. Alternately, if all the multipliers possess magnitudes less than one, that is, $|\lambda_j| < 1$, the orbit is labelled stable. However, because the eigenvalues occur in reciprocal pairs, a real eigenvalue with magnitude less than one, λ_i, also implies the existence of its reciprocal multiplier such that $\lambda_j = 1/\lambda_i$, i.e. $|\lambda_j| > 1$. Therefore, only marginal stability is achievable for a periodic solution, that is, when all the eigenvalues are of unit magnitude. For a family of periodic orbits, the evolution of the eigenstructure along the family supplies information concerning the behavior of the orbits in terms of linear stability. This process is also a useful tool for investigation of the existence of new families of orbits.

4.4.3 The Stability Index and Bifurcations

For a periodic orbit, the eigenvalues of the corresponding monodromy matrix serve as the basis to explore the linear stability of the trajectory. Additionally, these characteristic multipliers can also be employed to investigate intersections between different families of periodic trajectories. Recall that three pairs of reciprocal eigenvalues, including a pair of unity multipliers, exist for a given periodic orbit. The other

four multipliers may include real or complex conjugate eigenvalues pairs. Define the stability index as the average of each reciprocal pair of eigenvalues, that is,

$$\nu = \frac{1}{2}\left(|\lambda| + |\lambda^*|\right), \tag{4.63}$$

for the reciprocal pair (λ, λ^*), where ν is a single numerical quantity to assess the stability of a given solution. For a periodic orbit, one pair of eigenvalues is always unity, thus, the four remaining multipliers define two stability indexes. A first 'horizontal' index is associated with stability in the plane of the orbit, $\nu = \nu_h$, and a 'vertical' index that corresponds to out-of-plane stability, that is, $\nu = \nu_v$. For values of ν less than 1, the orbit is defined as stable, and alternately, an orbit is labelled unstable for values of ν greater than 1. The orbit is unstable if either index exceeds 1. Finally, a graphical approach is proposed to quickly assess the stability properties of a given solution as a part of a family of periodic orbits without losing visibility concerning the overall behavior of the family of interest. Specifically, consider the maximum stability index defined as $\nu_{max} = max\left\{|\nu_v|, |\nu_h|\right\}$. Then, for values of ν_{max} less than 1, the orbit is defined as stable, otherwise it is unstable. However, using such a representation, the form of the instability is not necessarily clear.

4.4.4 Bifurcations

A bifurcation is a change in the structure or behavior along a set of solutions, and can also represent the intersection between one or more families of solutions. Within the context of periodic orbits, a sudden change in stability properties indicates the presence of a bifurcation and the possible intersection with other families of orbits. In this investigation, families of solutions are restricted to periodic orbits, but other type of solutions, such as torii, are also related to bifurcations. To each type of bifurcation corresponds a particular change in stability, that is, a specific change in the eigenstructure of the family corresponds to a particular bifurcation. Bifurcation theory is complex and a number of different types of bifurcations are defined depend-

ing on the type of change in stability that the observed family undergoes. Another defining criteria for the classification of bifurcations is the existence of new family(ies) of solutions that intersect the known family as well as the type of stability change the new family(ies) undergo(es) at the bifurcation point.

Understanding of the basics of bifurcation theory is important to compute families of periodic orbits. From an isolated family, no insight concerning the existence of additional families of trajectories is available. The study of bifurcations within a family of orbits supplies information to locate new families as well as an initial guess to initialize the computation of the new set of solutions. This study is limited to simple and double period bifurcation, n^{th} period bifurcations are not addressed. Common bifurcation types include tangent and period doubling, and rarer types include secondary Hopf and modified secondary Hopf bifurcations, as illustrated in Figure 4.5. To aid the stability analysis of periodic solutions, the eigenvalues of the monodromy

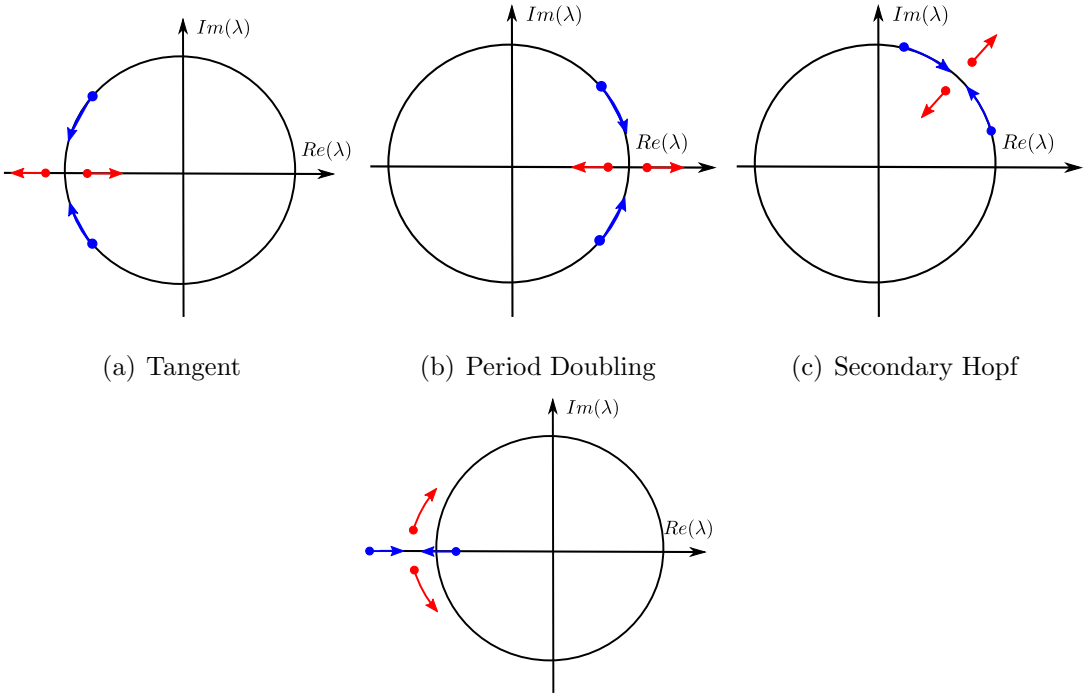

(a) Tangent (b) Period Doubling (c) Secondary Hopf

(d) Modified Secondary Hopf

Figure 4.5. Sample bifurcation types

matrix are conveniently represented on the complex plane $(\mathrm{Re}(\lambda), \mathrm{Im}(\lambda))$. In this plane, unstable multipliers, that is, $|\lambda| > 1$, lie outside of the unit circle, stable multipliers, i.e., $|\lambda| < 1$ are inside of this circle, and eigenvalues with unit magnitude fall on the circle. A tangent bifurcation occurs when one pair of complex eigenvalues that originally lie on the unit circle converges at -1, or $\nu = -1$, and splits onto the real axis into a real reciprocal pair.(Figure 4.5(a)) In most cases, a new family emerges at the bifurcation point from a tangent bifurcation, that also undergoes a change in stability as it passes through the bifurcation point, except for some special scenarios. A tangent bifurcation that does not yield a new family of orbits is labelled a cyclic fold. [10, 60] Then, when a complex pair converges at $+1$, or $\nu = 1$, and splits onto the real axis, a new family exists, in general, such that the first member of the new family possesses a period twice the period of the original family at the bifurcation point. [60] However, members of the new family do not undergo any stability change at the bifurcation point. This type of bifurcation is denoted period doubling.(Figure 4.5(b)) Rarer bifurcations include secondary Hopf and occurs when a pair of complex eigenvalues converges on the unit circle, off the real axis, and splits into the complex plane. (Figure 4.5(c)) In general, Hopf bifurcations yield a new family of invariant torii about a single periodic solution. [60, 61] This type of bifurcation has been observed in several families in another problem in astrodynamics, the Circular Restricted Three Body Problem. Finally, the modified secondary Hopf bifurcation occurs when a real pair of eigenvalues converges onto the real axis, off the unit circle, and splits in the complex plane. (Figure 4.5(d)) Note that in this case a change in the eigenstructure does occur, from real to complex conjugate eigenvalues, but does not result in a change in stability. The combination of eigenvalues before and after the collision yields unstable orbits in both cases. Little literature exists on this subject and more investigation is necessary to understand the existence and structure of new families from this type of bifurcation as well as the associated change in stability that potentially new families undergo at the bifurcation point.

4.4.5 Bifurcation Computation

The exact location of a bifurcation within a family of periodic orbits, that is, the periodic solution that corresponds to the bifurcation point, can be computed using an algorithm that combines continuation and a bisection method. Monitoring the evolution of the eigenstructure as the family is computed allows the detection of bifurcations, that is, a distinct change in the eigenstructure from one member to the next. Clearly, if such a change occurs from one member to the next, the associated bifurcating orbit is located between these two solutions. A bisection type method is proposed to compute the exact location of the bifurcation orbit. [62] Let $\bar{X}^{n-1}$ and $\bar{X}^{n-2}$ represent the converged free variable vectors for the current and previous solutions in the family. Then, define,

$$\bar{X}^{lower} = \bar{X}^{n-2} \tag{4.64}$$

$$\bar{X}^{upper} = \bar{X}^{n-1} \tag{4.65}$$

Also, let $\bar{X}^{mid}$ denote the free variable vector that is associated with a solution midway between the two orbits, that is,

$$\bar{X}^{mid} = \bar{X}^{lower} + \frac{1}{2}\Delta\bar{X} \tag{4.66}$$

where $\Delta\bar{X}$ represents the deviation between the design variable vectors that are associated with the previous and current solution. The nature of this step depends upon the continuation method employed. For the pseudo-arclength continuation technique, the deviation between two subsequent solutions in the family, in terms of free variable vectors, is related to the nullspace of the Jacobian matrix, labelled $\Delta\bar{X}^{lower}$, that is associated with the most recent converged solution. Recall that the Jacobian matrix is evaluated as the partial derivative of the constraint vector with respect to

the design variable vector. Also, the continuation constraint for the pseudo-arclength algorithm is formulated as,

$$\left(\bar{X}^{upper} - \bar{X}^{lower}\right) \Delta\bar{X}^{lower} - \Delta s = 0 \tag{4.67}$$

where Δs is the user defined step size selected for the pseudo-arclength continuation scheme. To explicitly formulate $\bar{X}^{mid}$, define $\Delta\bar{X} = \Delta s \Delta\bar{X}^{lower}$; $\bar{X}^{mid}$ is then employed as initial guess to compute a new periodic solution, labelled $\bar{X}^{mid*}$. Then, the location of the bifurcating orbit is available from observing the eigenstructure of the new solution, $\bar{X}^{mid*}$, that is, either between $\bar{X}^{lower}$ and $\bar{X}^{mid*}$ or, $\bar{X}^{mid*}$ and $\bar{X}^{upper}$. If it is evident from the change in the eigenstructure that the bifurcating orbit is located between $\bar{X}^{lower}$ and $\bar{X}^{mid*}$, then,

$$\bar{X}^{lower} = \bar{X}^{mid*} \tag{4.68}$$

Alternatively, if the bifurcating orbit is located between $\bar{X}^{mid*}$ and $\bar{X}^{upper}$, then,

$$\bar{X}^{upper} = \bar{X}^{mid*} \tag{4.69}$$

To compute the next periodic solution, redefine the prediction for the midway solution, $\bar{X}^{mid}$, such that,

$$\bar{X}^{mid} = \bar{X}^{lower} + \frac{1}{4}\Delta_s \Delta\bar{X}^{lower} \tag{4.70}$$

The prediction step size for $\bar{X}^{mid}$ is reduced by a factor of two for every new prediction, $\bar{X}^{mid}$. The process is repeated until the converged solution, $\bar{X}^{mid*}$, possesses the exact desired characteristic multipliers that are associated with the bifurcation, thereby yielding the exact location of the bifurcating orbit, within some numerical predetermined numerical tolerance.

4.4.6 New Family Computation from a Bifurcation

When a bifurcation is located along a family of periodic orbits, assuming that the type of bifurcation indicates the existence of a new family that intersects the observed family, to compute the entire or a subset of the new family is often desirable to broaden the understanding of the dynamical behavior in the vicinity of the primary system. Investigating the eigenspace of the bifurcating orbit allows to produce an educated initial guess to compute the first member of the new family. Consider a bifurcating periodic orbit and the corresponding monodromy matrix. The eigenvalues of the monodromy matrix supply linear stability information concerning the orbit, and the eigenvectors also contain useful information. The two eigenvectors that are associated with the unity eigenvalues, $\bar{V}_1^u$ and $\bar{V}_2^u$, as a result of the periodicity of the orbit, depict the natural direction of expansion for the family in terms of a six-dimensional vector. Then, let $\bar{X}^*$ represent the truncated free variable vector that is associated with the periodic orbit, that is, the vector that contains the states at the intermediate patch points. Perturbing the design variable vector in the particular direction that corresponds to the eigenvectors $\bar{V}_i^u$ is in essence how the pseudo-arclength continuation algorithm operates to produce an initial guess to compute the next member in a family. Similarly, the eigenvectors that are associated with the bifurcation eigenvalues, ± 1, indicate the direction of expansion for the new family. Thus, perturbing the free variable vector for the bifurcating orbit in this particular direction supplies an initial guess to compute a first member in the new family, that is,

$$\bar{X}^{new} = \bar{X}^* + d\bar{V} \tag{4.71}$$

where d is an arbitrary step size, and $\bar{V}$ is defined as the average eigenvector that is associated with the bifurcation eigenvalues, i.e.,

$$\bar{V} = \bar{V}(\lambda_{bif}) + \bar{V}(\lambda_{bif}^*) \tag{4.72}$$

where λ_{bif} and λ_{bif}^{*} are the reciprocal eigenvalues that are associated with the bifurcation. To initialize the generation of the new family of periodic orbits, a first member is computed employing the new state vector in Eqn. (4.71) as initial guess. In summary, if such a family exists, a first periodic orbit is computed exploiting the eigenspace associated with the bifurcation orbit to initialize the generation of the family, or part of the family.

4.5 Periodic Orbits Computation and Analysis in Non-Synchronous Systems

A similar procedure is developed to enable the computation of periodic orbits in time-varying dynamical systems. Of course, for third-body periodic trajectories to exist in a time-varying dynamical model, the underlying dynamics must be periodic, too. Recall the definition of the vector of free-variables for the multiple-shooting formulation for non-synchronous systems, augmented with the integration time that corresponds to the final arc, T_n,

$$\bar{X} = \begin{bmatrix} \bar{x}_1 \\ \vdots \\ \bar{x}_n \\ T_1 \\ \vdots \\ T_n \\ \tau_1 \\ \vdots \\ \tau_n \end{bmatrix} \tag{4.73}$$

Without any integral of the motion, the periodicity constraint is simply written as $\bar{x}_1^t - \bar{x}_1$. Also, the sum of the integration times, T_i, must be equal to the period

of the targeted orbit, P, that is, $\sum_{i=1}^{n} T_i = P$. Then, similar to the synchronous formulation, the first patch point is required to remain on the hyperplane, that is,

$$y_1 - y_{hyper} = 0 \tag{4.74}$$

The constraint vector is thus augmented with these additional constraints such that,

$$\bar{F}(\bar{X}) = \begin{bmatrix} \bar{x}_2^t - \bar{x}_2 \\ \vdots \\ \bar{x}_n^t - \bar{x}_n \\ \bar{x}_1^t - \bar{x}_1 \\ \tau_2 - (\tau_1 + T_1) \\ \vdots \\ \tau_n - (\tau_{n-1} + T_{n-1}) \\ y_1 - y_{hyper} \\ \sum_i = 1^n T_i - P \end{bmatrix} = \bar{0} \tag{4.75}$$

to yield the constraint equation $\bar{F}(\bar{X}) = \bar{0}$. The Jacobian matrix $D\bar{F}(\bar{X})$ is again defined as the partial derivatives of the constraint equations with respect to the free variables,

$$D\bar{F}(\bar{X}) =$$

$$\begin{bmatrix}
\Phi_1 & -I_{6\times6} & & & \dot{\bar{x}}_2^t & & & -\frac{\partial \bar{x}_2^t}{\partial \tau_1} & & & \\
& \ddots & \ddots & & & \ddots & & & \ddots & & \\
& & \Phi_{n-1} & -I_{6\times6} & & & \dot{\bar{x}}_n^t & & & -\frac{\partial \bar{x}_n^t}{\partial \tau_{n-1}} & \\
-I_{6\times6} & & & \Phi_n & & & & \dot{\bar{x}}_1^t & & & -\frac{\partial \bar{x}_1^t}{\partial \tau_n} \\
& & & & -1 & & & -1 & 1 & & \\
& & & & & \ddots & & & \ddots & \ddots & \\
& & & & & & -1 & & & -1 & 1 \\
D_{1\times6} & & & & & & & & & & \\
& & & & & & & 1 & \dots & \dots & 1
\end{bmatrix} \tag{4.76}$$

where the submatrix D is as previously defined,

$$D = \begin{bmatrix} 0 & 1 & 0 & 0 & 0 & 0 \end{bmatrix} \tag{4.77}$$

Note that the expression for the submatrix D depend on the specified hyperplane. In this example, the hyperplane is defined as $y - y_{hyper} = 0$ but, depending on the target orbit, a hyperplane defined in terms of the components x or z may be more suitable. The new Jacobian matrix is rectangular. Thus, an infinite number of solutions is available and a minimum norm solution algorithm is implemented to iteratively converge on the periodic orbit closest to the initial guess. This multiple shooting method can also be reduced to a single shooting algorithm by considering one arc defined by only one patch point, that is, the initial point or first patch point, without reformulating the problem.

4.6 Maps

Mapping techniques are powerful methods that allow to inspect the dynamical behavior in dynamical systems. Various types of maps are available and the best-suited map depends on the application and the dynamical model considered. In this investigation, the focus is on two types of maps: Poincaré maps and Finite Tine Lyapunov Exponent maps. The first one is best-suited for time-invariant dynamical models, i.e, for synchronous systems, while the second one is better adapted to time-varying models, or non-synchronous primary system models.

4.6.1 Poincaré Maps

The Poincaré map is a powerful tool that offers insight into the rich dynamical behavior in complex dynamical systems. To generate a Poincaré map, first define a surface of section, or hyperplane, Σ. Then, a map is produced by numerically propagating a set of initial conditions, typically for a given energy level, and displaying the crossings of the integrated trajectories with the defined hyperplane. Reducing the analysis to the planar problem, the state vector for any given trajectory is 4-dimensional. Note that, the use of a surface of section, in addition to a constrained value of the Jacobi constant, reduces the dimension of the system by two. Hence, considering only the CRTBP, synchronous SETBP, and synchronous EETBP, i.e., time-invariant dynamical systems, and limiting the analysis to the planar problem, the dynamical model is a two-degrees of freedom Hamiltonian system. Thus, in the planar problem, the state space is confined to a plane. For instance, a Poincaré map that is generated for $\Sigma : y = 0$, that is, the collection of crossings with the hyperplane $y = 0$, displayed on the set of axes $x - \dot{x}$ depicts the dynamical behavior at this energy level for the prescribed set of initial conditions.

Visualization: Winding Number

A typical representation for a Poincaré map is a puncture plot, or, directly displaying the points that corresponds to the recorded crossings on, or punctures of, the surface of section. One approach to highlight dynamical structures within a map is to leverage winding numbers, as discussed in details in [63] and outlined in this section. For integrable and near-integrable Hamiltonian systems with two-degrees of freedom, the dynamical behavior can be interpreted as the flow along a standard torus, or two-torus, and described by two frequencies, the poloidal and toroidal frequencies. The motion along the torus can be characterized by the ratio of the two frequencies,

$$\omega = \frac{\omega_1}{\omega_2} \tag{4.78}$$

where ω_1 and ω_2 are the poloidal and toroidal frequencies, respectively, and ω is labeled the winding number. Since the planar problem is a time-invariant Hamiltonian system, periodic and quasi-periodic motions are confined to a two-torus and, thus, are completely described by a unique winding number.([64–67]) However, the numerical evaluation of this winding number requires a transformation from state space to a more appropriate set of coordinates, such as action-angle variables. Such a procedure is excessively complex and computationally expensive for a practical implementation of the algorithm, especially considering that, in this analysis, the winding number is only sought for visualization purposes. As an alternative, one can demonstrate that multiple winding numbers exist for Hamiltonian systems of higher dimension ($N \geq 3$). ([65]) Although the planar problem is a two-degrees of freedom Hamiltonian system, Cartesian coordinates are most often employed as the set of variables for dynamical modeling. Within this context, a set of winding numbers is computed directly from the Cartesian space coordinates. For any given initial conditions, the computation of the set of winding numbers relies on tracking specific angles as the propagated trajectory rotates about the origin. Let θ_{ab} represent the cumulative rotation for the

Cartesian coordinates a and b that is traced by the 2D vector $\bar{r}_{ab}(t) = [a_t, b_t]^T$ through the numerical integration process,

$$\theta_{ab} = \sum_{t=0}^{t_n} \arccos\left(\frac{\bar{r}_{ab}(t+\Delta t).\bar{r}_{ab}(t)}{\parallel \bar{r}_{ab}(t+\Delta t) \parallel \parallel \bar{r}_{ab}(t) \parallel}\right) \tag{4.79}$$

where t_n is the integration time to complete n returns on the hyperplane and Δt represents the current integrator time-step. In this analysis, the hyperplane is selected as $y = 0$, thus, the set of winding numbers that are relevant is $W = (w_{x\dot{x}}, w_{x\dot{y}} w_{\dot{x}\dot{y}})$ such that,

$$w_{x\dot{x}} = \frac{2\pi n}{\theta_{x\dot{x}}},\ w_{x\dot{y}} = \frac{2\pi n}{\theta_{x\dot{y}}},\ w_{\dot{x}\dot{y}} = \frac{2\pi n}{\theta_{\dot{x}\dot{y}}} \tag{4.80}$$

Within this set, depending on the map and the objective of the visualization representation, one number may be more suited to represent the dynamical structures within the map. In subsequent map illustrations, one winding number is employed in terms of a color map to highlight the structures outlined by the returns.

Enhanced Visualization: Orbit Convolution

The orbit convolution process ([63,68,69]) is an alternative approach for displaying a Poincaré map, as disussed in details in [63]. Rather than a puncture plot, the orbit convolution produces a scalar field representation of the dynamical behavior. The domain of interest for a given map is overlaid with a colored noise image, $\sigma(x)$, that is, to each grid node in the domain is associated a random RGB color with value between $[0, 0, 0]$ and $[1, 1, 1]$. The initial conditions for each grid node are propagated for n returns and the corresponding pixel in the initial grid is colored as the averaged RGB color through the numerical simulation, that is, the average value $I(\bar{x})$ of the color codes that are associated with the successive map returns, $\mathbf{P}^p(\bar{x})$, for a given trajectory,

$$I(\bar{x}) = \frac{1}{n}\sum_{p=0}^{n}\sigma\left(\mathbf{P}^{p}(\bar{x})\right) \tag{4.81}$$

where p is an increasing integer that corresponds to the series of map iterates such that $\mathbf{P}^{p}(\bar{x})$ belongs to the domain of interest. As a result of this procedure, dynamical features on the map that are related to the same trajectories, or family of trajectories, appear in similar colors while chaotic regions are colored in gray. Note that this process relies on a high-density grid of initial conditions and a large number of map iterates to produce a high-resolution depiction of the dynamics and a sharp coloring of the map structures, respectively. The combination of these two factors, high-density grid and long-term numerical integration, makes this process very computationally intense. A significant reduction in computational cost is allowed by leveraging multiple orbit convolution passes with fewer map returns. Equivalently, the colored image that is obtained after the orbit convolution procedure is then employed as new initial image while the initial colored noise image is still employed to compute the color code for any map return. Also, to further sharpen the colored image that is produced for each orbit convolution pass, a high-pass filter is applied to the intermediate image between successive passes. The final image that is produced through this process is a smooth representation of the third-body behavior that highlights dynamical structures and may be of interest to emphasize the similarities and differences between a set of maps.

4.6.2 Stroboscopic Maps and the Finite Time Lyapunov Exponent

Stroboscopic maps are constructed similarly to Poincaré maps except that, rather than recording crossings with a hyperplane defined in terms of physical coordinates, the hyperplane condition for a stroboscopic map is selected as a particular or arbitrary time. Such an approach is well-suited for time-varying systems where the reduction of the dimensionality of the problem, via the selection of a physical hyperplane, is not sufficient due to the absence of any integral of the motion. One application of

stroboscopic maps is a first-return map, that is, only the set of first crossings with the defined hyperplane are retained. Then, rather than focusing on the final integrated states to depict the behavior, a derived quantity from the state is leveraged to represent the dynamical behavior of the third body, such as the Finite Time Lyapunov Exponent (FTLE). [70]

In essence, the FTLE measures the stretching between two adjacent trajectories over a defined time interval. Let $\phi_{t_0}^{t}(\bar{x})$ represent the flow map, i.e., the state of the system evolved from an initial state, $\bar{x}_0$ at t_0, until the time t. Then, the integration time, or truncation time, for the evaluation of the FTLE is $T = t - t_0$. The FTLE is computed as the largest eigenvalue, normalized by the integration time T, of $\sqrt{\frac{d\phi_{t_0}^{t}(\bar{x})}{d\bar{x}_0}^{T} \frac{d\phi_{t_0}^{t}(\bar{x})}{d\bar{x}_0}}$, that is, the matrix spectral norm of the Jacobian with respect to variations in the initial state. Note that, consistent with the shooting technique, $\frac{d\phi_{t_0}^{t}(\bar{x})}{d\bar{x}_0}$ is also the STM. The matrix product $\frac{d\phi_{t_0}^{t}(\bar{x})}{d\bar{x}_0}^{T} \frac{d\phi_{t_0}^{t}(\bar{x})}{d\bar{x}_0}$ is also labeled the Cauchy-Green strain tensor. Thus, the FTLE is defined as,

$$\lambda = \frac{1}{|T|} \ln \left\{ \tilde{\lambda}_{Max} \left[\sqrt{\frac{d\phi_{t_0}^{t}(\bar{x})}{d\bar{x}_0}^{T} \frac{d\phi_{t_0}^{t}(\bar{x})}{d\bar{x}_0}} \right] \right\} \tag{4.82}$$

where $\tilde{\lambda}_{Max}()$ represents the operation of extracting the largest eigenvalue from the operand. Note that, both 'forward' and 'backward' FTLE values can be computed from a given initial state, that is, the flow map is evolved forward or backward in time, respectively. While both flows contain valuable information independently, a more complete depiction of the behavior is available by conjointly inspecting forward and backward FTLE maps. In practical application, the generation of a FTLE map relies on the same procedure as for the orbit convolution technique. A grid of initial conditions is numerically integrated for the time duration T and the FTLE is computed for each grid node. Then, one approach to visualize the FTLE field is to produce an image of a two-dimensional projection of the initial condition domain, e.g, a map with axes $x, \dot{x}$ where $x_0 = [x, y, z, \dot{x}, \dot{y}, \dot{z}]$, and each pixel is colored according to the forward, backward, or a combination of two FTLE fields. Additional consideration must

be devoted to selecting an appropriate truncation time, i.e., the integration time, T, for the evaluation of the FTLE that yields the most insight. Unfortunately, there is no systematic method to select T, and in fact, the choice of T may vary depending on the application, the initial condition domain, and the underlying dynamical system.

5. NATURAL DYNAMICS BOUNDED MOTION IN SYNCHRONOUS SYSTEMS

Within the context of exploring third-body trajectories in the vicinity of two small irregular bodies, that is, a problem where investigating the motion in close proximity to the primaries is necessary, two spherical primaries may not, in general, be a reasonable assumption. This more specific problem motivates the introduction of a dynamical model that incorporates more complexity in the primary system model. In addition to the CRTBP, consider the synchronous Sphere-Ellipsoid Three-Body Problem (SETBP) and the synchronous Ellipsoid-Ellipsoid Three-Body Problem (EETBP). With similar equations of motion, both models possess attributes similar to those in the CRTBP. In particular, while no analytical solution for the motion of the particle is available, the EOMs are time-invariant and periodic solutions exist.

5.1 Periodic Orbits in Synchronous Systems

To explore the dynamical behavior of a third body within the vicinity of two primaries, periodic orbits are of special interest. A multi-phase technique based on differential corrections, as introduced in Section 4.4.1, is employed to compute a trajectory that is periodic in the nonlinear regime given some initial guess. The same algorithm is used to produce such trajectories for any of the simplified dynamical models, that is, CRTBP, SETBP, or EETBP.

5.1.1 Libration Point periodic Orbits. (LPO)

Most common families of periodic orbits within this regime are labeled libration point orbits and a preliminary exploration of the dynamical structures typically orig-

inates near any equilibrium solutions. The first-order variational equations of motion are employed to generate an initial guess in the vicinity of a given equilibrium point. First, the planar Lyapunov families corresponding to the equivalent collinear Lagrange points are computed for a sample system. Employing a continuation strategy, additional families of more complex orbits that include three-dimensional trajectories are also computed, as illustrated in Figure 5.1 for a sample ellipsoid-sphere system with one elongated primary. In this plot are displayed Lyapunov, halo, and axial families of periodic orbits associated with each of the three collinear points. Although not illustrated in this figure, similar families of orbits can also be constructed in the vicinity of the two equilateral points. Although these families of orbits may or may not offer options for any direct application in design or analysis scenarios, these trajectories are most useful in constructing even more complex trajectories.

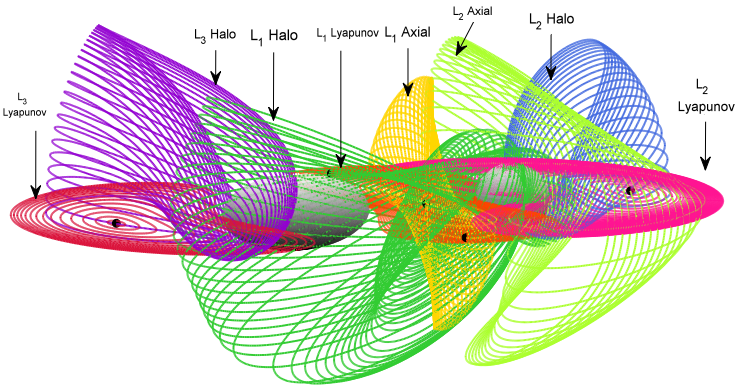

Figure 5.1. Libration point Periodic Orbits (LPO): ellipsoid axes ratios $\beta = \gamma = 0.5$ - primary mass ratio $\mu = 0.3$ - primary distance $r = 3$

5.1.2 Resonant periodic orbits.

Other families of periodic orbits within this regime include trajectories that are labeled resonant orbits. The classical restricted two-body problem is leveraged to

generate an initial guess to produce a periodic orbit in the three-body regime via a corrections strategy and/or continuation. Within the context of the restricted two-body problem, consider two bodies, A and B, that orbit a primary body. The primary body is massive while body A and B are assumed massless, consistent with the restricted two-body problem model. Body B is defined to be in $p : q$ resonance with body A if it completes p orbits with respect to the primary in the same time interval in which body A achieves exactly q orbits. [71, 72] In this definition, p and q are two positive integers where p is associated with body B and q refers to the period of body A. For instance, a spacecraft moves in a $1 : 2$ resonance with the Moon if it completes one revolution around Earth in the same time that the Moon completes two periods. In this analysis, the primary is the primary P_1, body A is the second primary, P_2, and the third body, B, is a spacecraft. Using the restricted two-body problem to produce an initial guess for a resonant orbit given some resonant ratio $p : q$, an orbit that is periodic and possesses approximately the initial resonant ratio in the three-body regime is computed. Employing a continuation method, a family of resonant orbits, or, a set of orbits that share some common characteristics, is computed. Also, exploiting bifurcations within the planar resonant family, other families with the same resonance ratio that include symmetric or asymmetric three-dimensional trajectories can be generated. First, families of planar resonant orbits for various $p : q$ ratios are computed for a sample point mass, ellipsoid-sphere, and ellipsoid-ellipsoid system. In Figure 5.2 is illustrated selected families of planar resonant orbits as computed for a sample ellipsoid-ellipsoid system with an elongated primary with largest equatorial P_1 radius of 5 km, ellipsoid axes ratios $\beta = \gamma = 0.5$, primary mass ratio $\mu = 0.2$, and primary distance $r = 6$. While the various families exhibit orbits with very different shapes and sizes, all offer one or more close encounters with at least one primary body. Then, in Figure 5.3 is illustrated selected sample three-dimensional families of symmetric and asymetric resonant orbits computed for a sample ellipsoid-sphere system with an elongated primary with largest equatorial P_1 radius of 5 km, ellipsoid axes ratios $\beta = \gamma = 0.5$, primary mass ratio $\mu = 0.2$, and primary distance $r = 6$.

Similar to the libration point orbits, these families of orbits may or may not offer options for any direct application in design scenarios, however, these trajectories are also useful in constructing even more complex trajectories.

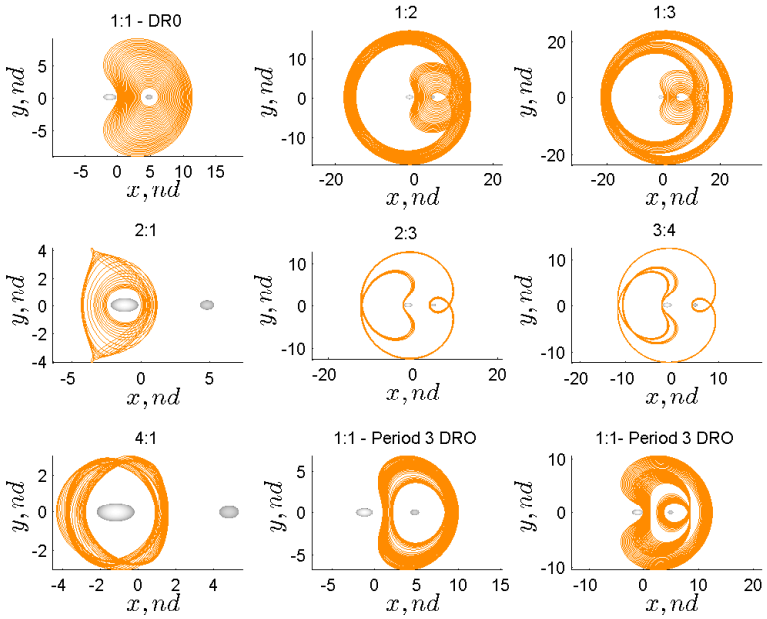

Figure 5.2. Sample families of planar resonant orbits: ellipsoid axes ratios $\beta_1 = \gamma_1 = 0.5$ - $\beta_2 = \gamma_2 = 0.65$ - primary mass ratio $\mu = 0.2$ - primary distance $r = 6$

5.1.3 Low Prograde Orbits (LoPO) and Distant Retrograde Orbits (DRO)

Periodic orbits labeled Distant Retrograde Orbits (DRO) and Low Prograde Orbits (LoPO) are also of special interest as these families feature numerous stable orbits. The DROs are, in fact, 1:1 resonant orbits. Planar LoPOs are also centered at one primary, P_1 or P_2. Exploiting bifurcations within the planar families, and employing a continuation technique, a three-dimensional family that branches from the planar family is also computed, as illustrated in Figure 5.4 for a sample sphere-sphere system with P_1 radius of 5 km. As clearly apparent in the figure, the orbits in the three-dimensional families allow regular close-range proximity of a third-body with

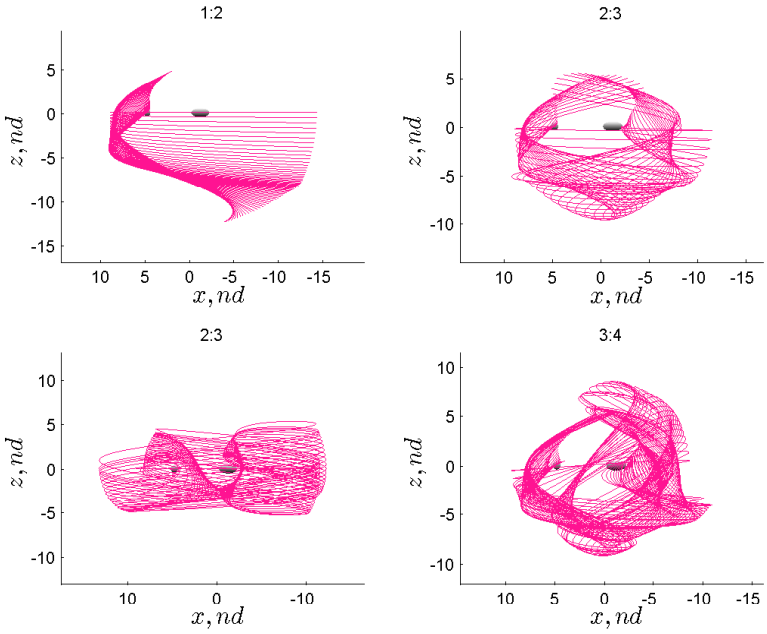

Figure 5.3. Sample families of 3D resonant orbits: : ellipsoid axes ratios $\beta_1 = \gamma_1 = 0.5$ - primary mass ratio $\mu = 0.2$ - primary distance $r = 6$

respect to either primary. In addition, the three-dimensional aspect of the trajectories offers extensive coverage of the surface of the attractive primary.

5.1.4 Stability analysis

A key factor to assess the suitability of a trajectory for a given application is often its stability. Significant information concerning the stability of a particular solution is available from the first-order variational equations relative to a reference. Recall the maximum stability index, specifically, for values of μ_{max} less than 1, a periodic orbit is defined as stable, otherwise it is unstable. First, consider selected families of libration point orbits. In Figure 5.5 is illustrated the maximum stability index as a function of the abscisse of the initial point of individual trajectories, scaled by the primary separation distance, within a given family of libration point orbits. Each of the families is computed for a sphere-sphere, sphere-ellipsoid, and ellipsoid-ellipsoid sample

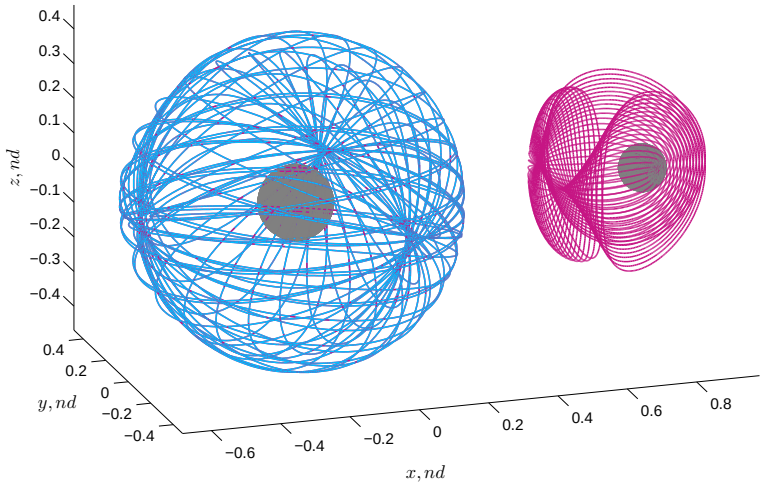

Figure 5.4. P_1 and P_2 centered 3D LoPO families: primary radius = 5 km - primary mass ratio $\mu = 0.2$ - primary distance $r = 6$

system to highlight the effect of the shape of the primary bodies onto the dynamical behavior of a third body in the vicinity of such a primary system. In the CRTBP, the selected families of orbits in this figure, that is, L_1 and L_3 Lyapunov, L_1, L_2, and L_3 halo, and L_3 vertical, all but the L_1 halo family exhibit some stable members, as depicted by the maximum stability index line achieving values less than one for some trajectories. The families that are computed for the sphere-ellipsoid system exhibit the same behavior in most instances, with the exception of the L_3 Lyapunov and halo families where no stable orbits exist. Note that, for the models that incorporate a massive body model in the primary system, i.e., an ellipsoid, as opposed to a point mass, the families are only computed until a trajectory first collides with one of the primaries. Further differences appear when considering the families computed for the ellipsoid-ellipsoid system. In particular, the ellipsoidal shape of the second primary has a significant impact on the behavior of the L_1 and L_2 halo orbits as these families feature orbits with very close approaches to P_2. Consequently, stable orbits exist in the L_1 halo family while only unstable trajectories are apparent for the sphere-sphere and sphere-ellipsoid families. Alternatively, while numerous stable orbits belong to

the L_2 halo families for the sphere-sphere and sphere-ellipsoid systems, only very few stable members exist for the ellipsoid-ellipsoid families. Overall, stable periodic orbits in close proximity of one or two primaries apparently exist even when considering dynamical models that incorporate non-spherical primary shape models. In Figure 5.6 is illustrated stable members from the families computed for the ellipsoid-ellipsoid model. A variety of shape and size is available and such trajectories may suggest interesting applications for mission scenarios that involve close observations of one or both primary bodies.

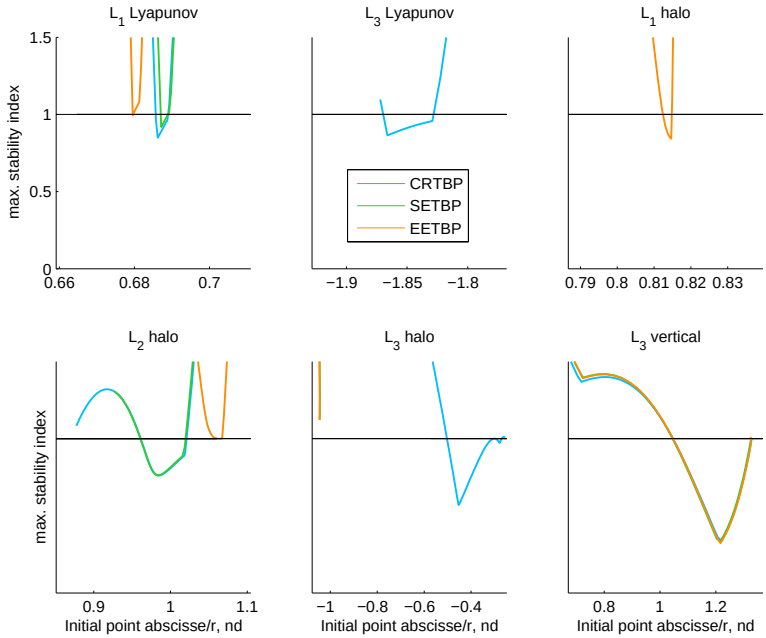

Figure 5.5. Maximum stability index for selected libration point families in the CRTBP, SETBP, and EETBP

A similar analysis is completed for some selected planar resonant orbits illustrated in Section 5.1.2. The stability properties associated with these families are depicted in Figure 5.7. Similar to the libration point families, the overall stability behavior of the members within a given family is similar between the three dynamical models examined. However, differences do exist and such discrepancies are emphasized for trajectories that include very close passages with one of the primary bodies.

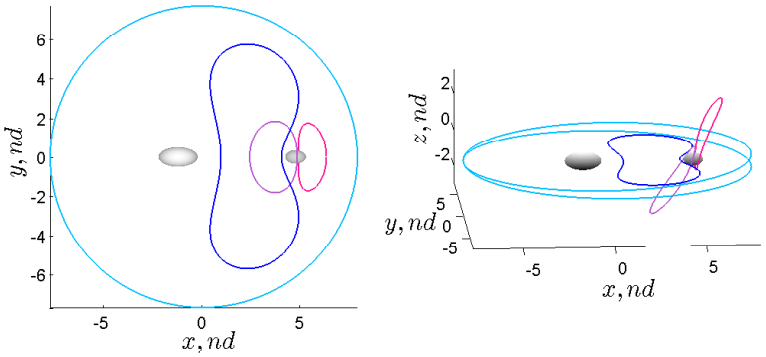

Figure 5.6. Sample stable libration point orbits in the EETBP

Again, stable periodic orbits that involve close proximity to one or two primaries exist even when employing dynamical models that incorporate non-spherical primary shape models. Finally, most three-dimensional resonant orbits are unstable as computed for the set of parameters in this analysis. Finally, the low prograde orbits that surround P_1 reflect another family of periodic orbits that feature close approaches to a primary. This family also possesses numerous members that are defined as stable, as illustrated for a sample sphere-sphere system in Figure 5.8. Note that the stability index is now plotted as a function of the period of the trajectories. The shortest period orbit corresponds to the bifurcation from the LoPO planar family. Recall that any member with a maximum stability index value less than one is labeled as stable. In the figure, two regions with trajectories that satisfy the stability criterion are apparent. Then, the two cusps where the maximum stability index reaches a local minimum correspond to trajectories such that the combination of both stability indexes yield a minimum, in a sense, these orbits are the most stable members in the family to some arbitrary perturbation.

5.1.5 Primary System Model Continuation

The specific existence, shape, and other relevant characteristics, e.g., stability, of an individual orbit or a family of trajectories depends on the physical and dynamical

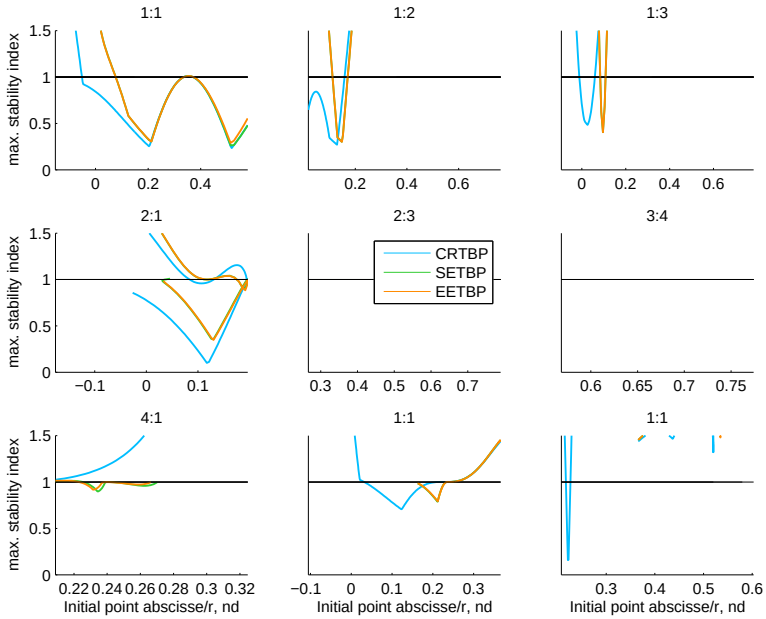

Figure 5.7. Maximum stability index for selected families of resonant planar orbits

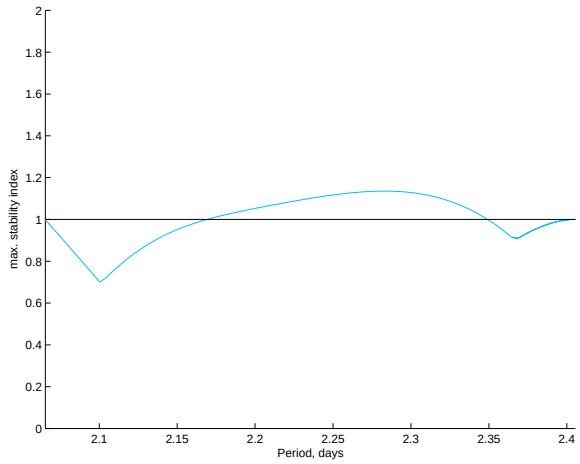

Figure 5.8. Maximum stability index for 3D P_1-centered LoPO family

properties of the primary system. Specifically, the mass ratio of the system, the primary separation distance, and the shape of the individual primary bodies are some of the most influential parameters. Within the context of preliminary mission design, it is impractical to produce an extensive catalog of the infinite number of potential periodic orbits for sample primary system models that cover the entire

design space. However, assume a pre-computed catalog for a few sample systems, one that is reasonably representative of the overall behavior. Then, an automated process that exploits natural parameter continuation is employed to produce a specific trajectory for any desired primary system model. As an example, a three-dimensional 2:3 symmetric resonant orbit is computed for the known binary system 1999 KW4; the trajectory is generated from a 2:3 symmetric resonant orbit initially computed in the CRTBP for a sample system. In Table 5.1 are summarized the characteristics that are associated with the sample system and the 1999 KW4 model. The initial and continued trajectories are illustrated in Figure 5.9. Although the mass ratio corresponding to the two primary models is very different, the continued trajectory retains the same overall characteristics as viewed in configuration space.

Table 5.1. Characteristic quantities associated with the sample system and the 1999 KW4 model

	μ	r	β_1	γ_1	β_2	γ_2
sample system	0.2	6	1	1	1	1
1999 KW4	0.0541	3.64	1	0.845	0.8109	0.6112

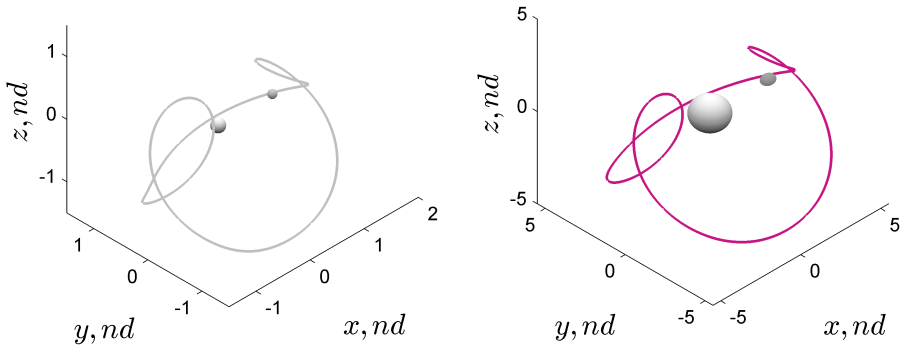

Figure 5.9. Sample 2:3 symmetric resonant orbit for the sample sphere-sphere system (left) and 1999 KW4 (right) computed using continuation

5.2 Tours: Natural Dynamics Baseline Trajectories

Within the context of exploring the regions near the primary bodies, isolated periodic orbits may or may not be suited for direct application in mission scenarios, however, such periodic orbits can be used to construct a trajectory that satisfies some desired characteristics. The goal is an automated strategy to construct a nearby sequence of arcs in such systems.

5.2.1 Homoclinic Cycles

Within the framework of the CRTBP, a closed trajectory that connects a periodic orbit with itself, that is, an arc that departs and returns to the same periodic orbit, is labeled a homoclinic connection. The construction of such a trajectory is often achieved by exploiting the unstable and stable manifold arcs that are associated with the periodic orbit of interest to produce an initial guess. Within the context of trajectory exploration within binary systems of small bodies, consider a scenario that involves periodic trajectories that shift back and forth between the libration points L_1, L_2 and L_3, as viewed in the rotating frame. An initial guess for such a trajectory is constructed from a double homoclinic connection for a periodic L_1 libration point orbit, that is, assembling two independent connections from the L_1 orbit, one that extends toward the L_3 point and the second that visits the vicinity of the L_2 point. This process is realized by selecting unstable and stable manifolds arcs that are associated with a L_1 Lyapunov periodic orbit. In Figure 5.10 are illustrated the unstable and stable manifold tubes for a L_1 Lyapunov orbit in a sphere-ellipsoid system with mass ratio $\mu = 0.3$, primary separation $r = 3$ and semi-major axes $\beta = \gamma = 0.5$. The corresponding manifold tubes extend toward both P_1 and P_2, visiting the vicinity of two other libration points, that is, L_3 and L_2, respectively. To facilitate the selection of suitable manifolds arcs, a Poincaré section is employed. In this planar analysis, each manifold tube is numerically propagated until the first intersection with a specified hyperplane, specifically, $y = 0$, as defined in the rotating frame. The end

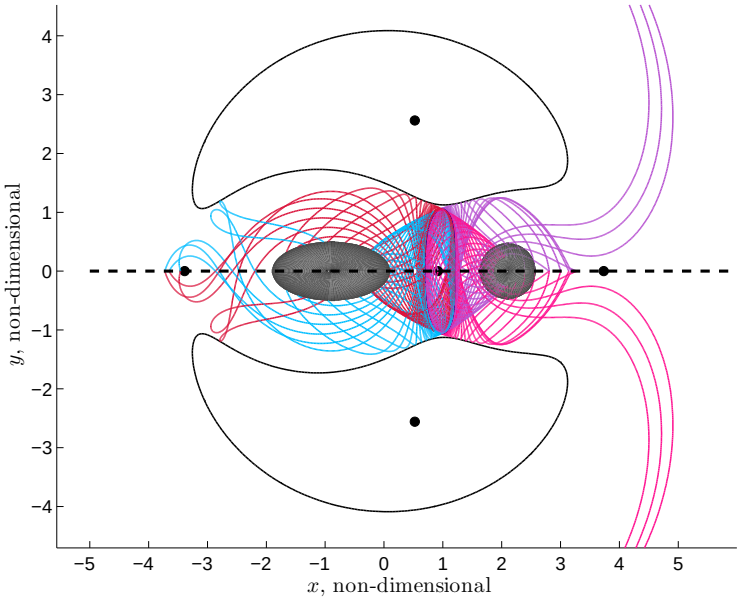

Figure 5.10. Unstable and stable manifold arcs for L_1 Lyapunov orbit for $\beta = \gamma = 0.5 - \mu = 0.3 - r = 3$

result is a trajectory that is continuous both in position and velocity at the originating periodic orbit and at the hyperplane intersection. Considering planar trajectories, the hyperplane reduces the dimensionality of the problem to three variables. In addition, recall the existence of one integral the motion, the Jacobi constant, that further reduces the problem to two dimensions. One possible representation for the selection of a suitable set of manifold arcs is a Poincaré map $x - \dot{x}$ of the first crossings of the manifold tube with the hyperplane. The manifolds associated with an L_1 Lyapunov orbit at a specified energy level are plotted in Figure 5.10 in configuration space. The Poincaré map that corresponds to the crossings of the manifolds with the hyperplane $y = 0$ are illustrated in Figure 5.11. The upper plot represents the crossings with negative x coordinates that correspond to crossings with the hyperplane to the left of P_1; the bottom plot depicts the crossings that occur on the right side of P_2. Red and magenta dots denote crossings of the unstable manifold arcs, blue and purple dots correspond to stable manifold arc crossings. An initial guess for a periodic orbit is

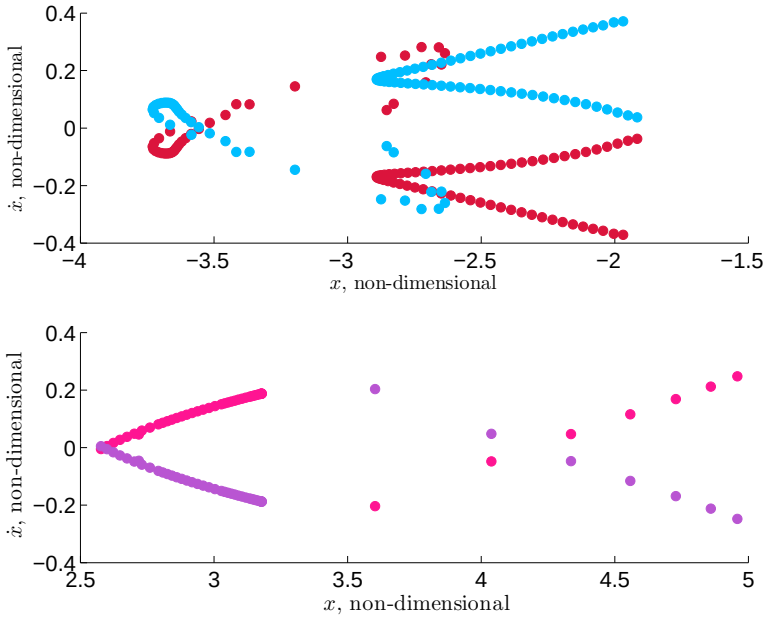

Figure 5.11. Unstable and stable manifold arc crossings for L_1 Lyapunov orbit for $\beta = \gamma = 0.5 - \mu = 0.3 - r = 3$

constructed from the selection of two manifold arcs, one stable and one unstable, that pass through the vicinity of the L_3 point and two arcs that extend toward L_2. On the Poincaré map representation, the objective is the selection of two points on each map (both the top and the bottom plot), one that corresponds to a stable manifold arc and the second to an unstable arc, that intersect both in position and velocity, that is, in terms of the coordinates x and $\dot{x}$. If no intersection is apparent, points with the smallest separation on the map are the most suitable candidates to produce a reasonable initial guess. Because of the symmetry properties of the problem, manifold arcs that cross the hyperplane with the smallest transversal velocity $\dot{x}$ often yield a satisfactory initial guess. A differential corrections algorithm is employed to produce a periodic trajectory that retains the desired characteristics present in the initial guess. Further, a continuation method allows the generation of a family of similar trajectories. A set of trajectories that result from this design process appears in Figure 5.12. The family of planar periodic trajectories includes members that all

shift back and forth between the libration points L_1, L_2 and L_3, as displayed in the rotating frame.

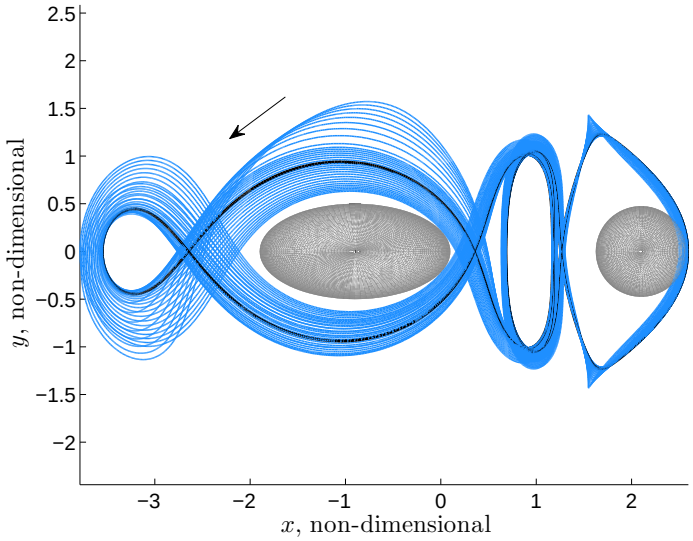

Figure 5.12. Family of double homoclinic periodic cycles for $\beta = \gamma = 0.5 - \mu = 0.3 - r = 3$

5.2.2 Heteroclinic Cycles

Another useful concept in the design of trajectories that exhibit behavior similar to the periodic orbits produced exploiting homoclinic connections, that is, trajectories that shift back and forth between the libration points L_1, L_2 and L_3 is often labeled a heteroclinic connection, that is, a trajectory arc that naturally links two periodic orbits with no position or velocity discontinuity. The process to construct an initial guess for such a heteroclinic connection is similar to the strategy to produce homoclinic connections but involves two distinct periodic orbits. Often, manifold arcs that are associated with both periodic orbits, stable and unstable, are computed and exploited to determine an initial guess for the desired connection. To design a periodic trajectory that visits the vicinity of all three collinear libration points,

consider an initial guess that is constructed from a double heteroclinic cycle, that is, an initially discontinuous path that is formed from two independent heteroclinic connections. Consider three libration point periodic orbits with similar Jacobi constant values that are centered around L_1, L_2, and L_3, respectively. Then, a double cycle is then constructed from two heteroclinic connections, one between the L_1 and L_3 orbits and the second between the L_1 and L_2 orbits. The initial guess process is initiated via unstable and stable manifold arcs that are associated with a L_1 and L_3 Lyapunov orbits at the same energy level, i.e., same value of Jacobi constant, respectively. A second arc is comprised of stable and unstable manifold arcs from the same L_1 trajectory and an L_2 Lyapunov orbit, as illustrated in Figure 5.13. Similar

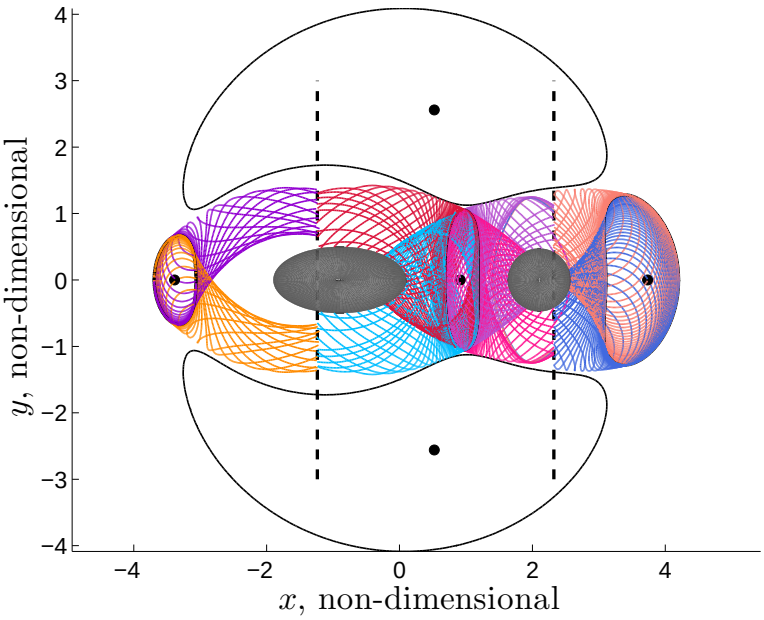

Figure 5.13. Unstable and stable manifold arcs for L_1, L_2, and L_3 Lyapunov orbit for $\beta = \gamma = 0.5 - \mu = 0.3 - r = 3$

to a homoclinic cycle, a Poincaré section approach is developed to aid the selection of suitable manifold arcs. Consider two hyperplanes, one defined as $x = 1/2(x_{L_1} + x_{L_3})$ where x_{L_1} and x_{L_3} denote the locations of the L_1 and L_3 libration points, and a

second hyperplane such that $x = 1/2(x_{L_1} + x_{L_2})$. The process to generate the initial guess is illustrated in Figure 5.13. Unstable and stable manifold arcs computed for the selected L_1, L_2, and L_3 Lyapunov orbits are displayed in the figure until the first intersection with the corresponding hyperplane. Also, similar to the approach for homoclinic connections, the crossings of the manifold arcs with the hyperplane for both unstable and stable manifolds are represented on a $y - \dot{y}$ Poincaré map. From this representation, the selection process for the manifold arcs that are used to construct the initial guess is guided by the same principles, that is, unstable and stable points on the map that intersect or nearly intersect are employed to create a reasonable, possibly discontinuous, trajectory. The complete initial guess is corrected to produce a periodic orbit that retains the desired characteristics. The orbit obtained from the correction process is subsequently exploited to initialize a continuation method to generate a family of similar periodic trajectories, as illustrated in Figure 5.14.

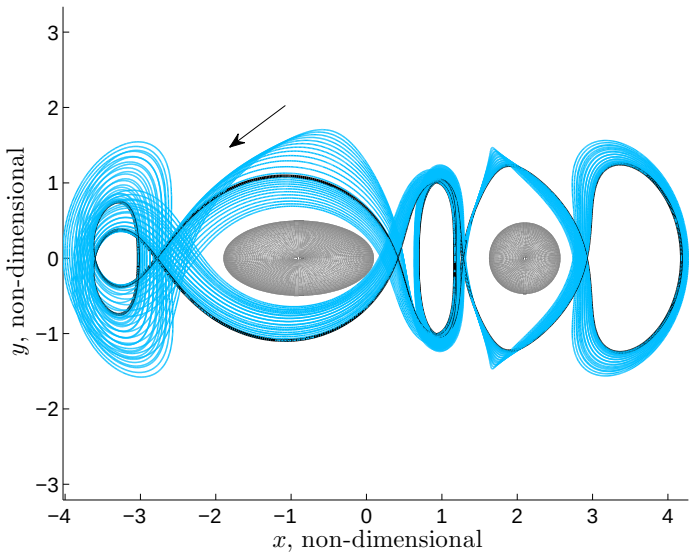

Figure 5.14. Family of double heteroclinic periodic cycles for $\beta = \gamma = 0.5 - \mu = 0.3 - r = 3$

5.2.3 Generalized Tours

Algorithm

In preparation for future tour design algorithms, a first step is to further understand how pathways in the vicinity of a binary system of irregular bodies can be exploited to construct a path with some desirable properties. The objective is an automated algorithm that leverages pre-computed periodic orbits to construct a continuous trajectory that exhibits some pre-specified characteristics. From a user-defined chain of periodic orbits, the task is the construction of a trajectory that travels between the specified orbits. The strategy is comprised of four tasks (i) Computation of transfer arcs between user-selected periodic orbits that are pre-computed. Originating from the first prescribed orbit in the chain, an arc that links one orbit to the next is constructed from the stable and unstable manifolds that are associated with two orbits that are to be linked, if such manifolds exist. If one of the two orbits is stable, the manifolds that are associated with the other orbit are solely employed to construct a direct transfer into the stable orbit. (ii) A number of user-defined revolutions of each selected periodic orbits are 'stacked' to anchor the correction process. (iii) Concatenation of the transfer arcs and periodic orbit revolutions into an initial discontinuous trajectory yields an initial guess. (iv) A continuous trajectory is then constructed from the initial guess in a differential corrections algorithm. To facilitate the corrections process and also to accommodate the differences in energy level between the selected periodic orbits, impulsive maneuvers are allowed at the nodes between a transfer arc and a periodic orbit and between two the manifold arcs that constitute one transfer arc.

Demonstration application

In an initial effort, a sample trajectory is computed for demonstration purpose. While the path is, in fact, too complex and risky to be used as a baseline solution for

flight, it does, however, demonstrate that the capability of the proposed algorithm. Consider a sample sphere-sphere system. In this application, three distinct periodic orbits are chained together to produce a trajectory that tours the primary system. Initially, an unstable 2:3 symmetric three-dimensional resonant orbit is selected as the departure orbit, and is periodic. Then, the construction scheme produces a first transfer arc to a three-dimensional unstable P_2 centered low prograde orbit, followed by a second transfer segment to a stable 3D P_1 centered low prograde orbit. Finally, a last arc is computed to return to the initial resonant orbit that evolves around the primary system. To allow more time for potential observations of each primary body, one revolution around each periodic orbit might be incorporated into the initial discontinuous trajectory. In Figure 5.15 is illustrated the resulting initial guess projected onto the (x, y) plane where each colored segment represents a different transfer arc. The initial guess is then corrected to produce a trajectory continuous both in position and velocity. To ensure velocity continuity, impulsive maneuvers are allowed at the nodes between the various segments that constitute the initial guess. Although some maneuvers may be reduced or entirely eliminated through iterative corrections, because the energy level of the orbits selected in this application are not equal, some maneuvers are required. Without attempting to reduce or remove any maneuvers, the thrust events as computed by the algorithm are summarized in Table 5.2 and the total required thrust is $|\Delta V| = 1.93$ m/s. Note that time is referenced with respect to the initial epoch t_0=0. Also, the approximate Time Of Flight (TOF) of each segment appears in Table 5.3.

Table 5.2. Maneuver history for tour

Time (d)	5.7	17.9	20.9	22.2	27.3	29	31.2	33.6	50.8
$\|\Delta V\|$ (m/s)	0.01	0.29	0.22	0.49	0.15	0.16	0.04	0.52	0.0009

An initial assessment of the viability of the produced trajectory is performed. The altitude of the third body with respect to each primary is evaluated as a func-

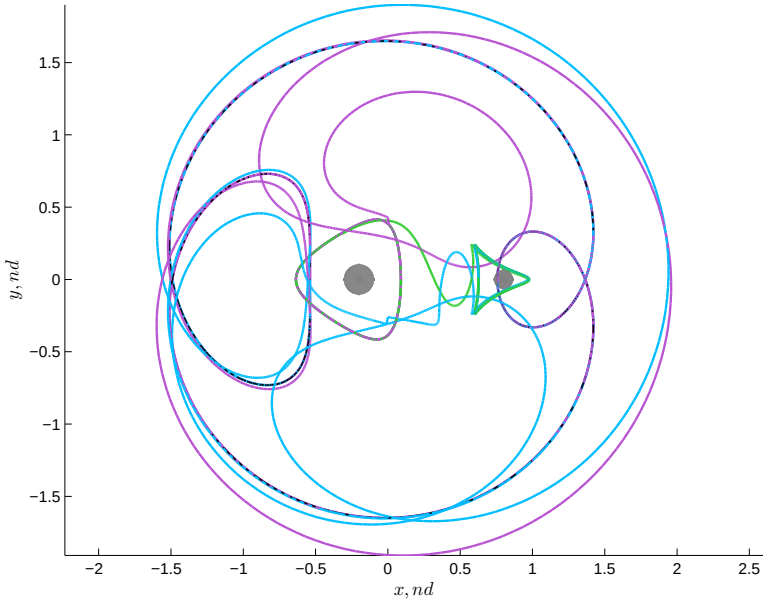

Figure 5.15. Initial guess from tour algorithm projected onto the (x, y) plane

Table 5.3. Time of flight for individual arcs in tour

	2:3 orbit	Transfer 1	P_2 LoPO	Transfer 2	P_1 LoPO	Transfer 3
TOF (d)	5.7	15	2	5.7	2	19.5

tion of time along the path. While low altitude phases are desired for observation campaigns, such trajectory segments are also the most demanding in terms of spacecraft operations. Realistically, the time frame in such systems is very fast, and there is no time for orbit determination and correction maneuvers between primary encounters. Within this context, autonomous guidance is required. In Figure 5.17 is illustrated the altitude of the third body with respect to P_1 and P_2 as a function of time, where color, from blue to red, also depicts time evolution and is matched on the left-hand figure that represents the trajectory in configuration space. The altitude is reported in terms of primary radii and the black horizontal line on the altitude plots represents 1 radii, that is, a third-body altitude of 1 body radii above the spherical primary body surface. For this particular tour, the lowest altitude with respect to P_1

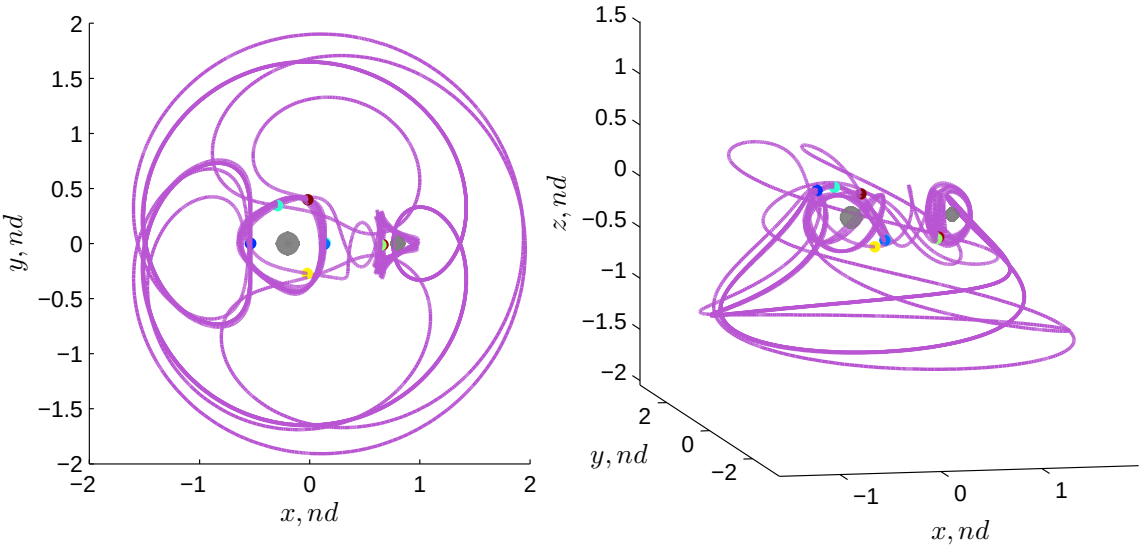

Figure 5.16. Converged trajectory from tour algorithm

is approximately equal to a few body radii while it is reduced to just above 1 radii with respect to P_2. Finally, given a converged path in a sphere-sphere system and using the continuation algorithm introduced in Section 5.1.5, a trajectory that exhibits the same characteristics is computed for an ellipsoid-ellipsoid system employing the pre-computed result from the sphere-sphere system as initial solution. The trajectory that is produced through this process appears in Figure 5.18 and it is apparent that the path is similar to the initial sphere-sphere solution without repeating the entire design process.

5.3 Poincaré Maps

Poincaré maps are useful for a variety of analyses and applications. In this investigation, the focus is on the evolution of map topology as the shape of the primaries is varied. A typical representation for a Poincaré map is a puncture plot, or, directly displaying the points that corresponds to the recorded crossings on, or punctures of, the surface of section. One approach to highlight dynamical structures within a map

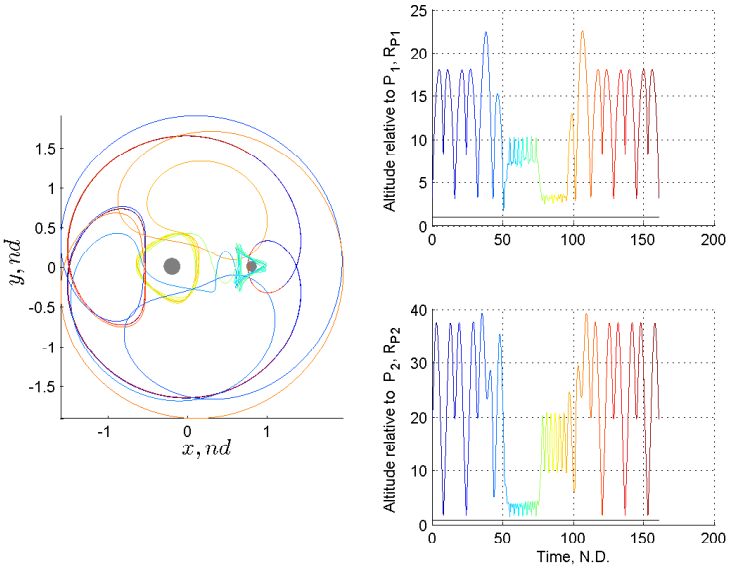

Figure 5.17. Altitude analysis

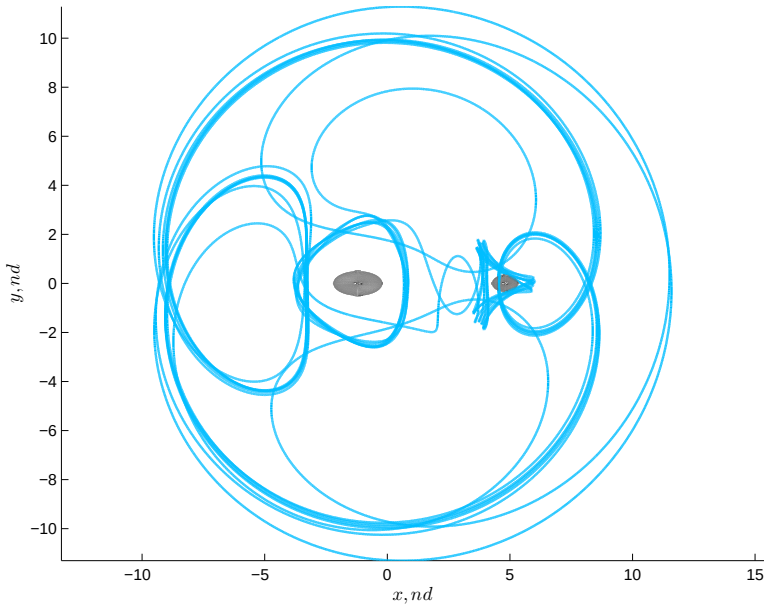

Figure 5.18. Converged tour for ellipsoid-ellipsoid system

is to leverage winding numbers, [63] as outlined in Section 4.6.1. The orbit convolution process is an alternative approach for displaying a Poincaré map. Rather than a puncture plot, the orbit convolution produces a scalar field representation of the dynamical behavior. (see Section 4.6.1)

5.3.1 Island identification: reference map

A first step in the analysis is to restrict the initial conditions to domains that contain structures of interest. This additional task allows a simpler examination of the produced maps and also greatly decreases the computational burden that is associated with the long-term integration of a large amount of initial conditions. This first goal is achieved through the generation of a series of one-sided maps for a set of Jacobi constant values such that the initial condition domain is the line of points $y = 0, \dot{x} = 0$. The remaining coordinate, $\dot{y}$, is computed using the Jacobi constant value as constraint. In Figure 5.19(a) is overlaid 15 maps for Jacobi constant values ranging from $C(L_1)$ to $C(L_4)$ for the sample sphere-sphere system considered in Section 5.1.3 for both retrograde and prograde initial conditions. Two regions that contain structures of interest are identified as illustrated in Figures 5.19(b) and 5.19(c). In the following discussion, the focus is on maps that are generated specifically for a region that contains one or more of these identified structures.

5.3.2 Considerations regarding initial conditions

To assess the effect of nonspherical primaries on the behavior of a third body, maps are generated for sample primary system models with increasingly elliptical primary shapes. Initially consider the region depicted in Figure 5.19(b), that is, an exterior region island that is associated with retrograde initial conditions, with respect to P_1 as viewed in the rotating frame. One approach to explore the effect of the nonspherical primaries is to generate maps for initial conditions that correspond to a given Jacobi constant value as computed for the sample sphere-sphere system.

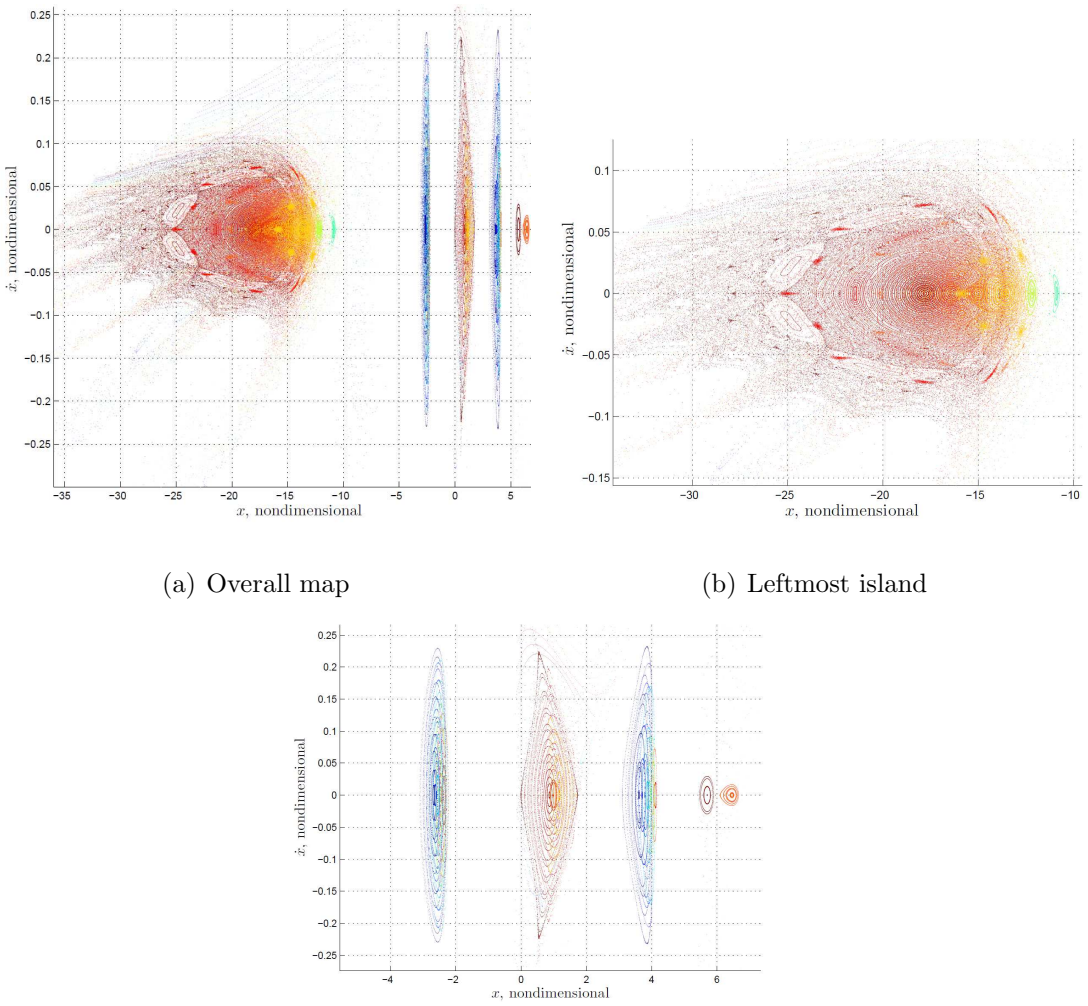

(a) Overall map

(b) Leftmost island

(c) Central islands

Figure 5.19. Reference Poincaré map in the CRTBP for $C(L_1) < C < C(L_5)$

In effect, the same initial conditions are employed to generate a map for each primary system model, both in terms of position and velocity initial states. Thus, if the effect of the shape of the primaries is insignificant, the maps that are produced are expected to be similar. In Figure 5.20 are illustrated three maps for a system where the primary P_1 is increasingly ellipsoidal and a fourth map for a system where both primaries are ellipsoids. First, note that the behavior of the third body is significantly affected as depicted by the evolving topology of the island for the first three maps. Since

this island corresponds to trajectories far in the exterior region, that is, trajectories that do not come in proximity to the less massive body, P_2, the effect onto the behavior of the ellipticity of the secondary is limited. However, it is critical to further note that this simplified approach, that is, using the same set of initial conditions for different primary system models is also violating some assumptions that are associated with the map. Through the modification of the mass distribution of the primaries, the gravitational potential as a function of the initial condition position is, in fact, modified. Consequently, employing the same initial velocities for all systems result in a nonconstant energy map, as depicted by overlapping features on the produced map, especially apparent for the most elliptical systems.

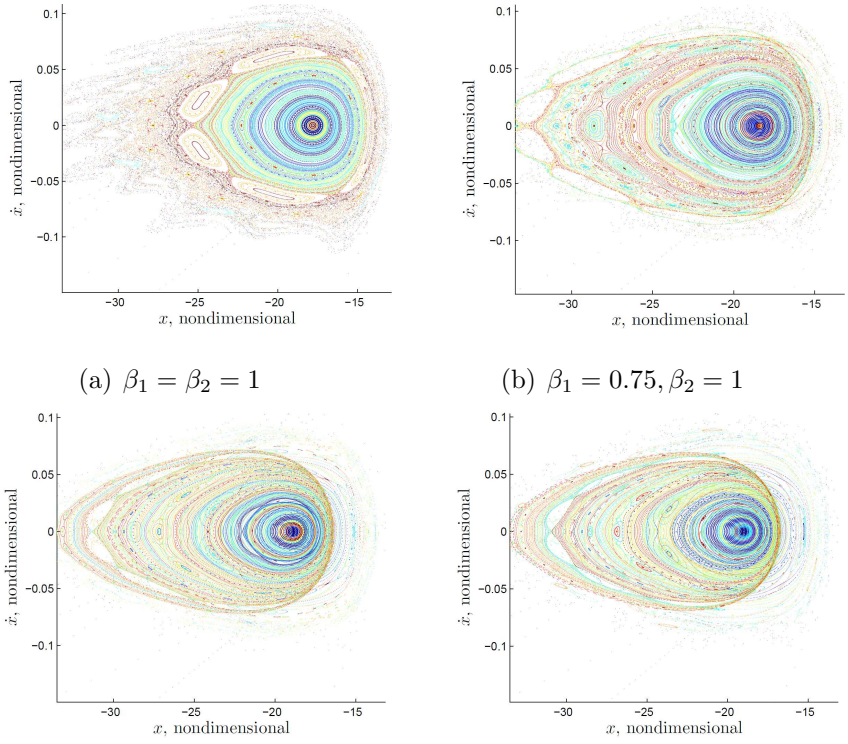

(a) $\beta_1 = \beta_2 = 1$

(b) $\beta_1 = 0.75, \beta_2 = 1$

(c) $\beta_1 = 0.5, \beta_2 = 1$

(d) $\beta_1 = 0.5, \beta_2 = 0.5$

Figure 5.20. Poincaré map for sample primary system models with same initial conditions

Rather than employing a constant set of initial conditions through the sample primary system models, consider an approach where the initial velocity state for each

initial condition is consistent with the mass distribution. Also, for further consistency, rather than using an arbitrary value for the Jacobi constant for any given map, a notable energy level is selected. For demonstration, the maps that are displayed in Figure 5.21 correspond to the same four sample systems as in Figure 5.20, however, the initial conditions are computed consistently with each primary system model and for the Jacobi constant that is associated with the equilibrium point L_1, as computed for each system. The resulting maps appear more similar, yet still different, across the sample systems. These two simulations indicate that, first, the effect of nonspherical primaries is significant, even with respect to third-body motion that lies far from the primary system. Secondly, while this effect is notable, taking into account the properties of the primary system model for the generation of the set of initial conditions demonstrates that similar structured and rich dynamical behavior exists even for systems with increasingly nonspherical primaries.

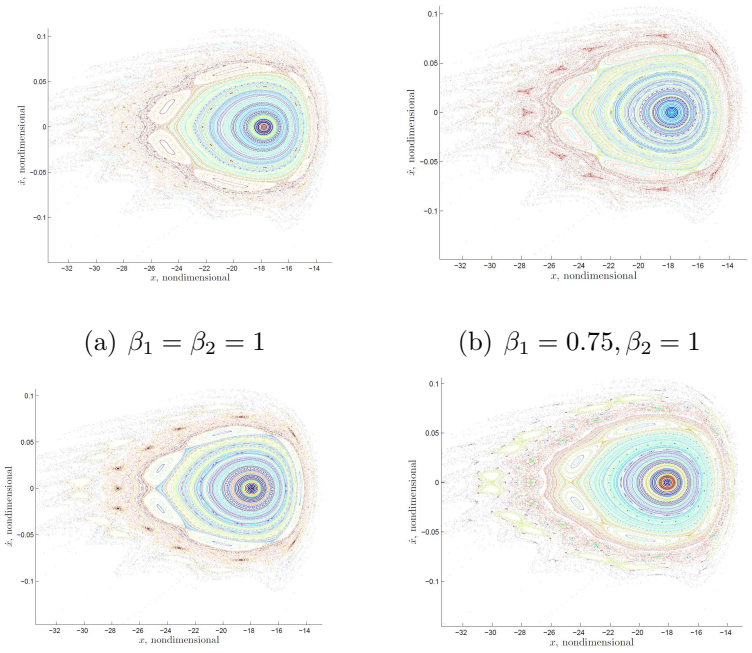

(a) $\beta_1 = \beta_2 = 1$ (b) $\beta_1 = 0.75, \beta_2 = 1$

(c) $\beta_1 = 0.5, \beta_2 = 1$ (d) $\beta_1 = 0.5, \beta_2 = 0.5$

Figure 5.21. Poincaré map for sample primary system models with consistent initial conditions

5.3.3 Exploiting orbit convolution

While the puncture plot representation for a Poincaé map offers dynamical acuity for the displayed map returns, the orbit convolution technique may be of interest to highlight the similarities and differences between a set of maps through the smooth scalar field representation of the dynamical behavior. Instead of a coarse linear grid of initial conditions, consider a 1024x768 rectangular grid to initialize the orbit convolution procedure. Each initial condition is numerically propagated for fewer returns than selected for the initial maps produced for the linear grid of initial conditions. Instead, three orbit convolution passes are completed to lighten the computation burden that is associated with the long-term numerical integration of such a large number of initial conditions. The maps in Figure 5.22 are generated for the same domain of initial conditions as in Figures 5.20 and 5.21 for three sample primary system models. In this representation, the rich dynamical structure of the behavior for the third body is evident, even for primary system with nonspherical primaries. While some of the dynamical features evolve as the shape of the primaries is varied, as one might expect, a structured behavior is retained, indicative of the existence of various periodic orbits and associated quasi-periodic orbits within this small domain. The existence of periodic solutions is already established in Section 5.1, however, the map representation supplies the additional information that, not only families of point solutions do exist, but a continuum of structured solutions, as indicated by the smooth evolution of the map topology between increasingly nonspherical systems, is apparent and is highlighted by the scalar field depiction that results from the orbit convolution procedure.

5.4 Bounded Motion in Higher-Fidelity Dynamical Models

The simplified models that are developed in this analysis to construct complex trajectories retain some interesting system dynamical properties, such as periodicity. However, although the complexity in the primary system model is gradually increased

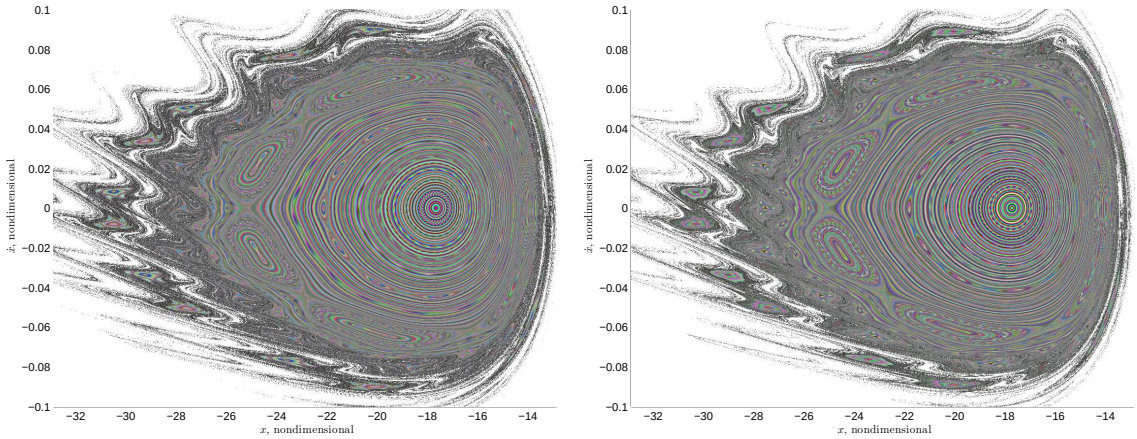

(a) $\beta_1 = \beta_2 = 1$

(b) $\beta_1 = 0.75, \beta_2 = 1$

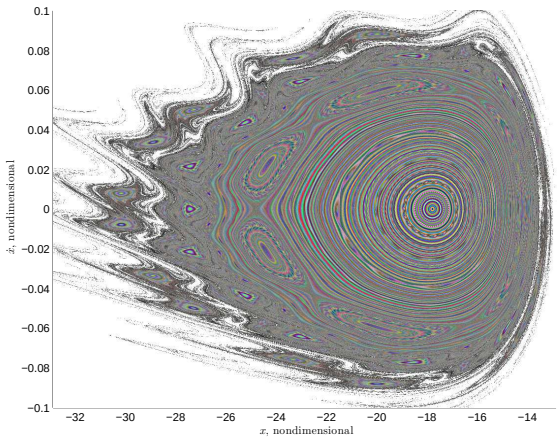

(c) $\beta_1 = 0.5, \beta_2 = 1$

Figure 5.22. Poincaré map for sample primary system models exploiting orbit convolution

with bodies modeled as ellipsoids rather than point masses, these models are still an idealized representation of an actual system of small bodies. An alternative approach to the ellipsoid-ellipsoid or sphere-ellipsoid models is based on modeling the primary bodies as geometric polyhedra. Such a methodology allows the representation of the actual shape of the body with a higher accuracy and, thus, enhances the fidelity. Trajectories computed from one of the simplified models can be used as an initial guess for the higher fidelity model. However, periodicity no longer exists and such a dynamical model is not well-suited for extensive analysis, but it is useful to assess the

robustness, stability, or feasibility of a given solution under more realistic simulation conditions.

5.4.1 Primary System Model: 1999 KW4

Primary shape model

In an initial investigation into the transition between the idealized dynamical models exploited thus far and a higher fidelity representation, consider the well-known Near Earth Asteroid (NEA) 1999 KW4. A medium resolution polyhedron shape model is illustrated in Figure 5.23 for the primary and secondary component of the KW4 binary asteroid. This shape model is derived from the full resolution model constructed in Ostro et al. [73] Also, some representative physical parameters for each body are summarized in Table 5.4. The primary exhibits the characteristic 'walnut' shape while the secondary, much smaller in size, is a very oblate and significantly elongated body.

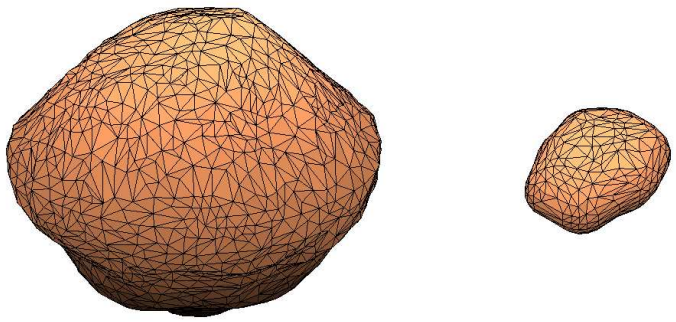

Figure 5.23. 1999 KW4 shape model: primary (left) and secondary (right)

Table 5.4. 1999 KW4 shape model

	A_X (km)	A_Y (km)	A_Z (km)	density (kg m^{-3})	rotation period (hr)
Primary	1.53	1.49	1.35	1970	2.76
Secondary	0.57	0.46	0.35	2810	17.42

Primary motion simulation

The irregular shape of the two bodies directly affects the relative motion of the two primaries; the fully coupled motion of the two-body system is modeled and numerically integrated, as outlined in Section 3.5.1. The initial orbital conditions and configuration for such a simulation are summarized in Table 5.5 for the orbital motion, in terms of semi-major axis and eccentricity, and the initial orientation of both bodies. The angles ψ_i, θ_i, and ϕ_i correspond to the Euler angles for a $3-1-3$ sequence and $i = 1, 2$ for the primary and secondary, respectively. The mutual motion, both orbital and rotational, is numerically integrated for approximately 15 revolutions of the primary system. Recall that the computation of the mutual force and torque one body exerts on the other at each time step during the numerical integration process relies on an infinite series expansion of the gravitational potential. In this simulation, only the first five terms in this series are retained, that is, four orders beyond the point mass solution. Selected results from this simulation appear in Figure 5.24. As expected, the irregular shape of the body directly impacts the mutual orbital motion, as clearly illustrated by the oscillating semi-major axis and eccentricity as time evolves; also, it is directly apparent in the primary-centered inertial view of the trajectory. Although, not presented here, the attitude of each body is also affected by the mutually irregular shape. For this problem, energy and angular momentum are conserved, however, it is sometimes challenging to achieve conservation of these quantities, to some tolerance, during the numerical integration process over long time

intervals. In this analysis, the symplectic algorithm selected allows energy and angular moment to be conserved within reasonable and bounded values throughout the simulation.

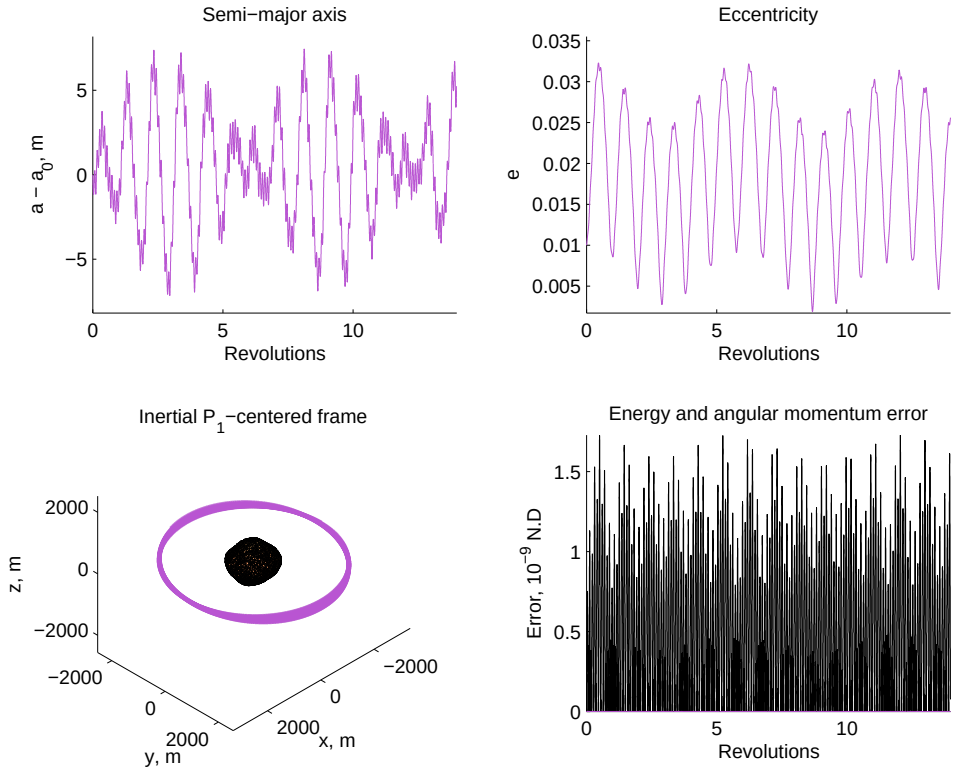

Figure 5.24. 1999 KW4 simulation

Table 5.5. 1999 KW4 initial conditions

a (km)	e	ψ_1 (deg)	θ_1 (deg)	ϕ_1 (deg)	ψ_2 (deg)	θ_2 (deg)	ϕ_2 (deg)
2.54	0.01	27.04	10	-83.93	0	0	180

5.4.2 Sample Third-Body Bounded Trajectories

In an initial assessment of the robustness, stability, or feasibility of a given solution under more realistic simulation conditions, selected orbits that are pre-computed with an idealized model are employed as initial guesses in a differential corrections algorithm to produce bounded trajectories that retain similar characteristics. The third-body motion is numerically integrated based upon the relative motion of the primary system and the shape of each body. In Figures 5.25-5.27 are illustrated selected Lyapunov, halo, and axial orbits transitioned into the polyhedron-polyhedron model as viewed in a synodic primary-centered frame. Since the orbit of the primary system is not planar or circular, and the orientation of the bodies is time-varying, the primary orientation representation in these figures is only valid at the initial time. Overall, the third body remains on or near the reference trajectory for multiple revolutions, including close encounters with one primary. These simulations demonstrate that trajectories in an idealized model can easily be transitioned into a higher-fidelity dynamical model, assuming the required information about the primary system to construct such a model is in fact available.

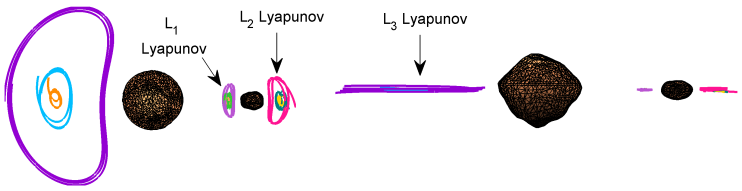

Figure 5.25. Sample Lyapunov orbits for polyhedron-polyhedron system

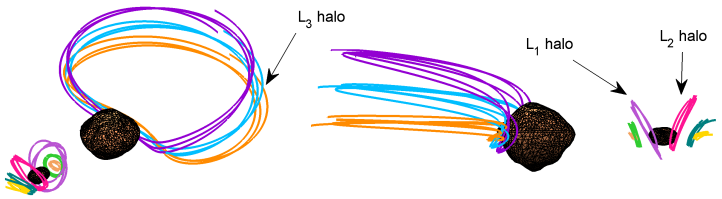

Figure 5.26. Sample halo orbits for polyhedron-polyhedron system

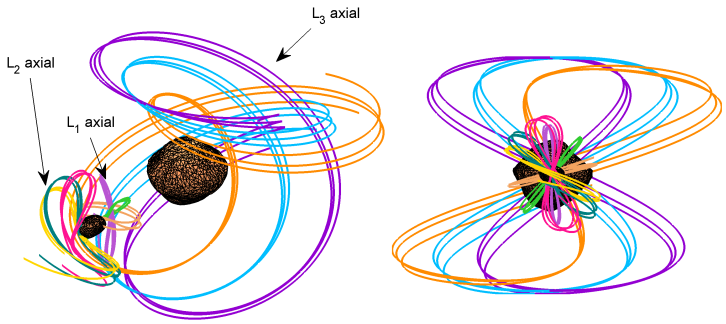

Figure 5.27. Sample axial orbits for polyhedron-polyhedron system

6. TRAJECTORY DESIGN FOR BOUNDED MOTION NEAR UNCERTAIN BINARY SYSTEMS EXPLOITING SLIDING CONTROL MODES

The focus of the analysis in Chapter 5 is the behavior of a third body in the vicinity of a system comprised of two irregular bodies that might represent a binary. So far, the investigation is focused on the exploration of bounded trajectories in the vicinity of a simplified system. However, these types of dynamical models are idealized representations of the actual dynamical regime and do not incorporate uncertainties in the physical properties of the bodies and other non-gravitational perturbing effects. In this analysis, a strategy to maintain a spacecraft near reference third-body trajectories that exhibit some desired characteristics is constructed incorporating multiple sliding surfaces guidance. [24–26] Such a control law can be demonstrated to be globally stable and robust. In practical applications, the exact physical properties of the massive bodies in the system are not known. It is reasonable to assume sufficient knowledge to construct an 'estimated' model that approximates the properties of the 'true' system. For the true system, each primary is modeled as a polyhedron and the 'estimated' system employs a sphere-ellipsoid or an ellipsoid-ellipsoid model. Then, to maintain the spacecraft in orbit near a desired reference path, a 'coast and thrust' scheme is proposed.

6.1 Multiple Sliding Surfaces Guidance (MSSG)

A robust guidance law to control the motion of a spacecraft in the vicinity of a pair of irregular bodies is introduced. The multiple sliding surfaces guidance [24–26] development relies on higher order sliding control theory. [74, 75] The objective is to

develop an acceleration law, one that is robust against unmodeled perturbations, and sufficiently flexible to accommodate the design objectives. The MSSG guidance law is developed in detail in Furfaro et al. (2013) and the derivation is outlined in this section.

6.1.1 MSSG guidance law development

To explore and direct the behavior of a spacecraft near a binary system comprised of irregular bodies, the objective is an acceleration guidance law that is robust against unmodeled perturbing effects. Since the gravity field is an approximation and additional unmodeled forces may exist, such a strategy is well-suited for such perturbed dynamical environments. Initially consider the derivation of the MSSG guidance law without perturbing accelerations. First, rewrite the vector EOMs, as expressed in terms of the inertial frame, in a first-order form,

$$\dot{\bar{\rho}} = \bar{v} \tag{6.1}$$

$$\dot{\bar{v}} = \frac{\partial U}{\partial \bar{\rho}} + \bar{a}_c \tag{6.2}$$

where $\bar{a}_c$ is the acceleration command. It is clear that the control $\bar{a}_c$ appears in the second time derivative of the output, that is, $\ddot{\bar{\rho}}$ or $\dot{\bar{v}}$. Thus, the motion of the guided spacecraft exists on a 2-sliding mode. For a 2-sliding mode control scheme, [74,75] the goal is the selection of a sliding surface vector $\bar{s}$ such that $\bar{s} = \dot{\bar{s}} = \bar{0}$ when the control objective is achieved. Also, the dynamics of the sliding system must possess relative degree 2, that is, the acceleration command appears in the second time derivative of the sliding surface vector. Define a first sliding vector surface as,

$$\bar{s}_1 = \bar{\rho} - \bar{\rho}_D \tag{6.3}$$

where $\bar{\rho}_D$ is the desired nondimensional position vector of the spacecraft. Differentiating $\bar{s}_1$ with respect to time yields,

$$\dot{\bar{s}}_1 = \dot{\bar{\rho}} - \dot{\bar{\rho}}_D = \bar{v} - \bar{v}_D \tag{6.4}$$

where $\bar{v}_D$ is the desired nondimensional velocity vector of the spacecraft. Note that the sliding surface is, in fact, of relative degree 2. The second time derivative of $\bar{s}_1$ is evaluated as,

$$\ddot{\bar{s}}_1 = \dot{\bar{v}} - \dot{\bar{v}}_D = \frac{\partial U}{\partial \bar{\rho}} + \bar{a}_c - \dot{\bar{v}}_D \tag{6.5}$$

The guidance problem is formulated as follows: determine the acceleration command, $\bar{a}_c$, such that the sliding vector surface $\bar{s}_1$, and its time derivative, both converge to zero in a finite time, i.e., $t \to t_f, \bar{s}_1, \dot{\bar{s}}_1 \to 0$. The objective is achieved by selecting $\dot{\bar{s}}_1$ as a virtual control coupled with a backstepping method. First, $\dot{\bar{s}}_1$ is selected such that the first sliding surface reaches zero in a finite time. One choice for the virtual control such that $\bar{s}_1 \to 0$ as $t \to t_f$ is,

$$\dot{\bar{s}}_1 = -\frac{\Lambda}{t_f - t}\bar{s}_1 \tag{6.6}$$

where $\Lambda = diag\left[\Lambda_1 \; \Lambda_2 \; \Lambda_3\right]$ is a diagonal matrix and Λ_i are guidance gains such that $\Lambda_i > 0$. To prove that the virtual control $\dot{\bar{s}}_1$ is globally stable and, thus, effectively drives the first sliding surface to zero in a finite time, consider the candidate Lyapunov function,

$$V_1 = \frac{1}{2}\bar{s}_1^T \bar{s}_1 \tag{6.7}$$

Clearly, $V_1(\bar{s}_1 = \bar{0}) = 0$ and $\forall \bar{s}_1 \in \mathbb{R}^3 - \{\bar{0}\}, V_1\left(\bar{s}_1\right) > 0$, therefore V_1 is positive definite. Then,

$$\dot{V}_1 = \bar{s}_1^T \dot{\bar{s}}_1 = -\frac{1}{t_f - t}\bar{s}_1^T \Lambda \bar{s}_1 \tag{6.8}$$

where Λ, as recalled, is defined such that $\Lambda_i > 0$, i.e., Λ is positive definite. Then, $-\dot{V}_1$ is expressed as a quadratic form of the virtual state $\bar{s}_1$ with Λ positive definite, therefore, $\dot{V}_1$ is negative definite. Finally, with V_1 and $-\dot{V}_1$ positive definite, the

Lyapunov theorem concludes that the virtual control $\dot{\bar{s}}_1$ is globally stable. A solution for the virtual state, $\bar{s}_1$, can be explicitly derived and allows further constraints on the gain matrix Λ. Applying separation of variables on Eq. (6.6),

$$\frac{ds_{1i}}{s_{1i}} = \frac{\Lambda_i dt}{t_f - t} \tag{6.9}$$

where $i = 1, 2, 3$, i.e., $\bar{s}_1 = [s_1 \; s_2 \; s_3]^T$. Direct integration of Eq. (6.9) produces,

$$\log(s_{1i}) = \Lambda_i \log(t_f - t) + C_i \tag{6.10}$$

where s_{1i} are the components of $\bar{s}_1$ and the vector integration constant $\bar{C}$ is explicitly defined by imposing the initial condition $\bar{s}_1(0) = \bar{s}_{10}$. Also, after evaluation of the exponential of both sides in Eq. (6.10), the solution results in the expression,

$$s_{1i}(t) = s_{1i_0}(t_f - t)^{\Lambda_i} \tag{6.11}$$

The time derivative of the sliding surface is then directly derived as,

$$\dot{s}_{1i}(t) = \Lambda_i s_{1i_0}(t_f - t)^{\Lambda_i - 1} \tag{6.12}$$

Provided that $\Lambda_i > 0$, Eq. (6.11) guarantees that the sliding surface vector converges to zero in a finite time. However, if $\Lambda_i < 1$, the time derivative of the sliding surface in Eq. (6.12) diverges as $t \to t_f$. Therefore, the matrix gains are selected such that $\Lambda_i > 1$ to guarantee that both the sliding surface vector and its time derivative reach zero as $t \to t_f$. Recall that the goal is an acceleration command $\bar{a}_c$ that achieves the control objective. Thus, the virtual control $\dot{\bar{s}}_1$ must be explicitly related to the acceleration command to successfully achieve the objective $\bar{s}_1, \dot{\bar{s}}_1 \to \bar{0}$. Also note that, initially, the spacecraft position and velocity vectors may not, in general, satisfy Eq. (6.6). The next step in deriving the guidance law is the definition of a second sliding surface that forces the desired acceleration command to drive the virtual control from its initial value to a trajectory that follows the dynamics in the first-order nonlinear equation defined in Eq. (6.6). In addition, under the acceleration command, the

system must be maintained on the second surface until $\bar{s}_1, \dot{\bar{s}}_1 \to \bar{0}$ is attained. The second sliding surface vector is selected as,

$$\bar{s}_2 = \dot{\bar{s}}_1 + \frac{\Lambda}{t_f - t}\bar{s}_1 = \bar{0} \tag{6.13}$$

where it is easily verified that the second sliding surface is now of relative degree 1 with respect to the acceleration command, that is, $\bar{a}_c$ appears explicitly in the first time derivative of the second surface,

$$\dot{\bar{s}}_2 = \ddot{\bar{s}}_1 + \frac{\Lambda}{t_f - t}\dot{\bar{s}}_1 + \frac{\Lambda}{(t_f - t)^2}\bar{s}_1 \tag{6.14}$$

The expression for $\ddot{\bar{s}}_1$ derived in Eq. (6.5) is substituted in Eq. (6.14) to produce,

$$\dot{\bar{s}}_2 = \frac{\partial U}{\partial \bar{\rho}} + \bar{a}_c - \dot{\bar{v}}_D + \Lambda\frac{(t_f - t)\,\dot{\bar{s}}_1 + \bar{s}_1}{(t_f - t)^2} \tag{6.15}$$

To select an adequate acceleration command that guarantees global stability of the closed-loop system, the Lyapunov stability theory is again exploited. Consider the second Lyapunov candidate function,

$$V_2 = \frac{1}{2}\bar{s}_2^T\bar{s}_2 \tag{6.16}$$

Similar to V_1, V_2 is positive definite and its time derivative is explicitly computed as,

$$\dot{V}_2 = \bar{s}_2^T\dot{\bar{s}}_2 = \bar{s}_2^T\left[\frac{\partial U}{\partial \bar{\rho}} + \bar{a}_c - \dot{\bar{v}}_D + \Lambda\frac{(t_f - t)\,\dot{\bar{s}}_1 + \bar{s}_1}{(t_f - t)^2}\right] \tag{6.17}$$

Finally, for $\dot{V}_2$ to be negative definite, one possible choice for the command acceleration is,

$$\bar{a}_c\,(t) = -\left\{\frac{\partial U}{\partial \bar{\rho}} - \dot{\bar{v}}_D + \Lambda\frac{(t_f - t)\,\dot{\bar{s}}_1 + \bar{s}_1}{(t_f - t)^2} + \Phi sgn\,(\bar{s}_2)\right\} \tag{6.18}$$

where the coefficients for the second diagonal matrix $\Phi = diag\,[\Phi_1\Phi_2\Phi_3]$ can be selected such that,

$$\Phi_i = \frac{s_{2i_0}}{t_f^*} \tag{6.19}$$

where $t_f^* = nt_f, n < 1$. Recall that t_f is the prescribed time of flight, thus, the second sliding surface reaches zero in the finite time such that $t_f^* < t_f$. To demonstrate this property, substitute the acceleration command derived in Eq. (6.18) into the first time derivative of the second sliding surface vector in Eq. (6.15) to obtain,

$$\dot{\bar{s}}_2 = \Phi sgn\left(\bar{s}_2\right) \tag{6.20}$$

Further, noting that the vector $\bar{s}_2$ retains the same sign until reaching zero, the previous equation in Eq. (6.20) can be explicitly integrated,

$$\bar{s}_2\left(t\right) = s_{2i_0}\left(1 - \frac{t}{t_f^*}\right) \tag{6.21}$$

It is now apparent that the second sliding surface vector is driven to zero as $t \to t_f^*$. Finally, the derived control law is proven to be globally stable.

6.1.2 MSSG under uncertainty

The acceleration command derived in Eq. (6.18) does not currently accommodate unmodeled perturbing effects. Now consider the augmented system with an unknown or unmodeled perturbing acceleration, $\bar{a}_P$,

$$\dot{\bar{\rho}} = \bar{v} \tag{6.22}$$

$$\dot{\bar{v}} = \frac{\partial U}{\partial \bar{\rho}} + \bar{a}_c + \bar{a}_p \tag{6.23}$$

The first derivative of the Lyapunov function V_2 becomes,

$$\dot{V}_2 = \bar{s}_2^T \dot{\bar{s}}_2 = \bar{s}_2^T\left[\bar{a}_P\left(t\right) - \Phi sgn\left(\bar{s}_2\right)\right] \tag{6.24}$$

Thus, to guarantee that $\dot{V}_2$ is negative definite, the gains Φ_i are selected such that $\Phi_i > max\left|a_{P_i}^{max}\right|$. The second Lyapunov function is decrescent and negative definite,

thus, the Lyapunov stability theorem for non-autonomous systems guarantees that $\bar{s}_2 \to \bar{0}$ when $t \to t_f^*$, and consequently, $\bar{s}_1, \dot{\bar{s}}_1 \to \bar{0}$ when $t \to t_f$. Finally, provided that a upper bound for each component in the unmodeled perturbing acceleration is available, the MSSG control law is globally stable. The derived law supplies a robust control for the spacecraft in the vicinity of a pair of massive bodies.

6.2 Strategy for Periodic Orbit Tracking with Primary Shape Uncertainty

The objective in this analysis is a strategy to maintain a spacecraft along a path that exhibits some desirable characteristics. Employing the multiple sliding surfaces guidance method, an acceleration command law is derived that delivers a spacecraft from an initial state to a desired state. Also, the guidance law is demonstrated to achieve global stability for the closed-loop system. In practical applications, such as mission scenarios that involve close proximity of a spacecraft within a binary system of asteroids, the exact physical properties of the massive bodies in the system are not known. It is reasonable to assume sufficient knowledge of the system to construct an 'estimated' model of the system that approximates the actual properties of the 'true' system.

6.2.1 Overview

A strategy to maintain a spacecraft near a desirable path with limited knowledge concerning the primary system is introduced. First, a reference orbit is computed for an estimated primary system model. Then, a scheme is constructed incorporating multiple sliding surfaces guidance to maintain the spacecraft near the reference. Within the context of mission scenarios that involve proximity to the primary system, it is not, in general, desirable to continuously operate the propulsive subsystem. For instance, during intervals of data collection such as science measurements, it may be important that the spacecraft is subject to minimal internal perturbations. Within

this context, a 'coast and thrust strategy' is proposed. The spacecraft coasts until it reaches a prescribed deviation from the reference path, at which point the spacecraft is driven back to the reference path within a defined time. This process is repeated as necessary such that the spacecraft orbit is maintained. Hence, the duration of the first coast arc, and any subsequent coast arc, is implicitly defined by the amount of time that is required for the spacecraft to drift from the reference path by the prescribed deviation from the reference state. Each coast arc is therefore of variable time duration. In contrast, the thrust arcs that drive the spacecraft back to the reference path are of fixed duration, as prescribed by the predefined finite time of flight, t_f. Thus, with such a scheme, as time evolves and the sequence of arcs, alternating coasting and thrusting, is constructed, the switching points, i.e., the points along the path between different arcs, are implicitly defined. The number of coast and thrust arcs is then determined autonomously, that is, coast and thrust arcs are alternated to maintain the spacecraft in orbit for the prescribed total time of flight.

6.2.2 Uncertain Binary Model

Consider two models for the binary system. First, a 'true' model is one that corresponds to the actual in situ system; the true gravitational model is, in fact, unknown or at least uncertain, prior to the mission. The true system is represented by the higher-fidelity dynamical model, that is, each primary is modeled as a polyhedron. Then, an 'estimated' system, that is, an approximate system, is constructed based upon prior knowledge of the system and is employed for trajectory design. The motion of the spacecraft is numerically integrated with the EOM and the gravity model that correspond to the higher-fidelity polyhedron model while the acceleration command is computed solely based upon the lower-fidelity estimated system, that is, assuming the system is comprised of ellipsoidal massive bodies. The deviation between the total gravitational acceleration exerted by the true and the estimated system contributes

to the perturbation acceleration vector $\bar{a}_p$ in Eq. (6.22). The control law is globally stable if the second matrix gains Φ are selected such that,

$$\dot{V}_2 = \bar{s}_2^T \left[\bar{a}_P (t) - \Phi sgn (\bar{s}_2) \right] < 0 \tag{6.25}$$

that is, such that $\Phi_i > max \left| a_{P_i}^{max} \right|$.

6.2.3 Simulation

For a binary system of interest, a true and estimated primary system models are constructed, and for a sample reference trajectory that is computed employing the estimated model, the 'coast and thrust' scheme is simulated. The initial state to generate the reference orbit from the ellipsoid-sphere system is numerically integrated using the EOM with the gravitational acceleration computed using the polyhedron model until the spacecraft state reaches a predetermined deviation from the reference path. Then, using the final state along the coast arc as the new initial condition state vector for the controlled trajectory, the EOM incorporating the MSSG acceleration command, as computed with the ellipsoid-sphere model, is numerically integrated for the prescribed finite time t_f.

6.3 Application to Known Binary 1999 KW4

The proposed strategy to maintain a spacecraft near a reference path with some desirable characteristics, assuming limited a priori knowledge of the primary system, is demonstrated for a sample system. The scheme is applied to the known binary system 1999 KW4.

6.3.1 True Primary System Model: 1999 KW4

Consider the well-known Near Earth Asteroid (NEA) 1999 KW4. The first step in the analysis is the construction of both true and estimated models for the motion

of the given primary system. The same primary system model as discussed in Section 5.4.1 is employed to construct the true KW4 system. For 1999 KW4, a medium resolution polyhedron shape model is illustrated in Figure 6.1 for the primary and secondary component that comprise the KW4 binary asteroid. This shape model is derived from the full resolution model constructed in Ostro et al. [73]

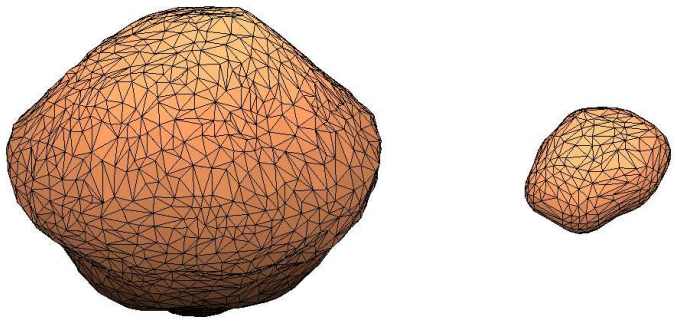

Figure 6.1. 1999 KW4 shape model: primary (left) and secondary (right)

The irregular shape of each of the two bodies directly affects the relative motion of the two primaries; the fully coupled motion of the two-body system is modeled and numerically integrated, as discussed in Section 5.4.1.

6.3.2 Estimated Model and Reference Trajectory

The reference trajectory is a three-dimensional symmetric 1 : 2 resonant orbit computed for a sample synchronous ellipsoid-ellipsoid system consistent with the dimensions of the 1999 KW4 primary bodies, as illustrated in Figure 6.2, as viewed in the rotating frame. In Table 6.1 are summarized the characteristics that are associated with the 1999 KW4 estimated model, including the system mass ratio, μ, the primary distance separation, r, and the ellipsoid axes ratios, α_i, β_i, γ_i for the primary P_i.

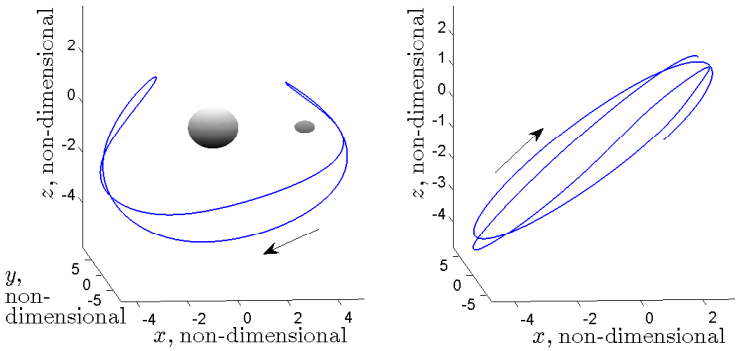

Figure 6.2. Reference trajectory: resonant 1:2 3D symmetric orbit in the EE3BP

Table 6.1. Characteristic quantities associated with the 1999 KW4 model

μ	r	β_1	γ_1	β_2	γ_2
0.0541	3.64	1	0.845	0.8109	0.6112

6.3.3 Simulation

The proposed guidance strategy is now applied to the known binary system 1999 KW4. In addition to the perturbing acceleration due to the uncertainty in the physical and dynamical properties of the primary system, solar radiation pressure exerted on the spacecraft is also incorporated into the simulation. The results of the simulation incorporating the MSSG guidance law appears in Figure 6.3, where the reference trajectory, the coast arcs, and the controlled arcs are plotted in red, blue, and purple, respectively. In this simulation, the allowed deviation from the reference path is arbitrarily selected to equal 1.25 nondimensional distance units, the time of flight is specified as $t_f = 1/10P$, $n = 1/3$, that is, the second sliding surface vector reaches zero at $t_f^* = t_f/3$. The time constants are also arbitrary. For test values of t_f^* equal to values between 1/4 and 3/4, similar simulations result in the same successful

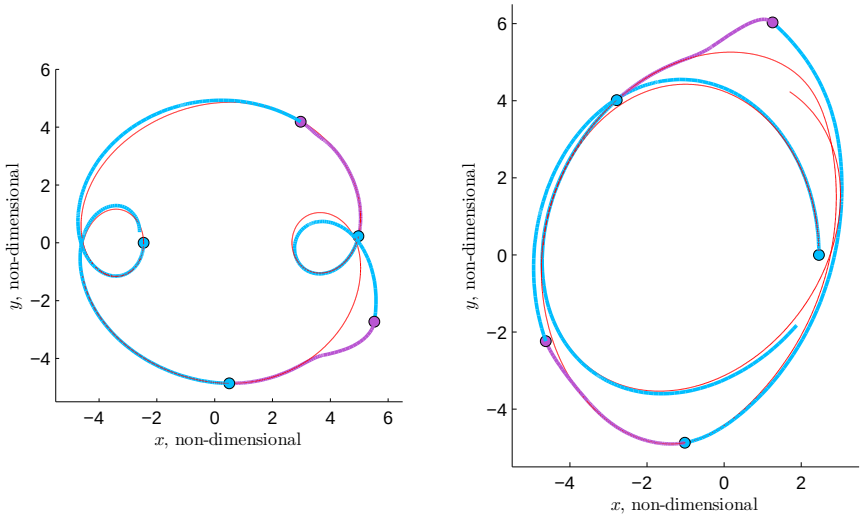

Figure 6.3. Simulation under uncertainty for 1999 KW4 viewed in rotating (left) and inertial (right) frame. Reference (red), coast (blue) and thrust (purple) arcs

outcome. A relatively small t_f value allows short thrust arcs to maximize scientific activities while requiring a larger control effort. In contrast, a longer time of flight would allow a smaller thrust magnitude, if required. While beyond the scope of this initial assessment, a more thorough analysis of the effect of the guidance parameters on the performance of the coast and thrust scheme is required to further assess the applicability of the proposed strategy. Other researchers have completed extensive sensitivity analyses of the guidance parameters in binary and tertiary system environments, [32, 33] in particular, within the context of precision asteroid landing [24] and asteroid close-proximity operations. [25] In such investigations, it is demonstrated that the selection of the guidance parameters is an important issue and, in fact, these parameters affect the magnitude of the acceleration command, accuracy and, consequently, propellant consumption. In particular, while in theory (see Section 6.1.1) a guidance gain $\Lambda > 1$ is sufficient, in practical environments, a gain value $\Lambda > 1.8$ is required to avoid accuracy degradation. Further, larger gain values may allow faster convergence but yield larger delta-V, i.e., propellant cost, and generally higher acceleration command peaks. In general, lower guidance parameter values ensure lower

peaks in the acceleration command. Also, selecting the time constants such that $t_f^* \to t_f$ appears to yield best performance in terms of propellant consumption.

The sequence of coast and thrust arcs is then determined autonomously, that is, coast and thrust arcs are alternated to maintain the spacecraft in orbit for the prescribed total time of flight, based on the prescribed allowed deviation and the thrusting time of flight. The design objective is achieved for the two thrust arcs that are required to maintain the spacecraft in orbit for one revolution along the reference trajectory. The acceleration profile and sliding surface vector time histories are illustrated in Figure 6.4. The first and second sliding surfaces converge to zero at

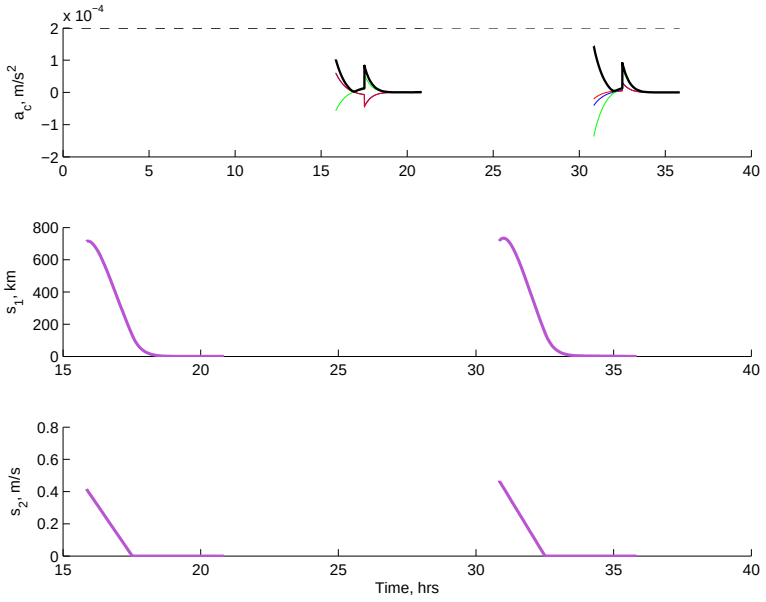

Figure 6.4. Acceleration and sliding surfaces history

t_f and t_f^* for the two controlled arcs, respectively, ensuring zero tracking state errors at the final time. The corresponding time history for the state errors is illustrated in Figure 6.5. Finally, this application successfully demonstrates the proposed 'coast and thrust' strategy for an actual binary system. The scheme is robust against unmodeled accelerations due to uncertainties in the physical and dynamical properties of the primary system, as well as the solar radiation pressure.

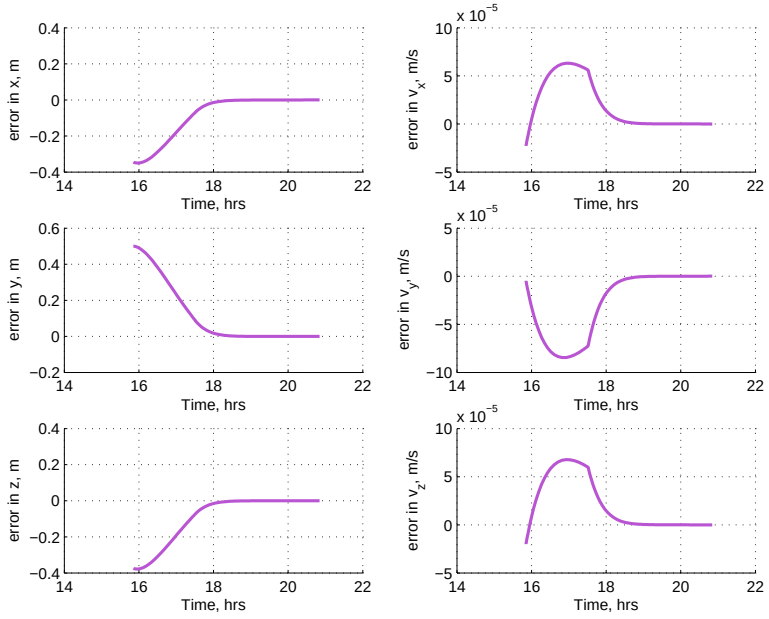

(a) Thrust Arc 1

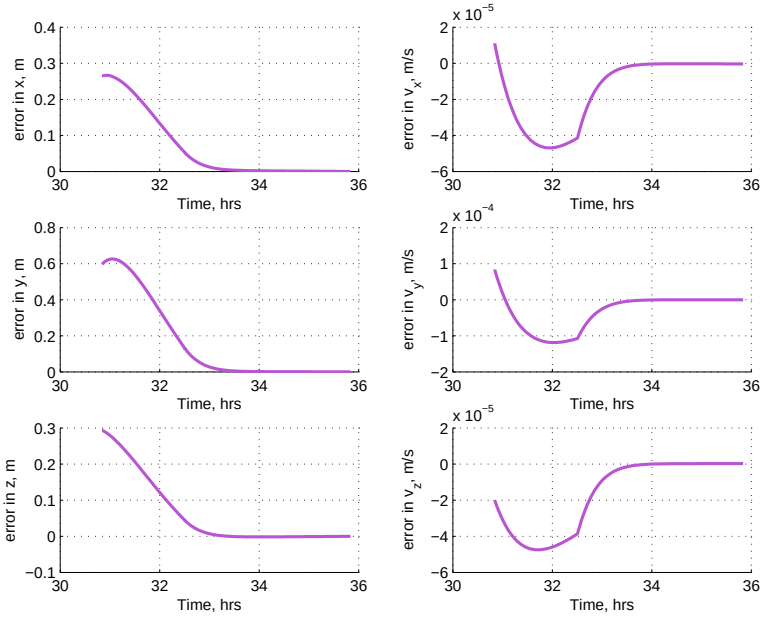

(b) Thrust Arc 2

Figure 6.5. State errors time history for the two thrust arcs

6.4 Improved Guidance Law

The acceleration law computed with the MSSG is initially implemented as a continuous guidance law and such a scenario may not be representative of actual spacecraft operations. The guidance law is modified to reflect more realistic operating conditions.

6.4.1 Guidance Law Computation and Propagation

A continuous control law that relies on the knowledge of the spacecraft states requires state information at all times, a scenario that is not reflective of actual spacecraft operations. Instead, assume that state information is only available every Δt time units. Then, at each instant t_i, a desired command acceleration, $\bar{a}_{c_D}$, is computed based on the MSSG algorithm and applied over the time interval, or control segment, Δt consistently with the assumed spacecraft operation constraints. Specifically, the constraints considered in this analysis are the maximum and minimum allowable thrust magnitude, T_{MAX} and T_{MIN}, the maximum thrust rate of change, $\dot{T}_{MAX}$, and maximum spacecraft reorientation rate, $\dot{\theta}_{MAX}$. Let $\bar{a}_{c_i}$ denote the MSSG control acceleration at the end of the previous control segment, t_i, then, the instantaneous acceleration magnitude, $T(t)$, over the next control segment, $[t_i, t_i + \Delta t]$, is computed as,

$$T(t) = T_i + \Delta T(t) \tag{6.26}$$

where $T_i = ||\bar{a}_{c_i}||$ and,

$$\Delta T(t) = min\left(\dot{T}_{MAX}\Delta t, \Delta T_c\right) \tag{6.27}$$

where $\Delta T_c = T_D - T_i$ and $T_D = ||\bar{a}_{c_D}||$. The comparison with the desired command through ΔT_c, ensures that once the required thrust level is achieved, the thrust com-

mand remains constant over the remaining control time. Also, additional bounds for the thrust magnitude, $T(t)$ are implemented such that,

$$T(t) = \begin{cases} T(t) & \text{if } T_{MIN} < T(t) < T_{MAX}, \\ T_{MAX} & \text{if } T(t) \geq T_{MAX}, \\ T_{MIN} & \text{if } T_{switch} \leq T(t) \leq T_{MIN}, \\ 0 & \text{otherwise.} \end{cases} \tag{6.28}$$

These additional conditions ensure that the thrust magnitude does not exceed an assumed maximum and minimum engine efficiency, T_{MAX} and T_{MIN}, respectively. Also, the engine is shut off if the thrust command is smaller than the prescribed threshold, T_{switch}. A similar procedure is applied for the computation of the instantaneous thrust direction, $\hat{a}_c(t)$, over the control segment that satisfies the spacecraft reorientation constraint,

$$\hat{a}_c(t) = \hat{a}_{c_i} + \Delta\theta(t)(\hat{a}_c - \hat{a}_{c_i}) \tag{6.29}$$

where $\hat{a}_{c_i} = \bar{a}_{c_i}/||\bar{a}_{c_i}||$ and,

$$\Delta\theta(t) = min\left(\dot{\theta}_{MAX}\Delta t, 1\right) \tag{6.30}$$

This expression for the thrust direction guarantees that, once the desired direction is achieved, the spacecraft orientation is maintained as designed through the remainder of the control segment. Finally, the acceleration command is constructed as,

$$\bar{a}_c(t) = T(t)\hat{a}_c \tag{6.31}$$

The instantaneous command acceleration, $\bar{a}_c(t)$, is applied over the control segment until an updated desired acceleration command is computed. This more complex guidance strategy that leverages the initial MSSG incorporates more realistic spacecraft operating conditions. This modified control input guarantees that the acceleration that is applied to guide the spacecraft remains within a feasible limit. However, it

is important to note that, while global finite-time stability is demonstrated for the unbounded MSSG, the insertion of a bound on the acceleration command may change the nature of the stability of the control law. A set of parameters may exist for any specific simulation that will achieve the guidance objective under bounded control, but such an outcome may not be, in general, guaranteed.

6.4.2 Application

A similar simulation to the scenario in Section 6.3.3 is repeated with the proposed augmented control strategy. Recall that, in addition to the perturbing acceleration due to the uncertainty in the physical and dynamical properties of the primary system, 1999 KW4, solar radiation pressure exerted on the spacecraft is also incorporated into the simulation. In this analysis, the maximum allowed thrust magnitude is assumed equal to 2×10^{-4} m/s^2, or equivalently a low thrust engine with an approximate thrust capability of 100 mN, consistent with current available technology. Also, a minimum efficiency of 5% of the maximum thrust magnitude is assumed for the minim allowed thrust, T_{MIN}. Then, the maximum rate of change for the engine thrust magnitude is equal to 3.5×10^{-6} m/s^3 and the reorientation rate of the spacecraft is constrained to a maximum value of 0.2 deg/s. [76] Finally, the duration of a control segment is taken equal to 1 minute. These values are only selected for the purpose of demonstrating the algorithm and can be arbitrarily adjusted depending on the available or desired spacecraft operating conditions. The results of the simulation incorporating the modified MSSG guidance law appears in Figure 6.6, where the coast arcs and the controlled arcs are plotted in blue and purple, respectively. In this simulation, the allowed deviation from the reference path remains arbitrarily selected to equal 1.25 nondimensional distance units, the time of flight is still specified as $t_f = 1/10P$, $n = 1/3$, that is, the second sliding surface vector reaches zero at $t_f^* = t_f/3$. The number of coast and thrust arcs is then determined autonomously and the design objective is achieved for the three thrust arcs that are required to

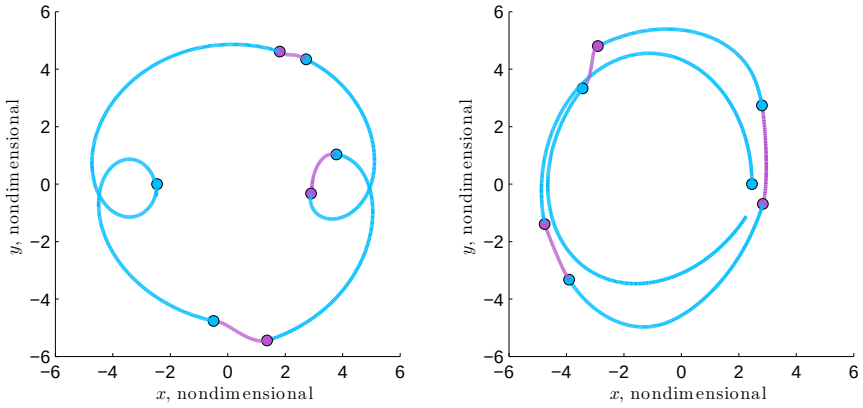

Figure 6.6. Simulation under uncertainty for 1999 KW4 viewed in rotating (left) and inertial (right) frame. Coast (blue) and thrust (purple) arcs

maintain the spacecraft in orbit for one revolution along the reference trajectory. The sliding surface vector time histories are illustrated in Figure 6.7. The first and

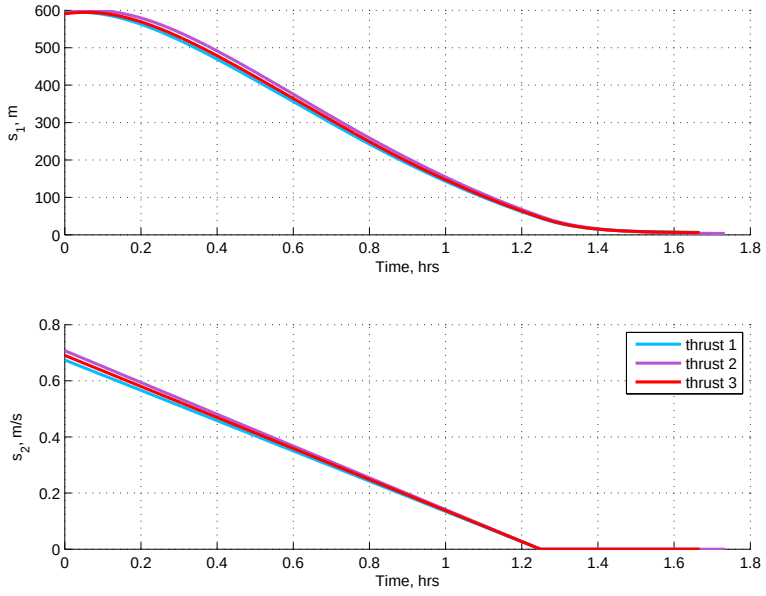

Figure 6.7. Acceleration and sliding surfaces history

second sliding surfaces converge to zero at t_f and t_f^* for the three controlled arcs, respectively, ensuring zero tracking state errors at the final time. The corresponding

time history for the state errors is illustrated in Figure 6.8. The acceleration profile is

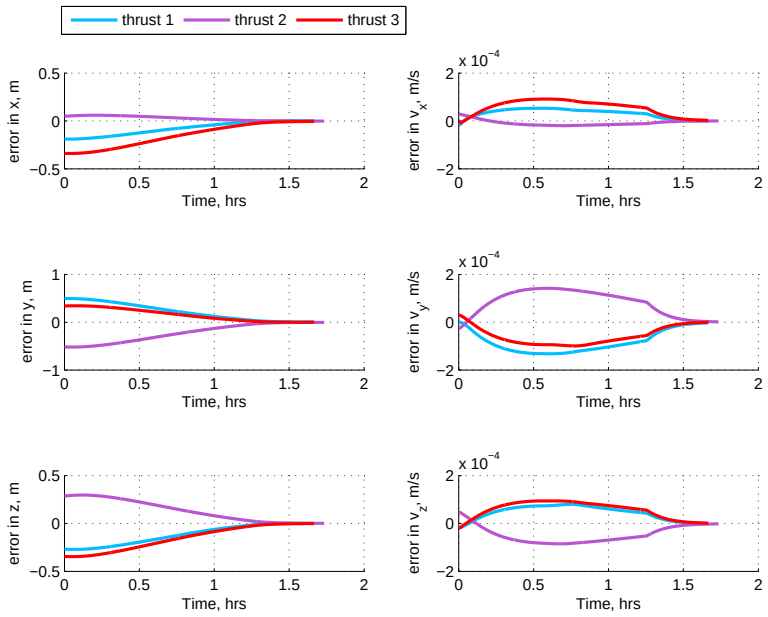

Figure 6.8. State errors time history for the three thrust arcs

now consistent with the updated guidance law and the time history of the acceleration command is illustrated in Figure 6.9 for the three thrust arcs. Focusing on the first thrust arc, the discrete nature of the control is now apparent, as depicted in Figure 6.10. In fact, focusing further on the acceleration profile along one control segment, the application of the control acceleration consistent with the operating constraints, both in terms of thrust magnitude and direction, is also apparent, as illustrated in Figure 6.11. Finally, the rate of change of the thrust magnitude and direction are displayed in Figure 6.12 to confirm that the imposed constraints on the spacecraft operating conditions are respected through the simulation. In this sample simulation, the selected set of parameters allows the control law to achieve the guidance objective under bounded control. In general, such an outcome may not be guaranteed depending on the guidance parameters, allowable reference deviation, and reference trajectory.

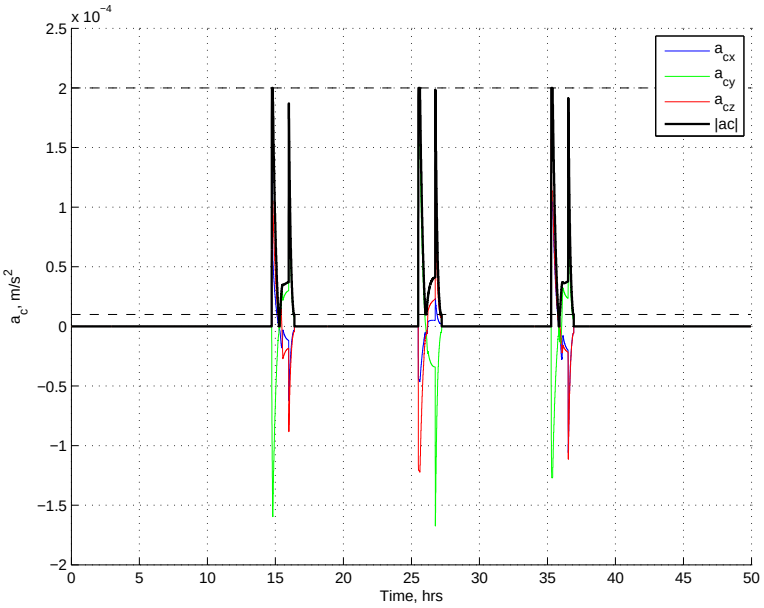

Figure 6.9. Acceleration time history for the three thrust arcs

The multiple sliding surfaces guidance algorithm is initially employed to derive an acceleration command for the control of a spacecraft in the vicinity of a pair of irregular bodies. The control law is demonstrated to achieve the design objective, that is, tracking a desired solution, in a finite time. Most importantly, the control law is globally stable. The guidance law is also robust and globally stable against unmodeled accelerations, provided an upper bound for the perturbing acceleration is available. A trajectory design strategy to maintain a spacecraft near reference third-body trajectories that exhibit some desired characteristics is constructed. In practical applications, the exact physical properties of the massive bodies in the system are not known. It is reasonable to assume sufficient knowledge to construct an 'estimated' model that approximates the properties of the 'true' system. For the true system, each primary is modeled as a polyhedron and the 'estimated' system is an ellipsoid-ellipsoid model. Then, to maintain the spacecraft in orbit near a desired reference trajectory, a 'coast and thrust' scheme is proposed. The spacecraft coasts until it reaches a prescribed deviation from the reference path, at which point the spacecraft

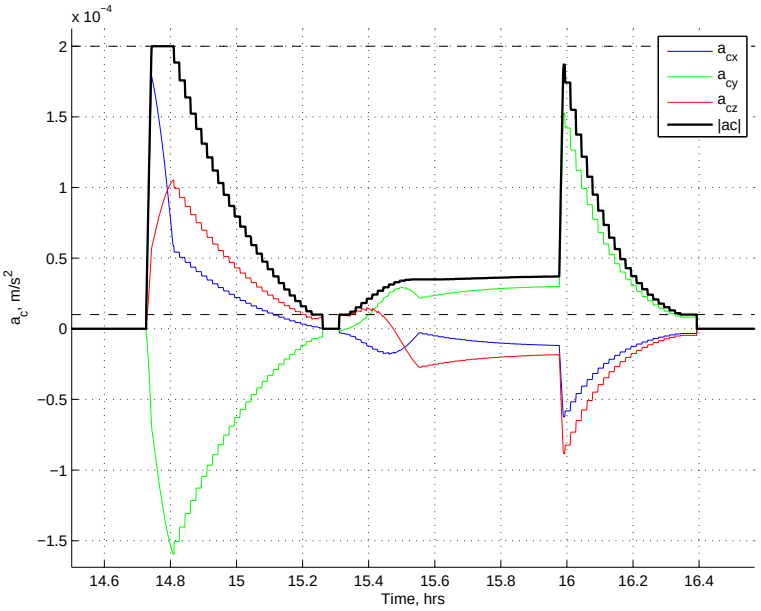

Figure 6.10. Acceleration time history for the first thrust arc

is driven back to the reference within a defined time. This process is automated to allow successive coast and thrust arcs to maintain the spacecraft orbit. Based upon the simulations, the design strategy achieves the objective under the perturbing acceleration due to the uncertainty in the system physical properties. The acceleration command magnitude is, in general, reasonable with respect to the assumed current available technology. Nevertheless, a continuous controller may not representative of actual spacecraft operating conditions. Thus, to better capture realistic thrust conditions based upon the attitude of the spacecraft and engine performance, additional constraints are incorporated in the guidance law to account for feasible deliverable thrust, both maximum and minimum, as well as feasible reorientation of the spacecraft. The augmented guidance law are implemented in a sample simulation to demonstration the capability of the strategy to achieve the control objective under these new constraints.

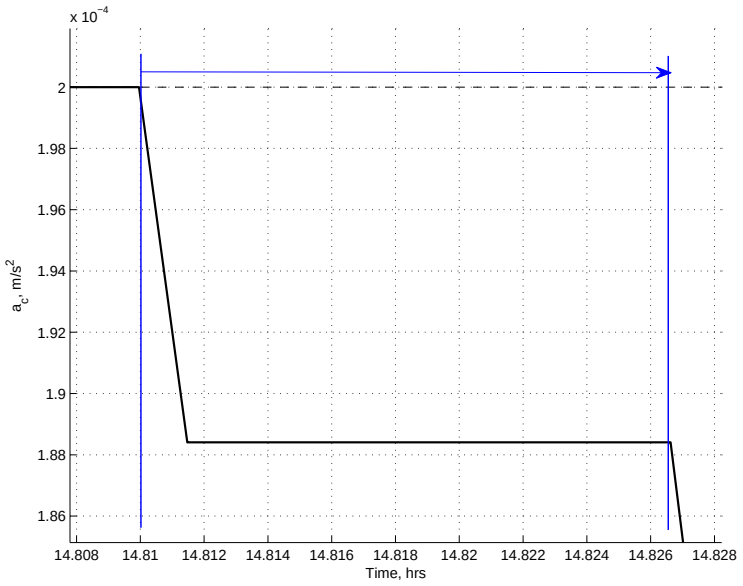

Figure 6.11. Acceleration time history over one control segment

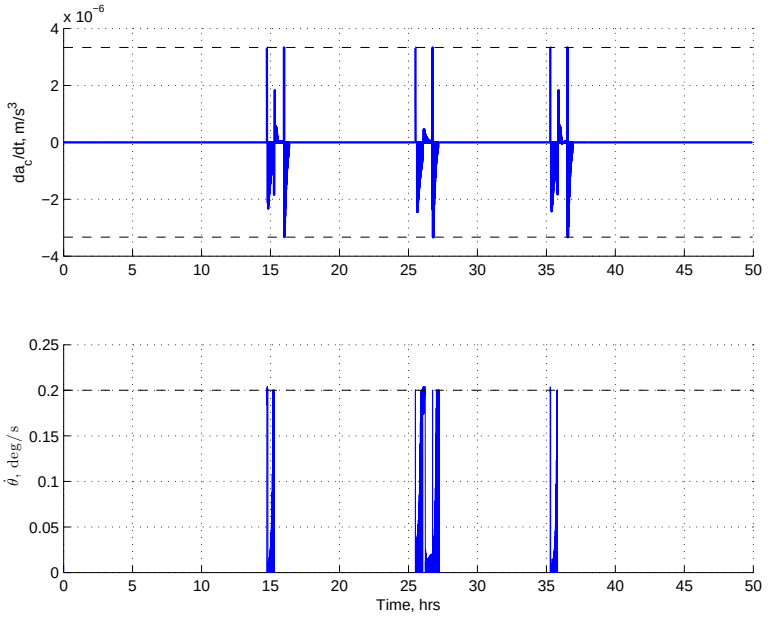

Figure 6.12. Rate of change for the thrust magnitude and direction over the simulation

7. BOUNDED MOTION IN NON-SYNCHRONOUS SYSTEMS

7.1 Primary System Motion Analysis

7.1.1 Non-Synchronous Sphere-Ellipsoid Systems

While synchronous systems, or close-to-synchronous systems, are available in the known asteroid population, systems also exist where the primaries move in a configuration that is not fixed relative to the rotating frame. For 'non-synchronous' systems, the spin rate of ellipsoidal body P_1 and the orbital rate of P_2 are different as viewed from the inertial frame. The initial challenge then is the motion of the two-body system. Given various possible approaches to this problem, initially consider an analogy with a simple problem, the simple pendulum. The motion of a simple pendulum is described by a simple scalar equation in terms of one time-dependent angular coordinate, θ, that is measured relative to the stable equilibrium orientation. The geometry of the problem is illustrated in Figure 7.1(a) and the EOM is written $\ddot{\theta} + \frac{g}{l} sin\theta = 0$, where g is the constant gravity acceleration and l is the length of the pendulum. Depending on the initial conditions, i.e., θ_0 and $\dot{\theta}_0$, different behavior for the motion of the pendulum is observed and a classic representation that clearly highlights the various types of behavior is a phase space portrait, that is, a θ-$\dot{\theta}$ plot, as illustrated in Figure 7.1(b). In the figure are labelled different behaviors that correspond to different characteristic curves in the phase portrait. The fixed points correspond to the equilibrium positions, both stable and unstable. Then, the libration-type behavior is depicted by a set of closed curves centered on a stable equilibrium position. For an alternative set of initial conditions that correspond to increasing total energy, a critical curve exists that divides the phase space into libration (blue) and circulation

(red) regions. The boundary is represented by the magenta curve (separatrix) in the phase portrait.

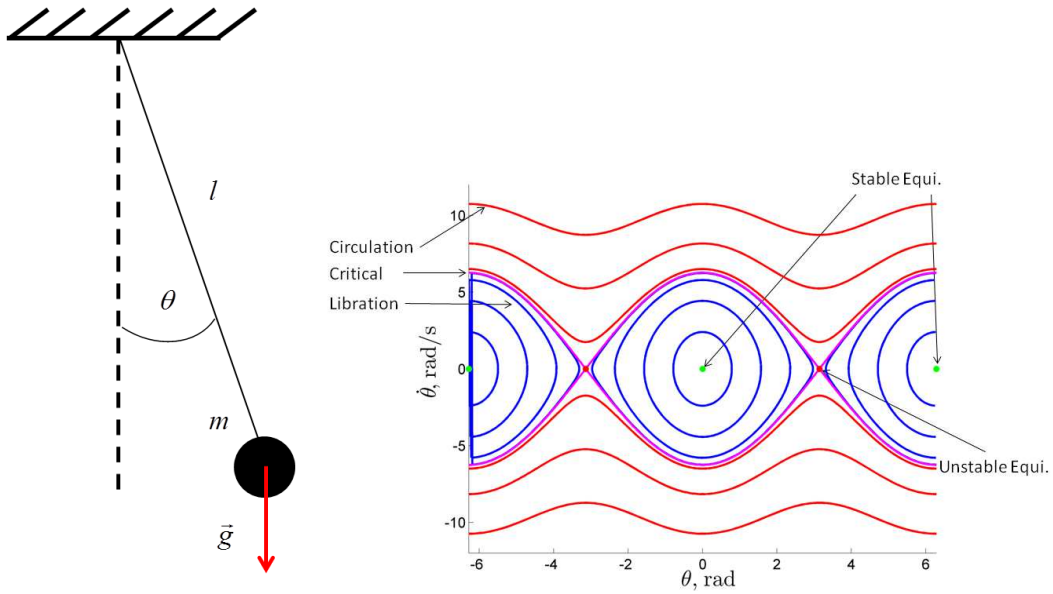

(a) Geometry (b) Simple pendulum phase portrait

Figure 7.1. Simple pendulum

The pendulum analysis is extended to the problem of interest, that is, the motion of a massive body moving relative to a fixed ellipsoidal body. To exploit the pendulum analogy, define the coordinate θ as the angle between the P_1-P_2 line that corresponds to the equilibrium system, or synchronous system, that is, the x-axis, and the time-dependent location of P_2. A sample path for a spherical P_2 is represented, along with the geometry of the problem, in Figure 7.2 where the trajectory for the sphere is obtained by perturbing the equilibrium initial conditions. To ensure that the path emerging for P_2 exhibits regular behavior for an extensive time duration, only trajectories that are successfully corrected to periodicity are retained. A set of periodic trajectories for P_2 is generated from the reference equilibrium configuration varying initial conditions such that the total energy of the system increases. The reference configuration corresponds to a librational motion and the periodic family evolves until the behavior becomes circulatory, as illustrated in Figure 7.3(a). Similar

to the pendulum analysis, the phase portrait that corresponds to the resulting set of trajectories is produced in Figure 7.3(b) and exhibits the expected characteristics.

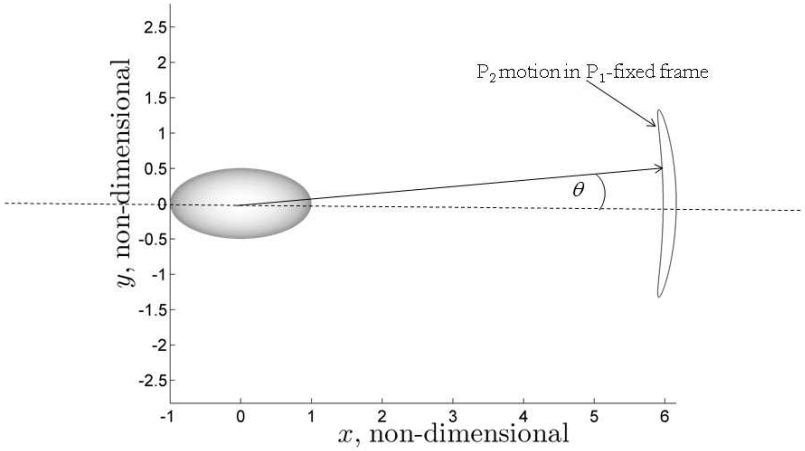

Figure 7.2. Non-synchronous full two-body problem geometry

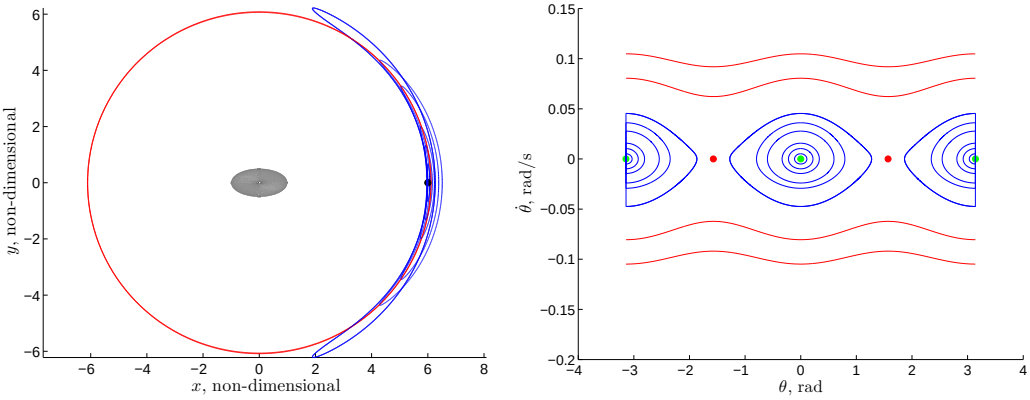

(a) Sample P_2 periodic paths for SE system

(b) Phase portrait

Figure 7.3. Non-synchronous sphere-ellipsoid full two-body problem

7.1.2 Non-Synchronous Ellipsoid-Ellipsoid Systems

The initial non-synchronous analysis that is applied to sphere-ellipsoid systems is further extended to ellipsoid-ellipsoid systems. For such systems, the search for a periodic motion of the secondary with respect to the primary is more challenging as the relative orientation of the two ellipsoids is also required to be periodic. For sphere-ellipsoids systems, the orientation of the secondary, a sphere, along the periodic path is irrelevant. Thus, the analysis of the motion of ellipsoid-ellipsoid non-synchronous systems represent a more complete view of the dynamical behavior. Exploiting an automated continuation procedure, periodic solutions for the motion of the primary system, both in terms of the orbital motion and orientation of the bodies, are constructed for increasing total energy of the system. The first non-synchronous solution is obtained by perturbing the equilibrium configuration, as illustrated in red in Figure 7.4. Specifically, in Figures 7.4(a), 7.4(b), and 7.4(b) are displayed the orbital path of P_2 in the P_1-fixed frame, the phase portrait, and the time-history of selected state variables. The history of these variables highlights the periodicity of the motion where ϕ_1, ϕ_2 are of particular interest as they relate to the relative orientation of the two bodies. Also represented in green and blue are two more solutions for slightly increasing total energy; these solutions depict increasingly librating motion near the equilibrium configuration.

This first set of periodic solutions depicts the transition from synchronous to non-synchronous systems. Next, the focus is on the evolution of the behavior as energy is further increased. Three sample solutions, for larger total energy values than the previous scenarios, are illustrated in Figure 7.5. The increasing amplitude of the path for the secondary is a reflection of the increasing energy that is associated with these systems. Also, note the coupling between the orbital motion is now more apparent, as highlighted in the time history of the angles ϕ_1, ϕ_2 and angular rates $\dot{\phi}_1, \dot{\phi}_2$. In contrast to the near-synchronous scenarios where the orientation of both primaries is very similar over time, for the solutions with larger libration motion, the orientation

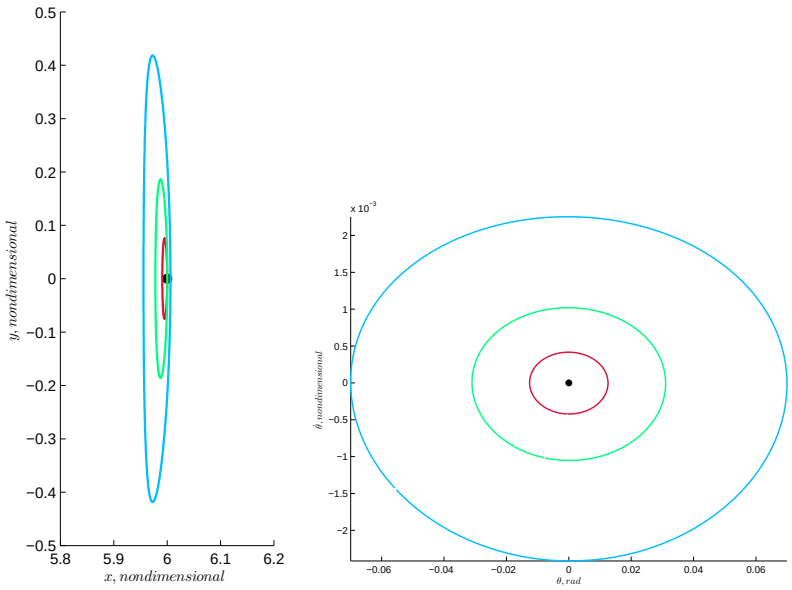

(a) Path in P_1-fixed frame (b) Phase portrait

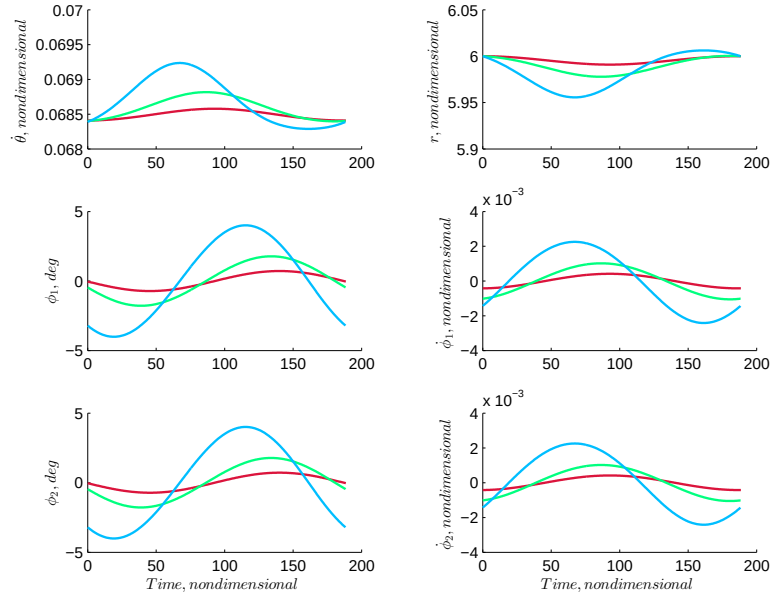

(c) State variables history

Figure 7.4. Transition from ellipsoid-ellipsoid synchronous to non-synchronous systems

of the secondary with respect to the primary is now directly affected by the orbital motion.

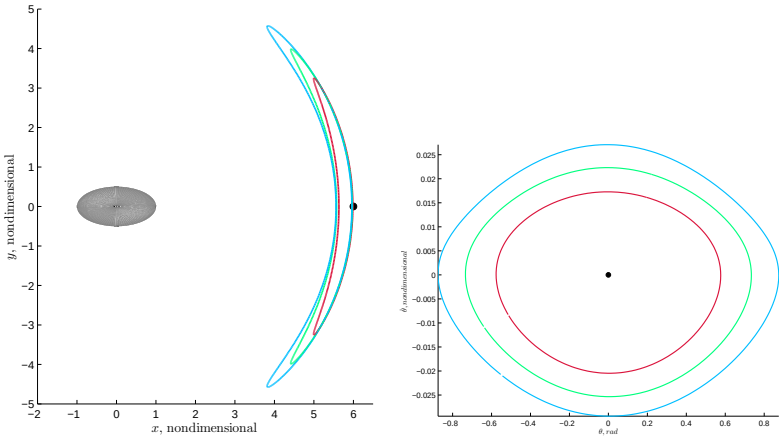

(a) Path in P_1-fixed frame

(b) Phase portrait

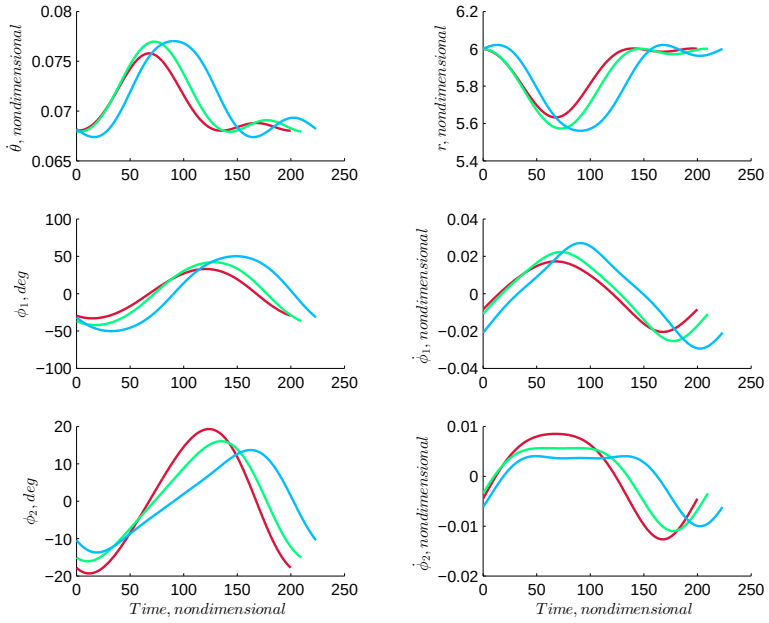

(c) State variables history

Figure 7.5. Ellipsoid-ellipsoid non-synchronous systems - large libration

As energy is further increased, another transition in the primary system motion occurs. From a libration regime, the motion of the secondary exhibits a circulatory behavior. The transition is evident both on the representation of the path of P_2 in

the P_1-fixed frame, where the path is now a pseudo-circular periodic orbit, and in the phase portrait. The initially closed curves, a characteristic of the libration motion, are now open and indicative of the circulatory motion, as depicted in Figure 7.6.

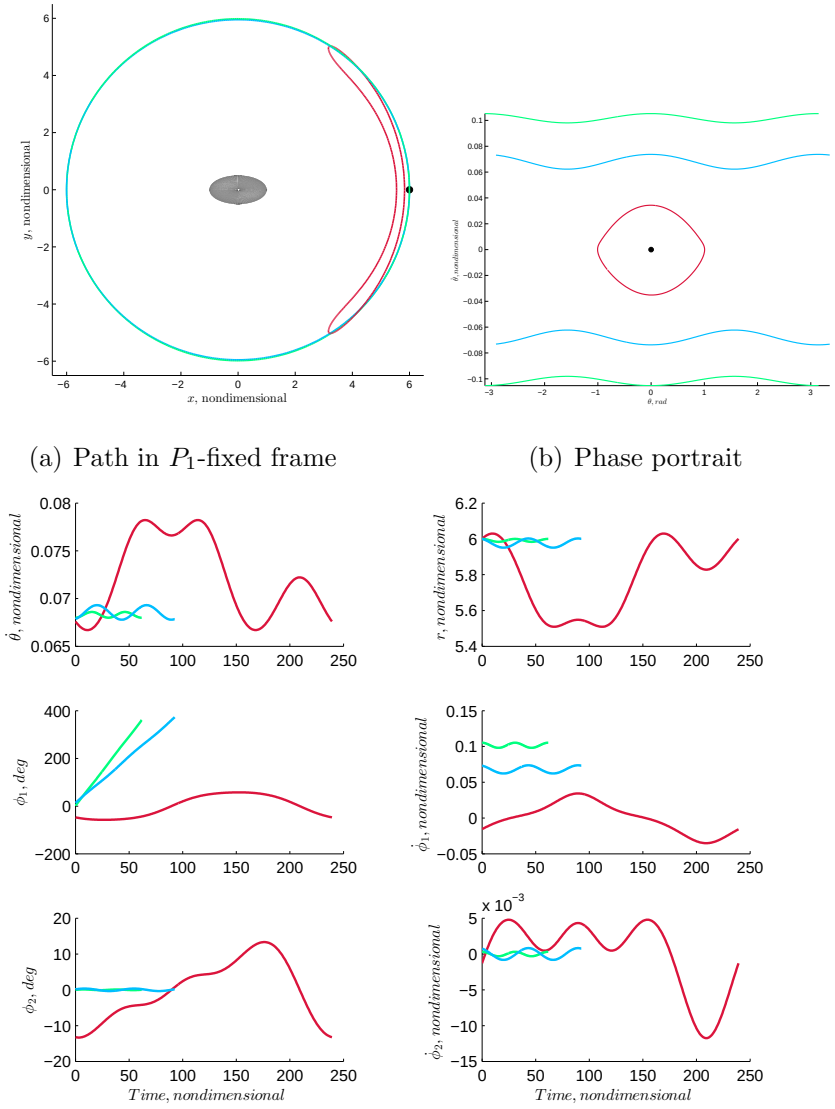

(a) Path in P_1-fixed frame

(b) Phase portrait

(c) State variables history

Figure 7.6. Ellipsoid-ellipsoid non-synchronous systems - Transition from libration to circulation

7.1.3 Dynamical Substitutes

With a time-dependent solution for the motion of P_2 with respect to P_1, equilibrium solutions to the 3BP EOMs, in the form of fixed stationary points, no longer exist. However, as the path of P_2 is constrained to be periodic, dynamical substitutes that form closed periodic path replace the equivalent Lagrange points from the synchronous case. [77–79] For any given non-synchronous system, the equivalent Lagrange points for the corresponding synchronous system are employed as initial guesses to compute the dynamical substitutes for the non-synchronous system of interest. In Figure 7.7, a set of non-synchronous systems that correspond to libration and circulation motions for a spherical P_2 are represented as well as the corresponding dynamical substitutes for the equivalent collinear Lagrange points. The upper left view corresponds to the periodic substitutes as viewed in the ellipsoid-fixed frame R_{P_1} and the three collinear dynamical substitutes as viewed in the sphere-fixed frame R_{P_2} are individually illustrated in the three other views.

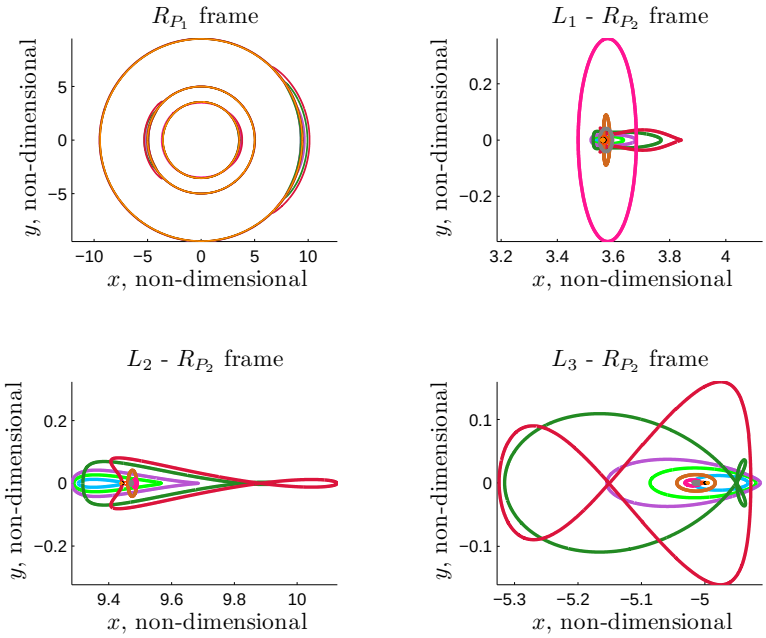

Figure 7.7. Dynamical substitutes for the equivalent colinear Lagrange points in sphere-ellipsoid systems

7.2 Periodic Orbits in Non-Synchronous Systems

A strategy to construct periodic orbits in non-synchronous systems relies on exploiting the insight gained from analysis in the synchronous problem. Periodic orbits previously computed from an equivalent synchronous problem are employed as an initial guess. Recall that, in this analysis, the trajectory for P_2 is periodic, thus, for a P_3 periodic trajectory to exist, the period of the desired P_3 orbit must be commensurate with the period of P_2. For convenience, the commensuration relationship between the two orbit periods is denoted as $p : q$ such that $P_{NS} = qP_S = pP_{2B}$, where P_{NS}, P_S, P_{2B} are the periods of the third body in the non-synchronous regime, the initial guess, and the non-synchronous primary system, respectively. Consequently, while there exists an infinite set of periodic orbits in the vicinity of a known orbit or a family of orbits in the synchronous case, periodic orbits in the non-synchronous problem are isolated based upon the possible integer ratios between the periods of P_3 and P_2. In summary, for any given non-synchronous system, a discrete set of periodic orbits that are equivalent to periodic synchronous orbits can be computed using the equivalent families of trajectories in the synchronous problem as initial guesses. Note that an initial guess from the synchronous problem is more closely related to a trajectory in a frame where the location of the primaries remains almost fixed, that is, only the relative orientation of the primaries significantly changes over time, labeled orbital frame. This fictitious frame is consistent with the frame that is defined by the unit vector basis $(\hat{s}_1, \hat{s}_2, \hat{s}_3)$ in Section 3.3. This initial guess is transformed from the orbital frame frame into the P_1-fixed frame prior to any corrections process in the non-synchronous regime. In this analysis, the focus is on the exploration of the behavior for near-synchronous systems, that is, systems that are exhibiting a relatively limited libration motion, similar to the the systems displayed in Figure 7.4. The trajectories that are discussed in the following sections are colored consistently with the the sample primary system models, that is, in red, green, and blue for increasingly non-synchronous systems.

Non-synchronous planar Lyapunov orbits

To demonstrate the existence of third-body periodic orbits in periodic non-synchronous systems, and explore the properties of such solutions, first consider periodic paths that are constructed leveraging planar Lyapunov orbits for an equivalent synchronous system. For the sample non-synchronous systems considered, sample Lyapunov trajectories that are periodic in the non-synchronous regime are computed with a commensuration ratio of 3:1, as illustrated in Figure 7.8. In the left figure, the trajectories are displayed as viewed in the P_1-fixed frame where the effect of the non-synchronous motion of the primary system on the behavior of the third body is most apparent. Alternatively, as viewed in the orbital frame, the three trajectories appear to overlay nearly perfectly, indicating that the characteristics of the initial guess are preserved.

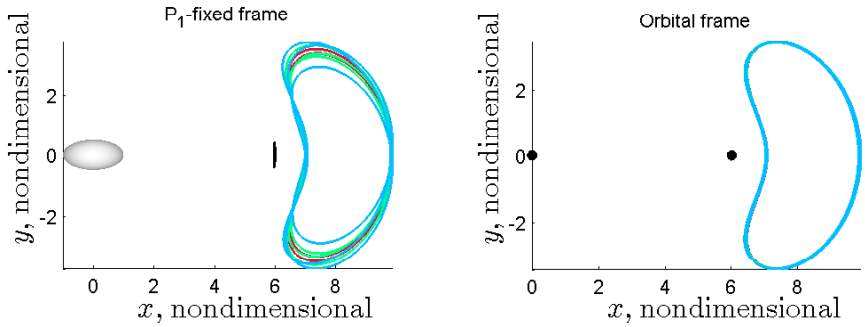

Figure 7.8. Lyapunov orbits for increasingly non-synchronous systems (7.4) as viewed in the P_1-fixed frame (left) and orbital frame (right)

Non-synchronous halo and vertical orbits

The analysis is extended to families of three-dimensional periodic orbits, such as halo and vertical families. Similar to the Lyapunov scenarios, sample halo orbits for all three colinear equilibrium points are selected as initial guesses to compute trajectories that are periodic in the three sample non-synchronous systems. In Figure 7.9 are illustrated the produced halo trajectories with a commensuration ratio of 5:1 as viewed

in the P_1-fixed frame. Similarly, vertical non-synchronous trajectories for the sample primary system models that correspond to the transition between synchronous to non-synchronous regime are illustrated in Figure 7.10. The larger orbits centered at the L_3 and L_2 point possess a commensuration ratio of 2:1 while the smaller L_2 trajectory is associated with a ratio equal to 3:1. The three-dimensional non-synchronous orbits, while exhibiting a behavior consistent with increasingly non-synchronous primary system models, retain the overall characteristics that are associated with the parent synchronous families.

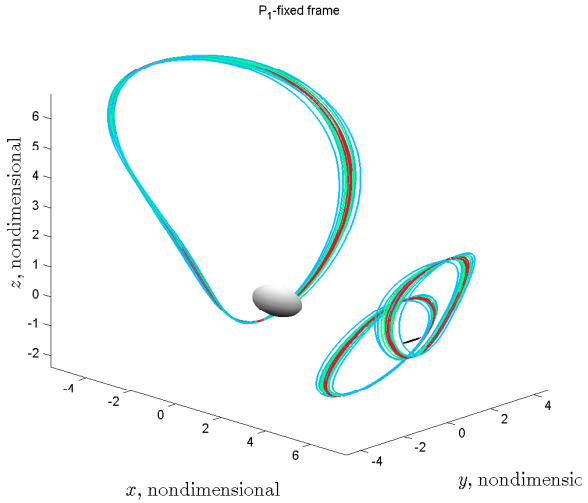

Figure 7.9. Halo orbits for increasingly non-synchronous systems (7.4) as viewed in the P_1-fixed frame (left) and orbital frame (right)

7.3 Non-Synchronous Tours

7.3.1 Strategy

A strategy is proposed to construct trajectories that exhibit some set of desired characteristics within the context of the non-synchronous 3BP. Similar to the analysis in the synchronous problem, a discrete set of isolated libration point orbits is likely not directly relevant for any practical application. However, these types of paths serve

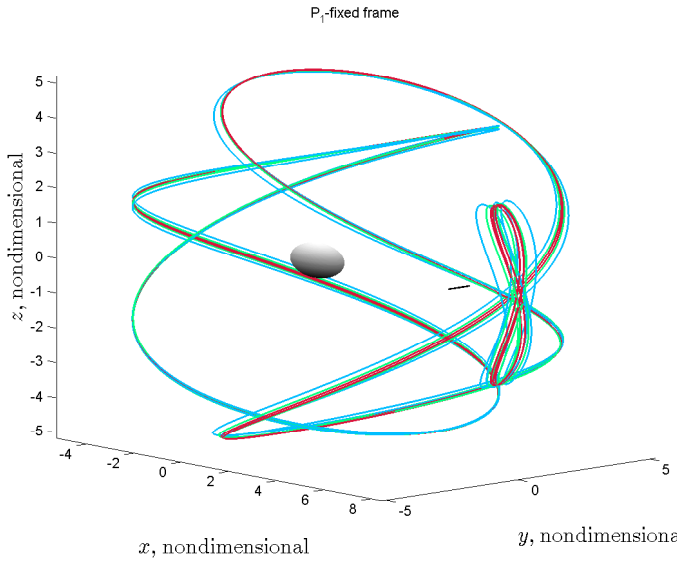

Figure 7.10. Vertical orbits for increasingly non-synchronous systems (7.4) as viewed in the P_1-fixed frame (left) and orbital frame (right)

as a basis for the construction of more complex trajectories that retain some desired characteristics. In fact, the same procedure that is developed within the context of the synchronous problem is adjusted to construct trajectories that visit the regions of the dynamical substitutes for the equivalent collinear Lagrange points. Because the problem is now time-variant, time continuity must also be maintained between trajectory arcs that are employed to construct a fully continuous orbit.

7.3.2 Application

Consider a sample ellipsoid-sphere non-synchronous system with a primary non-dimensional separation $r = 6$ such that the P_2 motion corresponds to circulation-type behavior, that is, in the ellipsoid-fixed frame the trajectory of P_2 resembles a pseudo-circular orbit and P_2 remains almost stationary in the sphere-fixed frame. In Figure 7.11(a), represented in black, a non-synchronous periodic orbit is plotted, as viewed in the sphere-fixed frame; this orbit is computed from an L_1 Lyapunov orbit for the equivalent synchronous system. The stable and unstable manifolds that correspond to

this periodic orbit are also computed. In Figure 7.11(a), the sample unstable arcs also appear. These arcs are those that exhibit a behavior of interest for the construction of an initial guess, similar to the synchronous case, to a path that progresses back and forth between the regions of the dynamical substitutes representing the equilibrium points, as viewed in the sphere-fixed frame. Then, consistent with the procedure for the design of double homoclinic cycles, a x-$\dot{x}$ Poincaré map with hyperplane $y = 0$ aids the selection of suitable arcs to construct a reasonable initial guess, as illustrated in Figure 7.11(b) where the left and right plot correspond to crossings near P_1 and P_2, respectively. Note that, because the manifold arcs are not time-invariant in the non-synchronous problem, the epoch corresponding to the endpoints along the different arcs that are concatenated to produce the initial guess must be very close to equal. This additional dimension is also represented on the Poincaré map by the color of the points that denote each crossing, in terms of the corresponding epoch of P_2 in its periodic orbit. Once the initial guess is constructed, a differential

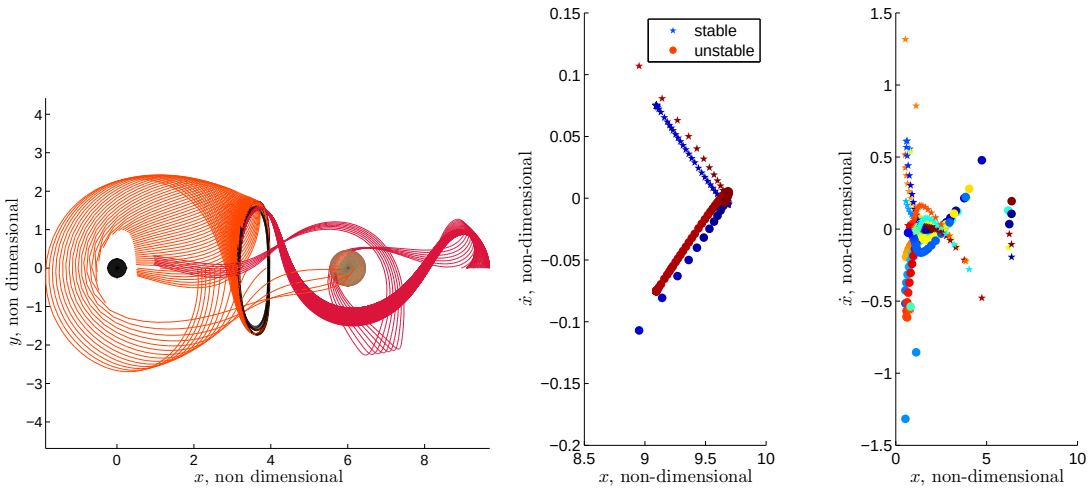

(a) NS Lyapunov orbit manifold arcs - R_{P_2} frame

(b) Poincaré Map x-$\dot{x}$

Figure 7.11. Strategy for non-synchronous trajectory exploration

corrector is employed to produce a trajectory that retains the desired characteristics. Ideally, such a trajectory is also periodic. However, similar to the results for the non-

synchronous periodic orbit, for the designed trajectory to be periodic, the period must be commensurate with the period of P_2. In Figure 7.12, the result of such a process is plotted, that is, a trajectory that visits the vicinity of all three collinear dynamical substitutes, as viewed in the ellipsoid- and sphere-fixed frame in the left and right view, respectively. However, although the initial guess for the period of P_3 is nearly commensurate with the P_2 orbit, the algorithm does not successfully achieve exact periodicity. In contrast, at the location marked by the red dot, a small maneuver is required to achieve velocity continuity, approximately equal to 0.0003 nondimensional units or 10^{-5} m/s for an ellipsoidal primary with the largest semi-major axis equal to $\alpha = 500$ m.

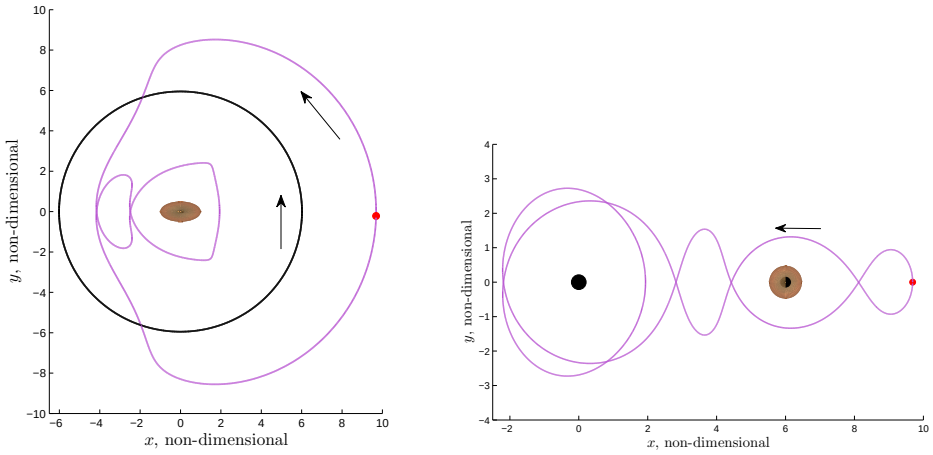

(a) Ellipsoid-fixed frame (b) Sphere-fixed frame

Figure 7.12. Non-synchronous double homoclinic cycle for $\beta = \gamma = 0.5 - \nu = 0.3 - r = 6$

7.4 Finite Time Lyapunov Element Maps

For synchronous systems, as discussed in Chapter 5, a set of families of periodic solutions is generated for sample systems comprised of nonspherical primaries and such orbits are further incorporated into a design strategy to construct more complex

trajectories that satisfies some desired characteristics. While in Sections 7.2 and 7.3, it is demonstrated that similar trajectories, even periodic ones, can also be computed in non-synchronous systems, these orbits are point solutions and may not be representative of the overall regime. Moreover, to assess the usefulness of the large set of synchronous trajectories that are rapidly available through numerical computation, the transition between synchronous and non-synchronous regime is of particular interest. In fact, while some systems may be reasonably modeled as synchronous, such system of small bodies may not be perfectly synchronous, and it is important to assess third-body behavior for near-synchronous systems. Poincaré mapping is a powerful tool for a variety of analyses and, in Chapter 5, such a technique is applied to investigate the effect of nonpsherical primaries onto the behavior of a third body in the vicinity of synchronous systems. However, Poincaré maps are best-suited for time-invariant dynamical models, i.e, for synchronous systems, while for time-varying models, or non-synchronous primary system models, stroboscopic maps are more adapted to the problem. Specifically, similar to the synchronous Poincaré map analysis, Finite Tine Lyapunov Exponent mapping techniques are sought to yield further insight in the overall behavior of the third-body for non-synchronous systems.

7.4.1 Integration Time Determination and First Remarks

The computation of the FTLE relies on an integration time, or truncation time, $T = t - t_0$. Unfortunately, there is no systematic method to select T, and in fact, the choice of T may vary depending on the application, the initial condition domain, and the underlying dynamical system. Initially, the same initial condition domain as in the Poincaré analysis is employed to produce FTLE maps for the same sample ellipsoid-ellipsoid system considered in Section 5.3 for various integration times. In this analysis, the focus is on the effect of increasingly non-synchronous systems on the behavior of a third body, with respect to initial behavior in the vicinity of an equivalent synchronous system. Hence, for the purpose of selecting an appropriate

integration time, consider values of T that are multiple of P_{sys_2}, i.e., the period of the secondary with respect to the primary for the first non-synchronous system as constructed in Section 7.1.2. Forward flow FTLE maps for the sample synchronous system considered for values of T equal to 2, 5, 8, 11, 13, and 14 P_{sys_2} are illustrated in Figure 7.13 for a 512×512 grid of initial conditions. It is apparent in the figure that the topology of the map greatly varies with the integration time considered. However, for values of T between 11 and 13 P_{sys_2}, the structures that emerge on the maps seem to be more consistent through these T values. Thus, for the purpose of this analysis, a value $T = 14P_{sys_2}$ is adopted.

The maps that are produced to enable the selection of the truncation time only include the forward FTLE flow, that is, the initial conditions are numerically integrated forward in time. Additional information is available by also exploiting the backward flow, i.e., integrating the numerical conditions in reverse time. The initial forward FTLE map for the selected truncation time is again illustrated in Figure 7.14(a), now for a finer 1024×1024 initial condition grid. Then, both forward and backward flows are combined to produced the colored map in Figure 7.14(b). On the combined flow representation, structures emerge that are analogous to the Poincaré map analysis, such similarities are especially evident when overlaying the FTLE and orbit convolution renditions for the same domain of initial condition and same primary system, as depicted in Figure 7.14(c). Recall that the eventual objective is to extend this analysis to the non-synchronous problem, however, this initial simulation for the equivalent synchronous system offers insight into the behavior of the FTLE map for the system and region considered. Without any restriction on the type of dynamical system considered, i.e., time-invariant and time-varying alike, the FTLE approach is useful within the context of the proposed analysis.

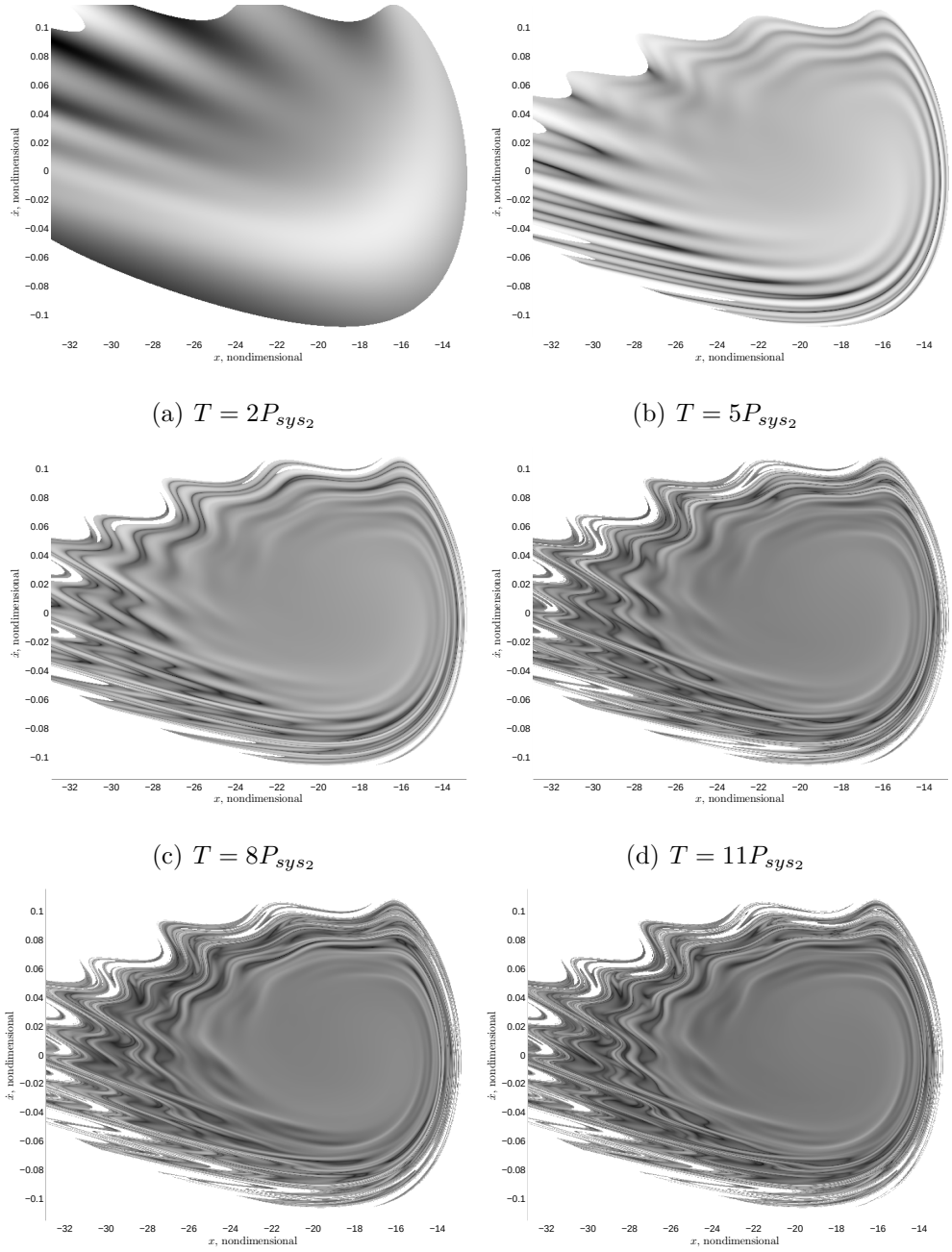

(a) $T = 2P_{sys_2}$

(b) $T = 5P_{sys_2}$

(c) $T = 8P_{sys_2}$

(d) $T = 11P_{sys_2}$

(e) $T = 13P_{sys_2}$

(f) $T = 14P_{sys_2}$

Figure 7.13. FTLE map for sample synchronous system with varying FTLE integration time - 512 x 512 grid

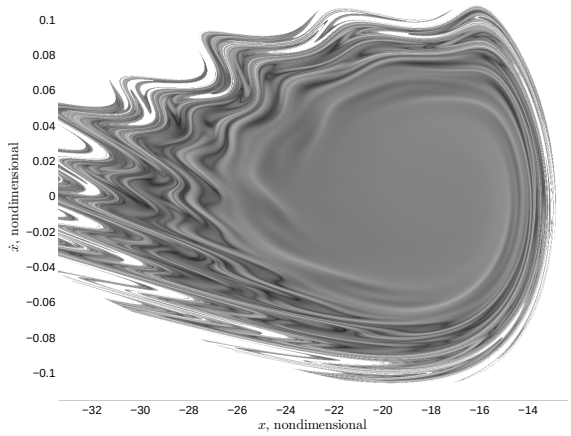

(a) Forward flow

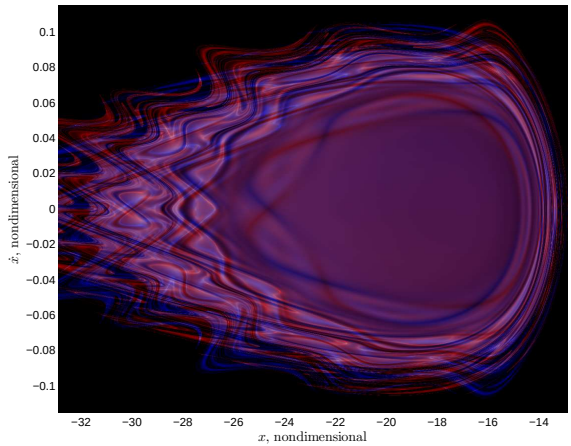

(b) Forward and backward flows combined

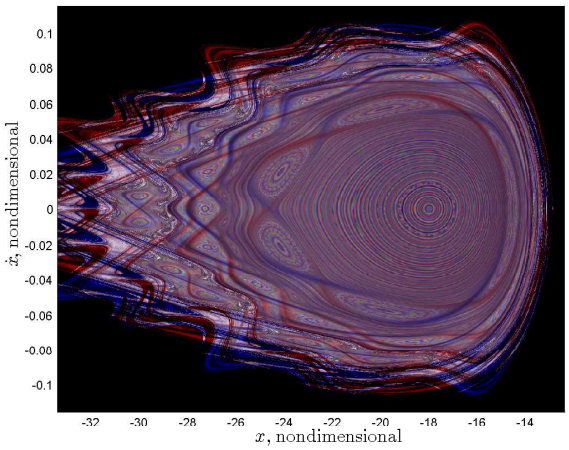

(c) Overlaid with orbit convolution Poincaré map

Figure 7.14. FTLE map for sample synchronous system - 1024 x 1024 grid

7.4.2 Application to Transition Between Synchronous and Non-synchronous Systems

Considerations for non-synchronous system FTLE mapping

For non-synchronous systems, the primaries do not remain fixed as viewed from any frame as time evolves. Rather, as viewed in the P_1-fixed frame, the secondary moves along a periodic path. Thus, to produce maps that are consistent for various non-synchronous systems, attention must be devoted to the initial primary system configuration, as the relative position and orientation of the primaries directly affect the behavior of the third body. Then, a phase variable, ϕ, that describes the initial orientation of the system is introduced. For any given non-synchronous system, ϕ is defined as t_0/P_{P_2} where t_0 is the initial time along the periodic path of the secondary with respect to the primary relative to a reference initial point along the path. For consistency through the non-synchronous systems, ϕ is always measured relative to the minimum approach to the primary, that is, $\phi = 0$ corresponds to the location of the secondary closest to P_1 and, similarly, $\phi = 0.5$ the farthest, as depicted in Figure 7.15. Employing this convention, the effect of increasingly non-synchronous systems onto the behavior of the third body is explored through the generation of a series of FTLE maps for various sample systems leveraging a consistent set of simulation parameters. Also, for any specific non-synchronous system, the effect of the initial primary system configuration can be assessed by varying the phase variable and producing the corresponding FTLE maps.

Effect of non-synchronous primary notion

The focus in this analysis is on the effect of increasingly non-synchronous systems onto the behavior of the third body. A first set of maps is produced for $\phi = 0.5$, that is, the initial conditions are numerically propagated for the set of non-synchronous systems illustrated in Figure 7.15 such that the secondary is initially located at apoap-

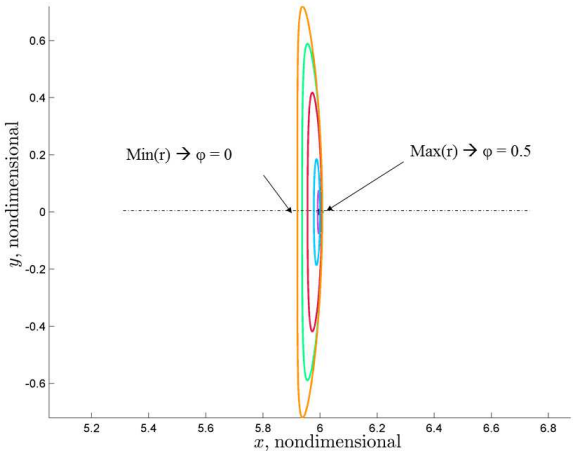

Figure 7.15. Definition for initial orientation of the primary system

sis relative to P_1 along its respective periodic path. From these maps, illustrated in Figure 7.16, it is apparent that the main structures that emerge in the FTLE field are consistent through all the systems considered. In other words, even for non-synchronous systems, similar dynamical structures to the synchronous case are apparent on the maps, in particular, a continuum of structures exist on any given map, and, from one system to another, a continuous evolution is observed. Then, in contrast to the direct periodic orbit analysis for non-synchronous systems, where it is noted that only isolated periodic orbits exist for such systems due to the requirement of commensuration between the period of the secondary and the third-body orbit, the mapping approach reveals a rich dynamical structure preserved even for increasingly non-synchronous system. In fact, for the phase variable value considered, the features on the various maps are closely similar while the motion of the primary system is significantly different.

A second set of FTLE maps, displayed in Figure 7.17, is produced for $\phi = 0$, that is, the initial conditions are numerically propagated for the set of non-synchronous systems illustrated in Figure 7.15 such that the secondary is initially located at the closest approach relative to P_1 along its respective periodic path. While the same

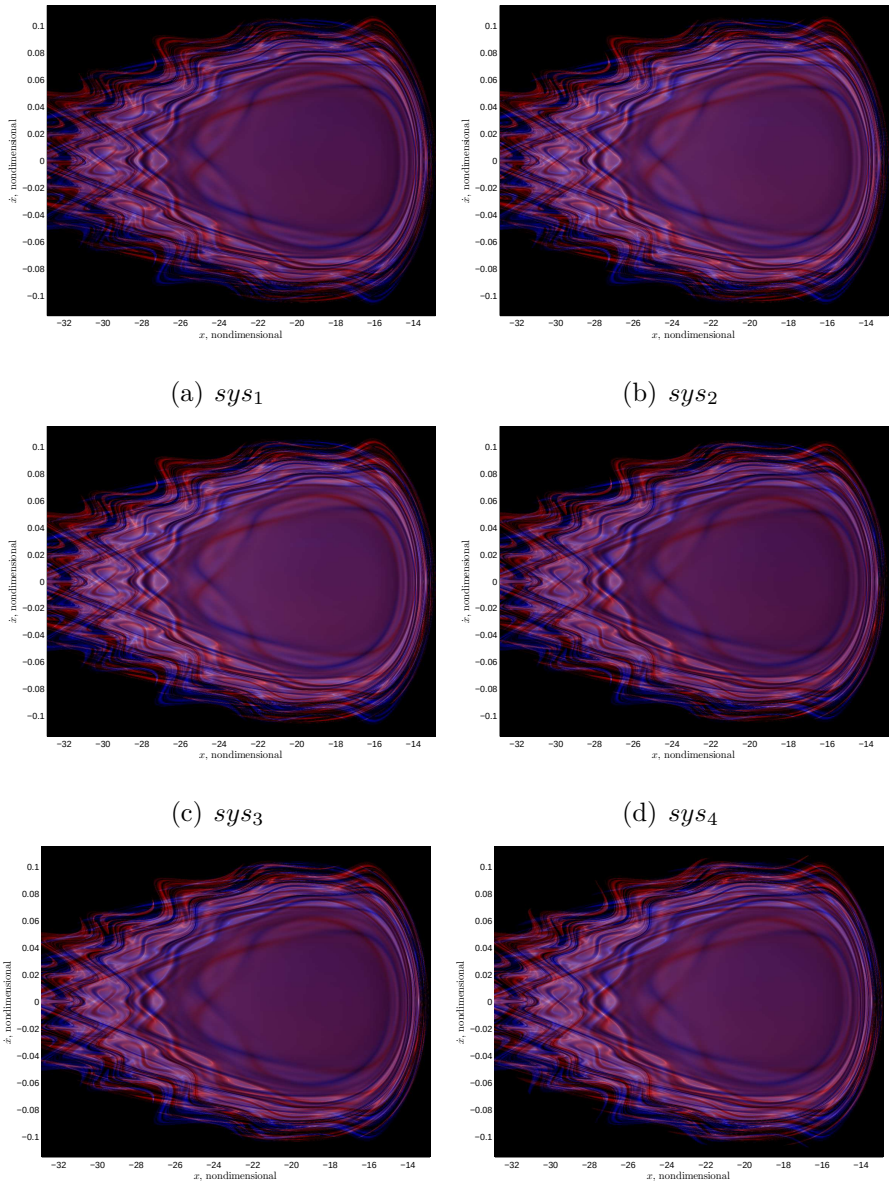

(a) sys_1 (b) sys_2

(c) sys_3 (d) sys_4

(e) sys_5 (f) sys_6

Figure 7.16. FTLE map for sample non-synchronous systems $\phi = 0.5$-1042 x 1024 grid

general observation is still valid, that is, a continuum of structures exist on any given map and between systems, the specific inner structures on the maps evolve as the non-synchronous systems are varied. In particular, some chains of islands seem to vanish while new ones are created. It is important to note that it is challenging to

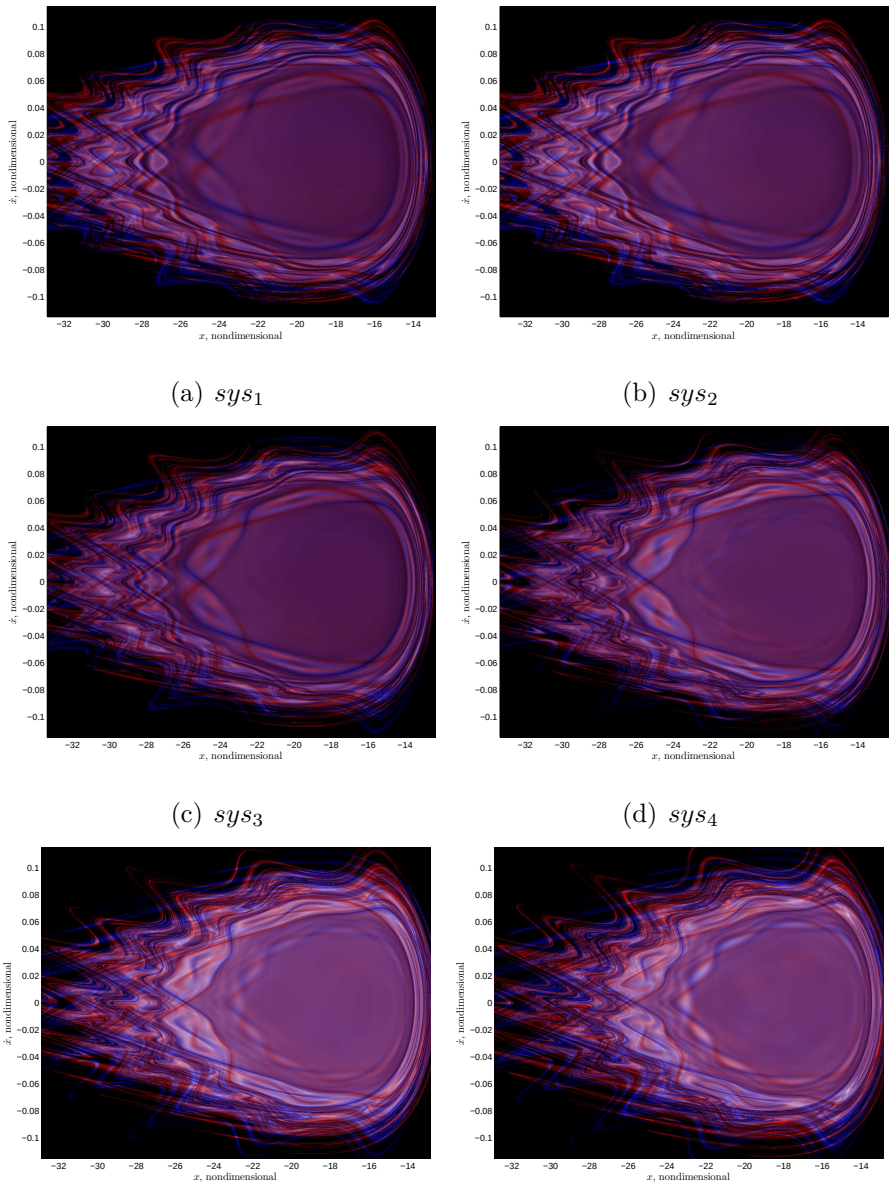

(a) sys_1 (b) sys_2

(c) sys_3 (d) sys_4

(e) sys_5 (f) sys_6

Figure 7.17. FTLE map for sample non-synchronous systems ϕ = 0-1042 x 1024 grid

isolate the possible causes of such an evolution. The systems are, in fact, different, and specifically, possess different energy levels. While efforts are devoted to generate maps that are as consistent as possible, these intrinsic discrepancies may yield the observed differences. However, an important point is that these maps feature a rich dynamical structure preserved even for increasingly non-synchronous system. Such observations indicate that, considering near synchronous systems rather than perfectly synchronous ones, the dynamical behavior of a third body may be preserved and similar trajectories to ones that are constructed under such assumptions may also exist.

Effect of initial orientation of the primary system

A first observation of the effect of the initial primary system relative orientation is noted in Section 7.4.2, this assessment is verified through a more detailed analysis of this effect for a sample non-synchronous system. Consider the non-synchronous system labeled sys_5, a series of maps for this sample system is produced for varying phase variable values and is illustrated in Figure 7.18. This analysis provides evidence that the dynamical structures smoothly evolve as the initial orientation of the system is varied.

Application to periodic orbits

Mapping techniques are powerful to gain insight into the overall dynamical behavior of a body in the vicinity of a pair of massive bodies, but such techniques are also powerful tools to identify certain type of trajectories, in particular, quasi-periodic and periodic orbits. In Figure 7.19, the focus is on the island near the $\dot{x} = 0$ axis that is part of the outer chain of island in the maps that are initially displayed in Figure 7.16. Recall that this set of maps is produced for the family of increasingly non-synchronous systems, starting from the synchronous problem, with a phase variable $\phi = 0.5$. Such a chain of islands is characteristic of the existence of a periodic orbit and a set of quasi-periodic periodic in its vicinity. Initially, consider an initial condition for each

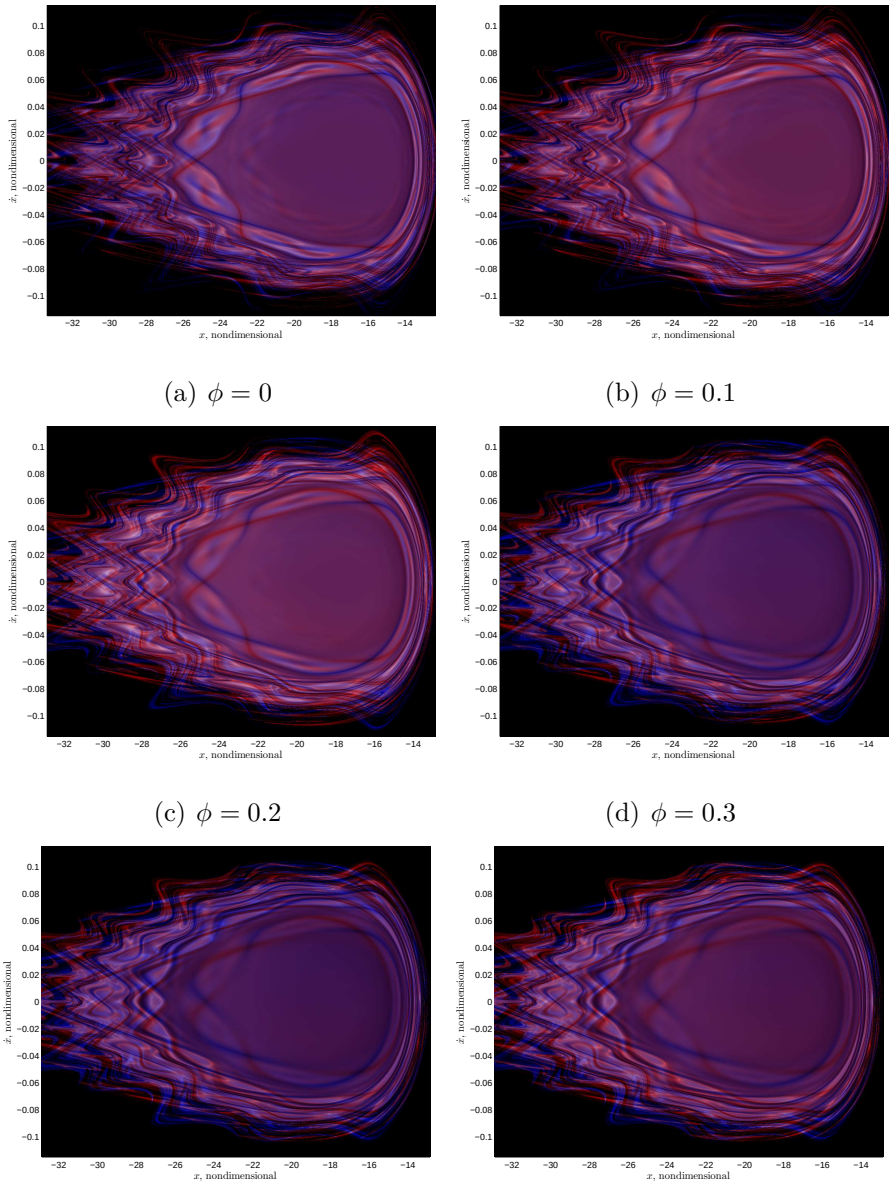

(a) $\phi = 0$ (b) $\phi = 0.1$

(c) $\phi = 0.2$ (d) $\phi = 0.3$

(e) $\phi = 0.4$ (f) $\phi = 0.5$

Figure 7.18. FTLE map for sample non-synchronous system 5 with varying initial phase angle - 1042 x 1024 grid

system that lies at the center of the island for each system considered, that is, an initial condition that lies close to the periodic orbits that is associated with this island chain. The initial conditions are numerically propagated for a time duration equal to the FTLE truncation time, i.e., $t_f = T = 14P_{sys_2}$. The resulting trajectories are

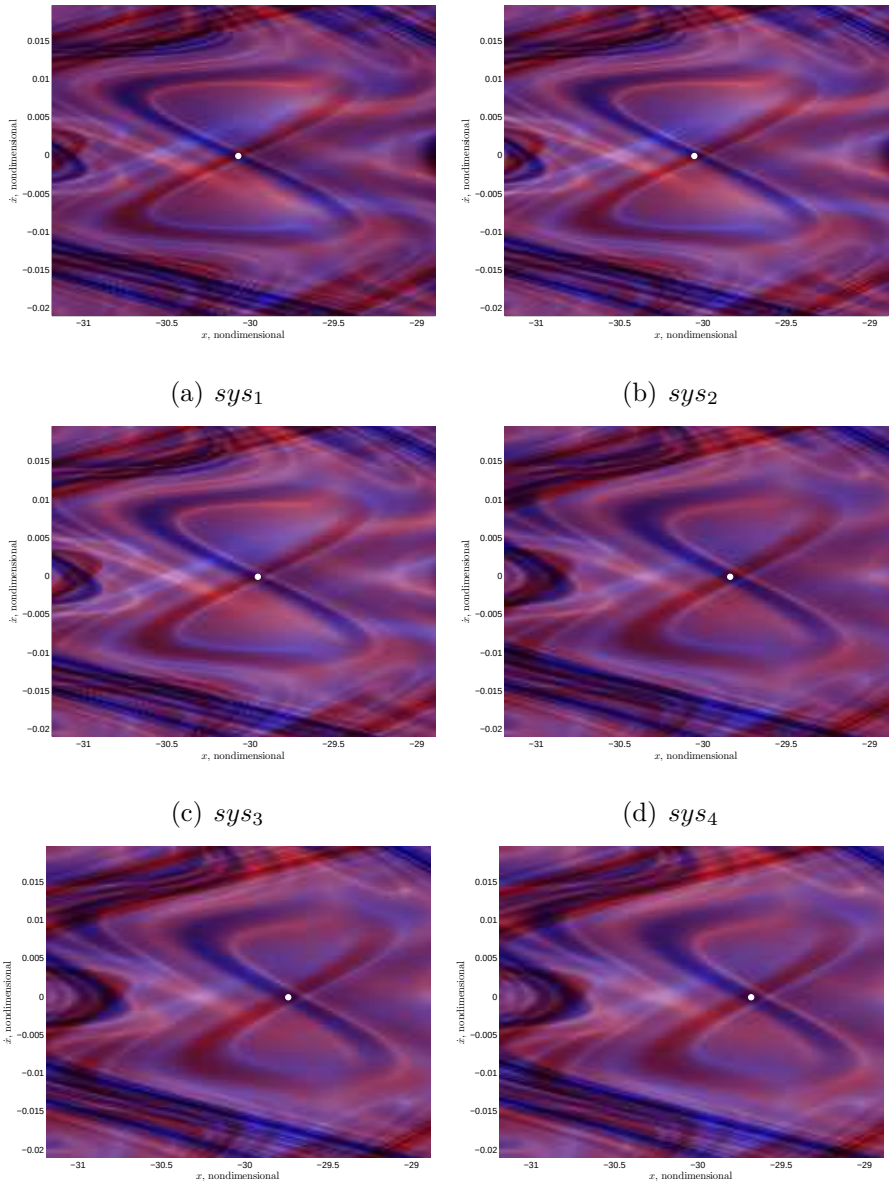

(a) sys_1 (b) sys_2

(c) sys_3 (d) sys_4

(e) sys_5 (f) sys_6

Figure 7.19. Zoom in FTLE map for sample non-synchronous systems $\phi = 0.5$

displayed in Figure 7.20 and appear to remain bounded and near-periodic for the duration of the simulation for all the systems considered. Also, the trajectories retain the same visual characteristics through the set of non-synchronous systems considered. For the synchronous problem, i.e., the system labeled sys_1, it is straight forward

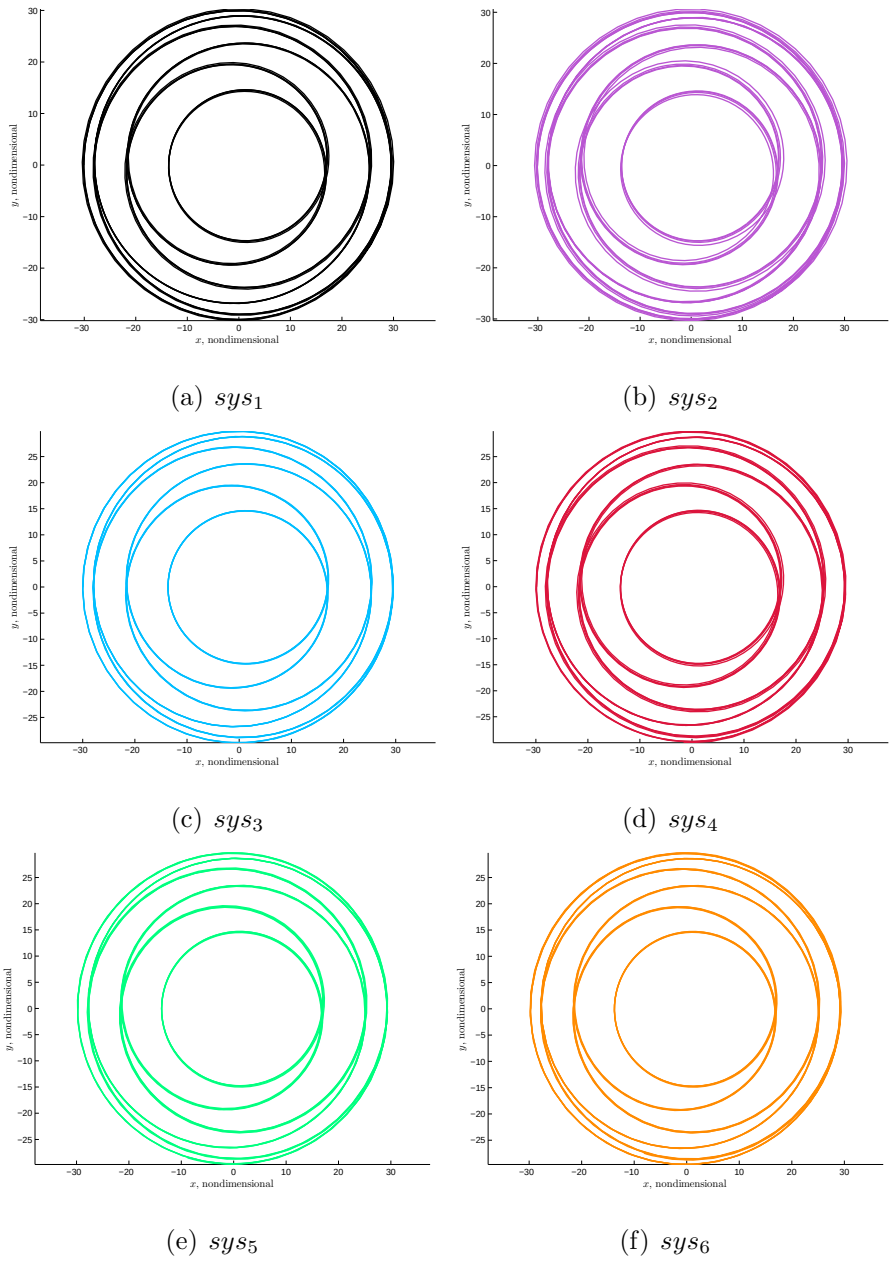

(a) sys_1 (b) sys_2

(c) sys_3 (d) sys_4

(e) sys_5 (f) sys_6

Figure 7.20. Integrated path from FTLE map for sample non-synchronous systems $\phi = 0.5$

to use this trajectory as an initial guess for a differential corrections algorithm and produce a periodic trajectory that closely resemble the initial solution, as illustrated in Figure 7.21(a). In contrast, as discussed previously, for non-synchronous systems, for a periodic orbit for a third body to exist, the period of the candidate trajectory

must be commensurate with the period of the path of the secondary. Recall the commensuration relationship between the two orbit periods is denoted as $p : q$ such that $P_{NS} = qP_S = pP_{2B}$, where P_{NS}, P_S, P_{2B} are the periods of the third body in the non-synchronous regime, the initial guess, and the non-synchronous primary system, respectively. For this particular example, the trajectory that corresponds the map-selected initial condition for the non-synchronous systems considered is close to periodic and close to commensurate with the period of P_2, such that $P_S/P_{2B} \approx 17/5$. For the non-synchronous system sys_7, similar to the synchronous case, a 5:17 periodic orbit is successfully computed employing the map-inferred trajectory as initial guess, as illustrated in Figure 7.21(b).

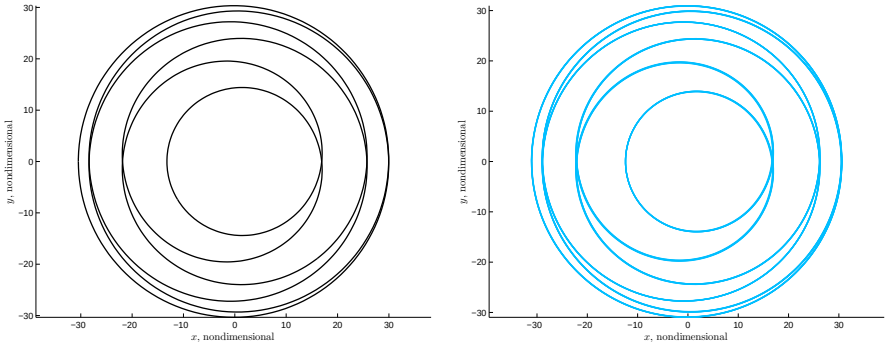

(a) sys_1 (b) sys_7

Figure 7.21. Sample periodic orbit for synchronous system and non-synchronous system 7

8. ORBITAL PERTURBATION ANALYSIS NEAR BINARY ASTEROID SYSTEMS

Within the context of exploring the dynamical behavior of a spacecraft near a pair of small irregular bodies, an important step in the analysis is an assessment of the perturbing effect that dominates the dynamics of the spacecraft in such a region as a function of the baseline orbit. Previous investigators examined this problem for a single body, e.g., an asteroid, [80] a comet, [81] or a planet [82], as well as considering the perturbations from the solar tide, Solar Radiation Pressure (SRP), and the small body oblateness. The objective in this investigation is an extension of the analysis to include the perturbation that arises from the existence of the secondary body in a binary system. To compare the relative strength of several perturbing effects across the parameter space, 'zonal maps' are introduced. Then, the prediction of the binary effect is initially validated using arbitrary initial conditions that are numerically propagated in the circular restricted three-body problem. The validity of the zonal map is further assessed through the numerical integration of initial conditions, that correspond to pre-computed periodic orbits, with a high-fidelity dynamical model.

8.1 Orbital Perturbations

To initially assess the perturbing effects that drive the behavior of the spacecraft, the Lagrange Planetary Equations (LPE) are exploited. First, assume that the reference or baseline trajectory of the spacecraft is an orbit about P_1. Then, to model the perturbation on a spacecraft that is associated with the existence of a secondary body in the primary system, labeled 'binary effect' in this analysis, the three-body disturbing function is exploited. [83] This function is derived as an infinite series expansion in terms of the orbital elements of both of the additional masses, i.e., the spacecraft

and the secondary, each moving with respect to a central body, i.e., the primary P_1. In this analysis, the investigation is limited to the secular effects. To second order in inclination and eccentricities, the averaged secular term in the disturbing function simplifies to a reasonably tractable expression and allows an approximation for the disturbing potential that corresponds to the binary effect.

8.1.1 Lagrange Planetary Equations (LPE)

The LPEs supply approximate equations of motion in terms of the classical orbital elements for the secular time evolution of the elements due to a specific perturbing effect. The LPEs rely on the availability of a scalar perturbing potential function, R, that represents the perturbing effect. Let $\bar{oe} = [a, e, i, \omega, \Omega, \sigma]$ denotes the classical set of orbital elements for the spacecraft in the inertial frame and n is the mean motion of the spacecraft. These equations are written as, [83]

$$\dot{a} = \frac{2}{na}\frac{\partial R}{\partial \sigma} \tag{8.1}$$

$$\dot{e} = \frac{1}{na^2 e}\left[\left(1-e^2\right)\frac{\partial R}{\partial \sigma} - \sqrt{1-e^2}\frac{\partial R}{\partial \omega}\right] \tag{8.2}$$

$$\dot{i} = \frac{1}{na^2\sqrt{1-e^2}}\left[\cot i\frac{\partial R}{\partial \omega} - \csc i\frac{\partial R}{\partial \Omega}\right] \tag{8.3}$$

$$\dot{\omega} = \frac{\sqrt{1-e^2}}{na^2 e}\frac{\partial R}{\partial e} - \frac{\cot i}{na^2\sqrt{1-e^2}}\frac{\partial R}{\partial i} \tag{8.4}$$

$$\dot{\Omega} = \frac{\csc i}{na^2\sqrt{1-e^2}}\frac{\partial R}{\partial i} \tag{8.5}$$

$$\dot{\sigma} = -\frac{1-e^2}{na^2 e}\frac{\partial R}{\partial e} - \frac{2}{na}\frac{\partial R}{\partial a} \tag{8.6}$$

One challenge in analyses that involve the use of the LPEs, besides the availability of a closed-form expression for the perturbing potential function, is an expression of this function in terms of the orbital elements. Such a form is required to compute the partial derivatives of the potential with respect to the orbital elements.

8.1.2 Classical Perturbing Effects

The classical perturbing effects that are considered in problems that involve single bodies, the main focus of previous developments, include the SRP, [80] solar tide, [84] and body oblateness. [80] For these effects, potential functions that describe the perturbing effect can be derived and substituted into the LPEs. While these equations provide an approximation for the secular evolution of the orbital elements due to any given effect, the objective is to assess the relative strength of the various perturbations. Then, as discussed in Scheeres [80], one approach to quantify the strength of a perturbation relies on identifying common coefficients in the LPEs, for a given effect. Such a coefficient is a measure of the strength of a perturbation. These coefficients are derived as, [80]

$$C_t = \frac{\dot{N}^2}{n} \tag{8.7}$$

$$C_g = \frac{3gna^2}{2\mu_{pb}} \tag{8.8}$$

$$C_s = \frac{3nJ_2\alpha_0^2}{2a^2} \tag{8.9}$$

for the solar tide, the SRP, and the body oblateness, respectively. The symbols N and n denote the mean motion of the small body and spacecraft in their orbits relative to the Sun, respectively. Then, in the expression for C_g, g denotes the SRP force and is defined as $g = G_1 B/R^2$, where G_1 is the solar flux constant ($\approx 1 \times 10^{14}$ kgkm/s^2), B is the effective projected area-to-mass ratio of the spacecraft, and μ_{pb} is the gravitational parameter of the small body. Also, the symbol J_2 describes the oblateness of the primitive body and α_0 is the largest equatorial radius of the body.

8.1.3 Third-Body Disturbing Function

The objective is to extend the analysis to include the perturbation that corresponds to the existence of a secondary component rather than a single central body.

To model this perturbation, labeled 'binary effect' in this analysis, the three-body disturbing function is exploited. [83] This function is derived as an infinite series expansion in terms of the orbital elements of the two additional masses, the secondary and the spacecraft, with respect to a central body, as illustrated in Figure 8.1. The disturbing function is derived in details in Murray and Dermott [83] and the application of this theory to the problem of interest in this investigation is briefly outlined in this section. Most often, the disturbing function is written as the sum of two parts, the direct and indirect term. In this analysis, the investigation is limited to the secular effects from the secondary. Considering only secular effects, the indirect term vanishes and only the direct part is relevant. Also, note that the form of the perturbing potential depends on the relative location of the spacecraft and secondary. When the spacecraft orbit lies outside of the secondary orbit with respect to the primary, the secondary is then an internal perturber. The perturbing function differs if it is due to an external perturber, when the spacecraft orbit is contained inside the orbit of the secondary with respect to the primary. It is further assumed that the orbits of the secondary and the spacecraft never intersect. Then, the perturbing functions R_1 and R_2 for an external and internal perturber, respectively, are expressed as,

$$R_1 = \frac{Gm_2}{a_2} R_d^{<sec>} = \frac{Gm_2}{a_1} \alpha_{12} R_d^{<sec>} \tag{8.10}$$

$$R_2 = \frac{Gm_1}{a_1} \alpha_{12} R_d^{<sec>} = \frac{Gm_1}{a_2} R_d^{<sec>} \tag{8.11}$$

where G is the universal gravitational constant, the subscripts $1, 2$ correspond to quantities that are associated with the perturber and perturbed body, respectively. Then, α_{12} is defined as the ratio a_2/a_1 and $R_d^{<sec>}$ is the averaged secular direct term of the disturbing function. In this analysis, the focus is the perturbation on the spacecraft that arises from the secondary,P_2, thus, the two relationships can be reduced to a single equation such that,

$$R_i = \frac{Gm_2}{a} \bar{\alpha} R_d^{<sec>}, i = 1, 2 \tag{8.12}$$

where $\bar{\alpha}$ is defined as,

$$\bar{\alpha} = \begin{cases} \alpha & \text{if } i = 1, \\ 1 & \text{if } i = 2. \end{cases} \tag{8.13}$$

and $\alpha = \alpha_{12}$ for clarity. To second order in inclination and eccentricities, the averaged direct term in the disturbing function, that is, the terms that correspond to secular effects, can be written as,

$$\begin{aligned} R_D^{<sec>} = \frac{1}{8}\alpha b_{3/2}^{(1)}\left(e^2 + e_2^2\right) - \frac{1}{2}\alpha b_{3/2}^{(1)}\left(s^2 + s_2^2\right) \\ -\frac{1}{4}\alpha b_{3/2}^{(2)} e e_2 \cos\left(\omega - \omega_2\right) + \alpha b_{3/2}^{(1)} s s_2 \cos\left(\Omega - \Omega_2\right) \end{aligned} \tag{8.14}$$

where $s = \sin\left(\frac{1}{2}i\right)$, and the subscript 2 now refers to the orbital elements that are associated with the secondary body, P_2. Then, the Laplace coefficient $b_s^{(j)}$ is defined as,

$$b_s^{(j)}(\alpha) = \frac{1}{2\pi}\int_0^{2\pi} \frac{\cos j\psi \mathrm{d}\psi}{\left(1 - 2\alpha\cos\psi + \alpha^2\right)^s} \tag{8.15}$$

Substituting Eqs. (8.14) and (8.15) into Eq. (8.12) provides an expression for the perturbing potential that arises from the existence of a secondary as a function of the classical orbital elements of the spacecraft.

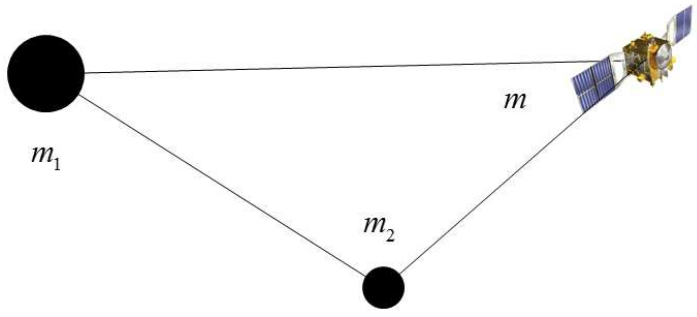

Figure 8.1. Problem geometry

8.1.4 Binary Effect

To construct the LPEs that correspond to the binary effect, the disturbing function, R_i, derived in Eq. (8.12) is employed as the perturbing potential, R. Then, the partial derivatives of R_i with respect to the classical set of orbital elements are required. However, the perturbing potential is averaged, hence, the LPE that is associated with the secular evolution of the true anomaly, σ is discarded. Consequently, the partial derivative of the perturbing potential with respect to the semi-major axis, a, is not required and the partial with respect to σ is set to equal to zero. Also recall that the disturbing function is expressed in terms of the variables s, s_2, rather than directly in terms of the inclinations i, i_2, where $s = \sin\left(\frac{1}{2}i\right)$. Thus, the following partial derivatives are required for the derivation,

$$\frac{\partial s}{\partial i} = \frac{1}{2}\cos\left(\frac{1}{2}i\right) \tag{8.16}$$

$$\frac{\partial s^2}{\partial i} = \cos\left(\frac{1}{2}i\right)\sin\left(\frac{1}{2}i\right) = \frac{1}{2}\sin i \tag{8.17}$$

The remaining partial derivatives are derived as,

$$\frac{\partial R_D^{<sec>}}{\partial e} = \frac{1}{4}\alpha b_{3/2}^{(1)} e_2 - \frac{1}{4}\alpha b_{3/2}^{(2)} e\cos\left(\omega - \omega_2\right) \tag{8.18}$$

$$\frac{\partial R_D^{<sec>}}{\partial i} = -\frac{1}{4}\alpha b_{3/2}^{(1)} i_2 + \frac{1}{2}\alpha b_{3/2}^{(1)} s_2\cos\left(\frac{1}{2}i\right)\cos\left(\Omega - \Omega_2\right) \tag{8.19}$$

$$\frac{\partial R_D^{<sec>}}{\partial \omega} = \frac{1}{4}\alpha b_{3/2}^{(2)} e e_2\sin\left(\omega - \omega_2\right) \tag{8.20}$$

$$\frac{\partial R_D^{<sec>}}{\partial \Omega} = -\alpha b_{3/2}^{(1)} s s_2\sin\left(\Omega - \Omega_2\right) \tag{8.21}$$

Assuming the orbit of the secondary with respect to the primary is planar and circular, i.e., $e_2 = i_2 = 0$, the partial derivatives reduce to,

$$\frac{\partial R_D^{<sec>}}{\partial e} = \frac{1}{4}\alpha b_{3/2}^{(1)} e \tag{8.22}$$

$$\frac{\partial R_D^{<sec>}}{\partial i} = -\frac{1}{4}\alpha b_{3/2}^{(1)} i \tag{8.23}$$

$$\frac{\partial R_D^{<sec>}}{\partial \omega} = 0 \tag{8.24}$$

$$\frac{\partial R_D^{<sec>}}{\partial \Omega} = 0 \tag{8.25}$$

Note that the inclination assumption can be made without loss of generality by defining the elements with respect to the binary orbit plane. Then, recall the definition of the perturbing potential for the perturbation of interest,

$$R = R_i = \frac{Gm_2}{a}\bar{\alpha} R_d^{<sec>}, i = 1, 2 \tag{8.26}$$

Thus, the partial derivatives with respect to the set of orbital elements, oe,

$$\frac{\partial R}{\partial oe} = \frac{Gm_2}{a}\bar{\alpha}\frac{\partial R_D^{<sec>}}{\partial oe} \tag{8.27}$$

and substituting $\frac{\partial R}{\partial oe}$ in the LPEs in Eq. 8.1,

$$\dot{a} = 0 \tag{8.28}$$

$$\dot{e} = 0 \tag{8.29}$$

$$\dot{i} = 0 \tag{8.30}$$

$$\dot{\omega} = \frac{\mu_2}{4na^3}\alpha\bar{\alpha} b_{3/2}^{(1)} \left\{ \sqrt{1-e^2} + \frac{\cos i}{\sqrt{1-e^2}} \right\} \tag{8.31}$$

$$\dot{\Omega} = \frac{-\mu_2}{4na^3}\alpha\bar{\alpha} b_{3/2}^{(1)} \frac{1}{\sqrt{1-e^2}} \tag{8.32}$$

Hence, define C_b the strength coefficient for the 'binary effect' as,

$$C_b = \frac{\mu_2}{4na^3}\alpha\bar{\alpha} b_{3/2}^{(1)} \tag{8.33}$$

where C_b is selected as the common factor in the two non-zero LPEs in Eqs. (8.28).

8.1.5 Eccentricity Terms

In the current expressions for the strength coefficients, note that there is no dependence on eccentricity. However, some commonality in terms of eccentricity exists in the LPEs that are associated with a given effect. [80, 84] Including the common eccentricity terms into the strength coefficients allows the derivation of an augmented set of coefficients that are now eccentricity dependent,

$$C_t' = \frac{\dot{N}^2}{n}\frac{1}{(1-e^2)^{1/2}} \tag{8.34}$$

$$C_g' = \frac{3gna^2}{2\mu_{pb}} \tag{8.35}$$

$$C_s' = \frac{3nJ_2\alpha_0^2}{2a^2}\frac{1}{(1-e^2)^{3/2}} \tag{8.36}$$

$$C_b' = \frac{\mu_2}{4na^3(1-e^2)^{1/2}}\alpha\bar{\alpha}b_{3/2}^{(1)} \tag{8.37}$$

Note that the SRP coefficient remains unchanged as the LPE that corresponds to the eccentricity evolution is non-zero. Thus, the eccentricity does not remain constant, on average, and it is not reasonable to include eccentricity in the strength coefficient. Such a coefficient only includes constant quantities, on average.

8.1.6 Binary Effect Initial Validation

The LPEs applied to the binary effect supply an approximation for the secular evolution of the orbital elements of a spacecraft orbit assuming the binary effect is the only perturbation considered. To assess the relevance of the binary effect strength coefficient, the prediction of the binary effect is initially validated using arbitrary initial conditions that are numerically propagated in the Circular Restricted Three-Body Problem. Then, consistent with the LPE derived in Eq. (8.28), the semi-major axis, eccentricity, and inclination are to remain constant, on average, while the argument of periapsis and the longitude of the right ascending node may vary linearly such that,

$$\omega(t) = C_b' \left(1 - e^2 + \cos i\right) t + \omega_0 \tag{8.38}$$

$$\Omega(t) = C_b' t + \Omega_0 \tag{8.39}$$

The initial conditions are numerically propagated for 10 revolutions and the corresponding paths, as computed both in the two-body problem and CR3BP, are illustrated in black and blue, respectively, in Figure 8.2. In the left and right plot, the paths are displayed as viewed in the inertial frame and synodic frame, respectively. The correspond osculating orbital elements for the 3BP trajectory are represented in Figure 8.3.

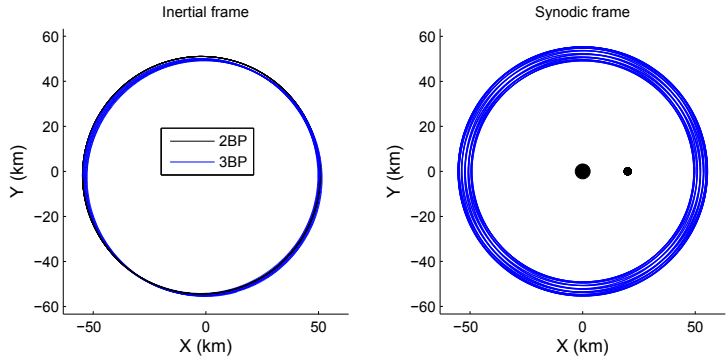

Figure 8.2. Conic orbit propagation with the 2BP and CR3BP.

While the two-body trajectory is a closed conic, one that retraces the same path over the revolutions, it is clear that the 3BP trajectory is no longer Keplerian, as a result of the presence of a secondary massive body. In the right plot, the same 3BP trajectory as viewed in the synodic frame further emphasizes the non-Keplerian nature of the path. Then, it is apparent from the osculating orbital elements representation that the semi-major axis, eccentricity, and inclination remain constant, on average, consistent with the LPE prediction. Also, the predictions for the secular variation of the two non-zero LPE, corresponding to the argument of periapsis and the longitude of the right ascending node, are overlaid on the corresponding figures in red. Clearly,

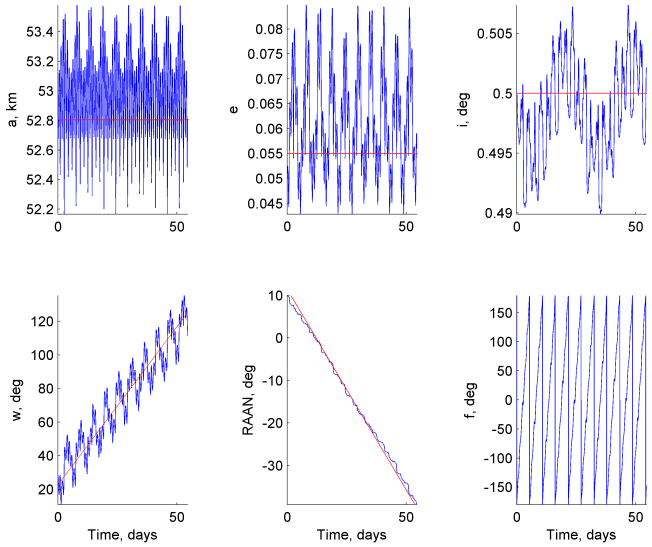

Figure 8.3. Orbital elements for CR3BP trajectory, red straight line is the LPE prediction.

the prediction captures the average secular evolution of the two orbital elements. This simple scenario provides an initial validation for the derived LPEs that correspond to the binary effect and, thus, also supplies some insight supporting the validity of the binary strength coefficient.

8.2 Zonal Maps

To compare the relative strength of several perturbing effects across the parameter space, 'zonal maps' are introduced, or, a two-dimensional representation similar to an exclusion plot [85]. A zonal map depicts the dominating perturbing effect as a function of the spacecraft orbit semi-major axis with respect to the primary, the eccentricity, and the mass ratio of the binary system, where the mass ratio is defined as the mass of the secondary to the total mass of the system. Note that these zones are also strongly dependent on the J_2 coefficient and β, the non-dimensional acceleration due to SRP, assuming a spherical spacecraft. For a sample binary system model, a

zonal map that is generated following the proposed strategy is illustrated in Figure 8.4 with $\beta = 5$, $J_2 \approx 0.057$, and $e = 0.05$. Colored in shades of blue, red, and green, the corresponding regions are dominated by the oblateness of the body, the binary effect, and the SRP, respectively. Note that the spacecraft semi-major axis is scaled by the primary separation distance; thus, a value of one corresponds to the location of the secondary. Also, filled contours labeled '10' and '100' correspond to regions where the dominating perturbation is stronger than any other effect in excess by the corresponding factor, labeled Maximum Strength Coefficient Ratio (MSCR).

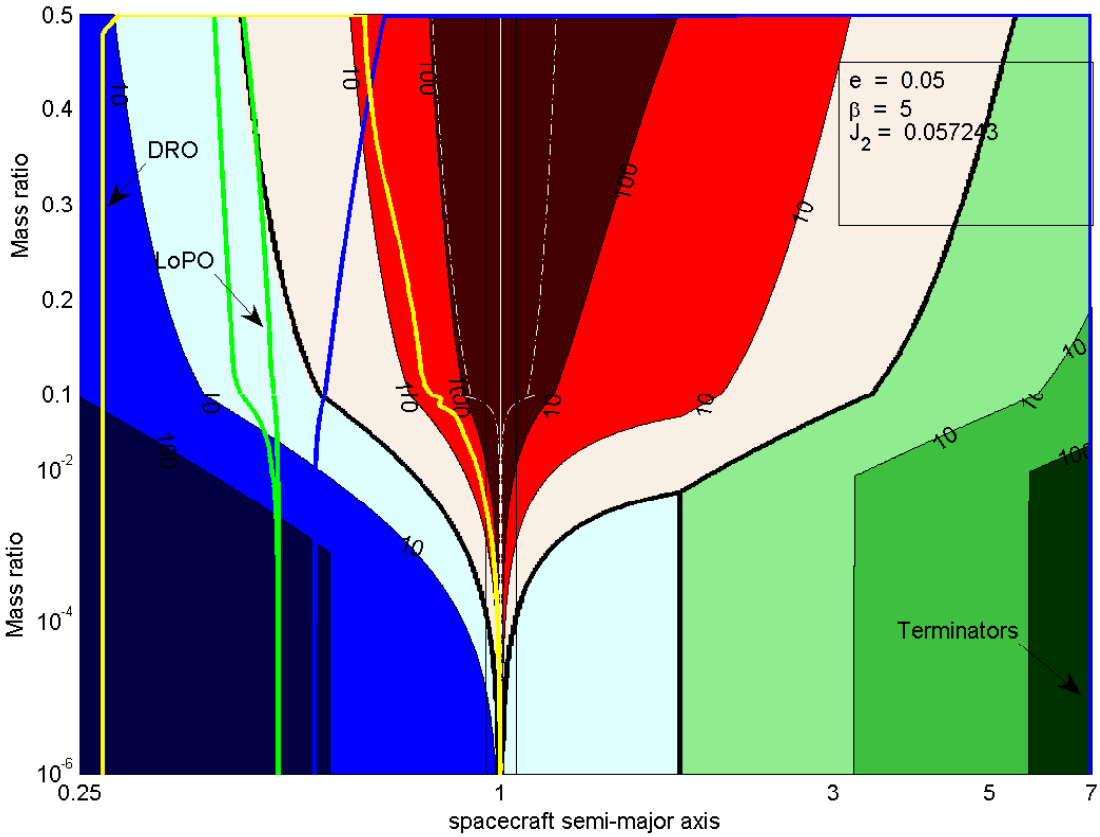

Figure 8.4. Zonal Map: semi-major axis against mass ratio. Blue: J_2 dominated, red: binary effect dominated, green: SRP dominated

In general, the binary effect dominates for values of the semi-major axis close to the secondary location. Also, as the mass ratio increases, that is, the mass of the secondary relative to the primary increases, the binary effect is stronger, as expected. Then, the primary oblateness perturbation dominates for the smallest semi-major axis values, and may also dominate over the binary effect for the smallest mass ratios. As semi-major axis values increase, the strongest perturbation is the SRP. Finally, while the perturbation from the solar tide is also incorporated into the analysis, this effect never dominates the other perturbations over the range of semi-major axes that are investigated.

The zonal maps are useful in determining the type of orbit that is practical to support a given mission scenario. For instance, for a scenario that involves close spacecraft proximity to either body, three-body trajectories are relevant, e.g., Distant Retrograde Orbits (DRO), Low Prograde Orbits (LoPO), and Halo orbits. [86] However, for a scenario such that the spacecraft orbit evolves further away from the primary system, trajectories that are driven by SRP are most useful, e.g., terminator orbits. [87] Within that context, information regarding sample types of periodic orbits is overlaid on the zonal map. For terminators, the range for the mean semi-major axis with respect to P_1 for the terminator family that corresponds to the β value in the map is represented by the blue line. For the P_1 centered LoPO and DRO families, since these orbits are constructed in a three-body model, the closest approach with respect to P_1 is employed as a proxy for the semi-major axis and reported on the zonal map with the green and yellow lines.

The zonal maps can incorporate other axes as well. In Figure 8.5(a), a similar map is illustrated in terms of spacecraft semi-major axis against eccentricity for a mass ratio equal to 0.05. Finally, a map depicting the same zones now in terms of spacecraft eccentricity against mass ratio appears in Figure 8.5(b) for $a = 2.5$. Depending on the type of spacecraft orbits or motion that is relevant to a particular analysis, the set of axes most suited to yield insight for the trajectory design process may vary.

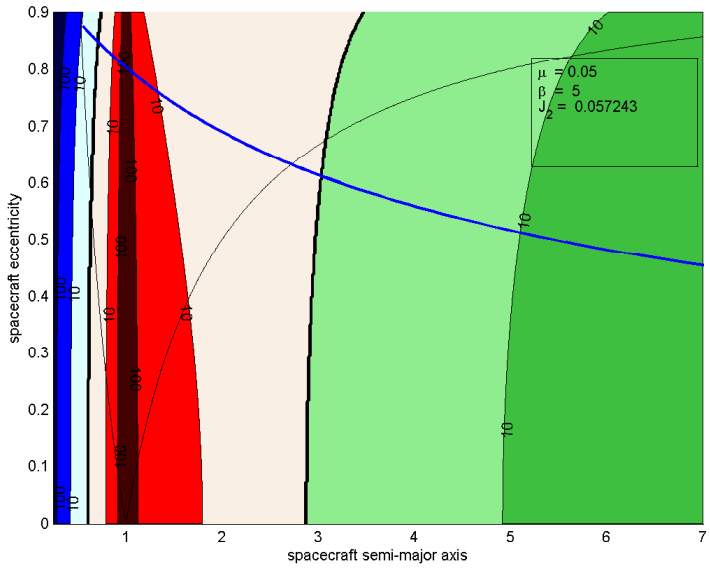

(a) Zonal map: semi-major axis against eccentricity

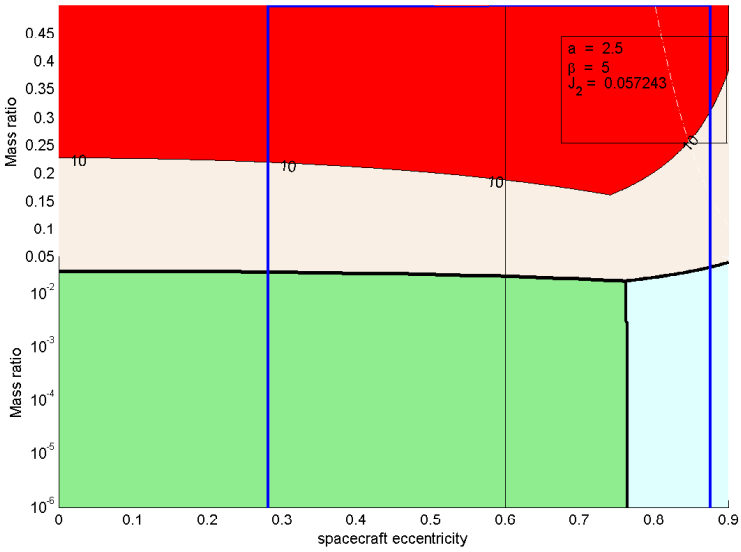

(b) Zonal map: eccentricity against mass ratio

Figure 8.5. Zonal maps including eccentricity information. Blue: J_2 dominated, red: binary effect dominated, green: SRP dominated

8.3 Application to Periodic Orbit Stability

The validity of the zonal map is further assessed through the numerical integration of initial conditions that correspond to pre-computed periodic orbits with a higher-fidelity dynamical model. The higher-fidelity model incorporates the various perturbing effects and the stability of periodic orbits that are initially computed in a simplified dynamical model is explored. Different types of families are considered: families that are constructed exploiting the three-body regime as well as orbits that rely on SRP, i.e. terminator orbits.

8.3.1 Periodic Orbits of Interest

To explore the dynamical behavior of a third body within the vicinity of two primaries, periodic orbits are of special interest. A multi-phase technique based on differential corrections is employed to compute a trajectory that is periodic in the nonlinear regime given some initial guess. A trajectory is labeled periodic if the discontinuity between the initial and final six-dimensional states along the path does not exceed a prescribed tolerance, typically 10^{-11} nondimensional units.

Libration Point periodic Orbits. (LPO)

Many families of periodic orbits within the three-body regime are associated with the equilibrium points and, thus, are labeled libration point orbits. In particular, L_1 and L_2 halo orbits are examples of families that possess a geometry that is especially interesting to observe one of the primaries and also feature some stable members, as illustrated in Figure 8.6 for a mass ratio equal to 0.1. The individual trajectories are colored in blue and red for stable and unstable orbits, respectively.

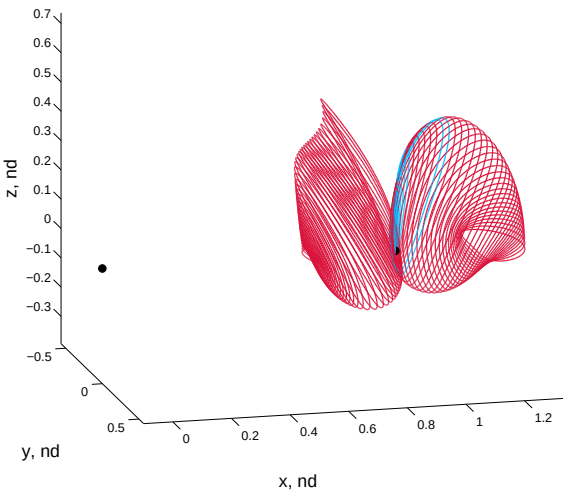

Figure 8.6. L_1 and L_2 halo families: mass ratio $\mu = 0.1$

Terminator Orbits

Terminator orbits are one of the few types of ballistic orbits known to exhibit stable and robust motion in the presence of strong solar radiation pressure. [80] Also, the robust stability characteristics of terminator orbits extend to long-term stable motion in the presence of an irregular gravitational field. [87] In scenarios such that stable orbital dynamics are desired, such properties suggest terminator orbits as ideal candidates for orbiting a small irregular body. Terminator orbits are oriented such that the orbital plane is approximately normal to the SRP acceleration through any time evolution, that is, the angular momentum vector for terminator orbits is parallel to the direction of the Sun. In this analysis, the robustness of such orbits is assessed by including a secondary massive body in the primary system. Terminator orbits are initially computed in the Augmented Hill Three-Body Problem and parameterized by the SRP nondimensional acceleration coefficient, β. [88] In Figure 8.7 are illustrated two families of such terminator orbits for β values equal to 1000 and 1; the larger the β value, the stronger the SRP acceleration relative to gravitational forces. The members in each family are repented in blue and red for stable and unstable orbits, respectively.

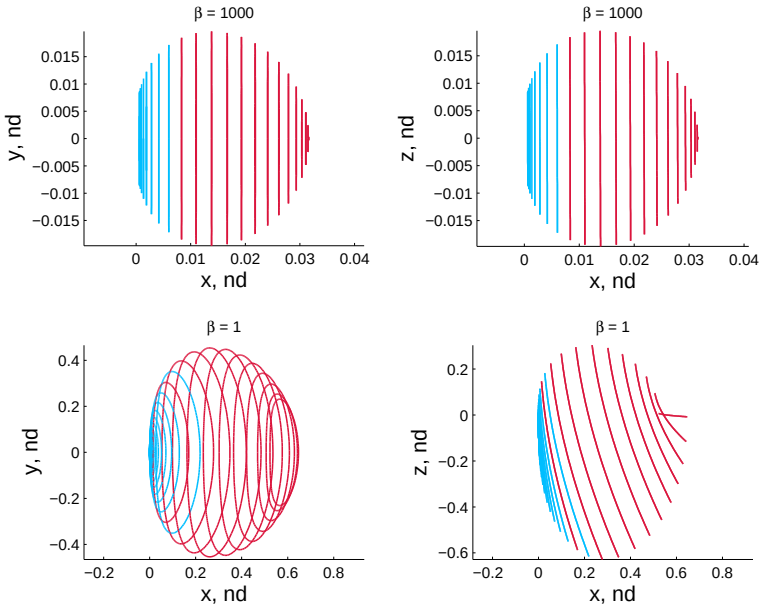

Figure 8.7. Terminator families for $\beta = 1000$ (top) and $\beta = 1$ (bottom).

Low Prograde Orbits (LoPO) and Distant Retrograde Orbits (DRO)

Periodic orbits labeled Distant Retrograde Orbits (DRO) and Low Prograde Orbits (LoPO) are also of special interest as these families feature numerous stable orbits. A sample family for a mass ratio equal to 0.2 is illustrated in Figure 8.8 where the individual trajectories are colored in blue and red for stable and unstable orbits, respectively. It is, then, clear that the DRO family features numerous stable orbits. Planar LoPOs are also centered at one primary, P_1 or P_2. Exploiting bifurcations within the planar families, and employing a continuation technique, a three-dimensional family that branches from the planar family is also computed, as illustrated in Figure 8.9 for a sample system with a mass ratio equal to 0.2. As clearly apparent in the figure, the orbits in the three-dimensional families allow regular close-range proximity of a third-body with respect to either primary. In addition, the three-dimensional aspect of the trajectories offers extensive coverage of the surface of the attractive primary.

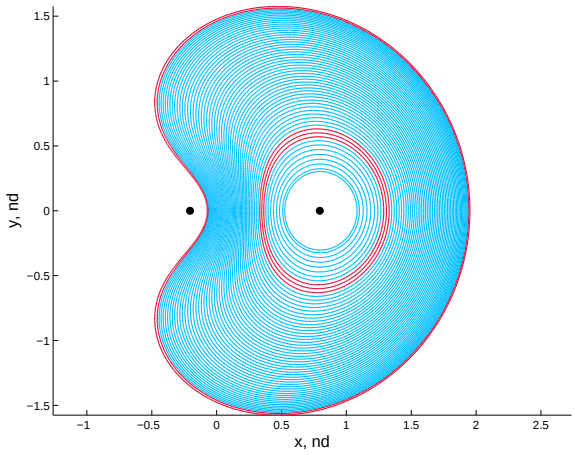

Figure 8.8. DRO family: mass ratio $\mu = 0.2$

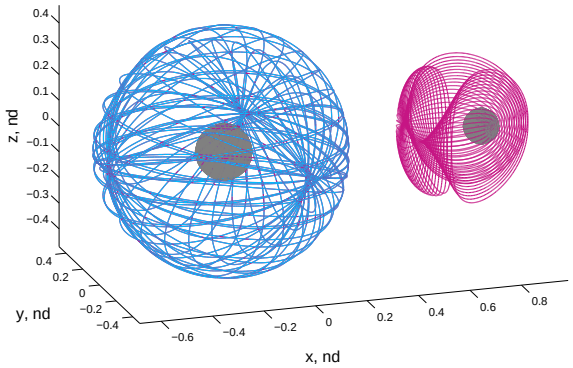

Figure 8.9. P_1 and P_2 centered 3D LoPO families: mass ratio $\mu = 0.2$

8.3.2 Application to Sample Orbits

Binary effect regime: L_2 halo orbit

The existence of halo orbits relies on the presence of a secondary massive body in the primary system, thus, such orbits are characteristic of a binary effect dominated regime. Although some stable orbits exist for most mass ratios, these orbits are only 'weakly stable'. Consider a sample stable L_2 halo orbit for a mass ratio approximately equal to 0.0034. First, the initial conditions that are associated with this orbit are

propagated in a higher-fidelity model that includes the solar tide (CR4BP) and an oblate P_2. The resulting trajectory is plotted in Figure 8.10(a) and appears to remain bounded and stable for 10 revolutions. However, repeating the same simulation, now also including the SRP (ACR4BP), the trajectory only remains bounded for 3 revolutions before escaping the vicinity of P_2, even though the MSCR (ratio of the dominating perturbation strength coefficient to the second stronger) is approximately equal to 20. While defined as linearly stable, halo orbits, in general, are quite sensitive to pertubations and may not be ideal candidates for long-term stable ballistic motion.

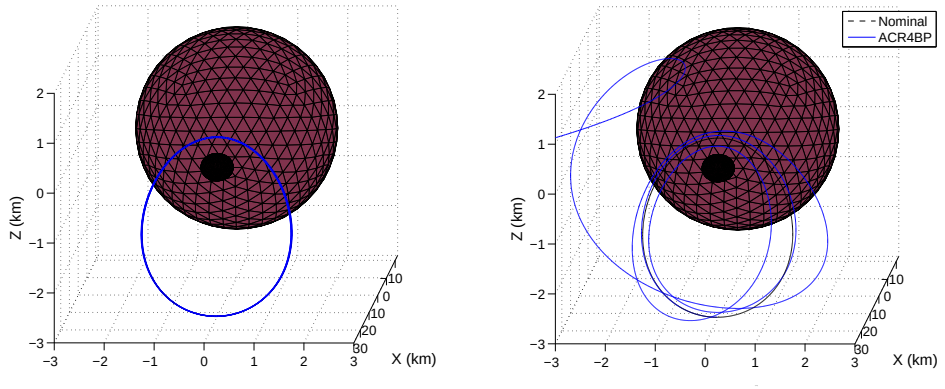

(a) CR4BP with oblate secondary (b) ACR4BP with oblate secondary

Figure 8.10. Sample stable L_2 halo orbit propagated in higher-fidelity dynamical model: mass ratio $\mu = 0.0034$

Binary effect regime: DRO

The DROs are another example of an orbit that only exists when the primary system is comprised of two massive bodies. However, in contrast to halo orbits, numerous stable and robust orbits for all mass ratios exist. To demonstrate these properties, a sample DRO for a mass ratio equal to 0.4 and a closest P_1 approach corresponding to a binary effect dominated regime with a MSCR approximately equal to 25 is numerically propagated in the ACR4BP. In this scenario, The higher-fidelity

model now includes the SRP acceleration, irregular shape models for the primaries, and the solar tide. Further, to also assess the out-of-plane stability of such an orbit, a initial out-of-plane velocity perturbation is introduced. The resulting trajectory is illustrated in Figure 8.11 and, while the path appears to be disturbed by the various perturbing effects introduced, the trajectory remains bounded and in the vicinity of the nominal DRO for 10 revolutions.

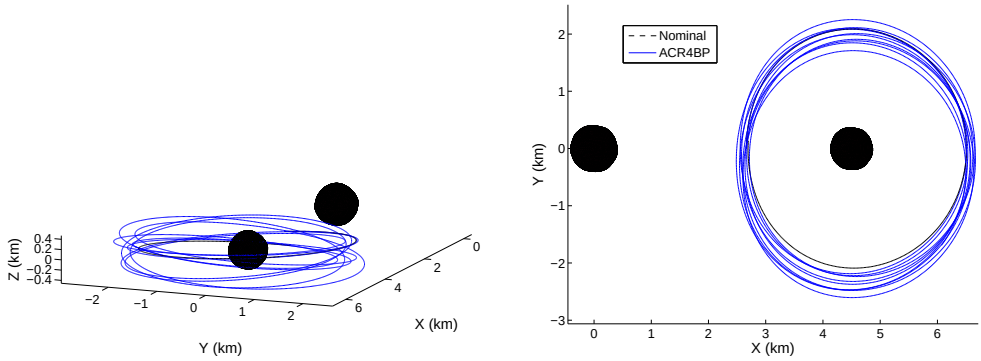

(a) 3D view (b) (x, y) projection

Figure 8.11. Sample stable DRO propagated in the RC4BP: mass ratio $\mu = 0.4$

SRP regime: terminator orbit

Terminator orbits are constructed assuming that the spacecraft is orbiting a single body in the presence of strong SRP. A sample stable terminator orbit with an initial semi-major axis approximately equal to 6 nondimensional units is selected to be propagated in the ACR4BP for a system with a mass ratio equal to 0.0162. On the zonal map, such initial conditions correspond to a SRP dominated region with a MSCR approximately equal to 70. The initial and perturbed trajectories appear in Figure 8.12(a) in black and blue, respectively. The perturbation from the irregular shape of the bodies and the existence of a secondary massive body are evident, however, the resulting trajectory retains characteristics similar to the originating terminator

orbit, in particular, the orientation of the orbital plane. Also, the trajectory remains bounded for the duration of the simulation, that is, 10 revolutions of the initial orbit. Then, a similar simulation is completed for a stable terminator orbit with a smaller semi-major axis value, $a = 3.3$, and a binary system with mass ratio increased to 0.196. These initial conditions now correspond to a binary effect dominated regime with a MSCR approximately equal to 5, and as expected, the perturbed trajectory is rapidly disrupted, as evident in Figure 8.12(b).

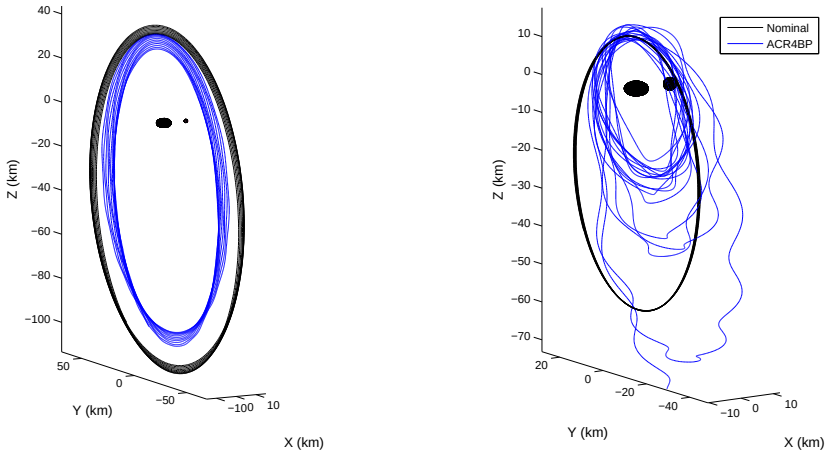

(a) mass ratio $\mu = 0.0162$, $a = 6$ (b) mass ratio $\mu = 0.196$, $a = 3.3$

Figure 8.12. Sample stable terminator orbits with $\beta = 5$ propagated in the ACR4BP

Binary effect regime: P_1 LoPO

Although the low-prograde P_1-centered family is constructed in a three-body model, the low altitude of these trajectories with respect to P_1 place this family in the J_2 dominated regime on a zonal map. To assess the stability of such orbits, a sample stable orbit for mass ratio equal to 0.15 and with a MSCR approximately equal to 3 is propagated in the ACR4BP with an oblate irregular shape model for P_1. Recall that the dynamical model also includes the SRP and solar tide. The perturbed

trajectory, propagated for 10 revolutions, is illustrated in Figure 8.13(a), and appears bounded in the vicinity of the initial trajectory. Further, the apparent precession of the blue perturbed orbit relative to the initial black orbit reflects the J_2 perturbation, however, the trajectory appears stable over the duration of the simulation. The same simulation is repeated for a significantly increased value of the SRP acceleration, from $\beta = 5$ to $\beta = 100$, and the corresponding perturbed trajectory is displayed in Figure 8.13(b). The inflated SRP force contributed to a more chaotic trajectory and the behavior of the spacecraft for longer-term propagation is unpredictable. Although this particular simulation results in a bounded orbit, slightly different initial conditions may yield undesired outcomes, such as an impact on the primary, given the large variation from the nominal trajectory.

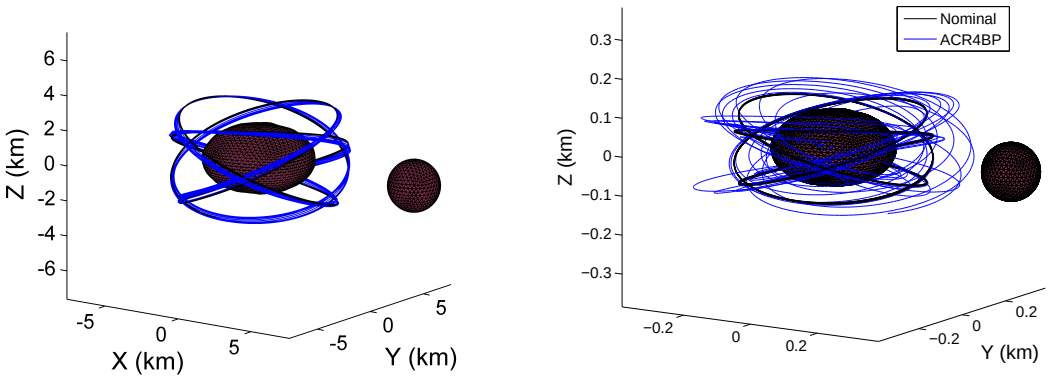

(a) $\beta = 5$ (b) $\beta = 100$

Figure 8.13. Sample stable P_1 LoPO propagated in the ACR4BP

8.4 Remarks

In an initial assessment of the perturbing effects that dominate the dynamics of a spacecraft in the vicinity of small irregular bodies, zonal maps are introduced. Such maps depict the dominating perturbations as a function of the orbit choice. Based on

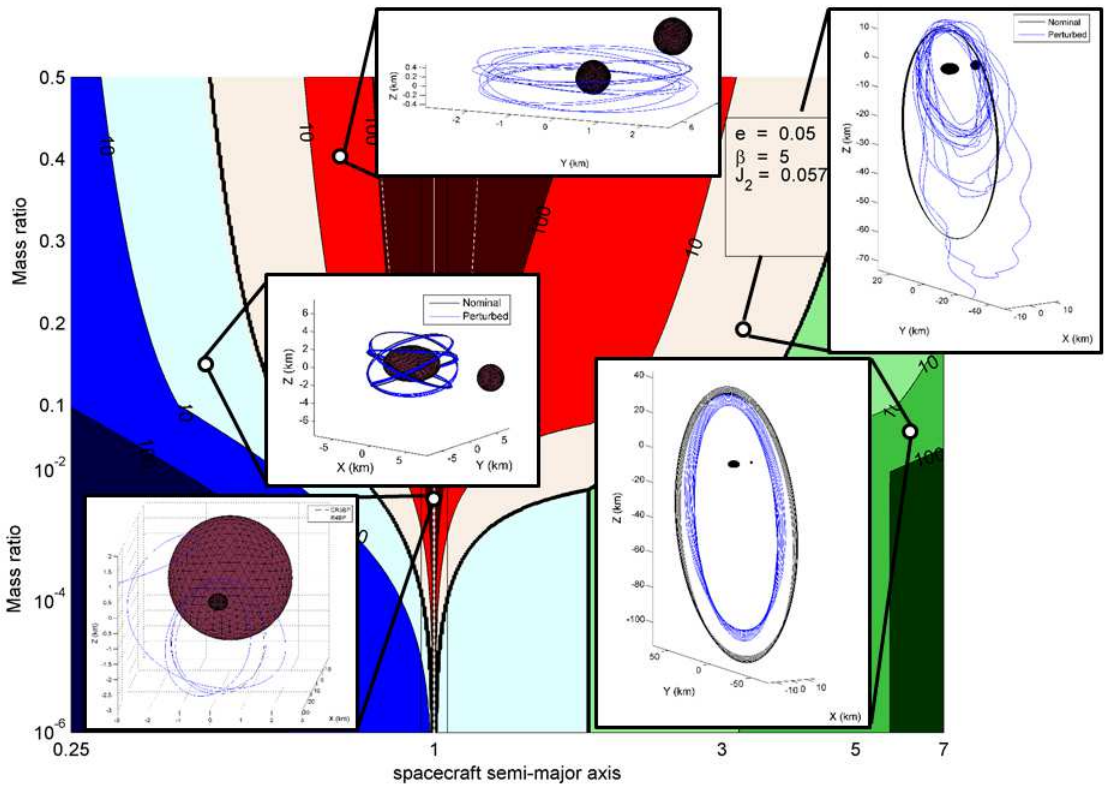

Figure 8.14. Summary of zonal map and sample trajectories

previous developments, classical perturbing effects are included, solar tide, SRP, and body oblateness. The analysis is extended to the binary effect, that is, the perturbation that arises from the existence of a binary system that includes a secondary body rather than a single body. The zonal maps are constructed from strength coefficients for the perturbations of interest, where these coefficients are derived exploiting LPEs. In addition, the binary effect strength coefficient leverages the third-body disturbing function. These mathematical tools rely on various assumptions and require validation. The strength coefficient for the additional perturbation, the binary effect, is initially validated by comparing the LPE predictions with the numerical propagation of sample initial conditions. Then, the zonal maps are useful in selecting a type of

orbit that is predicted to yield a stable ballistic motion under perturbations. Sample orbit types are considered as an initial application, including halos, terminators, DROs, and LoPOs, as summarized in Figure 8.14. Such an analysis may also aid in identifying which force ratios yield stable orbits for a given type. Future work involves further examination of the ballistic stability of sample types of orbits as a function of the ratio of the dominating strength coefficient to other perturbations.

9. BURIED SMALL SCALE FEATURES DETECTION WITH GRAIL DATA

9.1 Overview

The twin Gravity Recovery and Interior Laboratory (GRAIL) spacecraft, named GRAIL-A and GRAIL-B, also known as Ebb and Flow, were launched in September 2011 as a Discovery-class NASA mission to study the gravitational field of the Moon. [89] After a cruise of several months, each spacecraft was inserted into their respective lunar orbit. Building on the success of the GRACE (Gravity Recovery and Climate Experiment) mission, a twin-satellite Earth orbiter mapping the gravity field of Earth since 2002 [90], extremely accurate range-rate measurements between the two spacecraft in the Ka-band wavelength (KBRR) enable the derivation of the Moon's gravity field with unprecedented resolution and accuracy. The GRAIL data were collected during two science phases, the nominal and extended mission. During the nominal mission, from March to May 2012, the spacecraft altitude was, on average, 55 km above the surface enabling the determination of an initial lunar gravity field model in terms of a spherical harmonic expansion up to degree and order 420. [91] Initiated in August 2012, additional data were collected until mid-December 2012 during the extended mission with a spacecraft altitude of 23 km on average, allowing the refinement of the gravity model to produce, currently, spherical harmonic solutions up to degree and order 900. [92,93] Also note that the data are recorded every 0.1 second, but are released at intervals of 2 or 5 seconds for an average altitude of approximately 55 or 23 km for the nominal and extended mission, respectively, while the spacecraft orbital velocities are approximately 1.25 km/sec. Also, the maximum offset between adjacent tracks is only at most a few fractions of a degree at the equator. The low altitude at which some of these data were collected in the GRAIL

extended mission, with spacecraft altitude as low as a few kilometers over the lunar surface, potentially allows the detection of small-scale surface or subsurface features.

The focus of this investigation is the detection and extent of empty lava tubes beneath the mare surface. In addition to their importance for understanding the emplacement of the mare flood basalts, open lava tubes are of interest as possible habitation sites safe from cosmic radiation and micrometeorite impacts. [37] The possible or potential existence of such natural caverns is supported by Kaguya's recent discoveries of deep pits in the lunar mare. [38,94] Because the features of interest are beneath the lunar surface, traditional methods, such as surface imagery and altimetry, do not allow for the detection of such features. In contrast, since gravity is sensitive to both surface and subsurface features, gravity-like quantities can, in theory, be leveraged to probe the interior of the Moon. Thus, exploiting the gravity data collected by the GRAIL spacecraft, small buried features may be detectable. In this investigation, tools are developed to best exploit the rich gravity data toward the numerical detection of these small features. Two independent strategies are considered: one based on gradiometry techniques, that is, a method that exploits gravity gradients, and a second that relies on cross-correlation of individual data tracks. Techniques that exploit gravity gradients are also employed on Earth to detect subsurface cavities [34], changes in the crustal structure [35], and even faulting events. [36] However, one key advantage to Earth-based analyses is the possibility for in-situ gravity surveys. For the lunar problem, both proposed strategies rely critically upon the unprecedented resolution and accuracy of the gravity data.

In this analysis, both detection approaches, that is, the gradiometry technique and the strategy that relies on cross-correlation, are combined into an automated algorithm that aims to construct local maps of the lunar surface and highlight the possible detection of features of interest. In addition, forward modeling is leveraged to further support possible detections and to attempt to characterize the physical parameters of a feature. The proposed algorithm is first validated using Schroeter Vallis, the largest known lunar sinuous rille, as a test feature. Then, another region

near a South channel of Rima Sharp is introduced, where a persistent anomaly consistent with an underground mass deficit is identified. Finally, in an initial step toward inspecting the entire mare emplacements on the Moon, a global search strategy is introduced.

9.2 Lava Tube, Sinuous Rilles, and Skylights

9.2.1 Definition and Formation

Sinuous rilles have been extensively studied over the last several decades, starting with the Apollo missions, yet although a general formation mechanism is accepted, the details of the formation of such structures are not fully understood. [95, 96] Sinuous rilles (SR) are usually characterized by sinuous channels of varying widths and depths with continuous walls. Often, these structures are associated with the presence of depressions of various morphologies that are interpreted as potential source vents for the lava flow that initially formed the channel. A rille typically terminates in a mare region, either abruptly as it intersects with a different mare unit, or by gradually fading into the mare. Most SRs are observed on the lunar near side in mare emplacements rather then on the far side or in the highlands. With the current understanding of the lunar environment and the surface geology, SRs are thought to be formed through lava flow and erosion processes, either in subsurface lava tubes that eventually collapsed or in surface lava channels. These features are numerous on the lunar surface and exhibit a wide variety in their morphology, including width, depth, length, and sinuosity. Although these features appear mostly in maria regions, the overall direction of the rille, if any, varies. In this analysis, the focus is directed toward the detection of potential empty subsurface channels, or lava tubes. However, because of the large number and the detailed information available for sinuous rilles, these structures represent relevant objects to test and validate the tools developed in this analysis. Also, SRs are most likely larger in dimension than potential lava tubes, hence, these features can be used to assess the limitations of the detection algorithm.

The formation of lava tubes is often associated with the formation mechanism of SRs. In essence, as an active lava flow, with sufficiently low viscosity, progresses along the lunar surface, a solid crust develops and thickens to form a roof due to radiating cooling driven by the high temperature gradient between the lava and the vaccuum. As the lava continues to flow in the now closed channel, it eventually leaves an empty subsurface tube with a hardened roof. Indication of the existence of such features is provided by the latest lunar missions. In particular, features labeled as 'skylights', that is, vertical holes that exhibit characteristics that cannot be explained as impact craters, are thought to be openings into empty subsurface lava tubes. [38, 94] Such lava tubes are also found on Earth, although in much smaller sizes than the expected lunar features, as Earth gravity is much stronger. Sample structures of interest are illustrated in Figure 9.1 with characteristics provided in Table 9.1. In addition to the feature type and its location in the Moon-fixed Principal Axis (PA) frame in terms of longitude (λ) and latitude (ϕ), estimated dimensions are also given. The field 'main dimension' corresponds to the estimated length for a rille and the estimated diameter for a skylight.

Table 9.1. Some features of interest

	type	λ, deg	ϕ, deg	main dimension	depth	width
Schroeter Vallis	Rille	301.7	24.5	175 km	534 m	4.27 km
Marius Hills Skylight	Skylight	303.230	14.091	$\simeq$ 50 m	$\simeq$ 50 m	N/A
Rima Sharp Channel	Rille	313.6	36.7	483 km	71 m	.84 km

9.2.2 Application to Human Exploration

Empty lava tubes are also interesting as possible habitation sites for human exploration endeavors, where the objective may be the establishment of a permanent

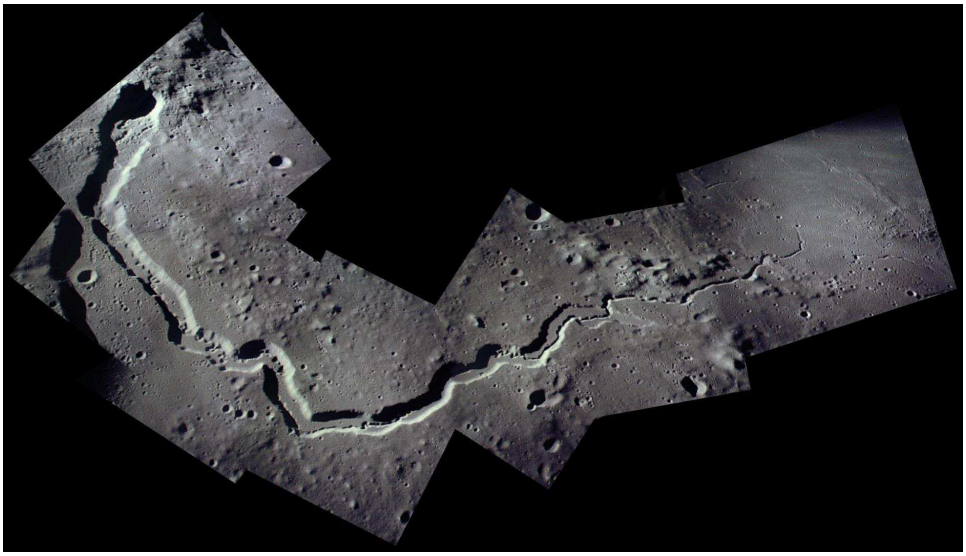

(a) Schroeter Vallis captured from orbit during Apollo 15 mission

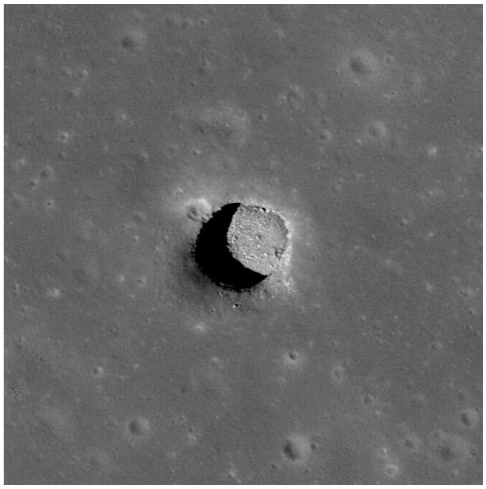

(b) Marius Hills pit near-nadir (0.5^o emission angle)image(M122584310L)

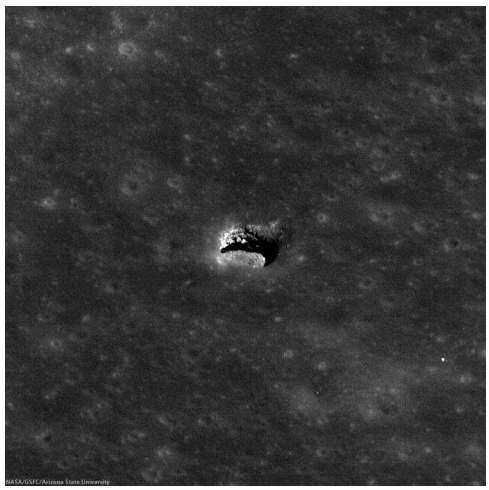

(c) M137929856R(34^o incidence angle and 45^o emission angle)

Figure 9.1. Schroeter Vallis and Marius Hills pit

base for lunar exploration or an outpost to support manned exploration beyond the Earth-Moon system. Such natural structures have been suggested as locations that are potentially safe from various hazards that are associated with the lunar environment, including cosmic radiation, micrometeorite impacts, and impact crater ejecta. Further, such sites would also provide a naturally regulated environment, with, in particular, a nearly constant temperature, in contrast to lunar surface conditions. [37] If such features exist in a preserved state, that is, empty channels - not collapsed - just beneath the lunar surface, these structure are not detectable through classical methods.

9.3 Detection Strategies and Validation Tools

9.3.1 Gravity Modeling

Extremely accurate range-rate measurements between the two GRAIL spacecraft in the Ka-band wavelength (KBRR) enable the derivation of the lunar gravity field with unprecedented resolution and accuracy. During the nominal mission, the spacecraft altitude was, on average, 55 km above the surface enabling the determination of an initial lunar gravity field model in terms of a Spherical Harmonic (SH) expansion up to degree and order 420. [91] Additional data were collected during the extended mission with a spacecraft altitude of 23 km, on average, that allowed the refinement of the gravity model to produce, currently, spherical harmonic solutions up to degree and order 900. [92, 93].

Free-air and Bouguer potential and gravity

The gravity models produced from the data that are collected by the GRAIL spacecraft correspond to 'free-air' gravity, that is, the gravitational potential or force that is exerted by the Moon onto any particle of interest. In this analysis, the objective is to assess the existence of buried empty lava tubes. Within this context,

'Bouguer' gravity is also useful. Bouguer gravity is equivalent to the free-air gravity where the gravitational contribution from the surface topography has been subtracted, assuming topographical information is available. For the Moon, the topography is well-known given that one of the instruments on-board the Lunar Reconnaissance Orbiter (LRO), i.e., the Lunar Orbiter Laser Altimeter (LOLA), provides a precise global lunar topographic model. [97] Note that the 'standard', or crustal average, density assumed for the topography is derived from GRAIL data and assumed equal to 2560 kg/m^3. This value is probably not equal to the actual density of the lava; in samples the density ranges between approximately 3090 and 3170 kg/m^3 [98] In essence, both surface and subsurface features can be observed in free-air gravity. Yet, some surface features may mask dimmer underground gravity anomalies. Assuming that the topography for a region of interest is well-known, Bouguer gravity only represents subsurface gravitational features and such a product may be more suited than direct free-air gravity, depending on the objective.

Truncation and taper

The SH model contains gravity information across the entire spectrum of frequencies, or wavelengths: from the lowest degrees that correspond to the tidal deformation of the Moon to the maximum degree of the expansion that depicts the subtle changes in density or topography of the Moon. To restrict the analysis to a domain that includes some features of interest, the SH expansion can be truncated on the low-end (low degree and order) to suppress the longer wavelength signals that correspond to the largest features (basins, tides,...) and on the high-end where the SH may not be representative of the actual data because of numerical artifacts. However, simple direct truncation of undesired degrees and order can result in a numerical challenge when evaluating the SH solution, an issue denoted as 'ringing'. To alleviate this effect, cosine tapers are applied where the field is truncated.

Gravitational potential and acceleration computation

The gravitational potential and the acceleration for the entire Moon are computed in this analysis using the high degree and order gravity models derived from GRAIL data. The evaluation of such SH series can be computationally expensive and also numerically challenging. Numerical errors in the computation of the Legendre polynomials for high degree and order computations generally cause concern. Thus, the spherical harmonic analyses are performed using the freely available software archive SHTOOLS (shtools.ipgp.fr) that is specifically developed to complete such tasks efficiently and accurately.

9.3.2 Gradiometry

The first strategy to investigate the existence of lava tubes relies on the numerical inspection of the lunar gravitational potential, computed from a set of spherical harmonics that is truncated and tapered to some predetermined degree and order to magnify the short wavelength structures of interest. From any scalar field, a widely employed method to detect or highlight ridges or valleys within the field of interest involves the computation of the Hessian, and consequently, the eigenvalues and eigenvectors that are associated with the Hessian of the scalar field. The Hessian of the gravitation potential is defined as the matrix of second partial derivatives of the potential function with respect to the spherical coordinates of the position vector, i.e.,

$$H_{ij} = \frac{\partial^2 U}{\partial x_i \partial x_j} \tag{9.1}$$

where $x_i, x_j = (\lambda, \phi, r)$, and r denotes the radial distance. In essence, the eigenvalue of largest magnitude and the corresponding eigenvector are associated with the direction of maximum gradient in the field. In this investigation, similar to the development in Andrews-Hanna et al. [99], eigenvalue maps that depict the magnitude of the largest magnitude eigenvalue for each point on a grid of the lunar surface are produced.

Either the free-air potential or the Bouguer potential (corrected for topography and terrain) can be employed in the analysis, depending on the objective. For the purpose of this investigation, localized maps that focus on specific regions are most relevant. Note that a sinuous rille or an empty lava tube corresponds to a negative gravity anomaly that reflects the relative mass deficit associated with the feature. Such a negative anomaly corresponds to a positive eigenvalue on the gradiometry map, or eigenvalue map, as a consequence of the additional derivative of the potential function in the computation of the Hessian.

9.3.3 Cross-Correlation

Method

A second strategy to explore the gravity data for evidence of lava tubes relies on directly exploiting the track data, that is, the relative acceleration of the two spacecraft as they move on their respective orbits. Only the horizontal component of the relative acceleration is directly available from the measurements, in contrast to the radial (i.e., vertical) or lateral components. In an initial effort to develop such a technique, proxy track data are created from available spherical harmonic models. The horizontal gravitational acceleration is computed along fictitious North-South tracks from the spherical harmonics. Then, track data are subdivided into individual tracks that correspond to a longitude value and a range of latitudes. Also, to exploit the assumed linearity of the lava tube, several tracks for a set of neighboring discrete longitudes are included within the same computation. The objective is then to identify the specific signature of a feature of interest within the generated track data. This task is accomplished by comparing the track data with a reference signal that represents the lava tube or sinuous rille through an analysis based on cross-correlations.

Reference signal

For a cross-correlation analysis, a reference signal, that is, a mathematical representation of the gravity anomaly due to the feature to be detected, is first constructed. Simple analytical expressions describe the acceleration anomaly experienced by a spacecraft along a flight path that is perpendicular to an infinitely long lava tube just beneath the surface; the tube is idealized as an empty horizontal cylinder. The horizontal acceleration component is calculated as,

$$g_{ref} = \frac{2Gm}{\sqrt{x^2 + h^2}} \sin\theta \tag{9.2}$$

where x is the along track distance from the feature, h is the spacecraft altitude, and $\theta = \arctan(x/h)$. Then, $m = \pi R^2 \rho$ is the mass deficit associated with the tube of radius R, ρ denotes the density of the surrounding terrain, assumed constant, and G is the gravitational constant. These relations are employed to construct a reference signal for the structures that are to be detected, that is, sinuous rilles or lava tubes. In Figure 9.2 is illustrated the horizontal acceleration sensed by the GRAIL spacecraft assuming an empty cylinder of diameter 1 km, given a flight altitude of 50 km (the average altitude for the nominal mission) as well as a distance of 20 km (the corresponding average altitude for the extended mission). Note the characteristic shape of the signal with an amplitude of some fraction of a milligal, where 1 mgal equals $10^{-5} m/s^2$. The magnitude of this signal is well within the level of resolution and sensitivity supplied by the GRAIL data.

Cross-correlation

Assuming a reference signal for the structures of interest is available, a mathematical construct is employed in the form of the cross-correlation between the reference signal and the spacecraft acceleration signal to assess the existence of such a feature within the data. In this implementation, the cross-correlation acts as a matching filter and the output of this comparison, the Cross-correlation Coefficient (CC), depicts the

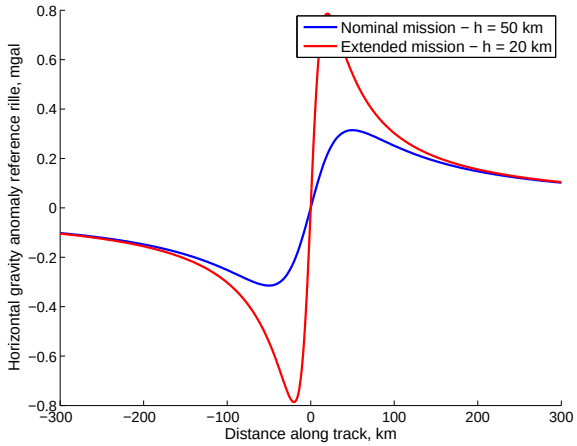

Figure 9.2. Analytical horizontal gravity anomaly.

similarity of the reference signal relative to the track data. The cross-correlation also operates as a convolution operation, that is, the reference signal sweeps through the track, then, the CC assesses the similarity of the two profiles for each relative position of the two signals. Hence, a large positive cross-correlation coefficient indicates a location along that track where the spacecraft acceleration profile closely resembles the reference signal. Ideally, if a signature similar to the reference signal is present in the track data, a peak in the cross-correlation of amplitude larger than the background CC profile should be observed. However, recall that the reference signal used in this analysis is only an approximation of the actual gravity anomaly for a sinuous rille or a lava tube. The cross-correlation is defined as,

$$R_{xy}(m) = E\left\{x_{n+m}y_n^*\right\} = E\left\{x_n y_{n-m}^*\right\} \tag{9.3}$$

where $-\inf < n, m < \inf$, the operator E is the expected value, x and y refer to the track and reference signals, respectively. However, as the signal is, in fact, finite, the cross-correlation sequence is estimated as,

$$\hat{R}_{xy}(m) = \begin{cases} \sum_{n=0}^{N-m-1} x_{n+m}y^* & \text{if } m \geq 0, \\ \hat{R}_{xy}(m) = \hat{R}_{y^*x}(-m) & \text{if } m < 0, \end{cases} \tag{9.4}$$

where N is the larger number of elements between x and y, and $m = 1, 2..., 2N - 1$. The CC is then defined as $CC = \hat{R}_{xy}(m-N)$ and is computed for any given track and scaled to values between -1 and 1. Also note that negative values of CC correspond to anti-correlation between the reference signal and track data, that is, the track data resemble the inverse of the reference signal.

Visualization

To address the challenge posed by the size of the features to be detected with respect to the gravity model resolution, the assumed linearity of shape of the lava tube is exploited. Several tracks from a set of neighboring but discrete longitudes are included in the same simulation. Then, rather than inspecting the raw CC for each individual track, the CC is employed as a scalar field and mapped onto the corresponding tracks to produce a two-dimensional cylindrical map, similar to the gradiometry approach. Since the cross-correlation analysis is performed on a set of discrete neighboring tracks, the CC computed for each track is used to interpolate a smooth CC field over the region covered by the tracks, labeled cross-correlation map.

9.3.4 Forward Modeling

The gradiometry and cross-correlation strategies rely on the gravity models derived from the GRAIL data to detect features of interest. It is useful to assess the validity of such detections. The concept that serves as a basis for the detection is a model that describes the gravitational signature of a feature and estimates the required parameters from the gradiometry or cross-correlation maps. Then, the gravitational potential and acceleration are computed for the forward model and incorporated into the simulation. The performance of the forward model is assessed by its ability to erase the observed signatures that should correspond to the feature of interest on the cross-correlation and gradiometry maps.

A strategy to represent the gravitational signature of a potential gravity deficit is a model that constructs the feature as a constant density polyhedron. There is no restriction on the geometric complexity in the polyhedron model and closed form expressions for the gravity potential, U, and acceleration, $\bar{\nabla}U$, are available, i.e., [23, 47, 86]

$$U = \frac{1}{2}G\sigma \sum_{edges} \bar{r}_e \bullet \bar{\bar{E}}_e \bullet \bar{r}_e \cdot L_e - \frac{1}{2}G\sigma \sum_{faces} \bar{r}_f \bullet \bar{\bar{F}}_f \bullet \bar{r}_f \cdot \omega_f \tag{9.5}$$

$$\bar{\nabla}U = -\frac{1}{2}G\sigma \sum_{edges} \bar{\bar{E}}_e \bullet \bar{r}_e \cdot L_e + \frac{1}{2}G\sigma \sum_{faces} \bar{\bar{F}}_f \bullet \bar{r}_f \cdot \omega_f \tag{9.6}$$

where G is the gravitational constant, σ is the constant density of the structure, $\bar{r}_e$ and $\bar{r}_f$ are the vectors from the point field to the edge e and face f, respectively. Then, $\bar{\bar{E}}_e$ and $\bar{\bar{F}}_f$ are the edge and face dyads, respectively. The same procedure as described for the point mass approach is employed to assess the ability of the forward model to match a signature that potentially corresponds to the detection of a notable feature.

To further assess the validity of the signature observed on the gradiometry maps, and in an initial attempt to physically characterize the feature that may cause such an anomaly, a forward model of the potential structure is developed in terms of a polyhedron mesh. The cross-section of the polyhedron model is assumed to be elliptic with a prescribed aspect ratio. Then, the polyhedron model is constructed as the concatenation of elliptic cross-sections along a prescribed center line. Both the center line and the initial width for the cross-section are inferred from the initial eigenvalue maps. The gravitational potential and the acceleration due to the shape model are then computed (25-27) and compared with the observed signatures. Note that the density for the structure is assumed equal to 2560 kg.m-3 to be consistent with the Bouguer model (28), however, it is not consistent with the density of mare basalt, the material that constitutes most of the mare (29, 30). To closely evaluate the agreement between the observed signature and the forward model, linear profiles across the structure of interest are constructed. Also, in addition to the largest eigenvalue from

the Bouguer gradiometry technique, profiles for the Bouguer gravity anomaly are also leveraged. Only the Bouguer quantities are leveraged to assess the validity of the forward model as the feature that is modeled is, in fact, underground. Of course, as the initial forward model is simply constructed from the observed signature, such an initial attempt does not supply a satisfying agreement between the data and the model. The task then consists in identifying the set of parameters that yield the best fit with respect to the observed signature on the maps. The shape model is then refined through an iterative process to produce a model that better reproduces the observed anomaly.

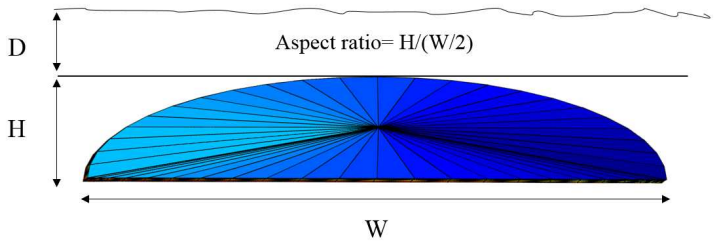

Figure 9.3. Cross-section parameterization for polyhedron model

9.4 Algorithm Development and Validation

9.4.1 Algorithm

A strategy is introduced to detect small scale features on or beneath the lunar surface, an approach exploiting gravity information derived from GRAIL. Some level of confidence in the validity of the detection scheme is necessary, of course. The process is currently automated and conjointly exploits the gradiometry and cross-correlation strategies. Recall that for the first method, gradiometry, the gravitational potential is inspected through the eigenvalues of the Hessian of the potential function, while the cross-correlation technique relies on analysis of the horizontal gravitational acceleration.

Challenges

The proposed strategy attempts to cope with some of the challenges associated with the detection of such small scale features. The predominant challenge in this analysis is the size of the features to be detected with respect to the spatial resolution of the spherical harmonics gravity model. Also, one consequence of evaluating the SH solution up to high degree and order, relative to the maximum degree and order of the field expansion, is numerical noise. Note that this numerical artifact does not correspond to noise in the measured data but is a product of the numerical methods involved in the representation of the data, that is, the spherical harmonics expansion. Further, for the gradiometry approach, the computation of the Hessian of the potential function and the corresponding eigenvalues also relies on numerical schemes that are subject to numerical errors. Thus, signatures on a gradiometry map or a cross-correlation map may or may not correspond to a physical feature on the Moon. Specific measures are adopted to increase the robustness of the detection process.

Computation

For a given gravity model, both free-air and Bouguer, the gravitational potential and the gravitational acceleration vector in spherical coordinates with respect to the Moon-fixed Principal Axis (PA) frame are computed using SHTOOLS for the entire Moon on a regular constant radius spherical grid. Additionally, the Hessian of the potential function and the eigenvalues that are associated with that functional are also computed. From this global computation, data that correspond to a region of interest are extracted to complete the cross-correlation analysis and produce cylindrical maps reflecting the largest eigenvalue and the cross-correlation coefficient. Recall that the Bouguer gravity is equivalent to the free-air gravity where the gravitational contribution from the surface topography has been subtracted. Thus, on a free-air map, both surface features, e.g., surface craters, sinuous rilles, and buried structures,

such as buried craters or potential lava tubes, appear. In contrast, on a Bouguer map, assuming the topography is known to a spatial resolution that is equal or smaller to that of the features of interest, only underground structures appear. In other words, a buried lava tube should appear in both free air and Bouguer gravity, while an open rille, such as Schroeter, should be visible in free air but not in a Bouguer map, assuming that the density destitute for the surrounding topography is correct. Therefore, producing both free-air and Bouguer maps allows assessment of a potential feature as a surface expression or a buried structure. Further, to assist the identification process, a third map that depicts the correlation between the free-air and Bouguer map for a given model is also produced. In this analysis, the focus is the detection of empty buried lava tubes, that is, a mass deficit or, equivalently, a negative gravity anomaly. Such an anomaly is depicted by a positive eigenvalue for the gradiometry method and a positive cross-correlation coefficient for the second strategy. To further highlight a correlation between signatures that corresponds to a mass deficit, any correlation between the free-air and Bouguer maps that corresponds to a negative signal, i.e., a mass surplus, for either the eigenvalue or cross-correlation maps, is set to zero. Hence, positive signatures on the third correlation map depict locations where a signal consistent with the expression of a buried feature is observed.

Visualization

To address the challenge posed by the size of the features to be detected with respect to the gravity model resolution, numerous individual simulations are leveraged. First, the initial gravity model is truncated and tapered to a range of degrees assumed to be reasonable and include the features of interest. Then, variations in the truncation on both ends of the field are employed to produce different SH solutions, yet all representative of the same data. The computation described in the previous section is performed for each modified gravity model to produce the corresponding maps. Finally, the results are inspected either through a static or dynamic represen-

tation. A map averaged over all simulations is produced as well as an animation of each individual map. While some signals may vary from one map to the next due to numerical artifacts, the average map supplies a cleaner representation of the region of interest. Similarly, the animation is insightful to emphasize signals that are persistent through the numerous simulations against signals that flicker and do not relate to physical features on the Moon.

9.4.2 Application to Schroeter Vallis

For the purpose of this analysis, localized maps that focus on specific regions are most relevant. Consider a region in the Aristarchus plateau that contains Aristarchus crater and one of the largest known lunar rilles, Schroeter Vallis, as illustrated in the LOLA topography map in Figure 9.4. For this application, four gravity models are considered, two up to degree and order 900, one up to degree 720, and a final model up to degree 780. Then, as outlined in section 9.4.1, each model is truncated on both ends of the SH expansion and tapered to attenuate the resulting ringing. To increase the robustness of the simulation, various truncations for the low-end are explored, ranging from no truncation to eliminating the first 90 degrees and orders in the SH series. Further, each of the models already truncated at the low-end is also truncated at the opposite end, that is, high degrees and orders are also eliminated. Similar to the low-end operation, several different truncations for the high-end truncations are applied. Thus, a multitude of modified gravity models are produced, all representative of the same initial data, but with various lower and upper truncations.

Gradiometry

A simulation is performed for the localized region near Aristarchus plateau for the specified gravity models, Figure 9.5 illustrates the corresponding local averaged eigenvalue map for free-air and Bouguer potential, overlaid with the local topography from LOLA. The color scale represents the signed magnitude of the largest magnitude

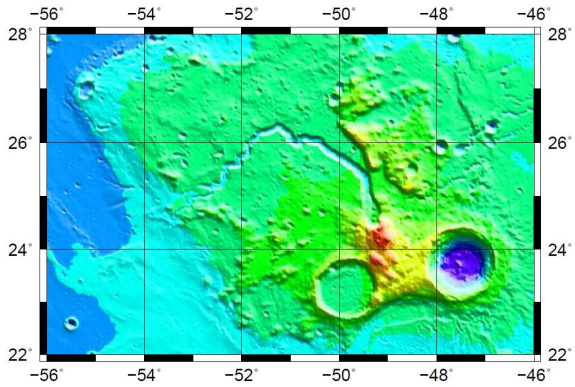

Figure 9.4. Local topography in the Schroeter Vallis region.

eigenvalue of the Hessian of the gravitational potential. From these local maps, it is now evident that the structure that emerges from the free-air map does, in fact, corresponds to the presence of the rille. Note that, as expected since the rille is a surface feature incorporated in the topography, there is no corresponding signal on the Bouguer map.

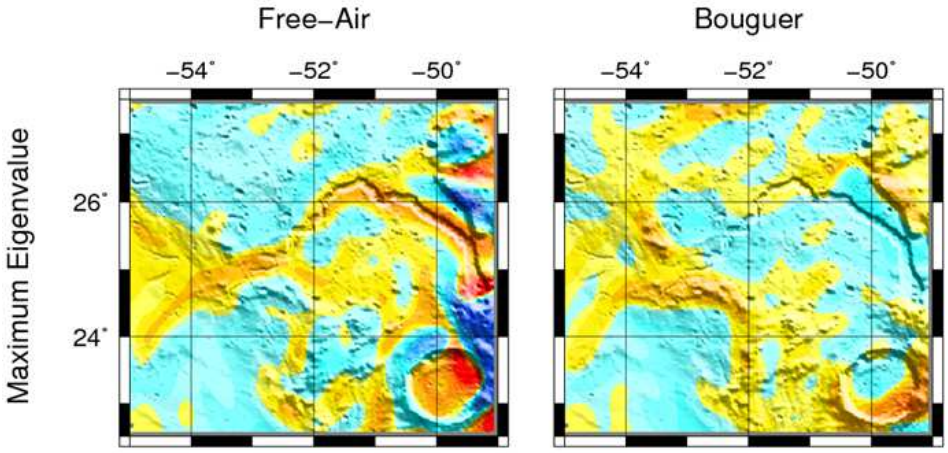

Figure 9.5. Local eigenvalues map in the Schroeter Vallis region with an overlay of topography.

Cross-correlation

The second strategy in an attempt to detect buried lava tubes relies on leveraging the gravitational acceleration as modeled by GRAIL data and the expected acceleration anomaly a spacecraft would experience as it flies over a mass deficit. Figure 9.6 illustrates the cross-correlation map obtained from the simulation. This figure is constructed from the cross-correlation between 80 tracks of data and a reference signal constructed assuming a 2 km diameter lava tube and an altitude consistent with the spherical harmonic model (the spherical harmonic data are presented at the reference altitude whereas the track data must be evaluated at the actual spacecraft altitude). The color scale represents the cross-correlation coefficient, from dark blue to red (a range from -1 to 1). The more positive the value of the coefficient, the more closely this portion of the track data resembles the reference signal, given that the cross-correlation operates as a matching filter. The rille signal corresponding to the topographic Schroeter Vallis clearly appears on the free-air cross-correlation map and is absent of the Bouguer map, consistent with the gradiometry results. This simulation offers a first validation of the scheme employed to detect the features of interest. These results also demonstrate the ability of the algorithm to produce clear maps of the eigenvalues and cross-correlation coefficient despite the numerical challenges that are associated with such computations.

9.4.3 Application to a Region without Known Features

The proposed algorithm successfully detects Schroeter Vallis, both with the gradiometry and cross-correlation strategies. However, because of the relative size of the features of interest compared to the resolution of the gravity field, combined with the numerical challenges that are associated with evaluating SH expansions at high degree and order, concerns regarding the validity of potential signatures that may be observed on the eigenvalue and cross-correlation maps naturally arise. Thus, another test is conducted that aims to demonstrate that a region with no known suface fea-

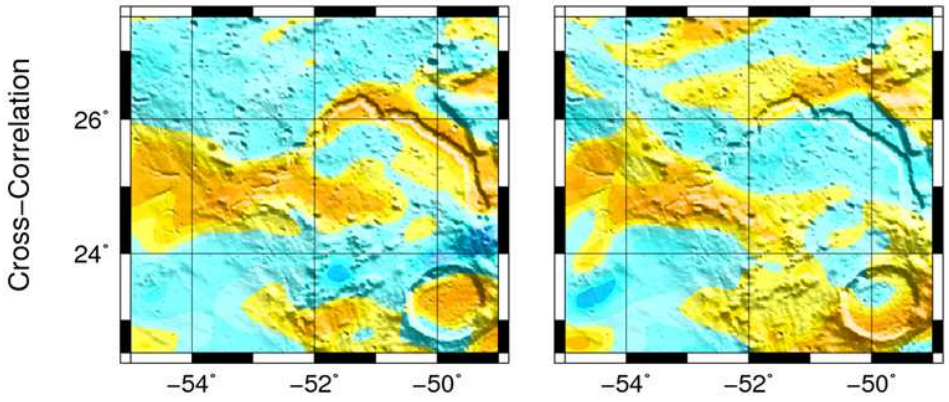

Figure 9.6. Local free-air (left) and Bouguer (right) cross-correlation map in the Schroeter Vallis region with overlay of topography.

tures triggers no detection when subjected to the same proposed analysis. Consider a small mare region southwest of the Aristarchus plateau region, as illustrated in Figure 9.7, no features of note within the context of detecting large sinuous rilles, are observed, in contrast to the Aristarchus region considered previously. For this region, a simulation sequence similar to the Schroeter region analysis is performed. Both the gradiometry and cross-correlation strategies are applied to a large number of gravity models to produce an averaged eigenvalue and cross-correlation map. In addition, given no a priori information regarding the existence of significant surface or subsurface features, a third map that depicts a bias correlation between free-air and Bouguer maps is also generated, as illustrated in Figure 9.8. As apparent on the gradiometry and cross-correlation maps, for free-air and Bouger gravity, no signature emerges from this simulation and this region does not appear to exhibit any significant surface or subsurface features that resemble a sinuous rille or lava tube. Further, the rightmost maps correspond to the correlation between free-air and Bouguer gravity, a strong correlation indicative of potential underground features would appear as a hot colored signature, however, no such signal is observed. This test achieves the simple purpose to validate that the averaging method successfully eliminates the numeri-

cal noise from the computation and produces a clear map that highlights physical significant features.

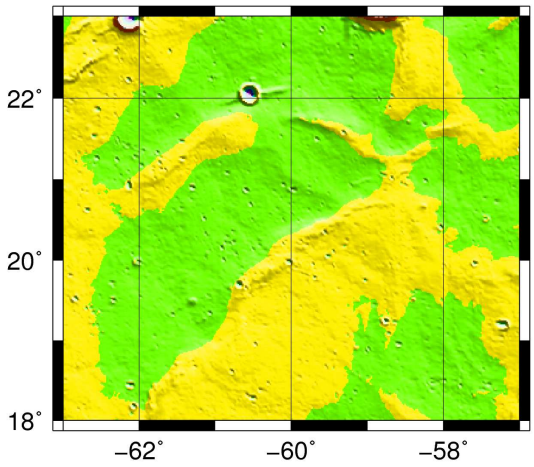

Figure 9.7. Local topography.

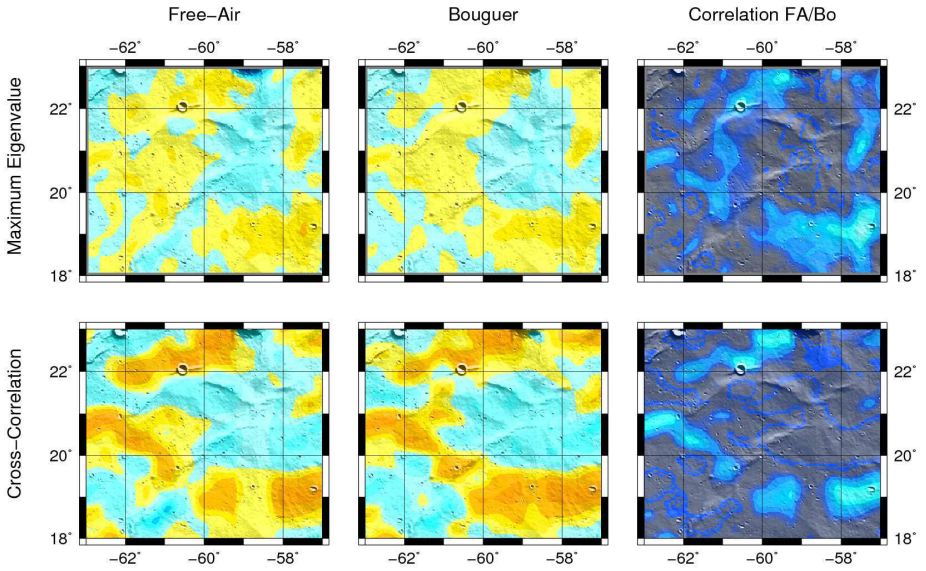

Figure 9.8. Local gradiometry (up) cross-correlation (down) map for free-air (left), Bouguer (center), and free-air/Bouguer correlation.

9.4.4 Detecting Underground Structures

Tools to detect small scale features on or under the lunar surface are developed and tested against the largest known lunar rille, Schroeter Vallis. The objective of this analysis is then to investigate the potential existence of intact empty lava tubes beneath the lunar surface. As features of interest, subsurface empty lava tubes, have no direct surface expression. The algorithm that combined both detection strategies is employed towards covering the mare regions of the Moon. The distribution of sinuous rilles on the lunar surface is now well-characterized and a global map of such features over the lunar surface is available. The majority of the observed features lie on the lunar nearside with a concentration in the mare region of the Moon. Sublunar voids and skylights have also been identified. Such developments and findings promote the ongoing search for uncollapsed lava tubes in the vast mare regions. As a result of the global search process, several potential candidates, consistent with subsurface mass deficits, are recognized. The anomalies lie in the vicinity of a rille or a skylight, a potential opening to an empty lava tube. Thus, these initial findings warrants further analysis to confirm the presence of these potential buried empty lava tubes. Amongst the identified candidates, two anomalies are analyzed in detail.

9.5 Schroeter Vallis Extension

Gradiometry and cross-correlation simulation

A first feature is located on the Aristarchus plateau that contains Aristarchus crater and one of the largest known lunar rilles, Schroeter Vallis. From the local maps that are produced for this region, as illustrated in Figure 9.9, it is now evident that the main structure that emerges from the free-air map does, in fact, corresponds to the presence of the rille. The focus is now on a signal that is present on the maps generated with both methods, gradiometry and cross-correlation, and on the free-air and Bouguer maps suggesting an underground feature. Indeed, a strong sig-

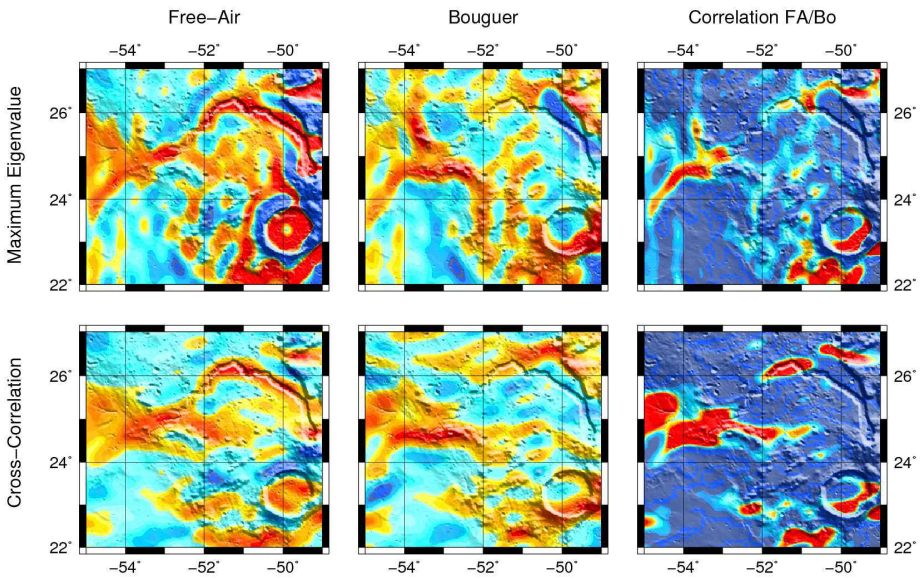

Figure 9.9. Local cross-correlation and eigenvalue map in the Schroeter Vallis region with overlay of the topography.

nature, especially evident on the gradiometry maps, is located in the continuation of the topographic rille. It is important to note that the cross-correlation strategy is only most sensitive to East-West features. Thus, while a signature is present on the cross-correlation map that is similar to the gradiometry map signature, it is not as sharp nor clearly outlined due to the orientation of the anomaly. Also note that these maps are the product of numerous simulations, a few hundred, and for a feature to appear on an averaged map it must be consistent through many individual computations. A less robust feature is eliminated from the map through the averaging process. Finally, the correlation map between the free-air and Bouguer gravity further highlights the observed signature. While few other signals that do not seem to correspond to surface features are observed on the gradiometry map, for free-air or Bouguer gravity, only the signature that corresponds to the identified potential underground feature is associated with a strong free-air/Bouguer correlation. All these observations strongly suggest the presence of an underground mass deficit that corresponds to a gravity anomaly. The free-air gravity is sensitive to both surface

and underground mass anomalies, while the Bouguer gravity, assuming sufficient topographic information is available, is only representative of underground features. To further verify that anomalies detected in this analysis are not, in fact, surface features, the topography-induced gravity is leveraged, that is, the gravitational contribution from the known surface topography. Then, the gradiometry detection technique is applied to the topography-induced gravity to reveal anomalies that are solely consistent with surface features. Such a simulation is completed for the Schroeter region, as displayed in Figure 9.10. From this complementary simulation, it is apparent that the anomaly interpreted as an underground mass deficit is not present either on the topography directly or on the topography-induced gradiometry, hence supporting the proposed hypothesis.

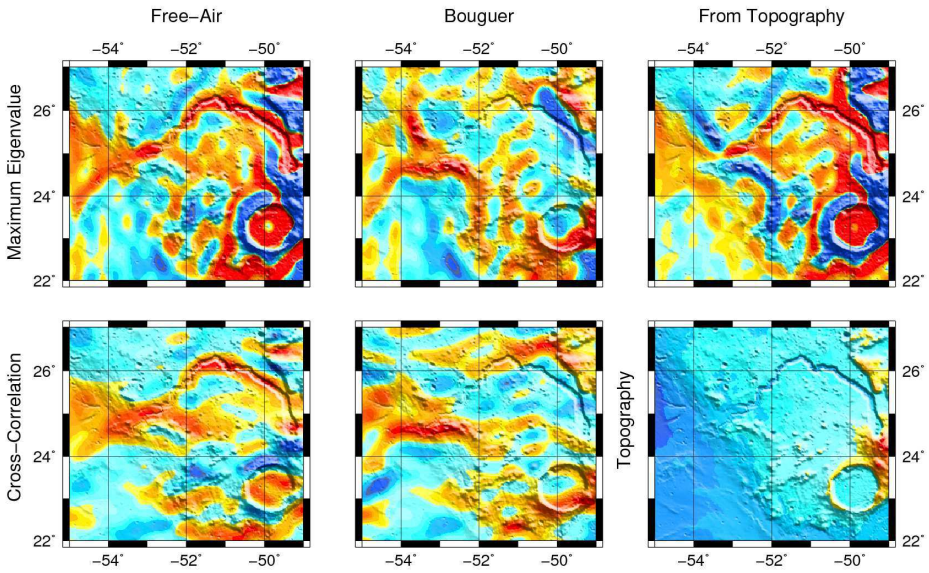

Figure 9.10. Local cross-correlation and eigenvalue map in the Schroeter Vallis region including topography-induced gravity gradiometry.

Forward modeling

To further assess the validity of the signature observed on the gradiometry maps, and in an initial attempt to physically characterize the feature that may cause such an anomaly, a forward model of the potential structure is developed in terms of a polyhedron mesh. The cross-section of the polyhedron model is assumed to be elliptic with a prescribed aspect ratio. Then, the polyhedron model is constructed as the concatenation of elliptic cross-sections along a prescribed center line. Both the center line and the initial width for the cross-section are inferred from the initial eigenvalue maps. The gravitational potential and the acceleration due to the shape model are then computed and compared with the observed signatures. Note that the density for the structure is assumed equal to 2560 $kg.m^{-3}$ to be consistent with the Bouguer model, however, it is not consistent with the density of mare basalt, the material that constitutes most of the mare. To closely evaluate the agreement between the observed signature and the forward model, linear profiles across the structure of interest are constructed. Also, in addition to the largest eigenvalue from the Bouguer gradiometry technique, profiles for the Bouguer gravity anomaly are also leveraged. Only the Bouguer quantities are leveraged to assess the validity of the forward model as the feature that is modeled is, in fact, underground. Of course, as the initial forward model is simply constructed from the observed signature, such an initial attempt does not supply a satisfying agreement between the data and the model. The task then consists in identifying the set of parameters that yield the best fit with respect to the observed signature on the maps. The shape model is then refined through an iterative process to produce a model that better reproduces the observed anomaly, as depicted in Figure 9.11. For the profiles along the anomaly considered, the forward model is successful in matching the gravity anomaly and eigenvalue anomaly that is observed on the initial gradiometry map, as illustrated in Figure 9.12. Further, the overall agreement between the observed anomaly and the model is visualized in a differential map in Figure 9.13. Note that these maps are preliminary results and

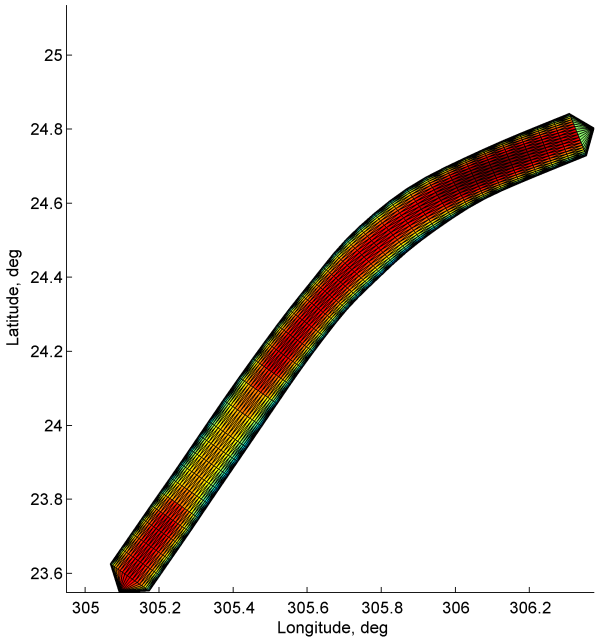

Figure 9.11. Forward model for Schroeter extension anomaly

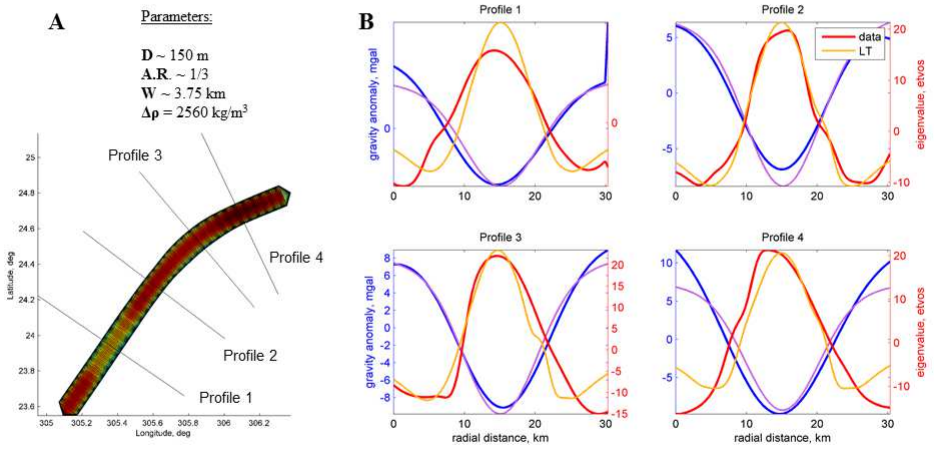

Figure 9.12. Profiles across Schroeter extension forward model.

the product of a simulation with a forward model that is constructed based on one set of parameters. Since gravity is non-unique, an infinite number of solutions can fit a given gravity anomaly, however, some constraints on the parameter space do exist and this solution represents a scenario that best satisfies the observations and constraints.

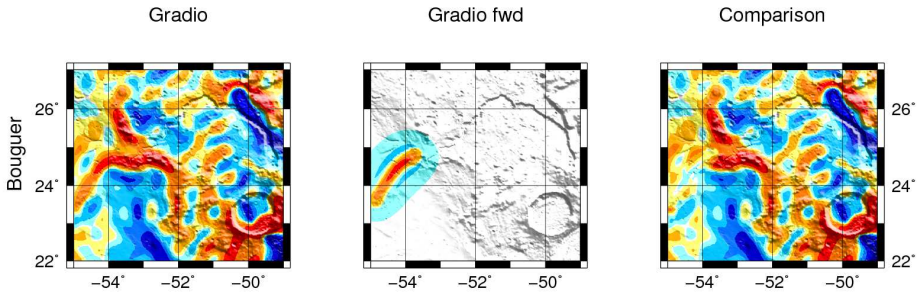

Figure 9.13. Local cross-correlation and eigenvalue map in the Schroeter region with forward model for observed anomaly.

9.6 Rima Mairan Anomaly

Besides Schroeter Vallis, another strong candidate for a lunar lava tube is located near a southern channel of Rima Sharp, Rima Mairan, much smaller in size than Schroeter Vallis. An image of the region of interest is displayed in Figure 9.14.

Gradiometry and cross-correlation simulation

For this region, a simulation similar to the Schroeter region analysis is completed. Both the gradiometry and cross-correlation strategies are applied to a large number of gravity models to produce an averaged eigenvalue and cross-correlation map, as illustrated in Figure 9.15. Although the Rima Sharp channel in the top of the figure is not resolved, another signal is observed along the center of the maps. This signal is present on the maps generated with both methods, gradiometry and cross-correlation,

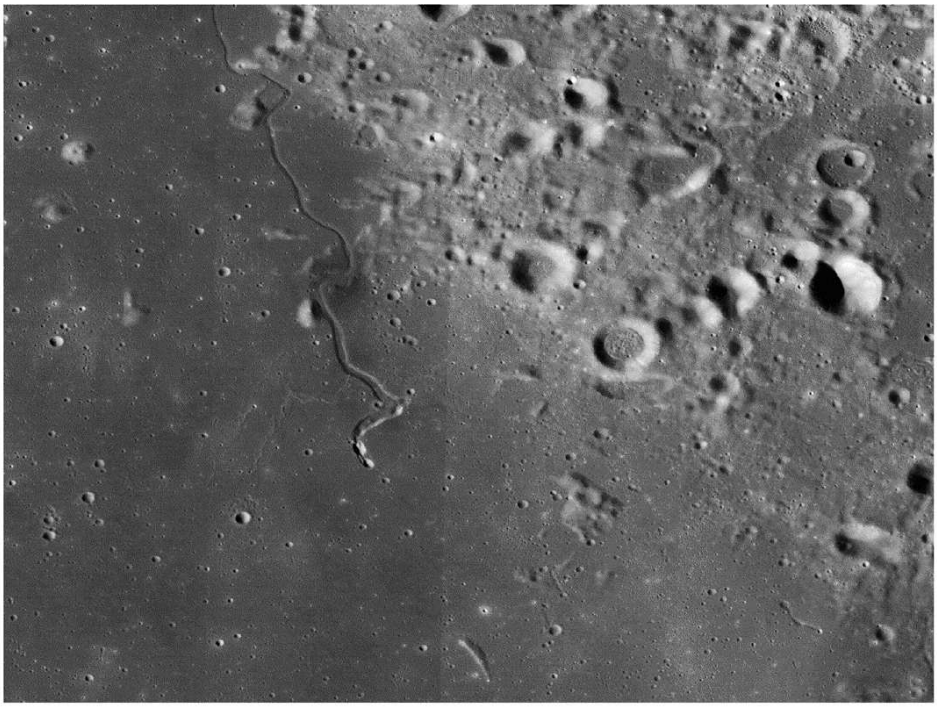

Figure 9.14. LROC WAC image near south channel of Rima Sharp.

and on the free-air and Bouguer maps suggesting an underground feature. Also recall that these maps are the product of numerous simulations, a few hundred, and for a feature to appear on an averaged map it must be consistent through many individual computations. A less robust feature is eliminated from the map through the averaging process. Finally, the correlation map between the free-air and Bouguer gravity further highlights the observed signature. While few other signals that do not seem to correspond to surface features are observed on the gradiometry or cross-correlation maps, for free-air or Bouguer gravity, only the signature that corresponds to the identified potential underground feature is associated with a strong free-air/Bouguer correlation for both strategies. All these observations strongly suggest the presence of an underground mass deficit that corresponds to a gravity anomaly. Finally, similar to the Schroeter region scenario, the topography-induced gravity is leveraged to further assess that anomalies detected in this analysis are not, in fact, surface features. From

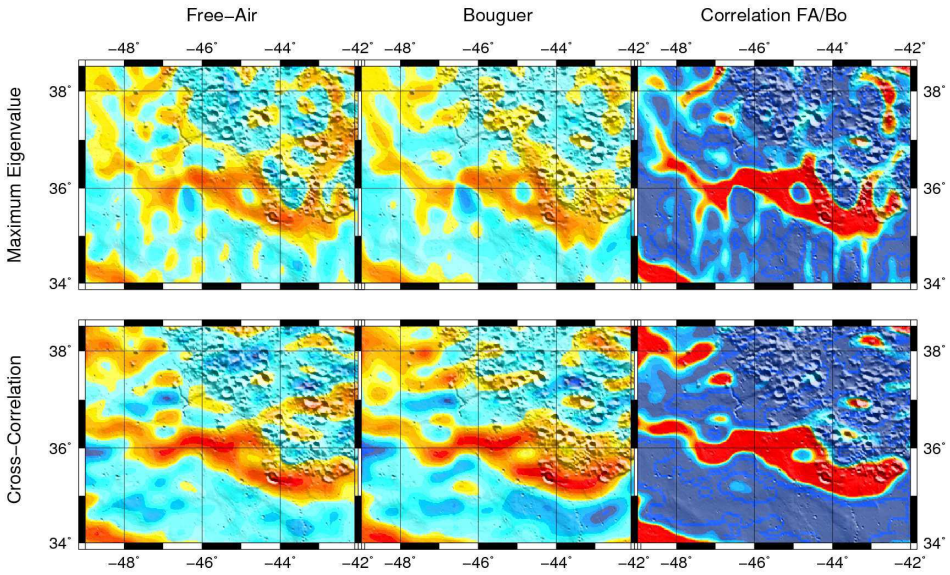

Figure 9.15. Local cross-correlation and eigenvalue map in the Rima Mairan region with overlay of the topography.

this additional simulation, it is apparent in the maps in Figure 9.16 that the anomaly interpreted as an underground mass deficit is not present either on the topography directly or on the topography-induced gradiometry, hence supporting the proposed hypothesis.

9.6.1 Forward modeling

This overall East-West signal is present on the maps generated with both methods, gradiometry and cross-correlation, and on the free-air and Bouguer maps suggesting an underground feature, similar to the Schroeter extension structure. This anomaly is another candidate for an empty lunar lava tube and, similar to the Schroeter scenario, a forward model for this anomaly is constructed and the corresponding shape model is displayed in Figure 9.17. The induced gravity anomaly is compared with the observed signatures. Similar to the previous anomaly, for the profiles along the anomaly considered, the forward model is successful in matching the gravity

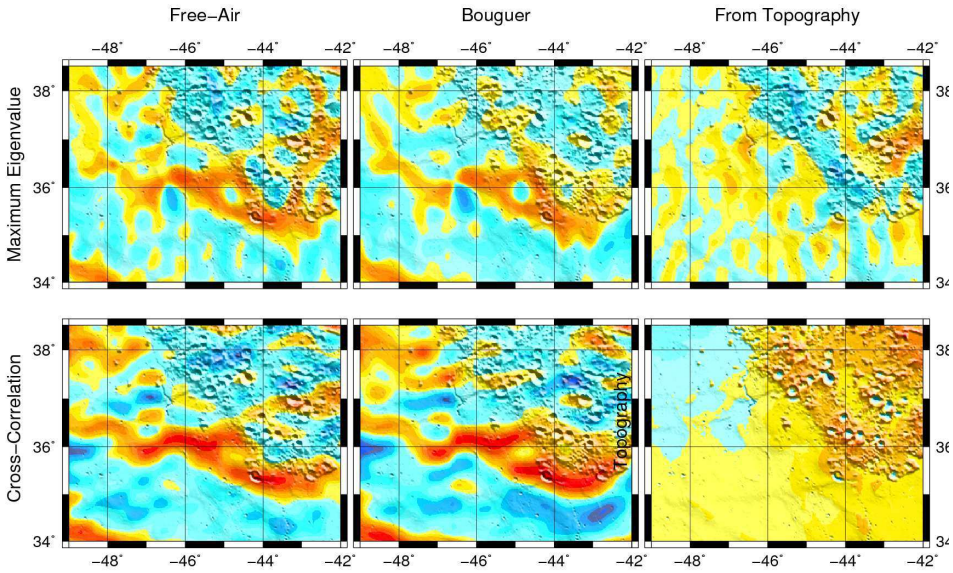

Figure 9.16. Local cross-correlation and eigenvalue map in the the Rima Mairan region including topography-induced gravity gradiometry.

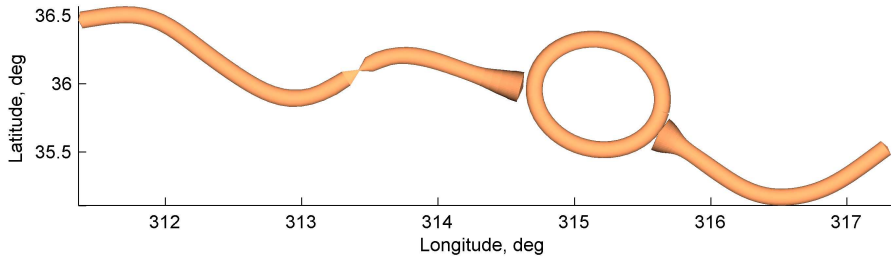

Figure 9.17. Forward model for Rima Mairan anomaly

anomaly and eigenvalue anomaly that is observed on the initial gradiometry map, as illustrated in Figure 9.18. Finally, the overall agreement between the observed anomaly and the model is visualized in a differential map in Figure 9.19. Further modeling may yield better agreement between the model and the observed signature, however, this initial model supplies sufficient agreement to promote the hypothesis of a large lava tube underneath the mare surface.

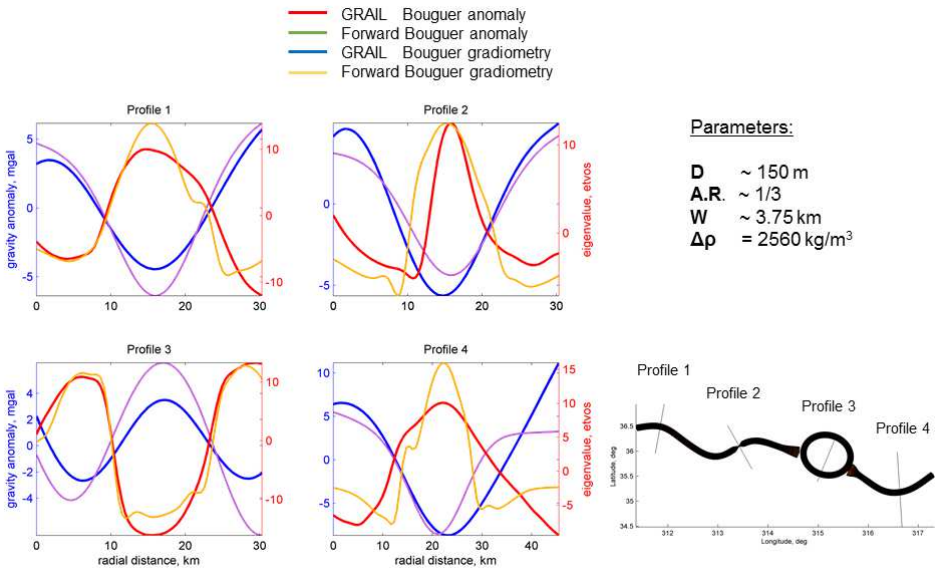

Figure 9.18. Profiles across Rima Mairan anomaly forward model.

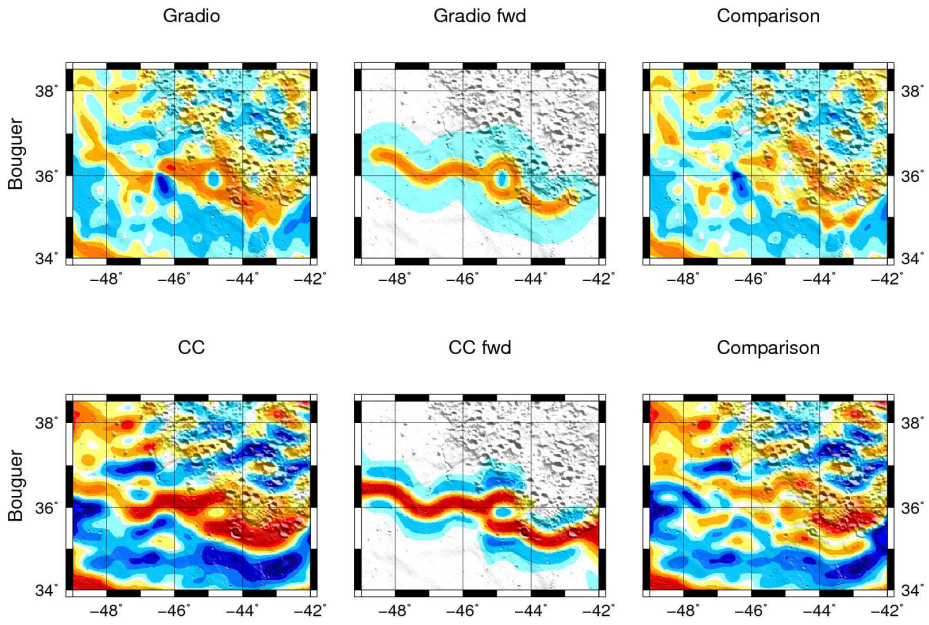

Figure 9.19. Local cross-correlation and eigenvalue map in the Rima Sharp region with forward model for observed anomaly.

10. CONCLUDING REMARKS

In this investigation, tools to model non-trivial gravity fields with high-accuracy are developed and strategies to exploit such information to achieve a specific goal are constructed. First, in trajectory design applications, a gravity representation for the bodies of interest is, in general, assumed and exploited to determine the motion of a spacecraft in any given system. The focus in this analysis is the exploration of trajectories in the vicinity of a system comprised of two small irregular bodies. Alternatively, the motion of the spacecraft around a given body may be known to extreme precision enabling the derivation of a very high-accuracy gravity field for that body. Such knowledge can subsequently be exploited to gain insight into specific properties of the body. The success of the NASA's GRAIL mission ensures that the highest resolution and most accurate gravity data for the Moon is now available.

10.1 Exploration of Bounded Motion near Binary Systems Comprised of Small Irregular Bodies

For primary systems that can reasonably be modeled as synchronous, a large survey of third-body periodic trajectories is completed. These trajectories are also subsequently incorporated into an algorithm to construct user-defined tours of the system to explore the regions near the primary bodies. Also, continuation techniques allow such trajectories to be produced for any desired system of bodies that can reasonably be modeled as a pair of ellipsoids. Finally, in an initial assessment of the feasibility and robustness of the trajectories that are constructed leveraging idealized dynamical models, sample trajectories for a known binary system, 1999 KW4, are transitioned into a higher-fidelity dynamical model where each primary body is modeled as a polyhedron and the motion of the primary system reflects the coupling

between orbital motion and attitude dynamics. To further explore the effect of the shape of the primaries, Poincaré maps are leveraged to depict the dynamical behavior of a third body in the vicinity of nonspherical primaries. Maps for various primary system models are produced and the topology of these maps is used as a basis to characterize the effect of the primary system model on the behavior of a third body. This initial analysis assumes that detailed knowledge of the primary system in terms of the physical and dynamical properties of the primaries is available prior to in situ operations. To include uncertainties in the physical properties of the bodies and other non-gravitational perturbing effects, a strategy to maintain a spacecraft near reference third-body trajectories that exhibit some desired characteristics is constructed incorporating multiple sliding surfaces guidance. To maintain the spacecraft in orbit near a desired reference path, a 'coast and thrust' scheme is proposed. The analysis is extended to the behavior of a third body in the vicinity of non-synchronous systems where the problem is now time variant. Yet, the insight gained from the synchronous system analysis is leveraged to construct third-body trajectories that are periodic in the non-synchronous problem, focusing on periodic primary system. Finally, mapping techniques, now leveraging finite-time Lyapunov exponent, are also exploited to specifically investigate the transition between synchronous and non-synchronous systems and the effect onto the third-body behavior.

10.2 Orbital Perturbations

The scope of the investigation is widened to assess the perturbing effect that dominates the dynamics of the spacecraft near a pair of small irregular bodies as a function of the baseline orbit. Specifically, the objective is to assess the perturbation that arises from the existence of the secondary body in a binary system, labeled 'binary effect'. To compare the relative strength of several perturbing effects across the parameter space, 'zonal maps' are introduced. After an initial validation of the prediction of the binary effect, the validity of the zonal map is further assessed through

the numerical integration of initial conditions, that correspond to pre-computed periodic orbits, with a high-fidelity dynamical model. Then, the zonal maps are useful in selecting a type of orbit that is predicted to yield a stable ballistic motion under perturbations. Sample orbit types are considered as an initial application, including halos, terminators, DROs, and LoPOs.

10.3 Lava Tube Detection with GRAIL

Tools specifically developed to best exploit the rich gravity data and advance the numerical detection of these small features are applied to the GRAIL data. Combined with forward modeling to further validate possible detections and to attempt to characterize the physical parameters of a feature, candidates for lunar lava tubes are identified. Specifically, two anomalies are considered for detailed analysis, one in the prolongation of one of the largest known lunar rille, Schroeter Vallis, and a second one, south of Rima Mairan. In addition to being consistent with underground mass deficits, both gravity anomalies are sufficiently robust to persist on averaged maps that are constructed based on two independent techniques. Further, forward modeling support the identified anomalies as possible lunar lava tube through the construction of a physical model for the potential structures and validation of the agreement between observed and modeled anomalies. The size of the observed anomalies and derived physical model for these signatures suggest very large structures, several kilometers wide and tens of kilometers to well over a hundred kilometers long. It is important to note that such massive lava tubes are much larger than the Earth counterparts, even accounting for gravity scaling between Earth and the Moon. However, a recent study using finite element simulation demonstrated that large lava tubes, up to several kilometers wide, are mechanically stable under lunar conditions. [100]

10.4 Recommendations for Future Work

As the complexity and boldness of emerging mission proposals increase, and with the rapid evolution of the available computational capabilities, high-accuracy and high-resolution gravity models and the tools to exploit such models are increasingly attractive within the context of spaceflight mechanics, mission design and analysis, and planetary science in general. Potential areas of future research efforts are as follows:

(i) Initially, for synchronous systems, a catalog of periodic orbits is produced for primary systems comprised of irregular bodies modeled as spheres or ellipsoids. Also, for non-synchronous systems, while isolated, periodic orbits are also computed. Additionally, the Poincaré and FTLE map analyses demonstrate that, even for increasingly complex primary system models, both synchronous and non-synchronous, a rich dynamical structure exists for the set of initial conditions considered. Specifically, in addition to periodic orbits, numerous quasi-periodic orbit regions exist. Thus, while in this investigation the focus is on periodic orbits, quasi-periodic orbits could also be considered for further analysis. In particular, such orbits may be of interest for non-synchronous systems. Recall that that for non-synchronous systems, the existence of periodic orbit is constrained by the commensuration requirement between the periodic of the third body and the primary system. Quasi-periodic orbits may offer an interesting alternative to these point solutions. Also note that the automated strategy developed in Chapter 5 for synchronous systems and adapted to non-synchronous in Chapter 7, that aims to construct trajectories from a series of user-defined periodic orbits, can also be adapted to exploit quasi-periodic orbits.

(ii) Within the context of the orbital perturbation analysis, a strength coefficient for the binary effect is derived and leveraged to explore the relative strength of the binary effect compared to other perturbations, as a function of the baseline orbit that is considered. Further examination of the ballistic stability of sample

types of orbits as a function of the ratio of the dominating strength coefficient to other perturbations may yield further insight. In particular, such further analysis may also aid in identifying which force ratios yield stable orbits for a given type.

(iii) Relying on the unprecedented resolution of the GRAIL gravity data, potential candidates for lunar lava tubes are identified. Some limitations and challenges remain. The size of the structures that are the object of this analysis is near the same order of magnitude or smaller than the resolution of the gravity data. It is then challenging to determine whether an observed signal is, in fact, the signature of a physical structure or is a numerical artifact. Also, numerical challenges are associated with spherical harmonics analysis for very high degree and order. To assess the robustness of an observed signal, rather than considering a single simulation, numerous computations are considered to produce an averaged map. Based on such considerations, while the techniques and strategies designed in this analysis allow to extract lava tube signatures from the GRAIL gravity data set, only sufficiently large features are accessible to detection. Thus, numerous smaller lava tubes may exist underneath the mare surface, such features, however, may require the inspection of alternative, unavailable at present, types of data set to be detected. Future lunar missions to produce complementary data sets, such as targeted ground-penetrating RADAR or seismic data, may support the existence of the current proposed anomalies and allow the identification of additional features.

REFERENCES

REFERENCES

[1] R. W. Farquhar, D. W. Dunham, and J. V. McAdams. NEAR Mission Overview and Trajectory Design, Special Issue on the Near Earth Asteroid Rendezvous Mission. *J. Astronautical Sciences*, 43(4):353–371, 1995.

[2] M. D. Rayman, T. C. Fraschetti, C. A. Raymond, and C. T. Russell. Dawn: A mission in development for exploration of main belt asteroids Vesta and Ceres. *Acta Astronautica*, 58:605–616, June 2006.

[3] K-H. Glassmeier, H. Boehnhardt, D. Koschny, E. Khrt, and I. Richter. The rosetta mission: Flying towards the origin of the solar system. *Space Science Reviews*, 128(1-4):1–21, 2007.

[4] E. Jurado, A. Blazquez, T. Martin, E. Canalias, T. Ceolin, R. Garmier, J. Biele, L. Jorda, J-B. Vincent, and J. Laurent-Varin. Philae landing site selection and descent trajectory design. In *25th AAS/AIAA Space Flight Mechanics Conference*, Williamsburg, Virginia, January 2015.

[5] http://osiris-rex.lpl.arizona.edu/. Last accessed 02-23-2013.

[6] J. L. Margot, M. C. Nolan, L. A. M. Benner, S. J. Ostro, R. F. Jurgens, J. D. Giorgini, M. A. Slade, and D. B. Campbell. Binary asteroids in the near-earth object population. *Science*, 296:1445–1448, 2002.

[7] P. Michel, M. A. Barucci, A. Cheng, H. Böhnardt, J. R. Brucato, E. Dotto, P. Ehrenfreund, I. Franchi, S. F. Green, L. M. Lara, B. Marty, D. Koschny, and D. Agnolon. MarcoPolo-R: Near Earth Asteroid Sample Return Mission Selected for the Assessment Study Phase of the ESA program Cosmic Vision. *Acta Astronautica*.

[8] A. Cook, J. Bellerose, B. Rozitis, T. Yamaguchi, C. Mester, N. Murdoch, and F. Marchis. Didymos Explorer: A Mission Concept for Visiting a Binary Asteroid. In *AAS/Division for Planetary Sciences Meeting Abstracts #40*, volume 40 of *Bulletin of the American Astronomical Society*, page 452, September 2008.

[9] A. F. Cheng, A. S. Rivkin, C. Reed, O. Barnouin, Z. Fletcher, C. Ernst, A. Galvez, I. Carnelli, and P. Michel. AIDA: Asteroid Impact & Deflection Assessment. In *64th International Astronautical Congress*, Beijing, China, September 23-27 2013.

[10] L. Perko. *Differential Equations and Dynamical Systems*. Springer, New York, 2001.

[11] W. D. McMillan. *The Theory of the Potential*. McGraw-Hill, New York, 1930.

[12] W. D. MacMillan. *Dynamics of rigid bodies*. Theoretical mechanics. McGraw-Hill Book Company, Inc., 1936.

[13] W. M. Kaula. *Theory of Satellite Geodesy; Applications of Satellite Geodesy; # Applications of Satellites to Geodesy*. Blaisdell, Massachusetts, 1966.

[14] W. A. Heiskanen and H. Moritz. *Physical geodesy*. W. H. Freeman, San Francisco, 1967.

[15] M. Lara. Repeat Ground Track Orbits of the Tesseral Artificial Satellite as Bifurcations of the Equatorial Family of Periodic Orbits. In *XV International Symposium of Spaceflight Dynamics*, Biarritz, France, June 26-30, 2000.

[16] A. Elipe and M. Lara. On the Dynamical Behavior of a Spacecraft Orbiting Elongated Celestial Bodies. In *AAS/AIAA Space Flight Mechanics Meeting*, Santa Barbara, California, February 11-15, 2001. Paper AAS 01-155.

[17] M. Lara and D. J. Scheeres. Stability bounds for three-dimensional motion close to asteroids. In *AAS/AAIA Space Flight Mechanics Meeting*, San Antonio, Texas, January 27-30, 2002.

[18] D. J. Scheeres, S. J. Ostro, R. S. Hudson, and R. A. Werner. Orbits Close to Asteroid 4769 Castalia. *Icarus*, 121:67–87, 1996.

[19] TJ. K. Miller, A. S. Konopliv, P. G. Antreasian, J. J. Bordi, S. Chesley, C. E. Helfrich, W. M. Owen, T. C. Wang, B. G. Williams, D. K. Yeomans, and D. J. Scheeres. Determination of Shape, Gravity, and Rotational State of Asteroid 433 Eros. *Icarus*, 155:3–17, 2002.

[20] R. A. Werner and D. J. Scheeres. Exterior Gravitation of a Polyhedron Derived and Compared with Harmonic and Mascon Gravitation Representations of Asteroid 4769 Castalia. *Celestial Mechanics and Dynamical Astronomy*, 65:313–344, 1996.

[21] S. W. Henriksen, A. Mancini, and B. H. Chovitz. The Use of Artificial Satellites for Geodesy. In *Geophysical Monograph Series*, volume 15, pages 265–273. AGU, Washington, D. C., 1972.

[22] R. J. Turner. A model of PHOBOS. *Icarus*, 33:116–140, 1978.

[23] L. Chappaz. The Dynamical Environment in the Vicinity of Small Irregularly-Shaped Bodies and Application to Asteroids. M.S. Thesis, School of Aeronautics and Astronautics, Purdue University, West Lafayette, Indiana, December 2011.

[24] R. Furfaro, D. Cersosimo, and D. R. Wibben. Asteroid Precision Landing via Multiple Sliding Surfaces Guidance Techniques. *Journal of Guidance Control Dynamics*, 36:1075–1092, July 2013.

[25] R. Furfaro, D. Cersosimo, and J. Bellerose. Close Proximity Asteroid Operations Using Sliding Control Modes. In *22nd AAS/AIAA Space Flight Mechanics Meeting*, Charleston, South Carolina, January 2012.

[26] R. Furfaro. Hovering in Asteroid Dynamical Environments Using Higher-Order Sliding Control. *Journal of Guidance Control Dynamics*, 38:263–279, February 2015.

[27] J. Bellerose and D. J. Scheeres. Periodic orbits in the vicinity of the equilateral points of the restricted full three-body problem. In *AAS/AIAA Astrodynamics Specialist Conference*, August 7-11 2005.

[28] L. Chappaz and K. Howell. Trajectory Exploration within Binary Systems Comprised of Small Irregular Bodies. In *23rd AAS/AIAA Space Flight Mechanics Meeting*, Kauai, Hawaii, February 2013.

[29] D. J. Scheeres. Stability of the planar full 2-body problem. *Celestial Mechanics and Dynamical Astronomy*, 104(1-2):103–128, 2009.

[30] E. G. Fahnestock and D. J. Scheeres. Simulation and analysis of the dynamics of binary near-Earth Asteroid (66391) 1999 KW4. *Icarus*, 194:410–435, 2008.

[31] E. G. Fahnestock and D. J. Scheeres. Characterization of Spacecraft and Debris Trajectory Stability within Binary Asteroid Systems. In *AIAA/AAS Astrodynamics Specialist Conference and Exhibit*, Honolulu, Hawaii, August 18-21, 2000.

[32] J. Bellerose, R. Furfaro, and D. Cersosimo. Multiple Sliding Surface Guidance Applied at Binary Asteroid Systems. In *23rd AAS/AIAA Space Flight Mechanics Meeting*, Kauai, Hawaii, February 2013.

[33] D. Cersosimo, J. Bellerose, and R. Furfaro. Sliding Guidance Techniques for Close Proximity Operations at Multiple Asteroid Systems. In *AIAA Guidance, Navigation and Control Conference (Invited)*, Boston, Massachusetts, August 2013.

[34] D. K. Butler. Microgravimetric and gravity gradient techniques for detection of subsurface cavities. *Geophysics*, 49(7):1084–1096, 1984.

[35] V. L. Sharpton, R. A. F. Grieve, M. D. Thomas, and J. F. Halpenny. Horizontal gravity gradient: An aid to the definition of crustal structure in north america. *Geophysical Research Letters*, 14(8):808–811, 1987.

[36] L. Cordell, 1979, Gravimetric expression of graben faulting in Santa Fe country and the Espanola Basin, New Mexico, in: Santa Fe Country, R. V. Ingersoll, L. A. Woodward, and H. L. James, New Mexico Geological Society, Guidebook, 30th Field Conference, pp. 59-64.

[37] D. G. Angelis, J. W. Wilson, M. S. Clowdsley, J. E. Nealy, D. H. Humes, and J. M. Clem. Lunar lava tube radiation safety analysis. *Journal of Radiation Research*, 43(Suppl):S41–S45, 2002.

[38] J. Haruyama, K. Hioki, M. Shirao, T. Morota, H. Hiesinger, C. H. van der Bogert, H. Miyamoto, A. Iwasaki, Y. Yokota, M. Ohtake, T. Matsunaga, S. Hara, S. Nakanotani, and C. M. Pieters. Possible lunar lava tube skylight observed by selene cameras. *Geophysical Research Letters*, 36(21), 2009.

[39] W. M. Telford, L. P. Geldart, and R. E. Sheriff. *Applied geophysics*. Cambridge University Press, 1990.

[40] E. W. Hobson. *The Theory of Spherical and Ellipsoidal Harmonics*. Chelsea Pub Co, New York, 1965.

[41] P. M. Morse and H. Feshback. *Methods of Theoritical Physics, Parts I and II*. McGraw-Hill, New York, 1953.

[42] Committee on Earth Gravity from Space, National Research Council, *Satellite Gravity and the Geosphere: Contributions to the Study of the Solid Earth and Its Fluid Envelopes*. Washington, D. C.: The National Academies Press, 1997.

[43] T. M. MacRobert. Spherical harmonics; an elementary treatise on harmonic functions, with applications. In *International Series of Monographs in Pure and Applied Mathematics*, volume 98. Pergamon Press, New York, 3rd edition, 1967.

[44] G. Sansone. *Orthogonal Functions*. Dover, New York, revised english edition edition, 1991.

[45] J. Bellerose and D. J. Scheeres. The restricted full three-body problem: Application to binary system 1999 kw4. *Journal of Guidance, Control, and Dynamics*, 31(1):162–171, 2008.

[46] B. Khushalani. Asteroid tetrahedron shape models from spud data. *Current Science*, 79(11), Addison-Wesley 2000.

[47] R. A. Werner. The Gravitational Potential of a Homogeneous Polyhedron or don't Cut Corners. *Celestial Mechanics and Dynamical Astronomy*, 59(3):253–258, 1993.

[48] M. D. Greenberg. *Foundation of Applied Mathematics*. Prentice-Hall, Englewood Cliffs, New Jersey, 1978.

[49] D. J. Scheeres. Relative equilibria for general gravity fields in the sphere-restricted full 2-body problem. *Celestial Mechanics and Dynamical Astronomy*, 94(3):317–349, 2006.

[50] T. Lee, M. Leok, and N. H. McClamroch. Lie Group Variational Integrators for the Full Body Problem in Orbital Mechanics. *Celestial Mechanics and Dynamical Astronomy*, 98(2):121–144, 2007.

[51] E. G. Fahnestock and D. J. Scheeres. Simulation of the full two rigid body problem using polyhedral mutual potential and potential derivatives approach. *Celestial Mechanics and Dynamical Astronomy*, 96(3-4):317–339, 2006.

[52] M. Hirabayashi and D. J. Scheeres. Recursive computation of mutual potential between two polyhedra. *Celestial Mechanics and Dynamical Astronomy*, 117(3):245–262, 2013.

[53] R. A. Werner and D. J. Scheeres. Mutual potential of homogeneous polyhedra. *Celestial Mechanics and Dynamical Astronomy*, 91(3-4):337–349, 2005.

[54] A. J. Maciejewski. Reduction, relative equilibria and potential in the two rigid bodies problem. *Celestial Mechanics and Dynamical Astronomy*, 63(1):1–28, 1995.

[55] H. B. Keller. Numerical Solutions of Bifurcations and Nonlinear Eigenvalue Problems. In P. H. Rabinowitz, editor, *Applications of Bifurcation Theory*, pages 359–384. Academic Press, 1977.

[56] E. J. Doedel and V. A. Romanov. Elemental Periodic Orbits Associated with the Libration Points in the Circular Restricted 3-Body Problem. *International Journal of Bifurcation and Chaos*, 17(8), 2007.

[57] J. D. Hadjidemetriou. Symmetric and Asymmetric Librations in Extrasolar Planetary Systems: A Global View. In A. Celletti and S. Ferraz-Mello, editors, *Periodic, Quasi-Periodic and Chaotic Motions in Celestial Mechanics: Theory and Applications*, pages 225–244. Springer, 2006.

[58] D. W. Jordan and P. Smith. *Nonlinear Ordinary Differential Equations: An Introduction to Dynamical Systems*. Oxford University Press Inc., New York, 3rd edition, 1999.

[59] B. T. Barden. Using Stable Manifolds to Generate Transfers in the Circular Restricted Problem of Three Bodies. M.S. Thesis, School of Aeronautics and Astronautics, Purdue University, West Lafayette, Indiana, December 1994.

[60] E. T. Campbell. Bifurcations from Families of Periodic Solutions in the Circular Restricted Problem with Application to Trajectory Design. Ph.D. Dissertation, School of Aeronautics and Astronautics, Purdue University, West Lafayette, Indiana, August 1999.

[61] G. Iooss and D. D. Joseph. Bifurcation and stability of nT-periodic solutions branching from T-periodic solutions at points of resonance. *Archive for Rational Mechanics and Analysis*, 66:135–172, 1977.

[62] D. J. Grebow. Generating Periodic Orbits in the Circular Restricted Three Body Problem with Applications to Lunar South Pole Coverage. M.S. Thesis, School of Aeronautics and Astronautics, Purdue University, West Lafayette, Indiana, May 2010.

[63] W. Schlei, K. Howell, X. Tricoche, and C. Garth. Enhanced Visualization and Autonomous Extraction of Poincar Map Topology. In *AAS/AIAA Astrodynamics Specialist Conference*, Hitlon Head, South Carolina, August 2013.

[64] G. Gómez, W. S. Koon, M. W. Lo, J. E. Marsden, J. Masdemont, and S. D. Ross. Connecting orbits and invariant manifolds in the spatial restricted three-body problem. *Nonlinearity*, 17(5):1571, 2004.

[65] A. J. Lichtenberg and M. A. Lieberman. *Regular and Chaotic Dynamics*. Springer-Verlag, New York, 2nd edition, 1992.

[66] J. Guckenheimer and P. Holmes. *Nonlinear Oscillations, Dynamical Systems, and Bifurcations of Vector Fields*. Springer-Verlag, New York, 1983.

[67] S. H. Strogatz. *Nonlinear Dynamics and Chaos*. Westview Press, Perseus Books Publishing, Cambridge, Massachusetts, 1994.

[68] X. Tricoche, C. Garth, A. Sanderson, and K. Joy. Visualizing invariant manifolds in area-preserving maps. In Ronald Peikert, Helwig Hauser, Hamish Carr, and Raphael Fuchs, editors, *Topological Methods in Data Analysis and Visualization II*, Mathematics and Visualization, pages 109–124. Springer Berlin Heidelberg, 2012.

[69] B. Cabral and L. C. Leedom. Imaging vector fields using line integral convolution. In *Proceedings of the 20th Annual Conference on Computer Graphics and Interactive Techniques*, SIGGRAPH '93, pages 263–270, New York, NY, USA, 1993. ACM.

[70] C. R. Short and K. C. Howell. Lagrangian coherent structures in various map representations for application to multi-body gravitational regimes. *Acta Astronautica*, 94(2):592 – 607, 2014.

[71] M. Vaquero and K. Howell. Leveraging Resonant Orbit Manifolds to Design Transfers between Libration Point Orbits. *Journal of Guidance, Control, and Dynamics*, 37(4):1143–1157, 2014.

[72] M. Vaquero and K. Howell. Design of Transfer Trajectories between Resonant Orbits in the Restricted Three-Body Problem with Application to the Earth-Moon System. *Acta Astronautica*, 94:302–307, 2014.

[73] S. J. Ostro, J-L. Margot, L. A. M. Benner, J. D. Giorgini, D. J. Scheeres, E. G. Fahnestock, S. B. Broschart, J. Bellerose, M. C. Nolan, C. Magri, P. Pravec, P. Scheirich, R. Rose, R. F. Jurgens, E. M. De Jong, and S. Suzuki. Radar imaging of binary near-earth asteroid (66391) 1999 kw4. *Science*, 314(5803):1276–1280, 2006.

[74] A. Levant. Sliding Order and Sliding Accuracy in Sliding Mode Control. *International Journal of Control*, 58(6):1247–1263, 1993.

[75] A. Levant. Higher-order sliding modes, differentiation and outputfeedback control. *International Journal of Control*, 76:924–941, 2003.

[76] B. Wie and J. Lu. Feedback control logic for spacecraft eigenaxis rotations under slew rate and control constraints. *Journal of Guidance Control Dynamics*, 18:1372–1379, November 1995.

[77] G. Gomez, J. J. Masdemont, and J. M. Mondelo. Dynamical substitutes of the libration points for simplified solar system models. In *Libration Point Orbits and Applications: Proceedings of the Conference, Aiguablava, Spain, 10-14 June 2002*, page 373, 2003.

[78] X. Y. Hou and L. Liu. On quasi-periodic motions around the triangular libration points of the real earth–moon system. *Celestial Mechanics and Dynamical Astronomy*, 108(3):301–313, 2010.

[79] X. Y. Hou and L. Liu. On quasi-periodic motions around the collinear libration points in the real earth–moon system. *Celestial Mechanics and Dynamical Astronomy*, 110(1):71–98, 2011.

[80] D. J. Scheeres. Satellite Dynamics About Asteroids. In *Spaceflight Mechanics 1994, Part I, Advances in the Astronautical Sciences Series*, volume 87, pages 275–292, San Diego, California, 1994. Univelt.

[81] K. Richter and H. U. Keller. On the stability of dust particle orbits around cometary nuclei. *Icarus*, 114(2):355 – 371, 1995.

[82] D. P. Hamilton and Alexander V. K. Circumplanetary dust dynamics: Effects of solar gravity, radiation pressure, planetary oblateness, and electromagnetism. *Icarus*, 123(2):503 – 523, 1996.

[83] C. D. Murray and S. F. Dermott. *Solar System Dynamics*. Cambridge University Press, 2000.

[84] F. Mignard and M. Henon. About an unsuspected integrable problem. *Celestial Mechanics*, 33(3):239–250, 1984.

[85] N. Bosanac, K. Howell, and E. Fischbach. Stability of Orbits Near Large Mass Ratio Binary Systems. In *2nd IAA Conference on Dynamics and Control of Space Systems*, Roma, Italy, March 24-26 2014.

[86] L. Chappaz and K. Howell. Bounded Orbits near Binary Systems Comprised of Small Irregular Bodies. In *AIAA/AAS Astrodynamics Specialist Conference*, San Diego, California, August 2014.

[87] D. J. Scheeres, S. B. Broschart, S. J. Ostro, and L. A. Benner. The Dynamical Environment About Asteroid 25143 Itokawa, Target of the Hayabusa Mission. In *AIAA/AAS Astrodynamics Specialist Conference and Exhibit*, Providence, Rhode Island, August 16-19, 2004.

[88] S. B. Broschart, G. Lantoine, and D. J. Grebow. Quasi-terminator orbits near primitive bodies. *Celestial Mechanics and Dynamical Astronomy*, pages 1–21, 2014.

[89] M. T. Zuber, D. E. Smith, D. H. Lehman, T. L. Hoffman, S. W. Asmar, and M. M. Watkins. Gravity recovery and interior laboratory (grail): Mapping the lunar interior from crust to core. *Space Science Reviews*, 178(1):3–24, 2013.

[90] B. D. Tapley, S. Bettadpur, J. C. Ries, P. F. Thompson, and M. M. Watkins. Grace measurements of mass variability in the earth system. *Science*, 305(5683):503–505, 2004.

[91] M. T. Zuber, D. E. Smith, M. M. Watkins, S. W. Asmar, A. S. Konopliv, F. G. Lemoine, H. J. Melosh, G. A. Neumann, R. J. Phillips, S. C. Solomon, M. A. Wieczorek, J. G. Williams, S. J. Goossens, G. Kruizinga, E. Mazarico, R. S. Park, and D-N. Yuan. Gravity field of the moon from the gravity recovery and interior laboratory (grail) mission. *Science*, 339(6120):668–671, 2013.

[92] A. S. Konopliv, R. S. Park, D-N. Yuan, S. W. Asmar, M. M. Watkins, J. G. Williams, E. Fahnestock, G. Kruizinga, M. Paik, D. Strekalov, N. Harvey, D. E. Smith, and M. T. Zuber. High-resolution lunar gravity fields from the grail primary and extended missions. *Geophysical Research Letters*, 41(5):1452–1458, 2014.

[93] F. G. Lemoine, S. Goossens, T. J. Sabaka, J. B. Nicholas, E. Mazarico, D.D. Rowlands, B. D. Loomis, D. S. Chinn, G. A. Neumann, D. E. Smith, and M. T. Zuber. Grgm900c: A degree 900 lunar gravity model from grail primary and extended mission data. *Geophysical Research Letters*, 41(10):3382–3389, 2014.

[94] M. S. Robinson, J. W. Ashley, A. K. Boyd, R. V. Wagner, E. J. Speyerer, B. R. Hawke, H. Hiesinger, and C. H. van der Bogert. Confirmation of sublunarean voids and thin layering in mare deposits. *Planetary and Space Science*, 69(1):18 – 27, 2012.

[95] V. R. Oberbeck, W. L. Quaide, and R. Greeley. On the Origin of Lunar Sinuous Rilles. *Modern Geology*, 1:75–80, 1969.

[96] D. M. Hurwitz, J. W. Head, and H. Hiesinger. Lunar sinuous rilles: Distribution, characteristics, and implications for their origin. *Planetary and Space Science*, 79-80(0):1 – 38, 2013.

[97] D. E. Smith, M. T. Zuber, G. B. Jackson, J. F. Cavanaugh, G. A. Neumann, H. Riris, X. Sun, R. S. Zellar, C. Coltharp, J. Connelly, R. B. Katz, I. Kleyner, P. Liiva, A. Matuszeski, E. M. Mazarico, J. F. McGarry, A.-M. Novo-Gradac, M. N. Ott, C. Peters, L. A. Ramos-Izquierdo, L. Ramsey, D. D. Rowlands, S. Schmidt, V. S. Scott, G. B. Shaw, J. C. Smith, J.-P. Swinski, M. H. Torrence, G. Unger, A. W. Yu, and T. W. Zagwodzki. The Lunar Orbiter Laser Altimeter Investigation on the Lunar Reconnaissance Orbiter Mission. *Space Science Reviews*, 150:209–241, January 2010.

[98] W. S. Kiefer, R. J. Macke, D. T. Britt, A. J. Irving, and G. J. Consolmagno. Regional Variability in the Density of Lunar Mare Basalts and Implications for Lunar Gravity Modeling. In *Lunar and Planetary Science Conference*, volume 43 of *Lunar and Planetary Science Conference*, page 1642, March 2012.

[99] J. C. Andrews-Hanna, S. W. Asmar, J. W. Head, W. S. Kiefer, A. S. Konopliv, F. G. Lemoine, I. Matsuyama, E. Mazarico, P. J. McGovern, H. J. Melosh, G. A. Neumann, F. Nimmo, R. J. Phillips, D. E. Smith, S. C. Solomon, G. J. Taylor, M. A. Wieczorek, J. G. Williams, and M. T. Zuber. Ancient igneous intrusions and early expansion of the moon revealed by grail gravity gradiometry. *Science*, 339(6120):675–678, 2013.

[100] D. M. Blair, L. CHappaz, R. Sood, C. Millbury, A. Bobet, H. J. Melosh, and K. C. Howell. Determining the structural stability of lunar lava tubes. *Icarus*, Submitted.

VITA

VITA

Loic Patrice Rene Chappaz was born to Gilles and Sylvie Chappaz in Annecy. France on June 23, 1987. He graduated from Lycee Charles Baudelaire in June 2005 and studied at the Superior School of Automotive Construction and Aeronautic Techniques (ESTACA) in France, towards his 'Diplome d'ingenieur' in Aerospace Engineering.

Loic began his graduate studies at Purdue in August 2009, in parallel with his studies in France, allowing him to obtain a double degree in December 2011, Master of Science in Aeronautics and Astronautics (MSAA) from Purdue and Diplome d'ingenieur from ESTACA. During graduate school, Loic spent some time at the Jet Propulsion Laboratory, working as a summer intern in 2014 under the guidance of Dr. Steve Broschart.